August 2013

Fibrinogen-Conjugated Gold-coated Magnetite Nanoparticles for Antiplatelet Therapy

Evan Schuerer Krystofiak
University of Wisconsin-Milwaukee

FIBRINOGEN-CONJUGATED GOLD-COATED MAGNETITE NANOPARTICLES

FOR ANTIPLATELET THERAPY

by

Evan Krystofiak

A Dissertation Submitted in

Partial Fulfillment of the

Requirements for the Degree of

Doctor of Philosophy

in Biological Sciences

at

The University of Wisconsin-Milwaukee

August 2013

ABSTRACT
FIBRINOGEN-CONJUGATED GOLD-COATED MAGNETITE NANOPARTICLES
FOR ANTIPLATELET THERAPY

by

Evan Krystofiak

The University of Wisconsin-Milwaukee, 2013
Under the Supervision of Professor Julie Oliver

Ischemic stroke is the world's second leading cause of death and accounts for 2-4% of

total worldwide healthcare costs. Ischemic stroke is caused by the occlusion of arteries

responsible for supplying blood to the brain, which can result in disability or death.

Arterial blood clots consist of aggregates of activated platelets wrapped in a mesh of

fibrin. Tissue plasminogen activator, the only current FDA-approved treatment for

ischemic stroke, functions by lysing fibrin in a blood clot. Unfortunately, tissue

plasminogen activator significantly increases bleeding risks, which restricts its use.

Alternatively, targeting and disrupting platelets within a clot could improve stroke

outcome. To test this hypothesis, we have developed a targeting system utilizing

fibrinogen to specifically target nanoparticles to activated platelets. Human fibrinogen

was evaluated for targeting both human and murine platelets under conditions that are

similar to an *in vivo* blood clot. Our results indicate that human fibrinogen conjugated to

gold nanoparticles was capable of targeting activated human and murine platelets.

Further, human fibrinogen conjugates bound to preformed platelet aggregates while in the

presence of plasma levels of unconjugated fibrinogen. To disrupt platelets, we developed

a system to cause localized hyperthermia to the platelet surface by utilizing inductively

heated magnetic nanoparticles. Magnetic gold-coated magnetite nanoparticles were

synthesized and characterized. The morphology of the gold-coated magnetite product

ii

differed substantially from the expected core-shell structure often reported for such nanoparticles. Despite the unexpected morphology, the nanoparticles could still be functionalized with protein and targeted to activated platelets. Localized hyperthermia was created when platelet-bound, fibrinogen-conjugated, gold-coated magnetite nanoparticles were exposed to an oscillating magnetic field. The effects of the hyperthermic treatment to surface-activated and aggregated platelets were evaluated by electron microscopy. The treated platelets demonstrated considerable structural damage, with the cell membrane showing significant disruption when compared to controls. A method to quantify platelet damage was developed and utilized to refine the length of exposure to the oscillating magnetic field and dose of nanoparticles. In the future, it may be feasible to use fibrinogen-conjugated, gold-coated magnetite to target and disrupt platelets in a thrombus *in vivo*, thereby restoring blood flow to ischemic brain.

TABLE OF CONTENTS

LIST OF FIGURES

LIST OF TABLES

LIST OF ABBREVIATIONS

1. $\alpha_{IIB}\beta_3$: The integrin $\alpha_{IIB}\beta_3$ also known as glycoprotein IIB/IIIA

2. AC: Adenylate cyclase

3. ADP: Adenosine diphosphate

4. BSA: Bovine serum albumin

5. BSE: Backscattered electron

6. CD62P: P-selectin

7. CGS: Citrate glucose saline buffer

8. ddH_2O: Double deionized H_2O

9. FGN: Fibrinogen

10. FGN-Au: Fibrinogen conjugated to colloidal gold nanoparticles

11. FGN-Au-Fe3O4: Fibrinogen conjugated to gold-coated magnetite nanoparticles

12. $G\alpha12$: $G_{\alpha12/13}$

13. HEPES: 4-(2-hydroxyethyl)-1-piperazineethanesulfonic acid

14. HRTEM: High resolution transmission electron microscopy

15. HSA: Human serum albumin

16. MTT: 3-(4,5-dimethylthiazol)-2-diphenyltertrazolium bromide

17. OCS: Open canalicular system

18. OMF: Oscillating magnetic field

19. PAR: Protease activated receptor

20. PAR1: Protease activated receptor 1

21. PAR4: Protease activated receptor 4

22. PBS: Phosphate buffered saline

ACKNOWLEDGMENTS

I would like to express my gratitude to my advisor, Dr. Julie Oliver. She has helped me throughout my time at University of Wisconsin – Milwaukee. She has shape my view of biological sciences and further guided my understanding of the scientific method, academic publication, and future career options. Without Dr. Oliver's intellect and patient personality this dissertation would not be possible.

I would also like to thank Dr. Heather Owen and Dr. Marija Gajdardziska-Josifovska for mentoring me in electron microscopy. They provided me with a wealth of knowledge in electron microscopy and a future career path that bridges biological and physical electron microscopy.

I further want to thank my remaining committee member, Dr. Doug Steeber, Dr. Ralph Albrecht, and Dr. Peter Geissinger for their help in shaping my research and this dissertation.

Lastly I would like to acknowledge the love and support from my significant other Shannon Kordus and my family.

Chapter 1: Development of a novel treatment for ischemic stroke

Statement of the problem: Impact of stroke:

A stroke can be defined as a disturbance in blood supply to the brain that causes rapid loss of brain function. The result of most strokes is the infarction of tissue in the brain that can quickly lead to permanent brain damage which can cause disability or death (1). Stroke is the fourth leading cause of death in the United States (2) and the second cause of death worldwide (3). Many stroke survivors develop permanent physical and/or mental disabilities, including loss of mobility, speech, and emotional control. Strokes account for an annual cost of $25 billion in the United States (4) and 2-4% of the total healthcare costs globally (5), with large long term costs to society caused by disability and loss of work hours (6, 7). Despite the enormous impact of stroke, current treatments are extremely limited and new approaches to therapy are profoundly needed.

The majority of strokes are ischemic (see P*athology underlying stroke*) and caused by an arterial blood clot that blocks delivery of oxygen and nutrients to tissue downstream of the vascular occlusion. Arterial clots are composed of a combination of platelets and fibrin, both of which are potential targets for stroke therapy.

Platelets as a target for stroke treatment:

Blood clots form when an activation event triggers the blood coagulation cascade proteins and activates platelets. The blood coagulation cascade produces the serine protease thrombin which converts the plasma protein fibrinogen to fibrin. Activated

platelets stick to one another at the injury site to form a platelet aggregate in a fibrinogen-dependent process. The blood coagulation system works with platelets to form an arterial blood clot, shown in Figure 1. Under pathological conditions, inappropriate activation of the coagulation cascade (fibrin generation) predominates on the venous side of the vasculature, while inappropriate clotting on the arterial side depends on a combination of platelets and fibrin (8, 9). The majority of ischemic strokes occur in arteries within the brain and thus consists of a blood clot that contains both fibrin and activated platelets. The current ischemic stroke therapy lyses the fibrin component of the blood clot to attempt to dissolve the occlusion and restore blood flow.

Targeting the platelet component of the blood clot may provide an alternative and possibly superior method of disrupting blood clots in ischemic stroke. Inhibition of platelet activation is used successfully to prevent further thrombotic events in patients who have already had previous complications such as ischemic stroke or myocardial infarction. Platelet activation inhibitors such as acetylsalicylic acid (aspirin) (10) or clopridogrel (Plavix®) (11); or preventing platelet aggregation by blocking the platelet fibrinogen receptor (12, 13), have been shown to be effective in preventing heart attack. The use of aspirin to inhibit platelets, together with warfarin to inhibit the blood coagulation cascade, has been shown to reduce embolic risks in patients fitted with artificial heart valves (14). The effectiveness of these preventative treatments demonstrate that anti-platelet therapy can be a powerful tool in precluding arterial blood clotting.

Normal platelet physiology:

Platelets are circulating cell fragments that primarily function to maintain normal hemostasis. Platelets are derived from the bone marrow where they fragment from resident megakaryocytes and are released into the blood (15-17). Mammalian platelets normally lack a nucleus and much of the cellular machinery found in other cells but retains membrane, granules, and mitochondria that originated in the parent megakaryocyte. The lack of a nucleus results in the platelet having very limited ability to synthesize new protein during its entire lifespan. As a result, irreversible inhibitors such as acetylsalicylic acid can permanently impair the platelet proteins they bind to, having long lasting effects.

The morphology of resting platelets in circulation is discoid. This morphology is maintained by a ring-shaped bundle of microtubules at the platelet periphery, known as the circumferential band of microtubules. The platelet interior is filled with two types of granules. Degranulation occurs during platelet activation, allowing the contents of the granules to participate in hemostasis and wound healing. Platelet alpha granules contain growth factors and proteins important for blood clotting such as thrombospondin, von Willebrand factor, and fibrinogen (18). The adhesion molecule P-selectin (CD62P) is sequestered in the membrane of the alpha granules, and is exposed to the surface only upon membrane fusion that occurs during degranulation. CD62P recruits leukocytes expressing P-selectin glycoprotein ligand-1 to the site of platelet activation as an

inflammation response (19). Additionally CD62P can be used as a marker for platelet

degranulation to determine platelet activation level (20).

Platelet dense granules are named based on their appearance in electron micrographs, and

contain soluble mediators such as serotonin, adenosine diphosphate (ADP), and calcium

(21). Platelets also contain a network of membrane invaginations that extend throughout

the platelet interior, known as the open canalicular system (OCS) (22). The OCS is

continuous with platelet surface membrane, increasing the platelet surface area that is

available for interaction with its outside environment and acting as a reservoir of platelet

plasma membrane. These features in resting platelets are shown in Figure 2.

Upon exposure to a stimulus the platelets become activated which causes a myriad of

changes in platelet physiology. The platelet cytoskeleton undergoes extensive

rearrangement causing the shape of the platelet to change from discoid to a rounded ball

and creating pseudopodial extensions (23). The extent of the shape change and extension

of the pseudopodia is directly dependent on the platelet activation pathway (24). Platelets

exposed to an activating surface will spread over that surface, flattening out and greatly

increasing the apparent size of the platelet (23, 25). Strong activation signals will elicit

platelets to release their granules into the extracellular environment (20). The granule

contents can then recruit other platelets into an activated state (26), promote the blood

coagulation cascade (27), and promote healing by release of growth factors (28). The

platelets also become competent to bind fibrinogen which allows platelets to crosslink to

one another, forming a platelet aggregate (Figure 3); this process is described later in this chapter.

Platelet activation pathway:

Platelet activation can be caused by a variety of agonists or contact with a charged foreign surface. Physiologic agonists include adenosine diphosphate (ADP) (29-31), epinephrine (30, 32), thombin (30, 31, 33) and collagen (30, 31, 34, 35), with the latter two being the dominant platelet activators *in vivo*.

Platelet activation pathways make extensive use of G-protein coupled receptor signaling with the $G_{\alpha i}$, $G_{\alpha q,}$ and $G_{\alpha 12/13}$, subunits. $G_{\alpha i}$ functions by blocking adenylate cyclase activity within the platelet, preventing production of cAMP. $G_{\alpha q}$ activates phospholipase C-β which cleaves membrane phosphatidylinositol 4,5-biphosphate into inositol triphosphate and diacylglycerol; these molecules then cause calcium to be released into the cytoplasm. $G_{\alpha 12/13}$ activates the small GTPase Rho which goes on to cause cytoskeletal rearrangement. The signaling via G-protein couples receptors for common platelet activation and inhibition pathways is depicted in Figure 4.

Each platelet activation pathway has its own unique receptors and pathways but converge into a single common activation pathway (36). In the common pathway phospholipase A2 cleaves phospholipids in the platelet membrane to produce arachidonic acid. The free

arachidonic acid is converted to proinflammatory thromboxane A2 (TXA_2), prostacyclins

and prostaglandins in a cyclooxygenases COX-1 and COX-2 dependent manner (37).

TXA_2 then binds to the G-protein coupled thromboxane receptor. Activation of the

thromboxane receptor activates $G_{\alpha q}$ and $G_{\alpha i}$ (38, 39). The resulting drop in cAMP

production and calcium influx triggers many cellular responses, including the

cytoskeletal rearrangement and degranulation discussed above, and the conformational

change of receptors on the platelet surface.

Thrombin signals through a family of G-protein coupled receptors called the protease

activated receptors (PARs) (40, 41). These receptors have a protease cleavage site near

their C-terminal. Once cleaved, the newly exposed C-terminal becomes a tethered ligand

for itself (42, 43). The primary thrombin receptor in humans is PAR1, with PAR4 acting

as a secondary thrombin receptor (41). Mice lack PAR1 and utilize PAR4 as their

primary thrombin receptor (44). When studying platelets it is often desirable to activate

the PAR receptors to promote full platelet activation but to avoid proteolysis. The PAR

receptors can alternatively be activated with synthetic peptides of the sequences

corresponding to the tethered ligand portion of the receptor. For activating platelets, the

human PAR1 peptide SFLLRN-NH_2 and the murine PAR4 peptide AYPGKF-NH_2 can

be used as agonists (45, 46). The PAR1 and PAR4 couple to many different G proteins

including $G_{\alpha q}$ and $G_{\alpha 12/13}$, PAR1 additionally binds $G_{\alpha i}$ (47, 48).

Collagen signaling occurs through the platelets' primary collagen receptor glycoprotein VI (49) and a secondary receptor, the integrin $\alpha_2\beta_1$ (50). Signaling events lead to activation of phospholipase Cγ2, which leads to increase in cytoplasmic calcium levels (50, 51). The signaling response is most similar to the foreign surface activation pathway in which the platelet encounters a highly charged surface that does not exist in the vasculature. *In vitro* the foreign response pathway is used to create surface-activated platelets by exposing platelets to glass, polystyrene, or formvar surfaces which is a useful system in studying platelet/protein interactions (52-55).

Platelet degranulation releases ADP into the platelets' surrounding environment. This ADP recruits neighboring platelets into an activated state by signaling through the G-protein coupled puringergic receptors P2Y12 and P2Y1. P2Y12 couples to $G_{\alpha i}$ (56) and P2Y1 couples to $G_{\alpha q}$ (57). ADP contrasts with thrombin or collagen in that ADP itself does not typically cause the initial platelet activation event, but rather supports the growth of the secondary platelet response (26).

Platelet activation can be inhibited by preventing activation signals from propagating through the platelet, which is of interest both clinically and for understanding platelet function. Platelet activation can be prevented by the use of calcium chelating agents such as EDTA and sodium citrate. These agents are commonly employed as anticoagulants during venous blood draws to prevent platelet activation and blood coagulation cascade activation. Platelets that have been chelated of external calcium will require the

supplementation of calcium ions before they can become competent for activation again.

Prostacyclin (PGI_2) is produced by endothelial cells using a similar pathway to TXA_2 but

has the opposite effect and is thought to modulate the platelet activation response. PGI_2

binds to the prostacyclin receptor (IP) which activates adenylate cyclase resulting in

cAMP production (58-60). The increased cAMP production prevents platelet activation

(61, 62). Platelet activation may also be prevented by drugs that inhibit the COX

enzymes in the thromboxane pathway such as acetylsalicylic acid and non-steroidal anti-

inflammatory drugs (37). Treatment with COX inhibitors results in the impairment of the

platelet activation system by physiological activating agents.

Platelets and fibrinogen:

Fibrinogen is a 340 kDa plasma dimeric glycoprotein found at a relatively high

concentration of 3 mg/mL in human blood. Fibrinogen monomers consist of three

polypeptide chains (alpha, beta, and gamma), that are connected through a series of

disulfide bonds to form a fibular protein (63). Fibrinogen is vitally important for both the

blood coagulation cascade and platelet aggregate formation. In the blood coagulation

cascade, thrombin cleaves protective peptides off the ends of the fibrinogen alpha and

beta chains (64). With the protective end cap sequence removed from fibrinogen the

newly created fibrin spontaneously polymerizes with other nearby fibrin molecules

creating a dense meshwork around a site of injury. Fibrinogen has just as significant a

role in platelet response to injury. Platelet activation leads to fibrinogen binding which

allows the platelets to become cross-linked to one another to form an aggregate, a vital

step in the normal arterial bleeding response. As a result, fibrinogen binding to its receptor on activated platelets has been extensively studied and characterized (54, 65-69).

Platelets bind fibrinogen through the integrin $\alpha_{IIb}\beta_3$, also known as glycoprotein IIb/IIIa (70). $\alpha_{IIb}\beta_3$ is capable of both integrin inside-out and outside-in signaling. Inside-out signaling occurs during platelet activation when interactions between talin (71, 72) and kindlin (73) cause the cytoplasmic tails of $\alpha_{IIb}\beta_3$ to separate ("inside") causing a conformational change on the extracellular side of the integrin ("out"), which makes it competent to bind fibrinogen (67) in a calcium-dependent manner. This inside-out signaling is heavily dependent on platelet activation (65). Once activated, $\alpha_{IIb}\beta_3$ is capable of binding to a single fibrinogen binding site. The second fibrinogen binding site on the dimer is free to bind to an additional $\alpha_{IIb}\beta_3$ on the same platelet or on an adjacent activated platelet, crosslinking platelets together and forming a platelet aggregate. Outside-in integrin signaling occurs after $\alpha_{IIb}\beta_3$ binds fibrinogen and crosslinks adjacent receptors (69, 74, 75). The fibrinogen cross-linked receptor centralizes on the platelet membrane under the direction of the underlying platelet cytoskeleton. The final location of the migrated cross-linked receptors is dependent on the activated morphology of the platelet. Surface-activated platelets will centralize fibrinogen on the platelet surface to the vicinity of the granulomere, a structure created by unreleased platelet granules often located near the center of the platelet. Platelets activated in suspension or platelets participating in an aggregate will use fibrinogen to produce platelet/platelet junctions

where platelets have become cross-linked together or move bound fibrinogen within the OCS of the platelet (76).

The binding of fibrinogen to its receptor is essential for normal platelet function. Mutations in $\alpha_{IIb}\beta_3$ that prevent fibrinogen binding or blockage of $\alpha_{IIb}\beta_3$ by antibodies prevents platelet aggregation (77-80). One such antibody, abciximab, has been shown to be effective in preventing thrombotic events during percutaneous intervention (13, 81, 82) but has failed to show significant benefit in the treatment of ischemic stroke (83, 84). These trials demonstrated the importance of fibrinogen/$\alpha_{IIb}\beta_3$ interactions in arterial blood clot formation but also the limitation of using an antibody to disrupt a preexisting blood clot.

The interaction between fibrinogen and $\alpha_{IIb}\beta_3$ provides a potentially powerful mechanism to specifically target the platelets in a blood clot. $\alpha_{IIb}\beta_3$ on platelets has been targeted using arginine-glycine-aspartate (RGD) peptide sequences (85, 86). However, fibrinogen may prove superior to RGD peptides because it is thought to only bind to activated platelets that have competent $\alpha_{IIb}\beta_3$, which creates a method to distinguish between quiescent circulating platelets and activated platelets. This method of targeting would also be superior to $\alpha_{IIb}\beta_3$-directed antibodies like abciximab, which do not select for activated $\alpha_{IIb}\beta_3$, and have systematic effects on all platelets. Fibrinogen conjugated to gold nanoparticles has been successfully used to study the fibrinogen/$\alpha_{IIb}\beta_3$ interaction by electron microscopy (25, 52-55, 76, 87-89), suggesting that fibrinogen-conjugated

nanoparticles can be targeted towards activated platelets. We propose that we could use the full fibrinogen molecule to specifically target activated platelets in a blood clot.

Pathology underlying stroke:

Strokes are classified into two broad categories, hemorrhagic and ischemic. Hemorrhagic stroke is caused from bleeding of a vessel within the brain. In hemorrhagic stroke, a blood vessel wall weakens to form an aneurism which can further weaken until the vessel wall ruptures. The resulting blood leakage into the brain may increase intracranial pressure that can lead to neural damage. Further, exposure of neurons to high concentrations of the blood coagulation protease thrombin causes apoptosis via signaling through PARs (90, 91). The best available treatment for hemorrhagic stroke is early detection of the aneurism before it ruptures and to undergo a surgical repair of the vessel. After a rupture has occurred, treatment becomes more difficult. Attempts to repair the vessel or to reduce intracranial pressure may be taken. Prevention of the hemorrhagic stroke can be accomplished by reducing risk factors associated with high prevalence which include hypertension (92, 93), cholesterol imbalance (93), and head trauma.

Ischemic stroke is the occlusion of a blood vessel supplying the brain, leading to hypoxic conditions downstream of the blockage. Ischemic strokes are the most common form of stroke, accounting for more than 80% of all incidences (7). Types of ischemic stroke can be further broken down by cause of the occlusion. Embolic strokes are caused by

embolism where a piece of debris forms somewhere in the body, is swept up by blood flow, and then becomes lodged within a brain vessel. Debris often forms within the heart, in an unclosed foramen ovale (94, 95) or a damaged heart valve (95, 96); or in atherosclerotic arteries (95). Thrombotic strokes occur when an occlusive blood clot forms within an artery in the brain. The most common cause for a thrombotic stroke is the rupture of an atherosclerotic plaque, which initiates blood coagulation (97). Both types of ischemic stroke produce the same outcome, a blood clot restricting blood flow to the brain. The occlusion creates an ischemic core in the brain tissue which was directly fed by the occluded artery. The deprivation of oxygen and nutrition causes a metabolic drop in these cells which quickly leads to cell death by deregulation of cellular K^+ and Ca^{2+} ion gradients (98, 99). Moving outward from the ischemic core, affected brain tissue is referred to as the penumbra (100). This area was only partially fed by the occluded artery. These neurons become silent due to reduced metabolism and are at risk of degradation as the ischemic stroke progresses. The organization of the occluded vessel, ischemic core, and penumbra tissue within the brain in depicted in Figure 5. The penumbra tissue may be restored to normal function if blood flow is safely restored in a timely manner (101), leading to great interest in reperfusion of the penumbra as quickly as possible (102).

Current treatments for ischemic stroke:

The only treatment for ischemic stroke currently approved by the FDA is recombinant tissue plasminogen activator (tPA). The first generation product on the market carries the

generic name alteplase (Activase®, Genetech).   The drug is infused intravenously, where

it catalyzes the production of plasmin from the precursor plasma protein plasminogen.

Plasmin is a protease which lyses the fibrin meshwork within a blood clot, causing the

blood clot to dissolve, and restoring blood flow to the surrounding tissue, reperfusing

ischemic neurons. The treatment has produced positive outcomes in clinical trials (103-

105) but has temporal limitations to its safety and effectiveness (103, 106, 107). Infusion

of tPA causes systemic fibrin lysis not only at the site of ischemic stroke, but in other

regions of the brain and body, resulting in increased bleeding risks. The primary

bleeding risk associated with tPA is intracranial hemorrhage at the occlusion site or

downstream of the occluded vessel. For this reason treatment with tPA can treat an

ischemic stroke but cause a hemorrhagic stroke. Initial studies demonstrated that tPA

administered within 3 hours of stroke onset produced a statistically significant increase in

positive outcomes (103). More recent guidelines state that tPA administration up to 4.5

hours post onset improves outcomes in carefully selected patients (108-111). Treatment

with tPA after this time window results in poorer outcomes and particularly because of

increases in the risk of intracerebral hemorrhage (103). Treatment in this short

therapeutic window is difficult because the stroke patient must arrive at an emergency

room, be diagnosed with a stroke, and have hemorrhagic stroke ruled out.

Second generational tPA drugs have been developed to improve effectiveness. The

modified tPA drugs, reteplase (Retavase®, Boehringer Mannheim) and tenecteplase

(TNKase®, Genentech), have amino acid substitutions which were introduced to increase

their half-life in plasma. The increased half-life of the drugs allows more active drug to

reach the occlusion site and allows plasmin production over a longer time. Of tPA drugs, only alteplase is approved for treating ischemic stroke, reteplase and tenecteplase have undergone clinical trials to determine their effectiveness (112-114). It is unlikely that the increase in half-life of the newer tPA drugs will ablate the hemorrhagic risks already associated with tPA treatment, meaning the treatment window for administration of tPA is unlikely to change.

The FDA has approved the mechanical retrieval of blood clots in large blood vessels, using the MERCI Retrieval (115) and Penumbra devices (116). The MERCI device utilizes a catheter system with an expandable heat activated NiTi memory wire, the wire captures the blood clot which can then be pulled out of the artery (117). The Penumbra system utilizes a catheter to apply suction to a thrombus, allowing for recanalization (118, 119). These devices have less temporal restrictions than tPA and have been used up to 8 hours after occlusion, however they are only available for blood clots occurring in relatively large vessels and are not FDA approved for stroke therapy. The majority of ischemic strokes occurring in smaller vessels may currently only be treated using alteplase, with its temporal and safety limitations.

Development of targeted tPA:

Two general strategies have been attempted to overcome the limitations of infused tPA in treating ischemic stroke. One strategy utilizes nano-systems to control tPA localization or activity at the occlusion site using mechanical means. This strategy has utilized tPA

that is associated with magnetic nanoparticles either by encapsulated tPA and magnetite

nanoparticles in liposomes (120), or by SiO_2-coated Fe_3O_4 nanoparticles directly

conjugated to tPA (121). These treatments then propose utilizing an external static

magnet to direct the nanoparticles to the blood clot causing the stroke, with the intended

effect of limiting systemic effects of tPA by confining it to the desired site. A separate

system utilizing tPA conjugated to nanoparticle aggregates has also been developed.

Under normal conditions, the majority of the tPA is localized within the aggregated

nanoparticles, leaving little tPA exposed to the surrounding blood. Upon exposure to

high shear stress, such as occurs in a partially occluded artery, the aggregates break apart,

exposing tPA at the surface of the clot (122). Another method in development for

targeted tPA delivery to the occlusive clots utilizes tPA complexed to polyethylene glycol

grafted onto anionic gelatin which was reported to reduce the tPA activity. The

complexed tPA activity was restored by exposure to ultrasound at the site of the blood

clot which reportedly released the tPA from gelatin and allowed targeted therapy (123).

These studies represent innovative methods of localizing active tPA to the correct site but

may present issues with biocompatibility. Further, these systems may leave untargeted

tPA in circulation similar to the currently approved tPA therapy.

A second strategy utilizes molecular modifications to tPA that target the molecule to the

desired thrombus and/or modulate its activity. Methods to target tPA to platelets by

attachment of RGD peptide to tPA to target the platelet fibrinogen receptor (85) or

targeting blood clots by conjugating tPA with an anti-fibrin antibody (124) have also

been employed. These strategies suffer from the short half-life of tPA *in vivo* along with

systemic tPA activity. More recently, attempts to target platelets with inactivated tPA have utilized a complex system using tPA conjugated through electrostatic interaction to human serum albumin (HSA) modified with RGD peptides to target the fibrinogen receptor on platelets. The conjugation of tPA to HSA reduces tPA activity. Upon addition of negatively charged heparin, the electrostatic interaction between tPA and HSA is disrupted, dissociating the two proteins (86). The tPA is then active and free to produce plasmin.

Nanoparticle-based targeted cell death:

While the tPA based treatments focus on lysis of the fibrin within blood clots, we propose that targeted destruction of platelets within a blood clot may improve stroke treatments. There has been much interest in the use of nanosystems to specifically target and destroy specific cell types (125-130). The majority of this research has been focused on development of anti-cancer therapies, however, the concept can be applied to any cell types of interest that expresses unique targetable features. Typical therapies entail a two part strategy. The first part of the strategy is to specifically target cell populations of interest. Targeting can be performed through a variety of different targeting molecules such as proteins, lipids, carbohydrates, or organic modifications that can specifically bind to receptors or proteins on the cells of interest. Popular methods of targeting nanoparticles to specific cells often conjugate antibodies directed against proteins expressed on the cell surface or conjugation of ligands to nanoparticles that can target specific receptors. Nanoparticle size can also be used to specifically target phagocytotic

cells. Nanoparticles greater than 40 nm actively promote phagocytosis (131, 132).

Additionally, the size of the nanoparticle may also determine bioaccumulation sites

within the body, which is largely dependent on the ability of the nanoparticles to leave

the blood stream and whether the nanoparticles are phagocytosed (133-135). Careful

choice of a targeting strategy can allow for very specific targeting of a cell type, or even

selection between activated and unactivated cells of the same type.

The second part of the strategy relies on causing nanoparticle-mediated effects such as

death of the cells of interest. Nanosystem-based methods of causing cell death often

consist of cytotoxic agents or nanoparticles capable of causing cell death directly. By

combining cell targeting with a method of causing cell death, the nanoparticle effects can

be quite toxic or damaging as they will be confined to the targeted cells. An example of

such a system utilizes a functionalized liposome encapsulating the chemotherapy agent

doxorubicin. Doxorubicin is normally quite toxic to cardiac tissue, limiting its use as a

chemotherapy agent. Encompassing the drug in a liposome reduces the systematic

toxicity of the drug (136) and allows for targeting of cancer cells via functionalization of

the liposomes with folate (137). Other nanoparticle-based systems that can lead to

cellular destruction include the introduction genetic material to the cell, specific proteins

such as tPA as discussed above, or physical damage caused by hyperthermia.

Inductive hyperthermia as alternative therapy:

Hyperthermia has long been recognized as a method to damage or destroy unwanted cells or tissues. Observations that fever-like conditions could have therapeutic effects on cancer were made as early as 1866 (138). Raising the cell temperature as little as 5° C (from 37° C to 42° C) can have profound effects on cell survival (130, 139). The majority of hyperthermic studies thus far have focused on anti-cancer therapy, as many types of cancer are inherently more sensitive to temperature than normal cells (125, 129, 130, 140, 141). Many methods have been developed ranging from those that can raise the temperature of the whole body to highly localized cell-directed hyperthermia. Hyperthermia treatments may be performed by circulating heated liquid through the peritoneum (142), implanting devices within tumors that are then subsequently heated (143, 144), radio frequency (RF) based tissue heating (145), or using nanosystems that can absorb energy from an external source and convert it into localized heat (140, 146, 147). For most applications, it is preferred to have the treatment be as non-invasive as possible. Injected nanoparticle-based systems that can convert external energy to heat meet this requirement. These systems utilize either near infrared light (127) or RF electric (126, 148) or magnetic fields to cause specific heating of the nanoparticles. Further, nanoparticles can be targeted toward specific cells via functionalization which allows the hyperthermic damage to be confined to the cells or area of interest and prevent damage to healthy tissue.

For our applications, magnetic field-induced hyperthermia using magnetic nanoparticles are of most interest due to the ability to target the nanoparticles specifically towards cell types and the existing body of knowledge of inductive heating (141, 149, 150). Magnetic field frequencies used for inductive heating are relatively low, and are similar to frequencies used for magnetic charging in implantable devices. Nanoparticle hyperthermia performance is specific to composition, crystallinity, and size of the nanoparticles (151). Magnetic fields may transfer energy through three different, but sometimes overlapping, mechanisms (152, 153). The simplest mechanism involves reverse Brownian motion. Nanoparticles are caused to vibrate by the magnetic field, imparting increased kinetic energy on their surrounding environment, in a temperature- and solution viscosity- dependent manner. In nanoparticles large enough to possess a permanent magnetic axis, heating may also be performed via hysteresis loss caused by reordering a magnetic moment within the nanoparticles. The third type of heating may be performed on superparamagnetic nanoparticles that are too small to maintain a permanent magnetic axis. These nanoparticles switch magnetic axis based on the Néel relaxation time of each nanoparticle, which is a size- and temperature-dependent process. The superparamagnetic nanoparticles may be heated by an external oscillating magnetic field, which causes the magnetic axis to flip faster than the Néel relaxation time (149, 153). The RF used for heating superparamagnetic nanoparticles primarily through the Néel relaxation mechanism is preferred for treatments in biological systems due to the relatively simple RF circuitry required and viscosity independence, which is difficult to control *in vivo* and may change over time.

For hyperthermic applications, many types of superparamagnetic nanoparticles have been successfully employed. Of these, the iron oxides magnetite (Fe_3O_4) and maghemite (γ-Fe_2O_3) are the most attractive due to their highly magnetic behavior and safety for use in biological systems. Organically coated iron oxide is used as an injectable iron supplement known as ferumoxytol (Feraheme, AMAG Pharmaceuticals). It was clinically used as a MRI contrast agent but has since been removed from the market due to lack of efficacy. Magnetite- and maghemite-based nanoparticle treatments have been developed for anti-cancer therapy (129, 149, 152, 154-156). Initial treatments proposed for tumor metastases in lymph nodes involved injection of a suspension of sub-micron sized magnetic particles into the lymphatic system, followed by exposure to an oscillating magnetic field (157). Treatments were refined to use smaller (~10 nm) superparamagnetic magnetic nanoparticles that were injected in the vicinity of the tumor and heated by an external magnetic field; the heat generated by the nanoparticles caused hyperthermic cell death (125, 128, 129, 140, 151, 158-162). These treatments relied on physical placement of the particles near the tumor rather than specific targeting, and thus were dependent on bulk heating to produce the desired effect.

Hyperthermia via bulk heating has been applied only to large solid tumors, and has produced limited success. This is due to neighboring "bystander" cells being heated and killed along with the cancerous cells. Further, targeting cells not localized at a single site, such as cells circulating in the blood, requires that the nanoparticle specifically target the cell type. Targeting mechanisms for iron oxide nanoparticles have been developed such as imparting a positive charge to a liposome covering to make the particles pro-

phagocytotic (128), or conjugating antibodies against cell specific surface markers onto the nanoparticle (150, 163). The latter were used mainly for MRI imaging studies, but demonstrate the potential for targeting magnetic nanoparticles toward cells of interest.

Nanoparticles that contain a magnetic iron oxide core with a gold shell have been developed (154, 164, 165). The "core-shell" structure offers advantages over bare iron oxide. The shell is thought to protect the iron-oxide core from external pH, ionic, and oxidative conditions which can all negatively affect the hyperthermia performance of iron oxide nanoparticles (166). The gold coating also provides a surface that may be easily conjugated with proteins. Conjugation of proteins to colloidal gold has been established and used extensively for immunolabeling for transmission electron microscopy (TEM) and scanning electron microscopy (SEM) (25, 52, 167). Successful conjugation of antibodies to the core-shell particles is expected to be very similar. While the core-shell nanoparticle concept appears promising, in practice, synthesis of the core-shell particles is highly variable. Synthesis of magnetite under aqueous conditions leads to variations in size and composition of the iron oxide (151). Growth of gold on an oxide surface adds further complications, as the growth is not well understood. Gold growth on thin films of magnetite on the (001) and (111) surfaces has shown that gold does not easily wet the magnetite surface (168, 169) which leads to the question of how gold growth occurs to surround the iron oxide core in a core-shell like structure. Antibody-conjugated gold-coated magnetite nanoparticles have been successfully targeted to prostate (170) and breast cancer cells (171), producing cell death via magnetic field-induced hyperthermia. Using a protein-based targeting mechanism, these gold-coated magnetite nanoparticles

should be able to target and destroy nearly any type of cell that can be targeted using an antibody or protein, as long as nanoparticles reach the cell surface in sufficient numbers to convey hyperthermic damage.

Main hypothesis:

We hypothesize that localized hyperthermia on activated platelets within a blood clot could cause sufficient damage to dissolve blood clots. We propose targeting platelets within a blood clot using fibrinogen conjugated to gold-coated magnetite nanoparticles. We further hypothesize that conjugation of fibrinogen to the nanoparticles will allow specific targeting of activated platelets within a blood clot and provide a means for the nanoparticles to label the interior of the aggregate utilizing $\alpha_{IIb}\beta_3$ movement after ligand binding. Gold-coated magnetite is expected to provide a nanoparticle that is superparamagnetic and has a gold surface that is easily functionalized with fibrinogen by nonionic adsorption similar to that used with colloidal gold. Lastly, we propose that using these nanoparticles will create hyperthermic conditions highly localized to the platelet surface when the labeled platelets are exposed to an oscillating magnetic field at a frequency used for superparamagnetic-based heating. These conditions should cause structural damage to the platelets, causing them to break apart. The ultimate goal is to cause enough localized damage to cause a blood clot to dissolve, restoring blood flow. The scope of these aims is to develop the fibrinogen-conjugated gold-coated magnetite nanoparticle for targeted platelet destruction using hyperthermia *in vitro*. While all studies were performed *in vitro*, a strong emphasis was placed on how the methodology

is expected to perform *in vivo* in anticipation of future studies using a small animal model

of arterial thrombosis.

Figures and Figure Legends

Figure 1. A simplified diagram of arterial blood clot formation. An activation event leads to the blood coagulation production of thrombin. Thrombin activates resting platelets causing them to enter an activated state. Activated platelets aggregate together in a fibrinogen dependent process. Thrombin also cleaves fibrinogen to fibrin, the fibrin then forms a polymer meshwork. Together the fibrin and platelet aggregates form a blood clot.

Blood Coagulation Cascade

Thrombin

Platelet

Fibrinogen

Activated Platelet

Fibrin

Fibrinogen

Platelet Aggregate

Blood Clot
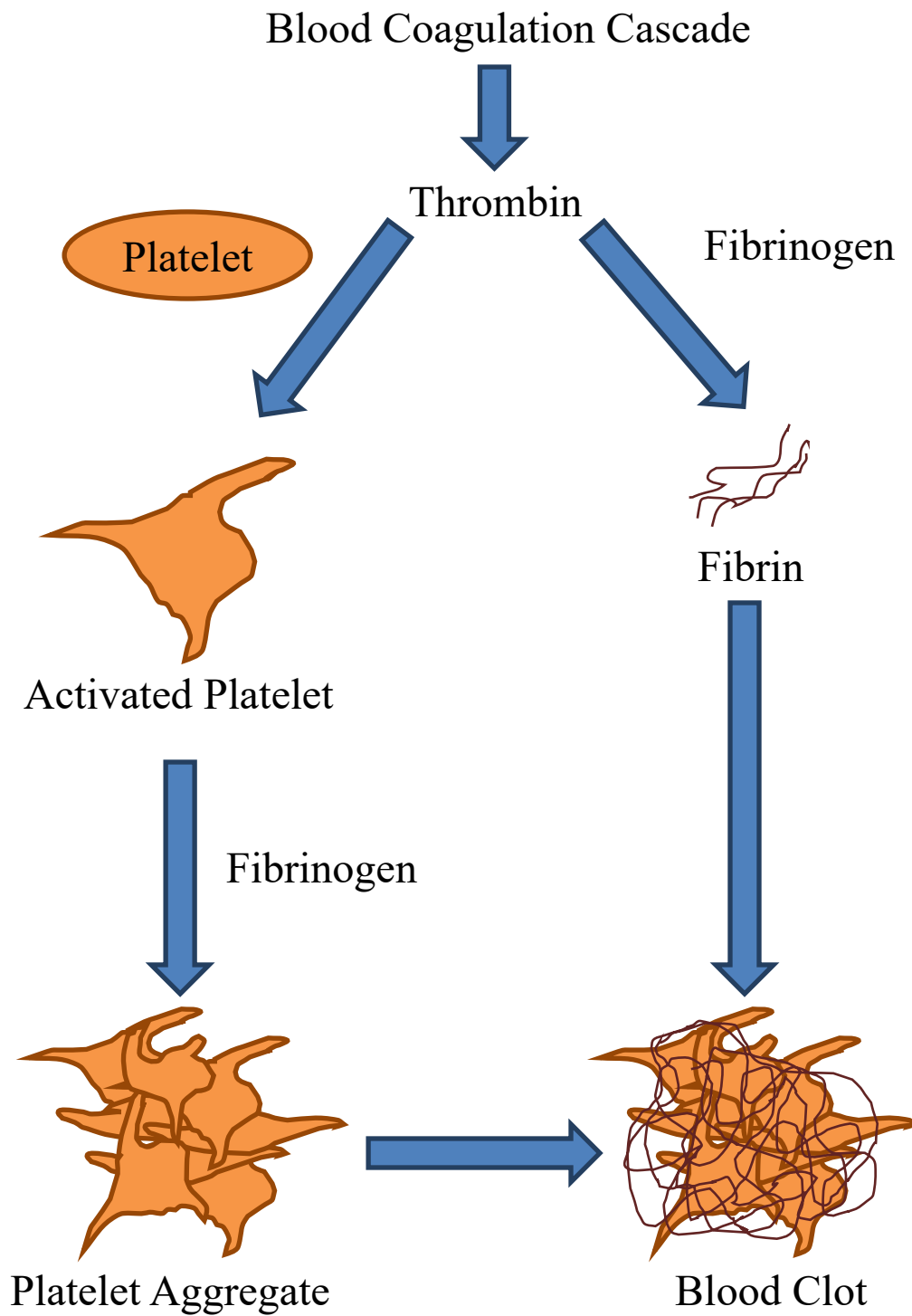
Figure 1

Figure 2. Structural features of a resting platelet. (A) depicts a cross section of a discoid

platelet. Microtubules (MT) are shown in cross section near the periphery of the platelet.

Granules and open canalicular system (OCS) are within the platelet. A top down view of

the platelet is shown in (B). Ultrathin sections of platelets sectioned similar to (A) and

(B) are shown in (C) and (D), respectively. Size bars are 1 μm.
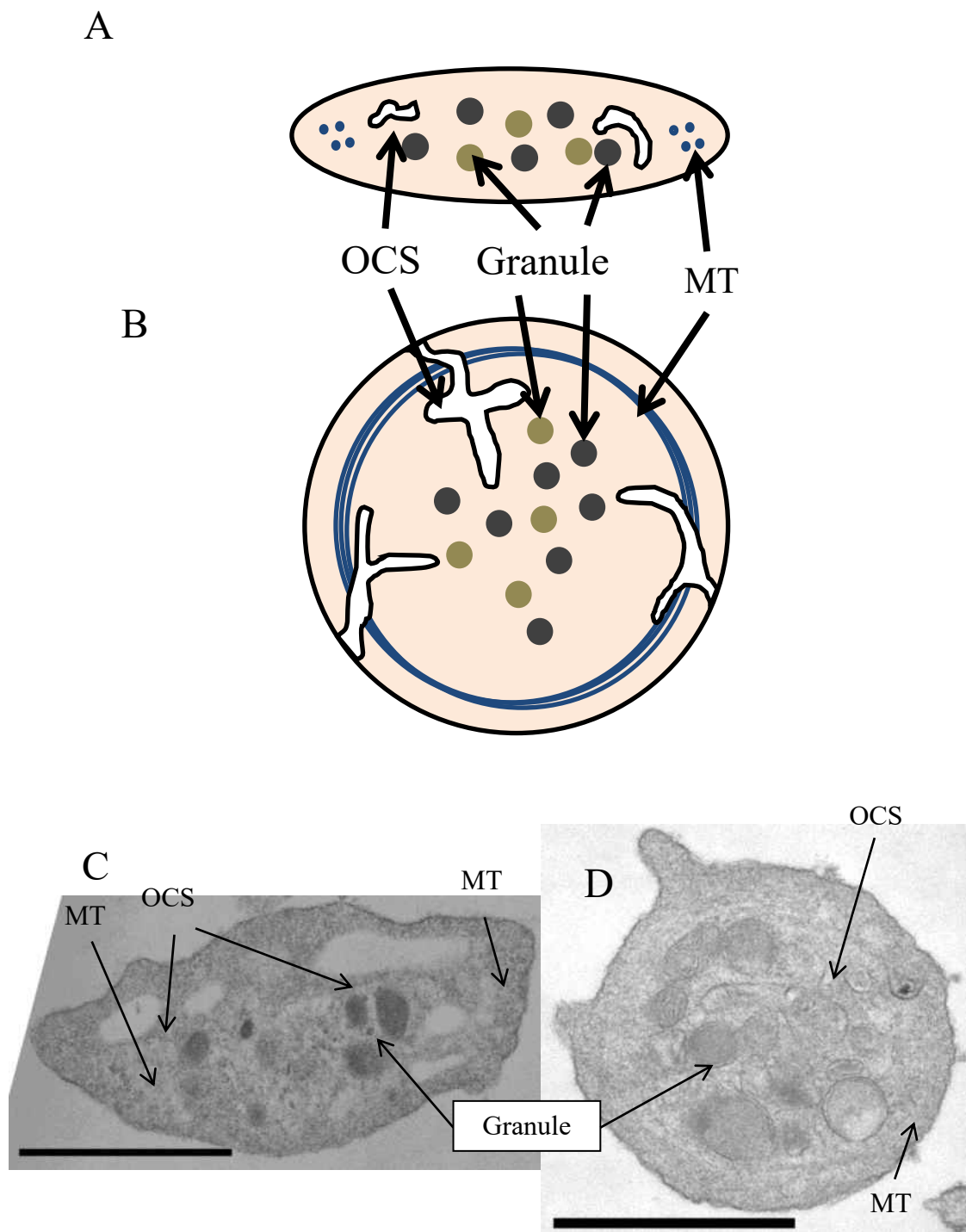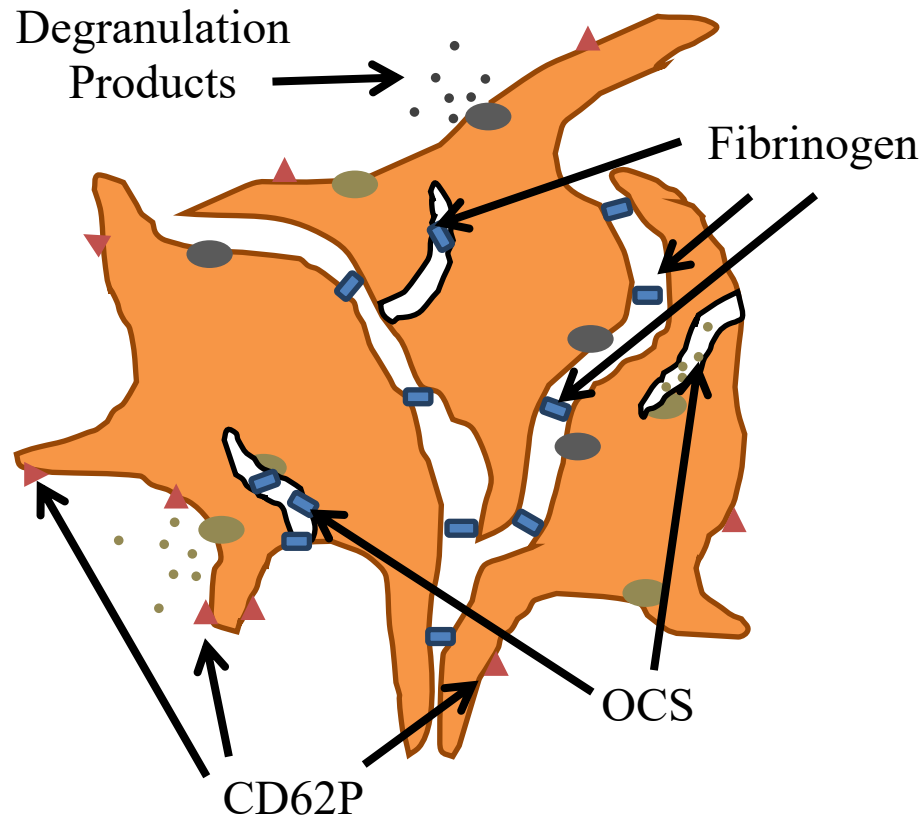
Figure 2

Figure 3. Structural features of activated platelets. Platelets that have experienced a strong activation signal degranulate, releasing the granule contents into the extracellular space either at the platelet surface or into the OCS. Fusion of granules with the platelet membrane causes P-selectin (CD62P) expression (triangles) which can recruit leukocytes to the inflammation site. Platelets aggregate together by binding fibrinogen (rectangles) which crosslinks the platelets. Fibrinogen bound that has crosslinked two adjacent receptors on the same platelet moves into the OCS of the platelet.
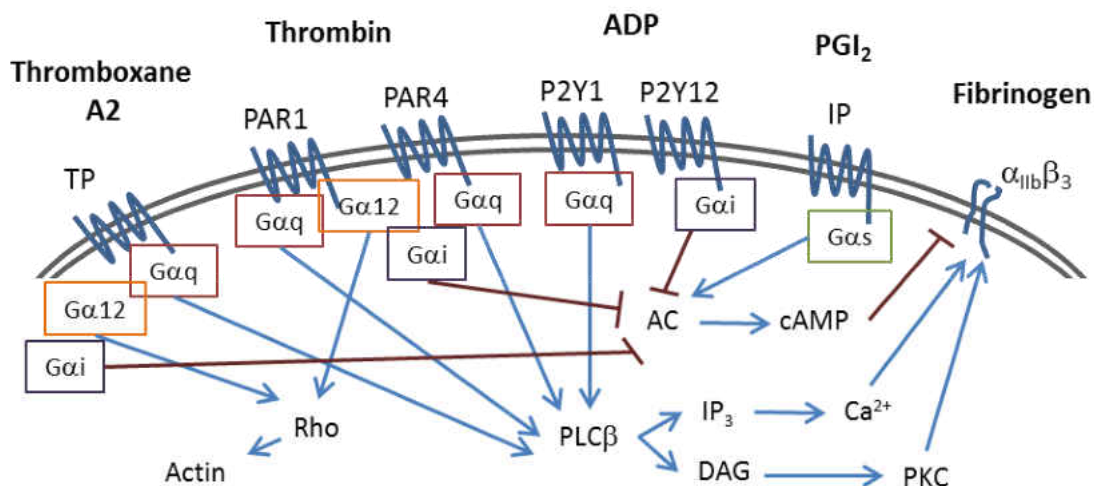
Figure 4. Platelet activation signaling by G-protein coupled receptors. Thrombin signals through protease activated rececptor 1 (PAR1) and protease activated receptor 4 (PAR4) receptors coupled to the $G_{\alpha q}$, $G_{\alpha i}$, and $G_{\alpha 12/13}$ ($G\alpha 12$) subunits. ADP signals through the P2Y1 and P2Y12 receptors which signal through $G_{\alpha q}$ and $G_{\alpha i}$, respectively. The thromboxane receptor (TP) in the common activation pathway signals through $G_{\alpha q}$, $G_{\alpha i}$, and $G_{\alpha 12/13}$. $G_{\alpha q}$ activates phospholipase C (PLCβ). PLCβ produces the secondary signaling molecules inositol triphosphate and diacylglycerol, which lead to calcium release in the cell and ultimately to a conformational change of the fibrinogen receptor $\alpha_{IIb}\beta_3$ into its active state. $G_{\alpha 12/13}$ signals through Rho which causes cytoskeletal changes resulting in platelet shape change. The $G_{\alpha i}$ subunit inhibits adenylate cyclase (AC) causing the cAMP levels in platelets to drop, which causes platelet activation. Prostacyclin (PGI$_2$) signals through the IP receptor which is coupled to a $G_{\alpha s}$ subunit. $G_{\alpha s}$ causes AC to produce cAMP which has inhibitory effects on platelet activation.
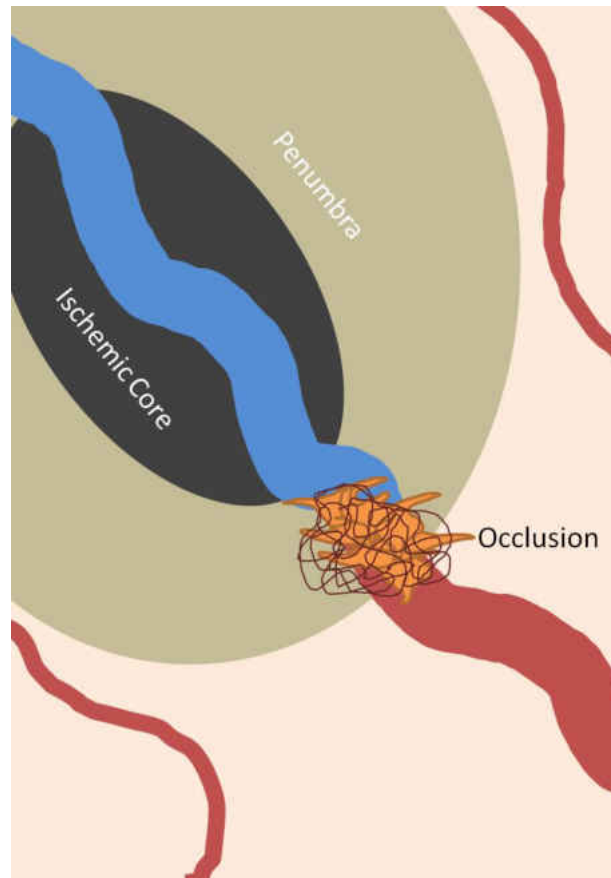
Figure 5. Diagram of ischemic tissues observed after occlusion of an artery supplying the brain. Tissue directly downstream of the occlusion site becomes the ischemic core, this tissue is deprived of oxygen and nutrients from the blood and will die. Tissue partially fed by the occluded artery is called the penumbra. This tissue suffers from less severe hypoxia and can recover if blood flow is restored in a timely manner.

References

1.   Sims, N. R., and H. Muyderman. 2010. Mitochondria, oxidative metabolism and cell death in stroke. *Biochim. Biophys. Acta* 1802:80-91.

2.   2010. Stroke drops to fourth leading cause of death in 2008 life expectancy declines slightly according to latest CDC deaths report. Centers for Disease Control and Prevention, Atlanta, GA. http://www.cdc.gov/media/pressrel/2010/r101209.html.

3.   Mathers, C. D., T. Boerma, and D. Ma Fat. 2009. Global and regional causes of death. *Br. Med. Bull.* 92:7-32.

4.   Roger, V. L., A. S. Go, D. M. Lloyd-Jones, R. J. Adams, J. D. Berry, T. M. Brown, M. R. Carnethon, S. Dai, G. de Simone, E. S. Ford, C. S. Fox, H. J. Fullerton, C. Gillespie, K. J. Greenlund, S. M. Hailpern, J. A. Heit, P. M. Ho, V. J. Howard, B. M. Kissela, S. J. Kittner, D. T. Lackland, J. H. Lichtman, L. D. Lisabeth, D. M. Makuc, G. M. Marcus, A. Marelli, D. B. Matchar, M. M. McDermott, J. B. Meigs, C. S. Moy, D. Mozaffarian, M. E. Mussolino, G. Nichol, N. P. Paynter, W. D. Rosamond, P. D. Sorlie, R. S. Stafford, T. N. Turan, M. B. Turner, N. D. Wong, and J. Wylie-Rosett. 2011. Heart disease and stroke statistics--2011 update: a report from the American Heart Association. *Circulation* 123:e18-e209.

5.   Donnan, G. A., M. Fisher, M. Macleod, and S. M. Davis. 2008. Stroke. *Lancet* 371:1612-1623.

6.   Taylor, T. N., P. H. Davis, J. C. Torner, J. Holmes, J. W. Meyer, and M. F. Jacobson. 1996. Lifetime cost of stroke in the United States. *Stroke* 27:1459-1466.

7.   Flynn, R. W., R. S. MacWalter, and A. S. Doney. 2008. The cost of cerebral ischaemia. *Neuropharmacology* 55:250-256.

8.   Kuijpers, M. J., K. Gilio, S. Reitsma, R. Nergiz-Unal, L. Prinzen, S. Heeneman, E. Lutgens, M. A. van Zandvoort, B. Nieswandt, M. G. Egbrink, and J. W. Heemskerk. 2009. Complementary roles of platelets and coagulation in thrombus formation on plaques acutely ruptured by targeted ultrasound treatment: a novel intravital model. *J. Thromb. Haemost.* 7:152-161.

9.   Smith, J. R., and A. M. White. 1982. Fibrin, red cell and platelet interactions in an experimental model of thrombosis. *Br. J. Pharmacol.* 77:29-38.

10.   Hirsh, J. 1985. Progress review: the relationship between dose of aspirin, side-effects and antithrombotic effectiveness. *Stroke* 16:1-4.

11. Mills, D. C., R. Puri, C. J. Hu, C. Minniti, G. Grana, M. D. Freedman, R. F. Colman, and R. W. Colman. 1992. Clopidogrel inhibits the binding of ADP analogues to the receptor mediating inhibition of platelet adenylate cyclase. *Arterioscler. Thromb. Vasc. Biol.* 12:430-436.

12. De Luca, G., E. Navarese, and P. Marino. 2009. Risk profile and benefits from Gp IIb-IIIa inhibitors among patients with ST-segment elevation myocardial infarction treated with primary angioplasty: a meta-regression analysis of randomized trials. *Eur. Heart J.* 30:2705-2713.

13. Tcheng, J. E., D. E. Kandzari, C. L. Grines, D. A. Cox, M. B. Effron, E. Garcia, J. J. Griffin, G. Guagliumi, T. Stuckey, M. Turco, M. Fahy, A. J. Lansky, R. Mehran, and G. W. Stone. 2003. Benefits and risks of abciximab use in primary angioplasty for acute myocardial infarction: the Controlled Abciximab and Device Investigation to Lower Late Angioplasty Complications (CADILLAC) trial. *Circulation* 108:1316-1323.

14. Turpie, A., M. Gent, A. Laupacis, Y. Latour, J. Gunstensen, F. Basile, M. Klimek, and J. Hirsh. 1993. A comparison of aspirin with placebo in patients treated with warfarin after heart-valve replacement. *N. Engl. J. Med.* 329:524-529.

15. Radley, J. M., and C. J. Haller. 1982. The demarcation membrane system of the megakaryocyte: a misnomer? *Blood* 60:213-219.

16. Choi, E. S., J. L. Nichol, M. M. Hokom, A. C. Hornkohl, and P. Hunt. 1995. Platelets generated in vitro from proplatelet-displaying human megakaryocytes are functional. *Blood* 85:402-413.

17. Josefsson, E. C., C. James, K. J. Henley, M. A. Debrincat, K. L. Rogers, M. R. Dowling, M. J. White, E. A. Kruse, R. M. Lane, S. Ellis, P. Nurden, K. D. Mason, L. A. O'Reilly, A. W. Roberts, D. Metcalf, D. C. Huang, and B. T. Kile. 2011. Megakaryocytes possess a functional intrinsic apoptosis pathway that must be restrained to survive and produce platelets. *J. Exp. Med.* 208:2017-2031.

18. Blair, P., and R. Flaumenhaft. 2009. Platelet α-granules: Basic biology and clinical correlates. *Blood Rev.* 23:177-189.

19. Diacovo, T. G., S. J. Roth, J. M. Buccola, D. F. Bainton, and T. A. Springer. 1996. Neutrophil rolling, arrest, and transmigration across activated, surface-adherent platelets via sequential action of P-selectin and the beta 2-integrin CD11b/CD18. *Blood* 88:146-157.

20. Holmes, M. B., B. E. Sobel, D. B. Howard, and D. J. Schneider. 1999. Differences between activation thresholds for platelet P-selectin and glycoprotein IIb-IIIa expression and their clinical implications. *Thromb. Res.* 95:75-82.

21. McNicol, A., and S. J. Israels. 1999. Platelet dense granules: Structure, function and implications for haemostasis. *Thromb. Res.* 95:1-18.

22. White, J. G., and C. C. Clawson. 1980. The surface-connected canalicular system of blood platelets--a fenestrated membrane system. *Am. J. Pathol.* 101:353-364.

23. Allen, R. D., L. R. Zacharski, S. T. Widirstky, R. Rosenstein, L. M. Zaitlin, and D. R. Burgess. 1979. Transformation and motility of human platelets: Details of the shape change and release reaction observed by optical and electron microscopy. *J. Cell Biol.* 83:126-142.

24. Siess, W., P. C. Weber, and E. G. Lapetina. 1984. Activation of phospholipase C is dissociated from arachidonate metabolism during platelet shape change induced by thrombin or platelet-activating factor. Epinephrine does not induce phospholipase C activation or platelet shape change. *J. Biol. Chem.* 259:8286-8292.

25. Loftus, J. C., and R. M. Albrecht. 1984. Redistribution of the fibrinogen receptor of human platelets after surface activation. *J. Cell Biol.* 99:822-829.

26. Dorsam, R. T., and S. P. Kunapuli. 2004. Central role of the P2Y12 receptor in platelet activation. *J. Clin. Invest.* 113:340-345.

27. Monroe, D. M., M. Hoffman, and H. R. Roberts. 2002. Platelets and thrombin generation. *Arterioscler. Thromb. Vasc. Biol.* 22:1381-1389.

28. Lynch, S. E., J. C. Nixon, R. B. Colvin, and H. N. Antoniades. 1987. Role of platelet-derived growth factor in wound healing: synergistic effects with other growth factors. *Proc. Natl. Acad. Sci. USA* 84:7696-7700.

29. Jarvis, G. E., R. G. Humphries, M. J. Robertson, and P. Leff. 2000. ADP can induce aggregation of human platelets via both P2Y(1) and P(2T) receptors. *Br. J. Pharmacol.* 129:275-282.

30. O'Brien, J. R., and J. B. Heywood. 1966. Effect of aggregating agents and their inhibitors on the mean platelet shape. *J. Clin. Pathol.* 19:148-153.

31. Koutts, J., P. N. Walsh, E. F. Plow, J. W. Fenton, 2nd, B. N. Bouma, and T. S. Zimmerman. 1978. Active release of human platelet factor VIII-related antigen by adenosine diphosphate, collagen, and thrombin. *J. Clin. Invest.* 62:1255-1263.

32. Mills, D. C., and G. C. Roberts. 1967. Effects of adrenaline on human blood platelets. *J. Physiol.* 193:443-453.

33. Kahn, M. L., M. Nakanishi-Matsui, M. J. Shapiro, H. Ishihara, and S. R. Coughlin. 1999. Protease-activated receptors 1 and 4 mediate activation of human platelets by thrombin. *J. Clin. Invest.* 103:879-887.

34. Legrand, C., V. Dubernard, and A. T. Nurden. 1985. Characteristics of collagen-induced fibrinogen binding to human platelets. *Biochim. Biophys. Acta* 812:802-810.

35. Gibbins, J. M., M. Okuma, R. Farndale, M. Barnes, and S. P. Watson. 1997. Glycoprotein VI is the collagen receptor in platelets which underlies tyrosine phosphorylation of the Fc receptor gamma-chain. *FEBS Lett.* 413:255-259.

36. Woulfe, D. S. 2005. Review articles: Platelet G protein-coupled receptors in hemostasis and thrombosis. *J. Thromb. Haemost.* 3:2193-2200.

37. Patrignani, P., P. Filabozzi, and C. Patrono. 1982. Selective cumulative inhibition of platelet thromboxane production by low-dose aspirin in healthy subjects. *J. Clin. Invest.* 69:1366-1372.

38. Ushikubi, F., K. Nakamura, and S. Narumiya. 1994. Functional reconstitution of platelet thromboxane A2 receptors with Gq and Gi2 in phospholipid vesicles. *Mol. Pharmacol.* 46:808-816.

39. Abe, T., K. Takeuchi, N. Takahashi, E. Tsutsumi, Y. Taniyama, and K. Abe. 1995. Rat kidney thromboxane receptor: molecular cloning, signal transduction, and intrarenal expression localization. *J. Clin. Invest.* 96:657-664.

40. Kahn, M. L., Y. W. Zheng, W. Huang, V. Bigornia, D. Zeng, S. Moff, R. V. Farese, Jr., C. Tam, and S. R. Coughlin. 1998. A dual thrombin receptor system for platelet activation. *Nature* 394:690-694.

41. Andersen, H., D. L. Greenberg, K. Fujikawa, W. Xu, D. W. Chung, and E. W. Davie. 1999. Protease-activated receptor 1 is the primary mediator of thrombin-stimulated platelet procoagulant activity. *Proc. Natl. Acad. Sci. USA* 96:11189-11193.

42. Vu, T. K., D. T. Hung, V. I. Wheaton, and S. R. Coughlin. 1991. Molecular cloning of a functional thrombin receptor reveals a novel proteolytic mechanism of receptor activation. *Cell* 64:1057-1068.

43. Brass, L. F., R. R. Vassallo, Jr., E. Belmonte, M. Ahuja, K. Cichowski, and J. A. Hoxie. 1992. Structure and function of the human platelet thrombin receptor. Studies using monoclonal antibodies directed against a defined domain within the receptor N terminus. *J. Biol. Chem.* 267:13795-13798.

44. Sambrano, G. R., E. J. Weiss, Y. W. Zheng, W. Huang, and S. R. Coughlin. 2001. Role of thrombin signalling in platelets in haemostasis and thrombosis. *Nature* 413:74-78.

45. Hollenberg, M. D., M. Saifeddine, S. Sandhu, S. Houle, and N. Vergnolle. 2004. Proteinase-activated receptor-4: Evaluation of tethered ligand-derived peptides as probes for receptor function and as inflammatory agonists in vivo. *Br. J. Pharmacol.* 143:443-454.

46. Faruqi, T. R., E. J. Weiss, M. J. Shapiro, W. Huang, and S. R. Coughlin. 2000. Structure-function analysis of protease-activated receptor 4 tethered ligand peptides: Determinants of specificity and utility in assays of receptor function. *J. Biol. Chem.* 275:19728-19734.

47. Hung, D. T., Y. H. Wong, T. K. Vu, and S. R. Coughlin. 1992. The cloned platelet thrombin receptor couples to at least two distinct effectors to stimulate phosphoinositide hydrolysis and inhibit adenylyl cyclase. *J. Biol. Chem.* 267:20831-20834.

48. Offermanns, S., K. L. Laugwitz, K. Spicher, and G. Schultz. 1994. G proteins of the G12 family are activated via thromboxane A2 and thrombin receptors in human platelets. *Proc. Natl. Acad. Sci. USA* 91:504-508.

49. Knight, C. G., L. F. Morton, D. J. Onley, A. R. Peachey, T. Ichinohe, M. Okuma, R. W. Farndale, and M. J. Barnes. 1999. Collagen-platelet interaction: Gly-Pro-Hyp is uniquely specific for platelet Gp VI and mediates platelet activation by collagen. *Cardiovasc. Res.* 41:450-457.

50. Inoue, O., K. Suzuki-Inoue, W. L. Dean, J. Frampton, and S. P. Watson. 2003. Integrin α2β1 mediates outside-in regulation of platelet spreading on collagen through activation of Src kinases and PLCγ2. *J. Cell Biol.* 160:769-780.

51. Pasquet, J.-M., B. Gross, L. Quek, N. Asazuma, W. Zhang, C. L. Sommers, E. Schweighoffer, V. Tybulewicz, B. Judd, J. R. Lee, G. Koretzky, P. E. Love, L. E. Samelson, and S. P. Watson. 1999. LAT Is required for tyrosine phosphorylation of phospholipase Cγ2 and platelet activation by the collagen receptor GPVI. *Mol. Cell. Biol.* 19:8326-8334.

52. Albrecht, R. M., J. A. Oliver, and J. C. Loftus. 1985. Observation of colloidal gold labelled platelet surface receptors and the underlying cytoskeleton using high voltage electron microscopy and scanning electron microscopy. In *The Science of Biological Specimen Preparation*. R. P. B. M. Mueller, A. Boyde, and J. J. Wolosewick, Eds., ed. AMF O'Hare, Chicago. 185-193.

53. Loftus, J. C., J. Choate, and R. M. Albrecht. 1984. Platelet activation and cytoskeletal reorganization: high voltage electron microscopic examination of intact and Triton-extracted whole mounts. *J. Cell Biol.* 98:2019-2025.

54. Olorundare, O. E., S. R. Simmons, and R. M. Albrecht. 1992. Cytochalasin D and E: effects on fibrinogen receptor movement and cytoskeletal reorganization in fully spread, surface-activated platelets: a correlative light and electron microscopic investigation. *Blood* 79:99-109.

55. Simmons, S. R., P. A. Sims, and R. M. Albrecht. 1997. Alpha IIb beta 3 redistribution triggered by receptor cross-linking. *Arterioscler. Thromb. Vasc. Biol.* 17:3311-3320.

56. Bodor, E. T., G. L. Waldo, S. B. Hooks, J. Corbitt, J. L. Boyer, and T. K. Harden. 2003. Purification and functional reconstitution of the human P2Y12 receptor. *Mol. Pharmacol.* 64:1210-1216.

57. Hollopeter, G., H. M. Jantzen, D. Vincent, G. Li, L. England, V. Ramakrishnan, R. B. Yang, P. Nurden, A. Nurden, D. Julius, and P. B. Conley. 2001. Identification of the platelet ADP receptor targeted by antithrombotic drugs. *Nature* 409:202-207.

58. Kennedy, I., R. A. Coleman, P. P. Humphrey, G. P. Levy, and P. Lumley. 1982. Studies on the characterisation of prostanoid receptors: a proposed classification. *Prostaglandins* 24:667-689.

59. Armstrong, R. A., R. A. Lawrence, R. L. Jones, N. H. Wilson, and A. Collier. 1989. Functional and ligand binding studies suggest heterogeneity of platelet prostacyclin receptors. *Br. J. Pharmacol.* 97:657-668.

60. Murata, T., F. Ushikubi, T. Matsuoka, M. Hirata, A. Yamasaki, Y. Sugimoto, A. Ichikawa, Y. Aze, T. Tanaka, N. Yoshida, A. Ueno, S. Oh-ishi, and S. Narumiya. 1997. Altered pain perception and inflammatory response in mice lacking prostacyclin receptor. *Nature* 388:678-682.

61. Weiss, H. J., and V. T. Turitto. 1979. Prostacyclin (prostaglandin I2, PGI2) inhibits platelet adhesion and thrombus formation on subendothelium. *Blood* 53:244-250.

62. Noé, L., K. Peeters, B. Izzi, C. Van Geet, and K. Freson. 2010. Regulators of platelet cAMP levels: clinical and therapeutic implications. *Curr. Med. Chem.* 17:2897-2905.

63. Doolittle, R. F. 1983. The structure and evolution of vertebrate fibrinogen. *Ann. N. Y. Acad. Sci.* 408:13-27.

64. Scheraga, H. A. 2004. The thrombin-fibrinogen interaction. *Biophys. Chem.* 112:117-130.

65. Shattil, S. J., J. A. Hoxie, M. Cunningham, and L. F. Brass. 1985. Changes in the platelet membrane glycoprotein IIb.IIIa complex during platelet activation. *J. Biol. Chem.* 260:11107-11114.

66. Sánchez-Cortés, J., and M. Mrksich. 2009. The platelet integrin αIIbβ3 binds to the RGD and AGD motifs in fibrinogen. *Chem. Biol.* 16:990-1000.

67. Peerschke, E. I., M. B. Zucker, R. A. Grant, J. J. Egan, and M. M. Johnson. 1980. Correlation between fibrinogen binding to human platelets and platelet aggregability. *Blood* 55:841-847.

68. Marguerie, G. A., E. F. Plow, and T. S. Edgington. 1979. Human platelets possess an inducible and saturable receptor specific for fibrinogen. *J. Biol. Chem.* 254:5357-5363.

69. Coller, B. S., and S. J. Shattil. 2008. The GPIIb/IIIa (integrin αIIbβ3) odyssey: A technology-driven saga of a receptor with twists, turns, and even a bend. *Blood* 112:3011-3025.

70. Nachman, R. L., and L. L. Leung. 1982. Complex formation of platelet membrane glycoproteins IIb and IIIa with fibrinogen. *J. Clin. Invest.* 69:263-269.

71. Tadokoro, S., S. J. Shattil, K. Eto, V. Tai, R. C. Liddington, J. M. de Pereda, M. H. Ginsberg, and D. A. Calderwood. 2003. Talin binding to integrin ß tails: A final common step in integrin activation. *Science* 302:103-106.

72. Wegener, K. L., A. W. Partridge, J. Han, A. R. Pickford, R. C. Liddington, M. H. Ginsberg, and I. D. Campbell. 2007. Structural basis of integrin activation by talin. *Cell* 128:171-182.

73. Ma, Y. Q., J. Qin, C. Wu, and E. F. Plow. 2008. Kindlin-2 (Mig-2): a co-activator of β3 integrins. *J. Cell Biol.* 181:439-446.

74. Naik, U. P., and M. U. Naik. 2003. Association of CIB with GPIIb/IIIa during outside-in signaling is required for platelet spreading on fibrinogen. *Blood* 102:1355-1362.

75. Shattil, S. J., H. Kashiwagi, and N. Pampori. 1998. Integrin signaling: the platelet paradigm. *Blood* 91:2645-2657.

76. Belitser, N., M. Anischuk, Y. Veklich, T. Pozdnjakova, and O. Gorkun. 1993. Fibrinogen internalization by ADP-stimulated blood platelets. Ultrastructural studies with fibrinogen-colloidal gold probes. *Thromb. Res.* 69:413-424.

77. Phillips, D. R., and P. P. Agin. 1977. Platelet membrane defects in Glanzmann's thrombasthenia. Evidence for decreased amounts of two major glycoproteins. *J. Clin. Invest.* 60:535-545.

78. Bennett, J. S., J. A. Hoxie, S. F. Leitman, G. Vilaire, and D. B. Cines. 1983. Inhibition of fibrinogen binding to stimulated human platelets by a monoclonal antibody. *Proc. Natl. Acad. Sci. USA* 80:2417-2421.

79. Coller, B. S., E. I. Peerschke, L. E. Scudder, and C. A. Sullivan. 1983. A murine monoclonal antibody that completely blocks the binding of fibrinogen to platelets produces a thrombasthenic-like state in normal platelets and binds to glycoproteins IIb and/or IIIa. *J. Clin. Invest.* 72:325-338.

80. Seligsohn, U. 2002. Glanzmann thrombasthenia: a model disease which paved the way to powerful therapeutic agents. *Pathophysiol. Haemost. Thromb.* 32:216-217.

81. Tcheng, J. E., S. G. Ellis, B. S. George, D. J. Kereiakes, N. S. Kleiman, J. D. Talley, A. L. Wang, H. F. Weisman, R. M. Califf, and E. J. Topol. 1994. Pharmacodynamics of chimeric glycoprotein IIb/IIIa integrin antiplatelet antibody Fab 7E3 in high-risk coronary angioplasty. *Circulation* 90:1757-1764.

82. Starnes, H. B., A. A. Patel, and G. A. Stouffer. 2011. Optimal use of platelet glycoprotein IIb/IIIa receptor antagonists in patients undergoing percutaneous coronary interventions. *Drugs* 71:2009-2030.

83. Adams, H. P., Jr., M. B. Effron, J. Torner, A. Dávalos, J. Frayne, P. Teal, J. Leclerc, B. Oemar, L. Padgett, E. S. Barnathan, and W. Hacke. 2008. Emergency administration of abciximab for treatment of patients with acute ischemic stroke: results of an international phase III trial: Abciximab in Emergency Treatment of Stroke Trial (AbESTT-II). *Stroke* 39:87-99.

84. Adams, H. P., Jr., W. Hacke, B. Oemar, A. Dávalos, R. A. Cook, P. Trouillas, F. Fazekas, J. Bogousslavsky, J. Hilburn, J. Torner, L. Jacques, A. Shuaib, and P. Reid. 2005. Emergency administration of abciximab for treatment of patients with acute ischemic stroke: results of a randomized phase 2 trial. *Stroke* 36:880-890.

85. Yamada, T., Y. Shimada, and M. Kikuchi. 1996. Integrin-specific tissue-type plasminogen activator engineered by introduction of the Arg-Gly-Asp sequence. *Biochem. Biophys. Res. Commun.* 228:306-311.

86. Absar, S., S. Choi, F. Ahsan, E. Cobos, V. C. Yang, and Y. M. Kwon. 2013. Preparation and characterization of anionic oligopeptide-modified tissue plasminogen activator for triggered delivery: An approach for localized thrombolysis. *Thromb. Res.* 131:e91-e99.

87.   Oliver, J. A., and R. M. Albrecht. 1987. Colloidal gold labelling of fibrinogen receptors in epinephrine- and ADP-activated platelet suspensions. *Scanning Microsc.* 1:745-756.

88.   Escolar, G., E. Leistikow, and J. G. White. 1989. The fate of the open canalicular system in surface and suspension-activated platelets. *Blood* 74:1983-1988.

89.   Grouse, L. H., and J. G. White. 1989. Gold-labeled bovine fibrinogen for study of human platelets. *Thromb. Haemost.* 62:1112-1115.

90.   Smirnova, I. V., S. X. Zhang, B. A. Citron, P. M. Arnold, and B. W. Festoff. 1998. Thrombin is an extracellular signal that activates intracellular death protease pathways inducing apoptosis in model motor neurons. *J. Neurobiol.* 36:64-80.

91.   Vaughan, P. J., C. J. Pike, C. W. Cotman, and D. D. Cunningham. 1995. Thrombin receptor activation protects neurons and astrocytes from cell death produced by environmental insults. *J. Neurosci.* 15:5389-5401.

92.   Woo, D., M. Haverbusch, P. Sekar, B. Kissela, J. Khoury, A. Schneider, D. Kleindorfer, J. Szaflarski, A. Pancioli, E. Jauch, C. Moomaw, L. Sauerbeck, J. Gebel, and J. Broderick. 2004. Effect of untreated hypertension on hemorrhagic stroke. *Stroke* 35:1703-1708.

93.   Sturgeon, J. D., A. R. Folsom, W. T. Longstreth, E. Shahar, W. D. Rosamond, and M. Cushman. 2007. Risk factors for intracerebral hemorrhage in a pooled prospective study. *Stroke* 38:2718-2725.

94.   Steiner, M. M., M. R. Di Tullio, T. Rundek, R. Gan, X. Chen, C. Liguori, M. Brainin, S. Homma, and R. L. Sacco. 1998. Patent foramen ovale size and embolic brain imaging findings among patients with ischemic stroke. *Stroke* 29:944-948.

95.   Adams, H. P., B. H. Bendixen, L. J. Kappelle, J. Biller, B. B. Love, D. L. Gordon, and E. E. Marsh. 1993. Classification of subtype of acute ischemic stroke. Definitions for use in a multicenter clinical trial. TOAST. Trial of Org 10172 in Acute Stroke Treatment. *Stroke* 24:35-41.

96.   Scharf, R. E., M. Hennerici, V. Bluschke, J. Lueck, and R. G. Kladetzky. 1982. Cerebral ischemia in young patients: it is associated with mitral valve prolapse and abnormal platelet activity in vivo? *Stroke* 13:454-458.

97.   Glass, C. K., and J. L. Witztum. 2001. Atherosclerosis: The road ahead review. *Cell* 104:503-516.

98. Gidö, G., T. Kristián, and B. K. Siesjö. 1997. Extracellular potassium in a neocortical core area after transient focal ischemia. *Stroke* 28:206-210.

99. Kristián, T., and B. K. Siesjö. 1998. Calcium in ischemic cell death. *Stroke* 29:705-718.

100. Astrup, J., B. K. Siesjö, and L. Symon. 1981. Thresholds in cerebral ischemia - the ischemic penumbra. *Stroke* 12:723-725.

101. Furlan, M., G. Marchal, F. Viader, J.-M. Derlon, and J.-C. Baron. 1996. Spontaneous neurological recovery after stroke and the fate of the ischemic penumbra. *Ann. Neurol.* 40:216-226.

102. Saver, J. L. 2006. Time is brain-quantified. *Stroke* 37:263-266.

103. Clark, W. M., S. Wissman, G. W. Albers, J. H. Jhamandas, K. P. Madden, and S. Hamilton. 1999. Recombinant tissue-type plasminogen activator (Alteplase) for ischemic stroke 3 to 5 hours after symptom onset. The ATLANTIS Study: a randomized controlled trial. Alteplase Thrombolysis for Acute Noninterventional Therapy in Ischemic Stroke. *JAMA* 282:2019-2026.

104. Marler, J. R., B. C. Tilley, M. Lu, T. G. Brott, P. C. Lyden, J. C. Grotta, J. P. Broderick, S. R. Levine, M. P. Frankel, S. H. Horowitz, E. C. Haley, Jr., C. A. Lewandowski, and T. P. Kwiatkowski. 2000. Early stroke treatment associated with better outcome: the NINDS rt-PA stroke study. *Neurology* 55:1649-1655.

105. Hacke, W., G. Donnan, C. Fieschi, M. Kaste, R. von Kummer, J. P. Broderick, T. Brott, M. Frankel, J. C. Grotta, E. C. Haley, Jr., T. Kwiatkowski, S. R. Levine, C. Lewandowski, M. Lu, P. Lyden, J. R. Marler, S. Patel, B. C. Tilley, G. Albers, E. Bluhmki, M. Wilhelm, and S. Hamilton. 2004. Association of outcome with early stroke treatment: pooled analysis of ATLANTIS, ECASS, and NINDS rt-PA stroke trials. *Lancet* 363:768-774.

106. Katzan, I., A. J. Furlan, L. E. Lloyd, J. Frank, D. Harper, J. Hinchey, J. Hammel, A. Qu, and C. Sila. 2000. Use of tissue-type plasminogen activator for acute ischemic stroke: The Cleveland area experience. *JAMA* 283:1151-1158.

107. Chao, A. C., H. Y. Hsu, C. P. Chung, C. H. Liu, C. H. Chen, M. M. Teng, G. S. Peng, W. Y. Sheng, and H. H. Hu. 2010. Outcomes of thrombolytic therapy for acute ischemic stroke in chinese patients. The Taiwan thrombolytic therapy for acute ischemic stroke (TTT-AIS) Study. *Stroke* 41:885-890.

108. Jauch, E. C., J. L. Saver, H. P. Adams, Jr., A. Bruno, J. J. Connors, B. M. Demaerschalk, P. Khatri, P. W. McMullan, Jr., A. I. Qureshi, K. Rosenfield, P. A. Scott, D. R. Summers, D. Z. Wang, M. Wintermark, and H. Yonas. 2013. Guidelines for the early management of patients with acute ischemic stroke: a

guideline for healthcare professionals from the American Heart Association/American Stroke Association. *Stroke* 44:870-947.

109. Hacke, W., M. Kaste, E. Bluhmki, M. Brozman, A. Davalos, D. Guidetti, V. Larrue, K. R. Lees, Z. Medeghri, T. Machnig, D. Schneider, R. von Kummer, N. Wahlgren, and D. Toni. 2008. Thrombolysis with alteplase 3 to 4.5 hours after acute ischemic stroke. *N. Engl. J. Med.* 359:1317-1329.

110. Ringleb, P. A., P. D. Schellinger, C. Schranz, and W. Hacke. 2002. Thrombolytic therapy within 3 to 6 hours after onset of ischemic stroke: useful or harmful? *Stroke* 33:1437-1441.

111. Otwell, J. L., H. M. Phillippe, and K. S. Dixon. 2010. Efficacy and safety of i.v. alteplase therapy up to 4.5 hours after acute ischemic stroke onset. *Am. J. Health Syst. Pharm.* 67:1070-1074.

112. Qureshi, A. I., A. M. Siddiqui, S. H. Kim, R. A. Hanel, A. R. Xavier, J. F. Kirmani, M. F. K. Suri, A. S. Boulos, and L. N. Hopkins. 2004. Reocclusion of recanalized arteries during intra-arterial thrombolysis for acute ischemic stroke. *Am. J. Neuroradiol.* 25:322-328.

113. Haley, E. C., J. L. Thompson, J. C. Grotta, P. D. Lyden, T. G. Hemmen, D. L. Brown, C. Fanale, R. Libman, T. G. Kwiatkowski, R. H. Llinas, S. R. Levine, K. C. Johnston, R. Buchsbaum, G. Levy, and B. Levin. 2010. Phase IIB/III trial of tenecteplase in acute ischemic stroke: Results of a prematurely terminated randomized clinical trial. *Stroke* 41:707-711.

114. Parsons, M., N. Spratt, A. Bivard, B. Campbell, K. Chung, F. Miteff, B. O'Brien, C. Bladin, P. McElduff, C. Allen, G. Bateman, G. Donnan, S. Davis, and C. Levi. 2012. A randomized trial of tenecteplase versus alteplase for acute ischemic stroke. *N. Engl. J. Med.* 366:1099-1107.

115. Becker, K. J., and T. G. Brott. 2005. Approval of the MERCI clot retriever: a critical view. *Stroke* 36:400-403.

116. Novakovic, R. L., G. Toth, S. Narayanan, and O. O. Zaidat. 2012. Retrievable stents, "stentrievers," for endovascular acute ischemic stroke therapy. *Neurology* 79:S148-157.

117. Tenser, M. S., A. P. Amar, and W. J. Mack. 2011. Mechanical thrombectomy for acute ischemic stroke using the MERCI retriever and penumbra aspiration systems. *World Neurosurg.* 76:S16-S23.

118. Clark, W., H. Lutsep, S. Barnwell, G. Nesbit, R. Egan, E. North, L. Yanase, T. Lowenkopf, B. Petersen, I. Q. Grunwald, T. Mayer, A. Doerfler, T. Struffert, T. Engelhorn, G. Richter, W. Reith, J. Berkefeld, M. Madison, M. Myers, J.

Goddard, J. Lassig, D. Lopes, H. Shownkeen, H. Echiverri, F. Nour, A. Mazumdar, R. Budzik, P. Pema, D. Frei, D. Huddle, R. Bellon, D. Heck, R. Ferguson, C. McDougall, M. Flaster, J. Frey, F. Albuquerque, M. Malkoff, O. Zaidat, V. Branca, N. Ahktar, M. Rymer, A. Rai, C. Brooks, J. Carpenter, T. Popovich, J. Chaloupka, F. Hellinger, P. Rasmussen, T. Masaryk, D. Fiorella, H. Woo, S. Rudolph, G. Spiegel, I. Silverman, S. Ohki, and J. Gomes. 2009. The penumbra pivotal stroke trial: safety and effectiveness of a new generation of mechanical devices for clot removal in intracranial large vessel occlusive disease. *Stroke* 40:2761-2768.

119. Hussain, S. I., O. O. Zaidat, and B. F. Fitzsimmons. 2012. The Penumbra system for mechanical thrombectomy in endovascular acute ischemic stroke therapy. *Neurology* 79:S135-141.

120. Kaminski, M. D., Y. Xie, C. J. Mertz, M. R. Finck, H. Chen, and A. J. Rosengart. 2008. Encapsulation and release of plasminogen activator from biodegradable magnetic microcarriers. *Eur. J. Pharm. Sci.* 35:96-103.

121. Chen, J. P., P. C. Yang, Y. H. Ma, S. J. Tu, and Y. J. Lu. 2012. Targeted delivery of tissue plasminogen activator by binding to silica-coated magnetic nanoparticle. *Int. J. Nanomedicine* 7:5137-5149.

122. Korin, N., M. Kanapathipillai, B. D. Matthews, M. Crescente, A. Brill, T. Mammoto, K. Ghosh, S. Jurek, S. A. Bencherif, D. Bhatta, A. U. Coskun, C. L. Feldman, D. D. Wagner, and D. E. Ingber. 2012. Shear-activated nanotherapeutics for drug targeting to obstructed blood vessels. *Science* 337:738-742.

123. Uesugi, Y., H. Kawata, J.-i. Jo, Y. Saito, and Y. Tabata. 2010. An ultrasound-responsive nano delivery system of tissue-type plasminogen activator for thrombolytic therapy. *J. Control Release* 147:269-277.

124. Runge, M. S., C. Bode, G. R. Matsueda, and E. Haber. 1987. Antibody-enhanced thrombolysis: targeting of tissue plasminogen activator in vivo. *Proc. Natl. Acad. Sci. USA* 84:7659-7662.

125. Gordon, R. T., J. R. Hines, and D. Gordon. 1979. Intracellular hyperthermia. A biophysical approach to cancer treatment via intracellular temperature and biophysical alterations. *Med. Hypotheses* 5:83-102.

126. Gannon, C. J., C. R. Patra, R. Bhattacharya, P. Mukherjee, and S. A. Curley. 2008. Intracellular gold nanoparticles enhance non-invasive radiofrequency thermal destruction of human gastrointestinal cancer cells. *J. Nanobiotechnology* 6:2.

127. Huang, X., P. K. Jain, I. H. El-Sayed, and M. A. El-Sayed. 2006. Determination of the minimum temperature required for selective photothermal destruction of

cancer cells with the use of immunotargeted gold nanoparticles. *Photochem. Photobiol.* 82:412-417.

128.   Ito, A., K. Tanaka, H. Honda, S. Abe, H. Yamaguchi, and T. Kobayashi. 2003. Complete regression of mouse mammary carcinoma with a size greater than 15 mm by frequent repeated hyperthermia using magnetite nanoparticles. *J. Biosci. Bioeng.* 96:364-369.

129.   Johannsen, M., B. Thiesen, A. Jordan, K. Taymoorian, U. Gneveckow, N. Waldöfner, R. Scholz, M. Koch, M. Lein, K. Jung, and S. A. Loening. 2005. Magnetic fluid hyperthermia (MFH) reduces prostate cancer growth in the orthotopic Dunning R3327 rat model. *Prostate* 64:283-292.

130.   Shinkai, M., M. Yanase, H. Honda, T. Wakabayashi, J. Yoshida, and T. Kobayashi. 1996. Intracellular hyperthermia for cancer using magnetite cationic liposomes: in vitro study. *Jpn. J. Cancer Res.* 87:1179-1183.

131.   Huang, J., L. Bu, J. Xie, K. Chen, Z. Cheng, X. Li, and X. Chen. 2010. Effects of nanoparticle size on cellular uptake and liver MRI with polyvinylpyrrolidone-coated iron oxide nanoparticles. *ACS Nano* 4:7151-7160.

132.   Chithrani, B. D., A. A. Ghazani, and W. C. W. Chan. 2006. Determining the size and shape dependence of gold nanoparticle uptake into mammalian cells. *Nano Lett.* 6:662-668.

133.   De Jong, W. H., W. I. Hagens, P. Krystek, M. C. Burger, A. J. A. M. Sips, and R. E. Geertsma. 2008. Particle size-dependent organ distribution of gold nanoparticles after intravenous administration. *Biomaterials* 29:1912-1919.

134.   Alexis, F., E. Pridgen, L. K. Molnar, and O. C. Farokhzad. 2008. Factors affecting the clearance and biodistribution of polymeric nanoparticles. *Mol. Pharm.* 5:505-515.

135.   He, C., Y. Hu, L. Yin, C. Tang, and C. Yin. 2010. Effects of particle size and surface charge on cellular uptake and biodistribution of polymeric nanoparticles. *Biomaterials* 31:3657-3666.

136.   Lu, W.-L., X.-R. Qi, Q. Zhang, R.-Y. Li, G.-L. Wang, R.-J. Zhang, and S.-L. Wei. 2004. A pegylated liposomal platform: Pharmacokinetics, pharmacodynamics, and toxicity in mice using doxorubicin as a model drug. *J. Pharmacol. Sci.* 95:381-389.

137.   Yang, X., J. J. Grailer, I. J. Rowland, A. Javadi, S. A. Hurley, V. Z. Matson, D. A. Steeber, and S. Gong. 2010. Multifunctional stable and pH-responsive polymer vesicles formed by heterofunctional triblock copolymer for targeted anticancer drug delivery and ultrasensitive MR imaging. *ACS Nano* 4:6805-6817.

138. Busch, W. 1866. Uber den Einfluss weichen Hefttigere Erysipelen zuweilen auf Organisierte Neubildugen Ausuken Verhandl. *Naturh. Ver. Preuss. Rheinl.* 23:28-30.

139. Muckle, D. S., and J. A. Dickson. 1971. The selective inhibitory effect of hyperthermia on the metabolism and growth of malignant cells. *Br. J. Cancer* 25:771-778.

140. Jordan, A., R. Scholz, P. Wust, H. Fähling, and F. Roland. 1999. Magnetic fluid hyperthermia (MFH): Cancer treatment with AC magnetic field induced excitation of biocompatible superparamagnetic nanoparticles. *J. Magn. Magn. Mater.* 201:413-419.

141. Strohbehn, J. W., and E. B. Douple. 1984. Hyperthermia and cancer therapy: A review of biomedical engineering contributions and challenges. *IEEE Trans. Biomed. Eng.* 31:779-787.

142. Shiu, M. H., and J. G. Fortner. 1980. Intraperitoneal hyperthermic treatment of implanted peritoneal cancer in rats. *Cancer Res.* 40:4081-4084.

143. Stauffer, P. R., T. C. Cetas, A. M. Fletcher, D. W. Deyoung, M. W. Dewhirst, J. R. Oleson, and R. B. Roemer. 1984. Observations on the use of ferromagnetic implants for inducing hyperthermia. *IEEE Trans. Biomed. Eng.* BME-31:76-90.

144. Stauffer, P. R., T. C. Cetas, and R. C. Jones. 1984. Magnetic induction heating of ferromagnetic implants for inducing localized hyperthermia in deep-seated tumors. *IEEE Trans. Biomed. Eng.* 31:235-251.

145. Storm, F. K., W. H. Harrison, R. S. Elliott, and D. L. Morton. 1980. Hyperthermic therapy for human neoplasms: Thermal death time. *Cancer* 46:1849-1854.

146. Zhao, D.-L., X.-W. Zeng, Q.-S. Xia, and J.-T. Tang. 2009. Preparation and coercivity and saturation magnetization dependence of inductive heating property of Fe3O4 nanoparticles in an alternating current magnetic field for localized hyperthermia. *J. Alloys Compd.* 469:215-218.

147. Hao-Yu, T., L. Chen-Yi, S. Ying-Hsia, L. Xi-Zhang, and L. Gwo-Bin. 2007. Hyperthermia cancer therapy utilizing superparamagnetic nanoparticles. In *2nd IEEE International Conference on Nano/Micro Engineered and Molecular Systems, 2007.*, Bangkok. 163-166.

148. Moran, C. H., S. M. Wainerdi, T. K. Cherukuri, C. Kittrell, B. J. Wiley, N. W. Nicholas, S. A. Curley, J. S. Kanzius, and P. Cherukuri. 2009. Size-dependent joule heating of gold nanoparticles using capacitively coupled radiofrequency fields. *Nano. Res.* 2:400-405.

149. Fortin, J. P., F. Gazeau, and C. Wilhelm. 2008. Intracellular heating of living cells through Neel relaxation of magnetic nanoparticles. *Eur. Biophys. J.* 37:223-228.

150. Pankhurst, Q. A., J. Connolly, S. K. Jones, and J. Dobson. 2003. Applications of magnetic nanoparticles in biomedicine. *J. Phys D: Appl. Phys.* 36:R167.

151. Gupta, A. K., and M. Gupta. 2005. Synthesis and surface engineering of iron oxide nanoparticles for biomedical applications. *Biomaterials* 26:3995-4021.

152. Rudolf, H., D. Silvio, M. Robert, and Z. Matthias. 2006. Magnetic particle hyperthermia: Nanoparticle magnetism and materials development for cancer therapy. *J. Phys: Condens. Matter* 18:S2919.

153. Laurent, S., S. Dutz, U. O. Häfeli, and M. Mahmoudi. 2011. Magnetic fluid hyperthermia: Focus on superparamagnetic iron oxide nanoparticles. *Adv. Colloid Interface Sci.* 166:8-23.

154. Lyon, J. L., D. A. Fleming, M. B. Stone, P. Schiffer, and M. E. Williams. 2004. Synthesis of Fe oxide core/Au shell nanoparticles by iterative hydroxylamine seeding. *Nano Lett.* 4:719-723.

155. Lee, S.-J., J.-R. Jeong, S.-C. Shin, J.-C. Kim, and J.-D. Kim. 2004. Synthesis and characterization of superparamagnetic maghemite nanoparticles prepared by coprecipitation technique. *J. Magn. Magn. Mater.* 282:147-150.

156. Jordan, A., R. Scholz, K. Maier-Hauff, M. Johannsen, P. Wust, J. Nadobny, H. Schirra, H. Schmidt, S. Deger, S. Loening, W. Lanksch, and R. Felix. 2001. Presentation of a new magnetic field therapy system for the treatment of human solid tumors with magnetic fluid hyperthermia. *J. Magn. Magn. Mater.* 225:118-126.

157. Gilchrist, R. K., R. Medal, W. D. Shorey, R. C. Hanselman, J. C. Parrott, and C. B. Taylor. 1957. Selective inductive heating of lymph nodes. *Ann. Surg.* 146:596-606.

158. Jing, Y., S. He, T. Kline, Y. Xu, and J. P. Wang. 2009. High-magnetic-moment nanoparticles for biomedicine. *Conf. Proc. IEEE Eng. Med. Biol. Soc.* 2009:4483-4486.

159. Ma, M., Y. Wu, J. Zhou, Y. Sun, Y. Zhang, and N. Gu. 2004. Size dependence of specific power absorption of Fe3O4 particles in AC magnetic field. *J. Magn. Magn. Mater.* 268:33-39.

160. Sonvico, F., C. Dubernet, P. Colombo, and P. Couvreur. 2005. Metallic colloid nanotechnology, applications in diagnosis and therapeutics. *Curr. Pharm. Des.* 11:2095-2105.

161. Zhao, D. L., H. L. Zhang, X. W. Zeng, Q. S. Xia, and J. T. Tang. 2006. Inductive heat property of Fe_3O_4/polymer composite nanoparticles in an ac magnetic field for localized hyperthermia. *Biomed. Mater.* 1:198-201.

162. Luderer, A. A., N. F. Borrelli, J. N. Panzarino, G. R. Mansfield, D. M. Hess, J. L. Brown, E. H. Barnett, and E. W. Hahn. 1983. Glass-ceramic-mediated, magnetic-field-induced localized hyperthermia: Response of a murine mammary carcinoma. *Radiat. Res.* 94:190-198.

163. Mornet, S., S. Vasseur, F. Grasset, and E. Duguet. 2004. Magnetic nanoparticle design for medical diagnosis and therapy. *J. Mater. Chem.* 14:2161-2175.

164. Park, H. Y., M. J. Schadt, L. Wang, Lim, II, P. N. Njoki, S. H. Kim, M. Y. Jang, J. Luo, and C. J. Zhong. 2007. Fabrication of magnetic core@shell Fe oxide@Au nanoparticles for interfacial bioactivity and bio-separation. *Langmuir* 23:9050-9056.

165. Wang, L., J. Luo, Q. Fan, M. Suzuki, I. S. Suzuki, M. H. Engelhard, Y. Lin, N. Kim, J. Q. Wang, and C. J. Zhong. 2005. Monodispersed core-shell Fe_3O_4@Au nanoparticles. *J. Phys. Chem. B* 109:21593-21601.

166. Lim, J. K., S. A. Majetich, and R. D. Tilton. 2009. Stabilization of superparamagnetic iron oxide core-gold shell nanoparticles in high ionic strength media. *Langmuir* 25:13384-13393.

167. Goodman, S. L., G. M. Hodges, and D. C. Livingston. 1980. A review of the colloidal gold marker system. *Scan. Electron Microsc.* Pt 2:133-146.

168. Gatel, C., and E. Snoeck. 2007. Epitaxial growth of Au and Pt on Fe_3O_4 (111) surface. *Surf. Sci.* 601:1031-1039.

169. Gatel, C., and E. Snoeck. 2006. Comparative study of Pt, Au and Ag growth on Fe_3O_4 (001) surface. *Surf. Sci.* 600:2650-2662.

170. Kaiser, M., J. Heintz, I. Kandela, and R. Albrecht. 2007. Tumor cell death induced by membrane melting via immunotargeted, inductively heated core/shell nanoparticles. *Microsc. Microanal.* 13:18-19.

171. Krystofiak, E. S., V. Z. Matson, D. A. Steeber, and J. A. Oliver. 2012. Elimination of tumor cells using folate receptor targeting by antibody-conjugated, gold-coated magnetite nanoparticles in a murine breast cancer model. *J. Nanomat.* 2012:431012.

Chapter 2:   Fibrinogen-based platelet targeting

Abstract:

Selective targeting of activated platelets is desirable for anti-platelet therapy as it allows for disruption of platelets involved in blood clots to be treated but prevents targeting of quiescent circulating platelets. We propose using human fibrinogen to target platelets through the integrin $\alpha_{IIB}\beta_3$ which is only competent to bind fibrinogen upon platelet activation. The function and selectivity of fibrinogen-conjugated nanoparticles was evaluated with an emphasis on potential *in vivo* application. While human systems are convenient for *in vitro* studies, future *in vivo* studies would require use of a murine animal model. The utility of human fibrinogen in a murine platelet system was examined through platelet aggregation studies, and with nanoparticle labeling was tested using either murine or human fibrinogen. The ability of fibrinogen-conjugated nanoparticles to bind to preformed platelet aggregates in the presence of unconjugated fibrinogen, which resemble *in vivo* conditions, was examined. To better understand the selectivity of fibrinogen-conjugated nanoparticles, a system in which tagged, unactivated platelets and activated platelets were mixed and labeled with fibrinogen-conjugates was developed. No significant differences between human and murine fibrinogen in aggregation or labeling of murine platelets were observed.   Fibrinogen-conjugated nanoparticles were found localized to the area around the granulomere in surface-activated platelets and at platelet-platelet junctions and the open canalicular system in aggregated platelets. Preformed aggregates exhibited a similar labeling pattern but with fewer labels present. Fibrinogen-conjugated nanoparticles were found to be selective for activated platelets.

The results suggest that fibrinogen is a suitable molecule to target nanoparticles specifically to activated platelets and may function well *in vivo*.

Introduction:

Successful destruction of platelet aggregates will require two features to be feasible: First, a nanoparticle capable of causing structural damage to platelets within a blood clot; and second, a mechanism to actively localize the nanoparticles to the platelets within the blood clot. Here we focus on the targeting mechanism we have proposed, using the ligand fibrinogen to specifically target activated platelets through binding to the platelet fibrinogen receptor. Ideal targeting molecules can specifically bind to the desired target, have low binding to all other cells and tissues, and can be obtained at high concentration and purity. Additionally, for our studies the molecule must retain biological activity following conjugation to nanoparticle surfaces in order to perform its intended function of delivering nanoparticles to activated platelets.

The ability of fibrinogen to bind to activated platelets is critical for platelet aggregation, and as a result, for overall platelet hemostatic function (1, 2). The primary platelet fibrinogen receptor is the integrin $\alpha_{IIB}\beta_3$, but the receptor can also bind von Willebrand factor and fibronectin via arginine-glycine-aspartate (RGD) amino acid sequences found on the ligands (3, 4). The importance of $\alpha_{IIB}\beta_3$ is demonstrated effectively in Glanzmann's thrombasthenia, a disorder in which platelets lack a functional fibrinogen receptor, resulting in bleeding problems caused by the inability of platelets to crosslink

and form effective aggregates (5-7). Due to the importance of integrin $\alpha_{IIB}\beta_3$, it has been studied extensively using antibodies (8-10) and small molecule inhibitors (11) against the integrin. Of particular interest is the 7E3 antibody against $\alpha_{IIB}\beta_3$ that appeared to show binding preference for $\alpha_{IIB}\beta_3$ on activated platelets (12), which was developed as a therapeutic antibody to block platelet aggregation. The original murine monoclonal antibody was made a chimeric Fab to reduce antigenicity of the antibody in humans (13) and prevent platelet clearance caused by the Fc portion of the intact antibody. The modified antibody received the name abciximab (trade name Reopro) and has since been employed in percutaneous interventions to prevent thrombus formation (14). Abciximab was further tested as an ischemic stroke treatment but during phase III clinical trials it was found to increase the rate of fatal intracranial hemorrhage while failing to show good efficacy in treatment of ischemic stroke (15, 16). However, abciximab demonstrated the potential utility and benefit of targeting $\alpha_{IIB}\beta_3$ on platelets as a means to treat thrombotic conditions.

The interaction between fibrinogen and the integrin $\alpha_{IIB}\beta_3$ has been well characterized (9, 17-20). The integrin $\alpha_{IIB}\beta_3$ exists in a non-binding conformation on quiescent platelets, unable to bind to fibrinogen. Upon platelet activation, the integrin undergoes a conformational change that renders it competent to bind its ligands (21) providing a useful mechanism for targeting of activated platelets. Once fibrinogen has bound and cross-linked receptors, the receptor undergoes integrin outside-in signaling where the receptor can signal back to the platelet that ligand has bound (22, 23). This causes the integrin with bound ligand to centralize in the plane of the platelet membrane by moving

along the underlying actin cytoskeleton. On surface-activated platelets, the movement

will be toward the area around the granulomere of the platelets (24-28). Platelets

activated in suspension will move bound fibrinogen along the surface of the platelet to a

final destination in the open canicular system (OCS) (29-33). The movement of

fibrinogen-conjugated labels to the interior of platelet aggregates is desirable, as it will

allow treatments to disrupt the entire volume of platelet aggregates rather than only those

platelets exposed on the thrombus surface.   The localization of fibrinogen-conjugated

nanoparticle labels is important for how nanoparticle-mediated highly-localized

hyperthermia will affect platelet structural integrity. Of particular interest is fibrinogen

labeling on platelets that have been activated and aggregated before being exposed to

fibrinogen-conjugated nanoparticles. Blood clots formed *in vivo* will have already

formed a platelet aggregate and bound fibrinogen from the circulation that will directly

compete with the binding of fibrinogen conjugated to nanoparticles. The feasibility of

using fibrinogen as an activated platelet targeting system needs to be evaluated under

conditions that approximate this *in vivo* competition.

The species of fibrinogen used for targeting is an important consideration. Nearly all *in vitro* studies may be performed using freshly isolated human platelets. For *in vivo* studies, an animal model is necessary to demonstrate effectiveness of targeting and destruction before further development of human applications. For *in vitro* systems human blood cells and proteins are generally preferred for their availability, purity, and lower commercial costs. However, effectively targeting platelets in an animal model may require a species matched, non-human fibrinogen. Many arterial injury models are

available in a variety of organisms. For our studies, the murine platelet system has appeal; it has been used to study effects of tissue plasminogen activator (tPA) (34) and plasmin (35) on arterial blood clots, using a ferric chloride arterial injury model. The injury model was originally developed in rat, and utilizes ferric chloride to denude endothelium in the carotid artery which leads to an occlusive thrombus (36). It has since been successfully employed in mice (34, 35, 37, 38). For our system it would be ideal to develop a targeting system that uses human fibrinogen for targeting both human platelets *in vitro* and murine platelets *in vivo*.

The vertebrate fibrinogen molecule is a complex glycoprotein consisting of 3 pairs of subunits: alpha, beta, and gamma (39, 40). Fibrinogen has several possible binding sites for the integrin $\alpha_{IIB}\beta_3$. Human fibrinogen contains two RGD amino acid sequences on the alpha chain at position 95-97 and 572-574 on the mature molecule (41), but while these RGD sequences are capable of binding to $\alpha_{IIB}\beta_3$ (42) they are not essential for fibrinogen binding (2, 18) or platelet function (43). Rodent $\alpha_{IIB}\beta_3$ lacks the ability to bind RGD sequences (44, 45). This leads to inability of these platelets to bind human von Willebrand factor; however, human fibrinogen is able to bind to rat $\alpha_{IIB}\beta_3$ (45, 46). The dodecapeptide sequence at the C-terminal of the fibrinogen gamma chain is the primary sequence bound by $\alpha_{IIB}\beta_3$ and is responsible for nearly all fibrinogen/platelet physiology (2, 18, 47, 48), rather than the RGD sequences. The dodecapeptide sequences of the C-terminus of the gamma subunits of human and murine fibrinogen differ by only two amino acids, HH<u>L</u>GG<u>A</u>KQAGDV for humans and HH<u>M</u>GG<u>S</u>KQAGDV for mice (differences underlined) (49, 50). A study comparing the binding of human and rat

dodecapeptides to rat platelets concluded that their affinity for $\alpha_{IIB}\beta_3$ was equal (51). Studies have utilized human fibrinogen in murine systems successfully to analyze fibrinogen binding to platelets (52-55). Currently no comprehensive study on the use of human fibrinogen in a murine platelet system has been conducted. Here we will evaluate the use of human fibrinogen for targeting and aggregating murine platelets *in vitro*. We will also determine the ability of fibrinogen-conjugated nanoparticles to label preformed platelet aggregates in competition with plasma fibrinogen, which will approximate labeling conditions *in vivo*. For successful therapies, fibrinogen-conjugated nanoparticles must bind to blood clots that have already been formed and in the presence of plasma fibrinogen.

We further developed an *in vitro* platelet system that creates a population of activated platelets along with a population of biotin-tagged unactivated platelets. This system can create an approximation of the conditions around blood clots and demonstrate fibrinogen labeling specificicity for activated platelets. This allowed us to observe the specificity of fibrinogen conjugated to nanoparticles for activated platelets while in the presence of the specifically tagged unactivated platelets. It is vitally important that unactivated platelets are left unlabeled as they would otherwise be destroyed during treatment, thus increasing bleeding risks, as well as acting as a sink that reduces the nanoparticle dose delivered to the thrombus.

Materials and Methods:

Isolation of human platelets:

Venous blood anticoagulated with 3.2% sodium citrate in evacuated blood collection tubes (Tyco Healthcare Group, Mansfield, MA) was centrifuged at 100 x g for 15 minutes. Platelet-rich plasma was applied to a 25 mm diameter x 90 mm high column of Sepharose CL-2B (Sigma-Aldrich, St. Louis MO) equilibrated with Tyrode's buffer (15 mM HEPES, pH 7.4, 3.3 mM Na_2HPO_4, 138 mM NaCl, 2.7 mM KCl, 5.5 mM glucose, 1 mM $MgCl_2$, 1 mg/mL bovine serum albumin (BSA)) to perform size exclusion chromatography on the platelet rich plasma. The gel-filtered platelets were then surface activated or aggregated as described below. Experiments were completed within 2 hours of the blood draw to preserve normal platelet functions.

Isolation of murine platelets:

Blood was collected by cardiac puncture of C57BL/6 mice immediately following euthanasia by CO_2 inhalation. Blood was drawn into a one cc syringe containing 90 μl of 3.2% sodium citrate. Pooled blood samples from 4 - 6 animals were used for aggregation studies; pooled samples from 2 mice were used for surface activation studies. Murine blood was centrifuged at 80 x g for 10 minutes. Gel-filtered platelets were produced using size exclusion chromatography similar to above but on a 10 mm diameter x 50 mm high Sepharose CL-2B column, and were subsequently used for surface activation or aggregation experiments.

Preparation of colloidal gold nanoparticles:

Glassware used for preparation of nanoparticles was washed thoroughly with diluted

7X® concentrate detergent (MP Biomedicals, Solon, OH) and rinsed extensively with

double deionoized H_2O (ddH_2O). Preparation of 18 nm colloidal gold nanoparticles was

performed as previously described (26). Briefly, 0.2 µm filtered ddH_2O was mixed with

4% tetrachlorogold (III) hydrate (MP Biomedicals) to a final concentration of 0.01%.

The solution was heated to boiling. Next, filtered 1% trisodium citrate (Fisher Scientific,

Pittsburgh, PA) was added to a final concentration of 0.02% or 0.01% for 18 nm and 38

nm colloidal gold, respectively. The solution was mixed thoroughly until a distinct red

color developed, then was refluxed for 30 minutes. Nanoparticles were air-dried onto

formvar coated TEM grids. Size distributions of the colloidal gold nanoparticles were

assessed by measuring diameters of the longest axis of the nanoparticles using ImageJ

(National Institute of Health, Bethesda, MD) to analyze micrographs acquired with a

Hitachi H-600 transmission electron microscope at 75 kV, or scanning electron

microscopy on a Hitachi S-4800 at 30 kV between 50,000 to 100,000 X magnification.

The mean nanoparticle diameter and standard deviation were determined from counting

500 nanoparticles in multiple fields of view.

Conjugation of proteins to colloidal gold nanoparticles:

Fibrinogen was conjugated to the nanoparticles by non-ionic protein adsorption (29). To

conjugate human or murine fibrinogen to 18 nm gold nanoparticles, the pH of the colloid

was adjusted to 6.8 for human or 7.3 for murine fibrinogen using 0.2 M K_2CO_3. The gold

nanoparticles were then incubated with 16 µg/mL of plasminogen-, von Willebrand

factor-, and fibronectin-depleted human fibrinogen (Enzyme Research Laboratories, South Bend, IN) or 16 µg/mL murine fibrinogen (Enzyme Research Laboratories) for 5 minutes. Polyethylene glycol (average MW 20,000, Sigma-Aldrich) was added at a final concentration of 0.004% as a stabilizing agent. The fibrinogen-conjugated nanoparticles were separated from free protein by centrifugation at 16,000 x g for 5 minutes, and the resultant soft pellet was resuspended in Tyrode's buffer at one-tenth the original nanoparticle volume.

Streptavidin (Southern Biotech, Birmingham, AL) was conjugated to 38 nm colloidal gold in a similar manner. The pH of the nanoparticle solution was adjusted to 5.5 and incubated with 20 µg/mL streptavidin for 1 minute prior to addition of polyethylene glycol. Attempted conjugation of streptavidin using the standard protein incubation times of 5 minutes produced conjugates that failed to form pellets during centrifugation. The nanoparticles were pelleted and resuspended in the same manner as the fibrinogen conjugates.

Aggregation of gel-filtered platelets:

Gel-filtered platelets were diluted in Tyrode's buffer with BSA to give a final concentration of 200,000 platelets/µL, and were supplemented with $CaCl_2$ to a final concentration of 2 mM for human and 5 mM for murine platelets. Unconjugated fibrinogen was added to the platelets at a final concentration of 200 µg/mL. When using fibrinogen-gold conjugates as the sole source of fibrinogen, 15 µL pelleted fibrinogen-conjugated colloidal gold was added per 235 µL of platelet volume which is a

concentration of approximately 96 µg/mL, based on a perfectly efficient protein

conjugation to the nanoparticles. The total volume of platelets, fibrinogen, and calcium

was 500 µL (aggrogometer) or 250 µL (24 well plate) per aggregation reaction.

Aggregation of human platelets was performed on a Chronolog Dual Aggregometer

(Havertown, PA) warmed to 37° C, stirring at setting 7, mated to an ADInsturments

Powerlab 4/30 analog-to-digital converter with LabChart software (ADInstruments,

Colorado Springs, CO) sampling at 10 Hz and a 100 mV range. After 30 seconds of data

acquisition, aggregation was initiated by addition of 67 µM of the peptide agonist

SFLLRN-NH$_2$ (Bachem Americas, Torrence CA), the ligand for human protease-

activated receptor 1 (PAR1), the primary thrombin receptor on human platelets (56, 57).

Aggregation was considered complete 5 minutes after aggregation initiation. The percent

aggregation was determined by the output voltage of the aggregometer using the equation

below, where Vout is the output voltage of the aggregometer and Vmax is an instrument-

specific maximum voltage, which is 80 mV for the Chronolog Dual Aggregometer. The

aggregometer uses a blank, consisting of Tyrodes's buffer supplemented with fibrinogen

and calcium to determine the voltage range.

$$\%Aggregation = \frac{Vmax - Vout}{Vmax} * 100$$

For some experiments using either human or murine platelets, aggregation was performed

in 24-well tissue culture plates with a small magnetic stir bar in each well. The reaction

wells were centered on a Corning PC-620D magnetic stirrer (14 x 18 cm surface), set at

~70% maximum speed, which was found to produce enough shear to reproducibly

aggregate platelets, and incubated at 37°C. To initiate aggregation, human or murine gel-

filtered platelets were supplemented with human or murine fibrinogen and calcium prior

to the addition of agonists. The agonists included: the human PAR1 peptide SFLLRN-

NH$_2$ (human platelets only), the murine PAR4 peptide AYPGKF-NH$_2$ (Bachem

Americas) (58, 59), ADP (Sigma-Aldrich), and ionomycin (Calbiochem, San Diego CA)

(60). Reactions were allowed to proceed for 5 minutes and terminated by the addition of

1 mL of 1% glutaraldehyde in 0.1 M HEPES, pH 7.3. Aliquots of 200 µL were removed

for determination of percent aggregation (see below), and the remaining sample volume

was diluted to 5 mL in 1% glutaraldehyde for electron microscopy preparation. Samples

were allowed to fix for a minimum of 30 minutes at room temperature.

The extent of aggregation was calculated from the light transmittance (%T) of the

samples. Aliquots of glutaraldehyde-fixed aggregation reactions were transferred to a 96-

well flat bottom plate and the %T was measured at 595 nm in a Molecular Devices

Versamax microtiter plate reader (Sunnyvale, CA). Control samples used to define the

minimum and maximum percent aggregation were diluted in glutaraldehyde in a manner

similar to the aggregated samples. Controls included (1) gel-filtered platelets

supplemented with fibrinogen, and calcium representing baseline, or zero aggregation

(0%T); and (2) Tyrodes's buffer with fibrinogen and calcium representing complete

aggregation (100%T), and serving as the de facto blank. Percent aggregation was

calculated as:

$$\%Aggregation = \frac{\%T_{sample} - \%T_{baseline}}{\%T_{complete} - \%T_{baseline}} * 100$$

Dose response curve aggregation data were presented as percent of maximal aggregation to better compare data between experiments. Percent of maximal aggregation normalizes responses obtained from different donors/animals or on different days, defined as:

$$\% \ Of \ Maximal \ Aggregation = \frac{\%Aggregation}{Maximium \ Oberved \ \% \ Aggregation} * 100$$

Statistical analysis was performed using Student's *t*-test to compare samples, with significance defined as $p < 0.05$.

Aggregation of platelet-rich plasma:

Human platelet-rich plasma was obtained by centrifugation of blood at 100 x g for 15 minutes. Aggregation of samples was performed in a Chronolog Dual Aggregometer, as above, using platelet- rich plasma supplemented with 2 mM Ca^{2+}.   Platelets were activated with the 67 μM of SFLLRN-NH$_2$ and allowed to aggregate for 5 minutes. The resulting platelet aggregates were labeled for 5 minutes with fibrinogen-conjugated nanoparticles derived from 6 mL of stock, which gives an approximate concentration of 96 μg/mL fibrinogen. Samples were then fixed and prepared for TEM as described below.

Fibrinogen labeling of surface-activated platelets:

Surface-activated platelets were prepared by placing 7 μL drops of Ca^{2+}-supplemented gel-filtered platelets onto Formvar-coated 400 mesh nickel grids (Electron Microscopy Supplies, Hatfield PA). Human platelets were allowed to adhere and spread for 15 minutes at room temperature, while murine platelets were given 30 minutes. Non-adherent platelets were washed away by gently dunking the grids in Tyrode's buffer.

Grids were then floated on 7 µL drops of colloidal gold-conjugated fibrinogen adjusted to OD_{522} of 0.5 just prior to supplementation with Ca^{2+}. Grids were incubated in the labels for 10 minutes, then washed by three, 5 minute incubations on drops of Ca^{2+}-supplemented Tyrode's buffer. After washing, samples were fixed in 1% glutaraldehyde in 0.1 M HEPES, pH 7.3, for 30 minutes at room temperature.

Fibrinogen labeling of mixed activated and unactivated platelet populations:

Blood was drawn from healthy adult volunteers and anticoagulated with 3.2% sodium citrate and 5 µg/mL prostaglandin E_1 (PGE_1, stock is dissolved in 100% ethanol, Sigma-Aldrich) and was centrifuged at 100 x g for 15 minutes. The resultant platelet-rich plasma was gel-filtered as described above. Gel-filtered platelets were split into thrombin activated and unactivated groups. The unactivated group was washed in CGS buffer (13 mM sodium citrate dihydrate, 123 mM NaCl, 33 mM dextrose, pH 7.4) by centrifugation at 300 x g for 10 minutes, supplemented with an additional 5 µg/mL PGE_1, to prevent activation (61), and incubated in 1 µM EZ-Link® Sulfo-NHS-LC-Biotin (Fisher Scientific, Pittsburgh PA) for 20 minutes at room temperature. Following the biotinylation, unreacted biotin was removed by gel filtration on a second 25 mm diameter x 90 mm high Sepharose CL-2B column equilibrated with Tyrode's buffer with BSA. After gel-filtration platelets, were supplemented with 2 mM calcium.

A separate group of gel-filtered platelets and a control group of biotinylated platelets were supplemented with calcium and activated with 2 nM thrombin (Haematolgoic Technologies, Essex Junction, VT) for 5 minutes at room temperature. Afterward the

thrombin activity was quenched by the addition of 20 nM antithrombin III (ATIII, Haematolgoic Technologies) and 5 units/mL heparin sodium (Elkins-Sinn, Cherry Hill, NJ) for 5 minutes at room temperature. The platelets were washed twice by centrifugation at 300 x g for 5 minutes in Tyrode's buffer with BSA to remove thrombin/ATIII complexes and secreted platelet degranulation products. The biotinylated, unactivated and thrombin-activated platelet populations were mixed together in equal proportions and labeled with Alexa Fluor® 488-fibrinogen (Invitrogen, Grand Island, NY) or fibrinogen conjugated to 18 nm colloidal gold. The samples were fixed in 1% paraformaldehyde for light microscopy and flow cytometry or 1% glutaraldehyde for SEM. The aldehydes were quenched and washed in 50 mM glycine in PBS twice at 300 x g for 10 minutes. Samples were incubated for 20 minutes with TRITC-streptavidin (Southern Biotech) for light microscopy, phycoerythrin-avidin (PE-avidin, Southern Biotech) for flow cytometry, or streptavidin conjugated to 38 nm colloidal gold for SEM. After labeling, samples were fixed again for 30 minutes by dilution in 1% paraformaldehyde for light microscopy and flow cytometry or 1% glutaraldehyde for SEM.

Epifluorsecence microscopy micrographs were generated with a Roper Scientific CoolSnap ES CCD mounted to a Nikon Eclipse TE2000-U inverted microscope using a Nikon Plan Apo 40x objective. Brightfield images were captured using DIC optics. Fluorescent Alexa 488-fibrinogen imaging was done using a FITC cube at 50 ms exposure, avidin-TRITC imaging was performed using a TRITC cube with a 100 ms

exposure. Fluorescent image channels were overlaid using Metavue software (Universal Imaging Corporation, Downingtown, PA).

For flow cytometry, some paraformaldehyde-fixed platelet samples were stained for the platelet degranulation marker P-selectin (CD62P) using a PE-anti human CD62P clone AK-4 (62) (BD Biosciences, San Jose, CA). Flow cytometry analysis was performed with a BD FACSCalibur using CellQuest™ Pro software, sampling at least 10,000 events gated on the platelet population on log forward and log side light scatter dot plots. Data in histograms was scaled and smoothed to better show differences between samples.

Scanning electron microscopy of platelets activated in suspension and aggregated: Following fixation, aggregates were collected by filtration onto 0.4 μm pore size Nuclepore® membranes (General Electric, Fairfield, CT). Membranes were post-fixed in 0.05% OsO_4 in 0.1M HEPES, pH 7.3, for 15 minutes and dehydrated through a graded series of ethanol to 100%. Samples were dried by the critical point procedure in a Balzers CPD020 unit (Schalksmühle, Germany) using 100% ethanol stored over type 3A molecular sieves (Grace Davison, Columbia, MD) as the intermediate fluid and liquid CO_2 as the transitional fluid. Dried samples were sputter coated with 2 nm iridium using an EMITECH K575x sputter coater (Ashford, Kent, United Kingdom). Analysis was performed on a Hitachi S-4800 scanning electron microscope (Dallas, TX) using 1-2 kV for secondary electron (SE) imaging and 30 kV for backscattered electron (BSE) imaging.

Transmission electron microscopy of platelets:

Gel-filtered platelet aggregates were fixed in 1% glutaraldehyde, 1% tannic acid in 0.1 M

HEPES, pH 7.3, at room temperature for an hour and then 4° C overnight. Aggregated

platelet-rich plasma was fixed in 2% glutaraldehyde in 0.1 M HEPES, pH 7.3 for 10

minutes and then centrifuged at 300 x g for 5 minutes to remove agglomerated plasma

proteins that pellet above the platelet sample. The samples were fixed a second time in

2% glutaraldehyde, 1% tannic acid in 0.1 M HEPES, pH 7.3 overnight at 4° C. All

samples were washed three times in HEPES and embedded into 1% agar (Difco, Detroit,

MI) in 0.1 M HEPES by combining warm agar and 4° C platelet samples in equal volume

in small TEM embedding molds. After the agar had become dense at 4° C, samples were

postfixed in 0.05% OsO_4 for 1 hour at room temperature, washed 3 times in ddH_2O, and

stained with 1% uranyl acetate for 30 minutes. Samples were dehydrated in a graded

ethanol series and then transferred from ethanol to propylene oxide. Samples were

infiltrated and embedded with low viscosity Spurr's resin (63) but substituting the

accelerant N,N-dimethylbenzylamine with 2(dimethylamino)ethanol (64) (Electron

Microscopy Sciences, Hartfield, PA). Ultrathin silver to pale gold sections were cut on a

RMC MT-7000 ultramicrotome and were stained with 1% uranyl acetate. Sections of

aggregates produced from platelet-rich plasma were additionally stained with lead citrate.

Sections were imaged on a Hitachi H600 TEM (Dallas, TX) at 75 kV.

Results

Aggregation of human and murine platelets:

To ensure that all aggregation data could be collected within 2 hours of the blood draw, we validated a method that allows multiple aggregation reactions to proceed simultaneously, the 24-well plate system. We directly compared the 24-well plate system to the standard assay performed in an aggregometer. Aggregation of gel-filtered human platelets with the maximal dose of the human PAR1 peptide agonist SFLLRN-NH$_2$ (67 μM) in the 24-well plate system gave percent aggregation results similar to the end point readings of aggrogometer tracings (56), following stimulation. Maximal aggregation measured in the aggregometer occurred within 5 minutes of stimulation, as observed by the plateau of the aggregation tracings (Figure 6A). Maximal achievable aggregation (times varied with sample) in the aggregometer was $76 \pm 5.7\%$ (standard deviation, n=3), at exactly 5 minutes after stimulation the platelets aggregated $76 \pm 5.6\%$, and platelets aggregated in the 24-well plate system demonstrated similar aggregation of $80 \pm 2.8\%$ 5 minutes after stimulation (n=4) (Figure 6B). There was no significant difference between the two methods, indicating that the methods produce and detect a similar extent of platelet aggregation under the same conditions. Therefore, further aggregation experiments utilized the 24-well plate system of platelet aggregation, which allowed for up to 16 conditions to be tested simultaneously.

The ability of either murine or human fibrinogen to support murine platelet aggregation through different activation pathways was testing using murine PAR4 activating peptide

AYPGKF-NH2, ADP, and ionomycin at their maximal agonist dosages. As shown in Figure 7A, murine platelets stimulated with 100 µM AYPGKF-NH$_2$ that were supplemented with murine fibrinogen aggregated 51 ± 14% and 51 ± 15% when supplemented with human fibrinogen (p=0.91, n=6), showing no significant difference between the two species of fibrinogen. Similarly, when murine platelets were activated with 10 µM ADP, aggregation supported by murine fibrinogen was found to be 46 ± 9.9% and 43 ± 9.1% with human fibrinogen (p=0.55, n=6). Aggregation with 10 µM ionomycin also did not produce a difference between murine fibrinogen (55 ± 19%) and human fibrinogen (53 ± 16%) (p=0.93, n=2) aggregation. Murine gel-filtered platelets that were not supplemented with fibrinogen and stimulated with 10 µM ADP aggregated to 24 ± 6% which is a 42 ± 2.6% reduction in aggregation when comparing to fibrinogen-supplemented murine platelets (n=3) (not shown).

Dose-response curves of murine platelet aggregation in response to the three agonists above, using gel-filtered platelets supplemented with either murine or human fibrinogen, were generated. Dose-response curves were reported in percentage of maximal aggregation, as defined in the methods above, rather than raw percent aggregation, to correct for differences in quality of blood draws and inter-experimental variability. AYPGFK-NH$_2$ doses ranging from 12.5 µM to 200 µM produced a dose-response curve with overlapping murine and human fibrinogen data points as shown in Figure 7B. Maximal aggregation occurred at 100 µM AYPGFK-NH$_2$, with no significant change in aggregation observed at 200 µM dose. No significant differences in the percent of maximal aggregation in the presence of murine or human fibrinogen at a given agonist

dosage were observed (n=6). ADP dose-response curves from 0.625 µM to 10 µM followed a similar trend, with murine and human fibrinogen data points completely overlapping, and no significant differences between the species of fibrinogen detected (Figure 7C) (n=6). Maximal aggregation was observed at 10 µM ADP. The response to ionomycin doses ranging from 0.025 µM to 2 µM is shown in Figure 7D (n=2). Maximal aggregation occurred at 2 µM ionomycin. Aggregation in the presence of human fibrinogen typically produced higher average percent of maximal aggregation than murine fibrinogen, but there were no significant differences between the data sets.

To demonstrate that fibrinogen conjugated to colloidal nanoparticles by nonionic adsorption retains its biological activity, the ability of fibrinogen conjugated to 18 nm colloidal gold to support aggregation was investigated. Optimum concentration and pH values for conjugation of murine and human fibrinogen were determined by an adsorption isotherm. Conditions for human fibrinogen were 16 µg/mL concentration at pH 6.8 as previously reported (26). Murine fibrinogen conjugated best at pH 7.3 maintaining the same 16 µg/mL concentration. Human gel-filtered platelets supplemented with conjugated human fibrinogen and stimulated with 10 µM ADP aggregated $64 \pm 15\%$ while similarly treated platelets supplemented with unconjugated human fibrinogen aggregated to $62 \pm 18\%$ showing no significant difference in aggregation when fibrinogen bound to nanoparticles is used (n = 3) (Figure 8A). Aggregation of human platelets supplemented with conjugated murine fibrinogen was $58 \pm 0.5\%$, compared to aggregation with unconjugated murine fibrinogen at $49 \pm 14\%$ (n=3). No significance difference in aggregation supported by conjugated or

unconjugated fibrinogen was observed. The level of murine platelet aggregation using conjugated fibrinogen followed a similar trend (Figure 8B). Murine platelets supplemented with conjugated murine fibrinogen aggregated to $43 \pm 4.3\%$ (n=3), while those supplemented with unconjugated fibrinogen aggregated $43 \pm 1.6\%$ (n=2). Human fibrinogen produced similar levels of aggregation whether conjugated to colloidal gold ($40 \pm 1.6\%$, n=3) or unconjugated ($39 \pm 1.5\%$, n=2).

Human and murine fibrinogen labeling of surface-activated and aggregated platelets:
The biological activity of human and murine fibrinogen conjugates were compared through their labeling to human and murine surface-activated platelets. Colloidal gold conjugates of human fibrinogen labeled human surface-activated platelets heavily, and displayed the typical, well characterized labeling pattern (25-27). Bound labels cleared from the periphery and moved toward the area around the granulomere on the platelet surface (Figure 9A). Human platelets incubated with murine fibrinogen conjugates exhibited similar labeling to that seen with human fibrinogen conjugates (Figure 9B).

In general, murine platelets exhibited less extensive surface activation than human platelets under similar conditions (Figures 9C and 9D). In order to find murine gel-filtered platelets with morphology comparable to that of the typical human surface-activated samples (Figures 9E and 9F), supplementing Ca^{2+} to 5 mM rather than 2 mM was required. The majority of murine surface-activated platelets labeled weakly with either murine fibrinogen (Figure 9C) or human fibrinogen (Figure 9D). However, the minority population of murine platelets at advanced stages of surface activation showed

similar levels of labeling with human fibrinogen (Figure 9E) and murine fibrinogen

(Figure 9F) to their human counterparts. As with the well-spread human platelets,

labeling of the strongly activated murine platelets was extensive around the granulomere

of the platelets and relatively clear in the periphery.

Different morphologies and fibrinogen labeling patterns are observed when platelets are

activated in suspension rather than by contact with and adherence to a foreign surface.

Platelets aggregated in suspension using fibrinogen conjugated to nanoparticles as the

sole source of supplemental fibrinogen were collected onto filter membranes and imaged

by SEM. Morphology of the platelet aggregates was observed using SE imaging at low

accelerating voltage to distinguish surface features, and BSE imaging at higher

accelerating voltage to distinguish the high atomic number nanoparticle labels from the

low atomic number cell components. Unstimulated murine platelets incubated with

murine fibrinogen conjugates were isolated (Figure 10A) and had very low levels of

fibrinogen binding (Figure 10B). Murine platelets aggregate when activated with 10 μM

ADP in the presence of either murine fibrinogen (Figures 10C and 10D) or human

fibrinogen (Figures 10E and 10F) conjugates. Labels are found on the surface of the

aggregates and in some areas that appear to be internal to the aggregate. Labeling in

either species was not homogeneous, some parts of the platelet aggregates labeled more

extensively than others. Some murine platelets appear to have no labeling despite being

involved in a platelet aggregate. Murine aggregation produced in the presence of human

fibrinogen conjugates appeared more compact than those formed with murine fibrinogen

conjugates. Fibrinogen labels can be observed using conjugates of either species of fibrinogen.

Human platelets aggregated with murine fibrinogen conjugated to colloidal gold as the sole source of supplemented fibrinogen and stimulated with ADP aggregated strongly, as shown in Figures 10G and 10H, and labeled extensively in most aggregates. Labels appeared predominately within the aggregates (Figure 10H), but were also visible on the surface of platelets. Human platelets aggregated with human fibrinogen conjugates were examined as a positive control, and showed robust response with large very compact aggregates produced (Figures 10I and 10J). Human fibrinogen labeled human platelets primarily in the internal areas of the aggregate. However, labeling was also observed on the platelet surfaces. In general, human platelets labeled more expensively with conjugates of fibrinogen of either species than did murine platelets.

Localization of fibrinogen conjugates within murine platelet aggregates:
Murine platelets were labeled with human fibrinogen conjugates and aggregated as described above. The samples were prepared for TEM and ultrathin sections were cut to further examine the distribution of fibrinogen-conjugated nanoparticles within platelet aggregates at higher resolution than can be achieved by low magnification BSE SEM imaging. Fibrinogen labels were found on the surface of the platelets as well as in the OCS of the platelets (Figure 11A) in a manner similar to nanoparticles clearing the periphery of surface-activated platelets. In sections of an aggregate with multiple platelets visible, labels were present in platelet/platelet junctions as shown in Figure 11B.

Labeling was very heterogeneous between platelets, similar to the SEM studies of
fibrinogen conjugates binding to platelet aggregates.

Fibrinogen binding to preformed human platelet aggregates under in vivo-*like*
conditions:

Fibrinogen conjugates must be able to bind to preformed platelet aggregates *in vivo* in the
presence of plasma fibrinogen for any strategy using fibrinogen targeting. To
approximate these conditions, platelets were aggregated with unconjugated fibrinogen
and labeled post aggregation with conjugated fibrinogen. As a positive control, human
platelets were aggregated with supplemental fibrinogen conjugated to colloidal gold,
which labeled the platelets extensively, as observed by SEM and TEM in Figures 12A
and 12B, respectively. The vast majority of labels are located between platelets at
platelet/platelet junctions as well as internally in the platelet OCS system with few labels
present on the surface of the aggregates, similar to the fibrinogen binding to murine
platelets as described above. Labels were often clustered together on individual platelets
within an aggregate with neighboring platelets labeling less substantially. To test
labeling under more challenging conditions, platelets were aggregated with unconjugated
fibrinogen and then incubated with fibrinogen conjugated to colloidal gold. These
samples displayed similar labeling patterns to those previously described, but at lower
levels of total labeling (Figures 12C and 12D). Labeling was heterogeneous with some
very well labeled platelets existing beside moderately labeled platelets within the same
aggregate, similar to the localization observed in platelets aggregated with conjugated
fibrinogen. To even better approximate *in vivo* conditions, labeling of aggregates formed

in platelet-rich plasma was tested. Platelet-rich plasma was aggregated with the addition

of 67 μM SFLLRN-NH$_2$ to maximally activate the platelets without overt production of

fibrin. After aggregation, fibrinogen conjugated to colloidal gold was added directly to

the platelet rich plasma to label the preformed aggregates. TEM analysis of these

aggregates showed that fibrinogen conjugates still bound and penetrated deeply into the

aggregate (Figure 12E). Nanoparticle labeling was readily detectable, although the

labeling density observed in the preformed platelet-rich plasma aggregates was lower

than that in gel-filtered platelets aggregated with unconjugated fibrinogen. Nanoparticles

were observed to be less clustered within the aggregate and primarily located at

platelet/platelet junctions. Fewer labels were observed in the OCS.

Selectivity of fibrinogen binding for activated platelets:

A method that allows discrimination between unactivated and activated platelets is

necessary to evaluate the ability of fibrinogen conjugates to selectively target activated

platelets in an *in vivo* thrombus, while leaving unactivated platelets unlabeled. Therefore,

a procedure to produce an unactivated, biotinylated platelet population beside an

activated platelet population was developed. Biotinylation of platelets without causing

activation required substantial modifications to the standard biotinylation procedure used

commonly for other cell types (65), requiring the use of PGE$_1$ to prevent platelet

activation. The gel-filtered platelets used as the starting material for both the

biotinylation and activation procedures showed no fluorescence when labeled with both

AlexaFluor-488 fibrinogen and streptavidin-TRITC (Figures 13A and 13B). After

biotinylation, about 5% of the unactivated platelets were positive for fibrinogen binding

(Figure 13C) and nearly 100% were positive for streptavidin (Figure 13D). Streptavidin staining was mostly uniform around the surface of individual platelets, indicating the biotinylation was successful. For activated platelets, about 90% were positive for fibrinogen binding (Figure 13E) and as expected, 100% were negative for streptavidin (Figure 13F). Fibrinogen labeling was heterogeneous on the activated population. It was strongest in partially aggregated platelets and some individual platelets, while other individual platelets stained relatively weakly with fibrinogen. When the two populations of platelets were mixed prior to labeling, they remained mostly segregated. When labeled with both fibrinogen and streptavidin, platelets demonstrated positive fluorescence signal for only one or the other, and showed virtually no overlap (Figure 13G and 13H).

The mixed platelet population experiment was quantified using flow cytometry. The relative fluorescence of bound fibrinogen or avidin was determined on singly labeled controls and compared to that in the doubly labeled mixed sample. Baseline fibrinogen binding was similar between the starting unactivated gel-filtered platelets and the unactivated biotinylated platelets. Activated platelets exhibited a 15-fold increase in fibrinogen binding, as shown in Figure 14A. Biotinylated platelets were stimulated with thrombin to assess their capacity to become activated after repeated exposure to PGE_1. A modest 3-fold increase in mean fibrinogen binding was observed as a shift in the entire platelet population as compared to the unactivated, biotinylated sample. Avidin binding was only detected on platelets that were biotinylated (Figure 14B). As a measure of activation, platelets were also stained for the degranulation marker CD62P. Data

averaged over 3 experiments showed 28% of biotinylated (n=3), 91% of activated (n=3), and 70% of activated biotinylated platelets (n=2) were CD62P positive, compared to 5% in the unactivated population. A representative experiment is shown in Figure 14C. Dot plots comparing fibrinogen and avidin binding to mixed biotinylated and activated platelets were generated. The dot plot was divided into four distinct regions: [1] fibrinogen negative, avidin negative; [2] fibrinogen positive, avidin negative; [3] fibrinogen negative, avidin positive; and [4] fibrinogen positive, avidin positive. The fibrinogen negative, avidin negative region was defined by the unactivated population that was labeled with both fibrinogen and avidin. The avidin positive population was defined using the biotinylated platelet population labeled with avidin. When the activated and unactivated, biotinylated populations were mixed together, $13 \pm 12\%$ of the platelets were both fibrinogen and avidin negative, $39 \pm 12\%$ were fibrinogen positive but avidin negative, $41 \pm 3\%$ were fibrinogen negative and avidin postive, and $2 \pm 1\%$ were fibrinogen positive and avidin postive (Figure 14D, n=3). The remaining $2\% \pm 1$ of events were not within one of the four defined regions.

The mixed platelet population system was adapted to evaluate the selectivity of nanoparticle labeling for activated platelets. Fibrinogen was conjugated to $18 \text{ nm} \pm 2$ gold nanoparticles and streptavidin was conjugated to $38 \text{ nm} \pm 5$ gold nanoparticles. Platelets were isolated, biotinylated and labeled as described for the fluorescence experiments, with gold conjugates of fibrinogen and streptavidin substituted for fluorochrome conjugates. Specimen preparation and analysis were as described for SEM. Gel-filtered platelets showed the discoid morphology expected for unactivated platelets

and had only background levels of nanoparticle labeling with either fibrinogen or streptavidin labels (Figures 15A and 15B). The biotinylated platelets were primarily discoid but the majority of them deviated from the completely unactivated morphology and had short, thick pseudopodia, indicating that a slight degree of activation occurred. Thrombin-activated platelets had a rounded morphology with multiple long pseudopodia. Similar to the starting gel-filtered platelets, unactivated, biotinylated platelets showed little labeling with fibrinogen (Figures 15C and 15D) and activated platelets showed little labeling with streptavidin (Figures 15E and 15F).

Biotinylated platelets labeled well with streptavidin and displayed a nearly uniform distribution of labels over the surface of the platelets (Figure 16). Thrombin-activated platelets labeled with fibrinogen (Figure 17) displayed two distinct labeling patterns. Heavily-labeled platelets had labels on the platelet surface membrane as well as numerous labels internally, most likely in the OCS. Other activated platelets exhibited weaker labeling, with fibrinogen only present on the surface of the platelet. Nearly all thrombin-treated platelets were in a rounded form with many pseudopodia projecting from the platelet body, demonstrating an activated morphology. After the two platelet populations were mixed together and labeled with both fibrinogen and streptavidin (Figure 18), the labels nearly exclusively segregated to the thrombin-activated population or the unactivated biotinylated population, respectively. Streptavidin consistently labeled platelets with an unactivated or weakly activated morphology, while fibrinogen labeled the platelets with obvious activated morphologies. The nanoparticle label types were

easily distinguished at 13,000 x magnification due to the difference in size, brightness intensity in BSE micrographs, and distribution on the surface and within the platelet.

Discussion

The use of fibrinogen as a specific targeting molecule to direct nanoparticles to activated platelets was evaluated with an emphasis on the feasibility of the method being adapted to an *in vivo* system. First, the utility of human fibrinogen for targeting in both human and murine platelet systems was evaluated. Human fibrinogen performed similarly to murine fibrinogen with no significant differences between the two species of fibrinogen in murine platelet aggregation induced through different activation pathways. This indicates that human fibrinogen may be used for either human or murine *in vitro* studies and in future murine *in vivo* studies. Further studies showed that fibrinogen conjugated to gold nanoparticles can bind to platelets that have already formed a platelet aggregate in the presence of plasma levels of unconjugated fibrinogen. The biological activity of fibrinogen conjugated to nanoparticles was confirmed by the ability of the conjugates to support platelet aggregation and produce a characteristic labeling pattern. A method to evaluate whether fibrinogen conjugates show selectivity for activated platelets in a system containing both unactivated and activated platelets was developed. The activated platelets approximated platelets that would be involved in an *in vivo* thrombus, while the unactivated platelets reasonably represented circulating quiescent platelets. The activated population bound fibrinogen conjugates heavily while the unactivated population remained untargeted by fibrinogen.

Human fibrinogen for use in the murine system:

Use of a single species of fibrinogen for targeting human and murine platelets is desirable for both experimental and practical aspects. Fibrinogen probes may be used to study the role of activated platelets in blood clot formation either *in vitro* or *in vivo*. For our purposes, fibrinogen targeting provides a method to specifically deliver nanoparticles to activated platelets involved in thrombus formation. Human platelets reproducibly aggregated to a greater extent than murine platelets under similar conditions. The murine blood samples were likely over-anticoagulated, when the blood collection produced less than the expected volume of blood, as the syringe was preloaded with enough citrate to anticoagulate 810 μL blood. The lower blood volume and higher effective concentration of citrate would lead to excess chelation of platelet internal calcium and could have led to lower activation response. We partially compensated for this issue by the addition of extra Ca^{2+} ions, 5 mM final concentration, when activating murine platelets as compared to 2 mM for human platelets. The differences in activation and aggregation were likely due to effects of processing the murine platelets for *in vitro* use rather than any true difference in the ability of human and murine platelets to aggregate. It is also possible that murine aggregation may be dampened when compared to human hemostasis due to the large difference in vessel diameter and coagulation response. The differences we observed between the species in maximum aggregation does not preclude comparison of how well human and murine fibrinogen can support aggregation. For this analysis murine platelet aggregates are not compared to human aggregates, but rather murine aggregates generated with human or murine fibrinogen are directly compared to one another. Murine platelet aggregation varied depending on the activation pathway and

dose of agonist used. Supplementing murine platelets with murine or human fibrinogen produced completely overlapping aggregation dose-response curves. It has been demonstrated that rabbit gel-filtered platelets can support aggregation using granule-derived fibrinogen at nearly the same level as platelets supplemented with fibrinogen (66, 67). Human gel-filtered platelets by contrast require supplemental fibrinogen to support aggregation (68). We demonstrated that moderate aggregation (24%) occurs in our murine gel-filtered platelet system without supplemented fibrinogen, but at a greatly reduced level. These results demonstrate that supplemental human fibrinogen supports aggregation similarly to murine fibrinogen regardless of whether the platelet activation pathway is stimulated with a strong agonist such as the thrombin receptor activating peptide AYPGKF-NH$_2$, a moderate platelet activator such as ADP acting on the P2Y12 puringergic receptor, or by bypassing surface receptors and directly activating platelets by increasing membrane calcium permeability (ionomycin). There was no shift of the dose-response curves toward lower agonist doses in the presence of murine fibrinogen as compared to human fibrinogen suggesting that there is no enhancement of sensitivity when using species-matched protein in this model.

The aggregation data was generated using a 24-well plate system of aggregating platelets rather than using the more commonly used aggregometer. The aggregometer is essentially a heated stir plate and single wavelength spectrophotometer. Stirring and temperature control allow platelets to clump together in a reproducible manner and the spectrophotometer measures the optical density which is used to determine the percent aggregation. The 24-well plate system essentially deconstructs the aggregometer into its

essential elements, by using 24-well plates with a stirbar in each well and a stir plate to aggregate platelets inside an incubator. After aggregation, the material is fixed and a microtiter plate reader is used to measure the optical density of each sample similarly to a 96-well plate based aggregometry protocol (69). The 24-well plate system produced similar end point aggregation values for human platelets as were obtained in an aggregometer, indicating the two methods are essentially equivalent for end point analysis. The advantage to the 24-well plate system is that many samples may be run simultaneously, with our methods 16 samples could be tested at once, while a typical aggregometer may only be able to aggregate up to 4 samples at the same time. This ensures that the comparisons between samples are of the highest possible biological significance as the platelet aggregation response is time dependent. Aggregation of gel-filtered platelets is especially challenging as their responsiveness decreases rapidly over time. The 24-well plate system removes the time-dependent variability from platelet aggregation, and is useful in experiments where direct comparison of multiple platelet aggregation responses under varying conditions is required.

Human fibrinogen for targeting nanoparticles to activated platelets:

The use of fibrinogen conjugated to colloidal gold to label platelets has been extensively studied in both the surface-activated system (26, 27) and in platelets activated in suspension (29, 30). We confirmed earlier studies (70) that fibrinogen conjugated to colloidal gold supports aggregation of platelets in a similar manner to platelets aggregated with unconjugated fibrinogen. This suggests that the conjugation to nanoparticles does not diminish the ability of the fibrinogen to bind to $\alpha_{IIB}\beta_3$ or to

crosslink platelets together. An individual molecule of fibrinogen on an 18 nm colloidal gold nanoparticle may have both of its binding sites available. Alternatively, molecules of fibrinogen may only have a single binding site available after conjugation, but the nanoparticle contains multiple fibrinogen molecules (71). Regardless, fibrinogen conjugates retain virtually all of their platelet-specific biological functions.

The only difference between the two species of fibrinogen observed was when murine platelets were aggregated using supplemental human fibrinogen conjugated to colloidal gold. In these experiments, more dense aggregates were produced than when supplemental murine fibrinogen conjugates were used. The aggregates supported by murine fibrinogen conjugates produced less cohesive aggregates, in that they showed less evidence of being tightly drawn together in a manner resembling clot retraction. It is unlikely that the structure or sequence of the human fibrinogen supports murine aggregation better; rather, the commercially available human fibrinogen is of higher purity which allows it to be conjugated to colloidal gold more effectively. Labeling between the conjugates within the aggregates appeared similar.

When studying labeling of surface-activated platelets, the majority of the murine platelets were not well spread or well labeled in these experiments, which is likely due to the effect of excess citrate in the blood sample. The well-spread murine platelets found in the minority of the population were used as a direct comparison to human surface-activated platelets, which had similar morphologies. Fibrinogen from both species labeled the well-spread human and murine surface-activated platelets in the expected

labeling pattern (26, 27, 72). We did not observe differences between human and murine fibrinogen in either percent aggregation supported or labeling pattern. This indicates that for purposes of targeting nanoparticles toward platelets and future murine *in vivo* work, human fibrinogen should behave quite similarly to murine fibrinogen, and because commercially available human products are more pure and less expensive, human fibrinogen can serve as a suitable substitute that will work well in both human and murine systems.

Fibrinogen conjugate binding to platelets in the presence of plasma levels of unconjugated fibrinogen:

Fibrinogen conjugates were capable of labeling platelet aggregates when used as the only source of supplemental fibrinogen to support aggregation, after the platelets were aggregated with unconjugated fibrinogen, and even in aggregated platelet-rich plasma. A population of platelets labeled intensely under all conditions tested, while other nearby seemingly similar platelets had lower levels of labeling and internalization of the conjugate. The difference in labeling could be due to the history of the platelet, its age, and/or its relative health. Alternatively, these platelets may have bound unconjugated fibrinogen released from platelet internal stores upon activation (73, 74). The amount of labels found within aggregates generated with conjugates was enormous. Aggregates labeled after aggregation with unconjugated fibrinogen bound less fibrinogen conjugates but still displayed large quantities of bound nanoparticles. The platelet-rich plasma aggregates better approximated what would occur *in vivo*, and showed dramatically reduced but readily detectable binding of fibrinogen conjugates. In all cases the labels

were observed primarily within the platelet aggregate at platelet/platelet junctions and in the OCS. The fibrinogen labels penetrated deeply within preformed aggregates even when high concentrations of competing unconjugated fibrinogen were present, showing that fibrinogen conjugates have excellent potential for therapeutic targeting of the entire aggregate, rather than just the surface of a thrombus.

Fibrinogen specificity for activated platelets:

Platelets activated with thrombin labeled strongly with fibrinogen. Labeling was similar to that observed in platelet aggregates produced with fibrinogen conjugates, where some platelets internalized the labels while other platelets only had labeling on their surfaces. When biotinylated platelets were utilized, they were easily distinguished using streptavidin conjugates. The binding patterns of fibrinogen and streptavidin make distinguishing the labels straightforward. When thrombin-activated and biotinylated platelet populations were mixed together, the two populations of platelets remain distinct in morphology (75, 76) and fibrinogen labeling patterns. The segregation of the two populations was quantifiable using flow cytometry. The method developed was successful in preventing the activated platelets from recruiting the unactivated platelets into an activated state, allowing evaluation of fibrinogen binding on the two distinct populations. Fibrinogen bound only to platelets that were activated with thrombin, suggesting that fibrinogen targeting, whether using a fluorochrome conjugate or nanoparticle conjugate, will select for truly activated platelets.

We tested whether the biotinylated platelets could be activated, and found they exhibited much weaker fibrinogen binding and CD62P expression after thrombin activation. The reduction in activation is likely due to their repeated exposure to PGE_1 and its solvent, ethanol. Diminished responsiveness of the biotinylated platelets is a flaw of this system but was unavoidable, as without the efforts taken to prevent activation during the biotinylation process, all of the resulting platelets would be at least partially activated, and not representative of circulating platelets. In the mixed population experiments, the activated and unactivated biotinylated platelets demonstrated distinctly different levels of fibrinogen binding.

Fibrinogen appears to be a good candidate for activated platelet targeting; this model suggests that the unactivated platelets in circulation would be left untargeted while activated platelets involved in a blood clot would become strongly labeled with fibrinogen. Further, it may be possible to utilize the mixed platelet population system developed here to show specific hyperthermic damage to activated platelets using fibrinogen-conjugated gold-coated nanoparticles while leaving unactivated platelets in healthy condition.

 Expected in vivo applications:
These results suggest that fibrinogen conjugated to nanoparticles is capable of targeting conjugated nanoparticles to activated platelets participating in an aggregate or thrombus while leaving unactivated platelets unlabeled. Human fibrinogen can be used as the preferred targeting molecule for both human and murine systems. Fibrinogen conjugates

are able to bind to platelet aggregates, even after formation with and in the presence of unconjugated fibrinogen. However, a reduction in labeling will need to be considered during development of any *in vivo* applications. The internal localization and clustering of fibrinogen labels in platelet aggregates supports the idea that inducing hyperthermia will be feasible. The depth to which the labels can penetrate aggregates is especially encouraging for the predicted success of the system in disruption of in *vivo* thrombi.
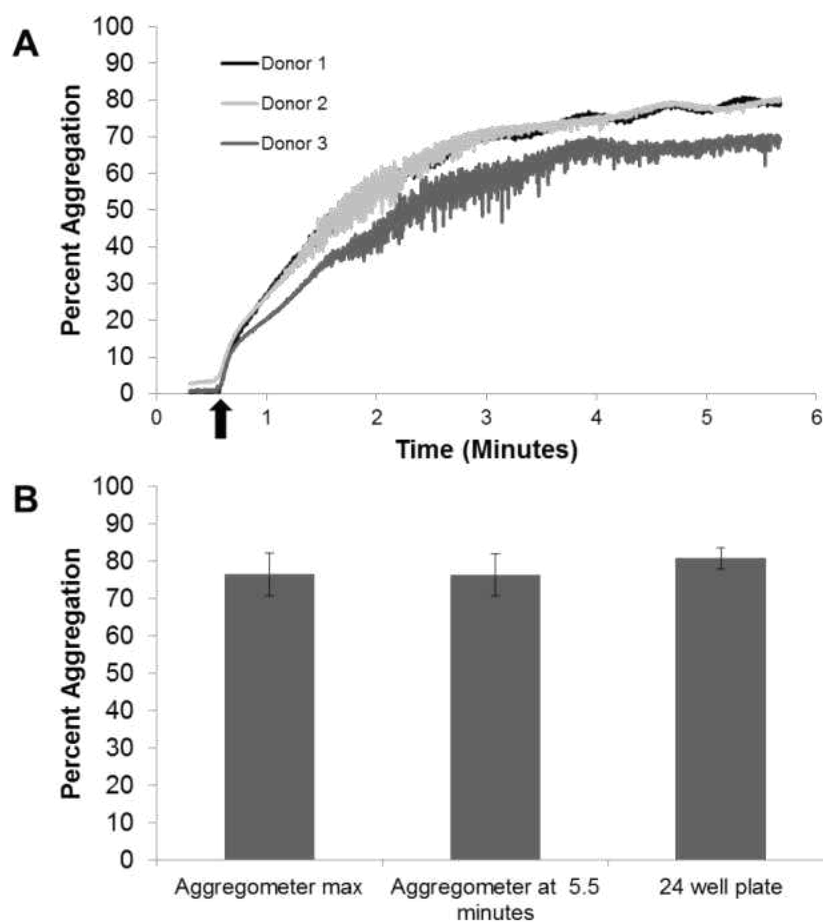
Figures and Figure Legends:

Figure 6. Aggregation of human platelets using different assay systems. (A) aggregometer tracing of gel-filtered platelets supplemented with 200 μg/mL human fibrinogen and 2 mM Ca^{2+}, and stimulated with 67 μM of SFLLRN-NH$_2$. Representative results obtained from 3 blood donors. Aggregation was initiated at 30 seconds (arrow), and was considered to have reached its maximal point by 5 minutes 30 seconds. The maximal aggregation from the aggregometer and the end point from aggregometer and the 24-well plate aggregation system (n=3) are shown in (B). Error bars are standard deviation. No significant difference in maximal aggregation was observed between the aggregometer and 24-well plate systems.
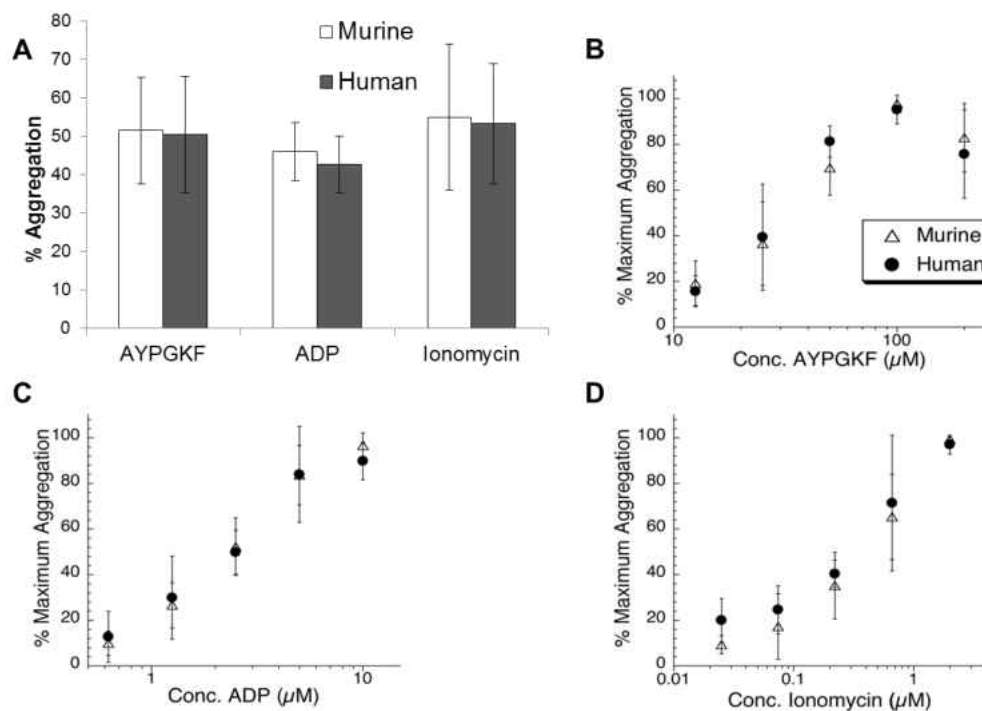
Figure 7. Aggregation of murine gel-filtered platelets supplemented with murine (open bars) or human (closed bars) fibrinogen. (A) Aggregation with maximal doses of AYPGKF-NH$_2$ (100 µM), ADP (10 µM), or ionomycin (2 µM). (B-D) Dose-response curves of murine platelet aggregation in the presence of 200 µg/mL murine fibrinogen (open triangles) or human fibrinogen (closed circles). Data are expressed as a function of the aggregation observed with the maximal dose of the indicated agonists. Error bars represent standard deviation, n = 6 (B, C) or n = 2 (D) for each data point. No significant differences between murine and human fibrinogen were detected at any dose of any agonist tested.
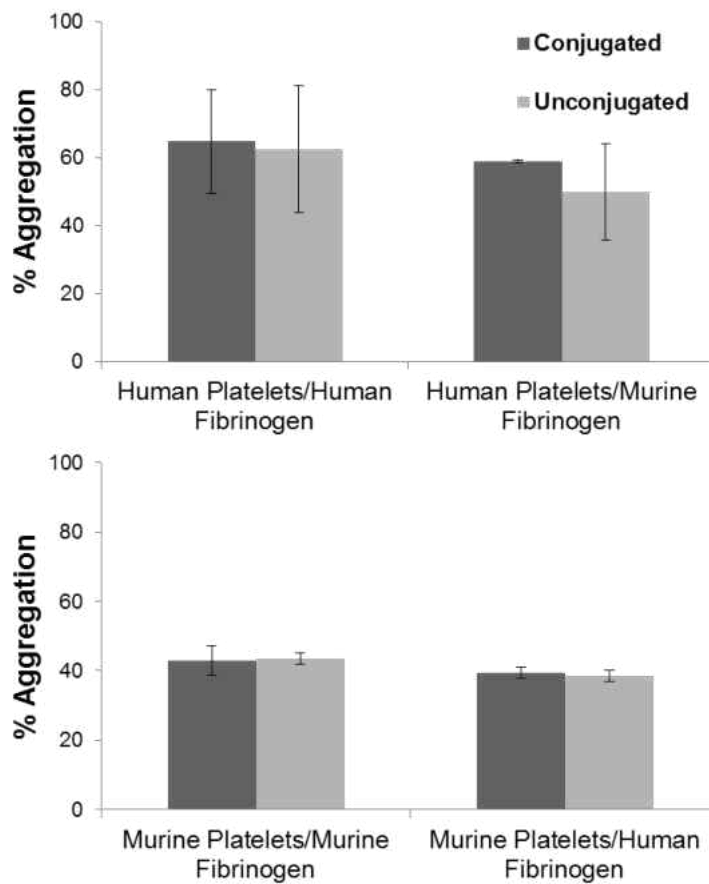
Figure 8. Direct comparison between unconjugated (open bars) and colloidal gold-conjugated (closed bars) fibrinogen in the aggregation of gel-filtered platelets in response to 10 μM ADP. (A) human platelets supplemented with human or murine fibrinogen; (B) murine platelets supplemented with murine or human fibrinogen. Error bars represent standard deviation; n = 3 for human platelets, n = 3 for murine platelets with conjugated fibrinogen and n = 2 for murine platelets with unconjugated fibrinogen.

Figure 9. Analysis of gold conjugated-fibrinogen labeling on surface-activated platelets by SEM. Well spread surface-activated human platelets were incubated with either gold-conjugated human (A) or murine (B) fibrinogen. Representative micrographs of murine surface-activated platelets labeled with human or murine conjugates are shown in (C) and (D), respectively. Less typical murine platelets at advanced stages of surface activation that more closely resemble human surface-activated platelets are shown labeled with human (E) or murine (F) conjugates. The colloidal gold nanoparticles appear as bright spheres in SEM; examples of the nanoparticles are indicated with arrows. Labels are primarily observed near the center of each platelet. Areas of the platelet periphery that have been cleared of labels through their centralization are indicated on some platelets with an arrowhead. Size bars are 3 μm.

89
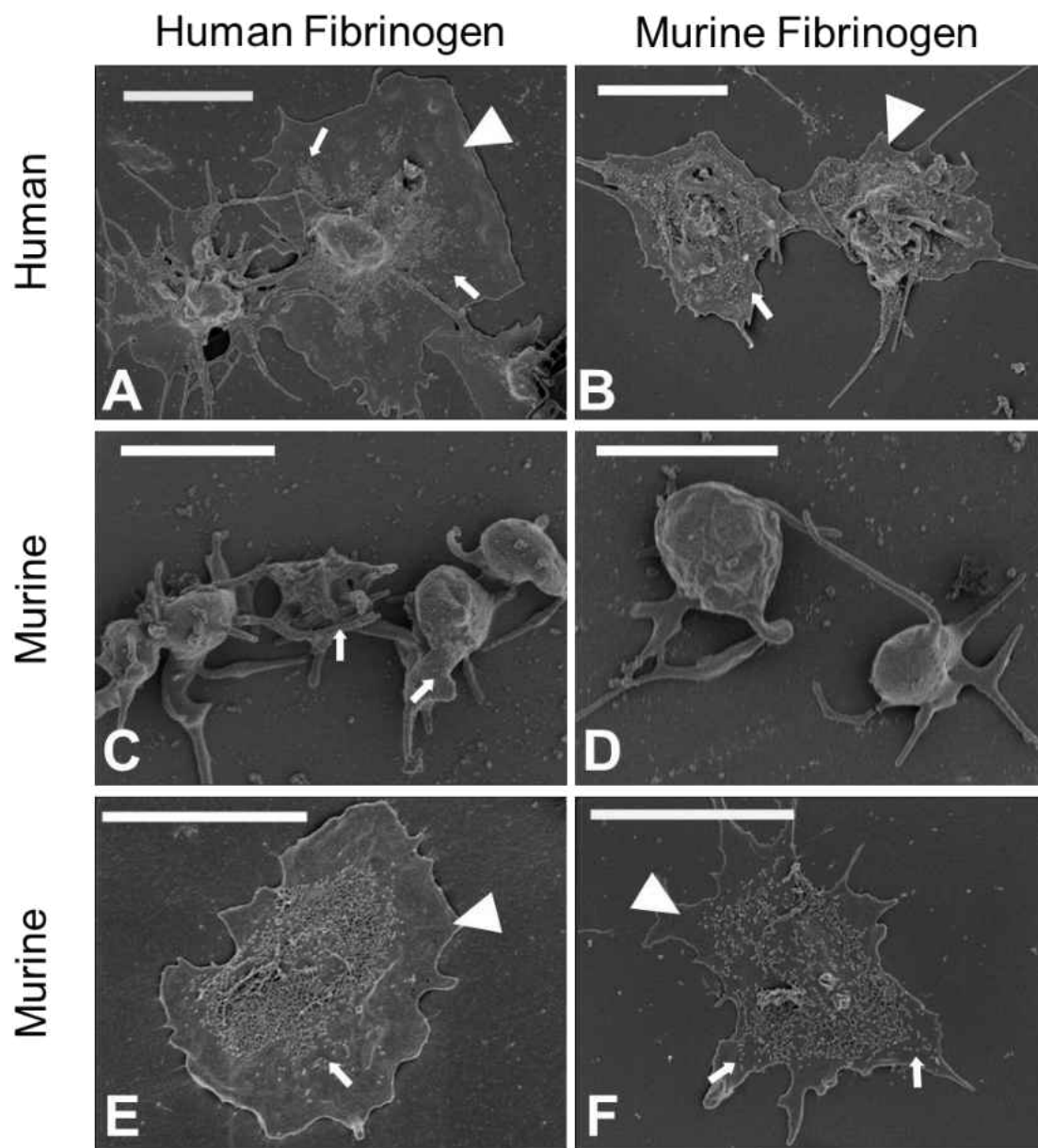
Figure 9

Figure 10. SEM analysis of platelets aggregated with colloidal gold-fibrinogen conjugates. Left column, low voltage (1 kV), high resolution secondary electron (SE) images that reveal fine surface detail. Right column, backscattered electron (BSE) images of the same field of view as shown on the left. (A, B) demonstrate murine gel-filtered platelets supplemented with murine fibrinogen conjugates in the absence of agonist. Representative micrographs showing murine gel-filtered platelets supplemented with either murine or human fibrinogen conjugates and stimulated with 10 mM ADP are shown in (C, D) and (E, F), respectively. Human gel-filtered platelets supplemented with murine or human fibrinogen conjugates with ADP stimulation are shown similarly in (G, H) and (I, J). Size bars are 5 μm.

SE BSE

A B

Murine Platelets/
Murine Fibrinogen
No Agonist

C D

Murine Platelets/
Murine Fibrinogen

E F

Murine Platelets/
Human Fibrinogen

G H

Human Platelets/
Murine Fibrinogen

I J

Human Platelets/
Human Fibrinogen
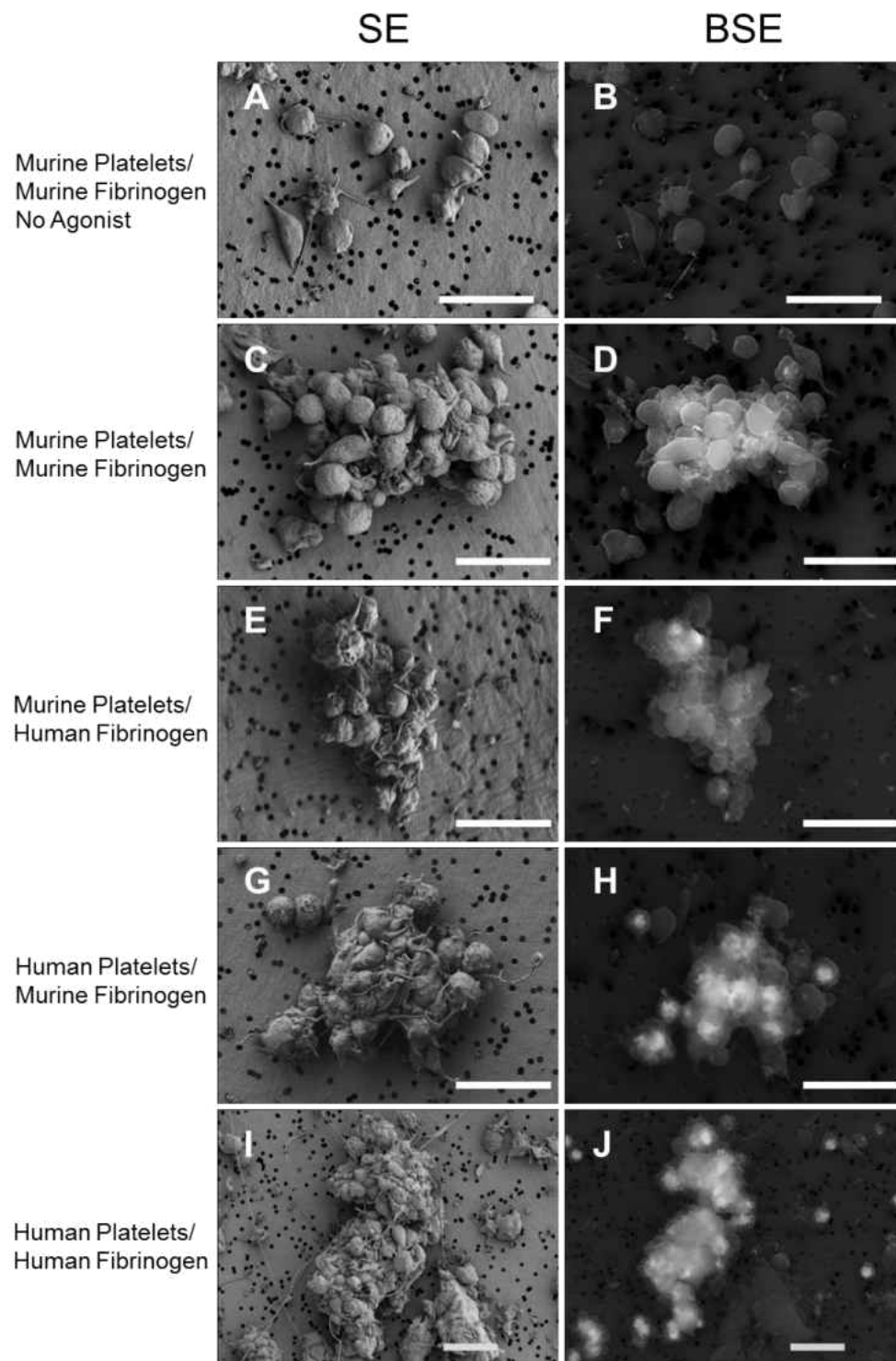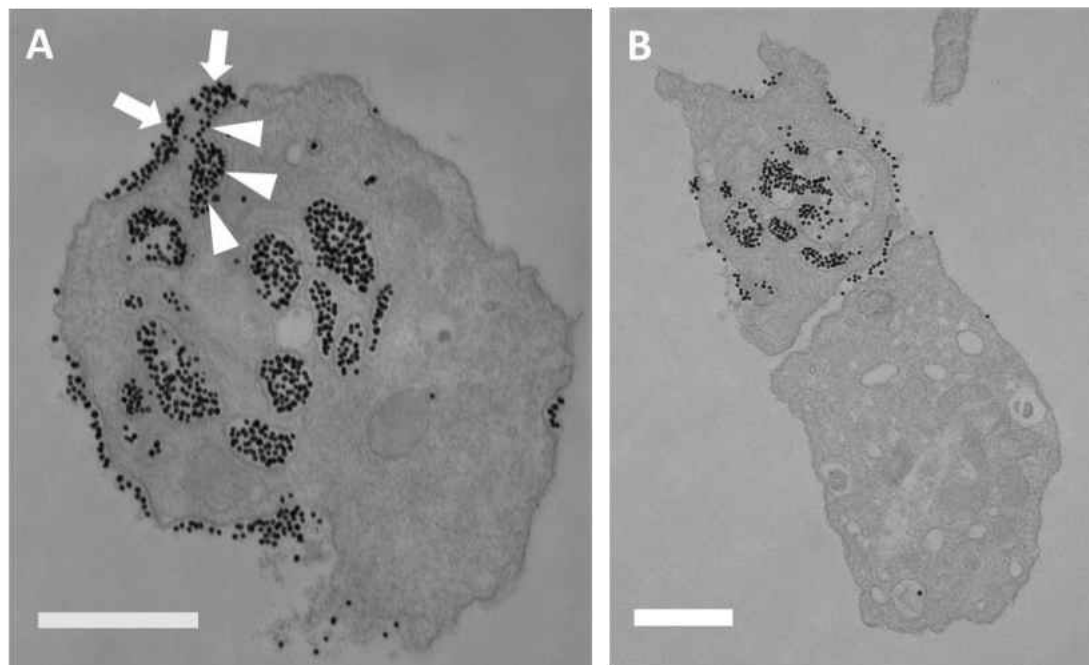
Figure 10

Figure 11. TEM analysis of ultrathin sections of murine platelets aggregated with human fibrinogen conjugated to colloidal gold nanoparticles. Fibrinogen-conjugated colloidal gold is observed around the membrane of the platelet, in platelet/platelet junctions, and in the OCS of some platelets. An area in which movement of conjugates into the OCS from the platelet surface is indicated by white arrows in (A); the progression of the conjugates deeper into the OCS is further indicated by arrowheads. The range of labeling intensity observed in individual sections is demonstrated in (B) where a heavily labeled platelet has interacted with a lightly labeled platelet. Fibrinogen conjugates can be observed at the platelet/platelet junction. Size bars are 500 nm.

Figure 12. Comparison of human fibrinogen binding to human platelets during and after platelet aggregation. Micrographs of a human platelet aggregate aggregated with colloidal gold conjugated fibrinogen and imaged in the SEM by backscattered electrons or by TEM are shown in (A) and (B), respectively. Platelet aggregates produced with unconjugated fibrinogen and then labeled post aggregation in competition with unconjugated fibrinogen are shown in a backscattered electron micrograph (C) and TEM micrograph (D). In all cases, fibrinogen conjugates are mostly observed within the aggregates at platelet/platelet junctions (arrows) or within the OCS of individual platelets (arrowheads). (E) demonstrates platelets aggregated in platelet-rich plasma and then labeled with fibrinogen conjugates, allowing them to compete with plasma fibrinogen. The outer edge of the aggregate is slightly to the right of the field of view. The number of nanoparticle conjugates observed was reduced in platelets labeled after aggregation with unconjugated fibrinogen when compared to platelets aggregated using the conjugates as the sole source of non-platelet-derived fibrinogen. Size bars are 4 μm for (A) and (C), 1 μm for (B), (D), and (E).
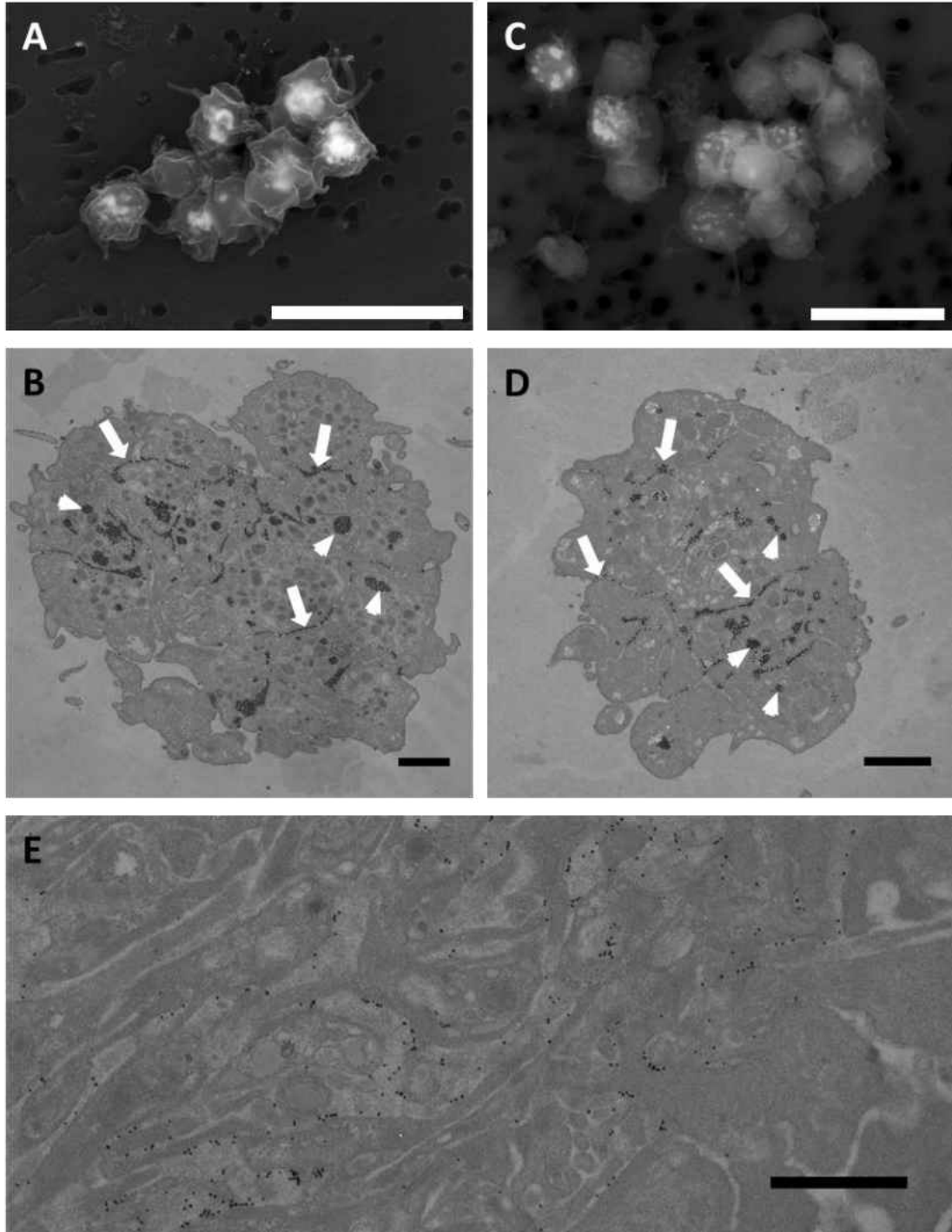
Figure 12

Figure 13. Fluorescent fibrinogen labeling of human platelets in a mixed population of activated and unactivated platelets. Gel-filtered platelets labeled with AlexaFluor 488-fibrinogen and streptavidin-TRITC shown are shown using DIC (A) and as an overlay of FITC and TRITC fluorescence channels (B). The fluorescence channels of biotinylated, unactivated platelets labeled with Alexa 488-fibrinogen and streptavidin-TRITC are shown in (C) and (D), respectively. Fluorescence channels of platelets activated with thrombin and labeled with AlexaFluor 488-fibrinogen and streptavidin-TRITC are shown in (E) and (F). The biotinylated, unactivated platelets and thrombin-activated platelets were mixed together and labeled with both fluorochromes. The resulting DIC image is shown in (G) to demonstrate platelet morphologies, including some small platelet aggregates (arrow). Overlaid FITC and TRITC fluorescence channels of mixed unactivated, biotinylated and thrombin-activated platelets are shown in (H). (C) and (F) include DIC images as insets to show platelets in the field of view. Size bar is 20 μm for all images.
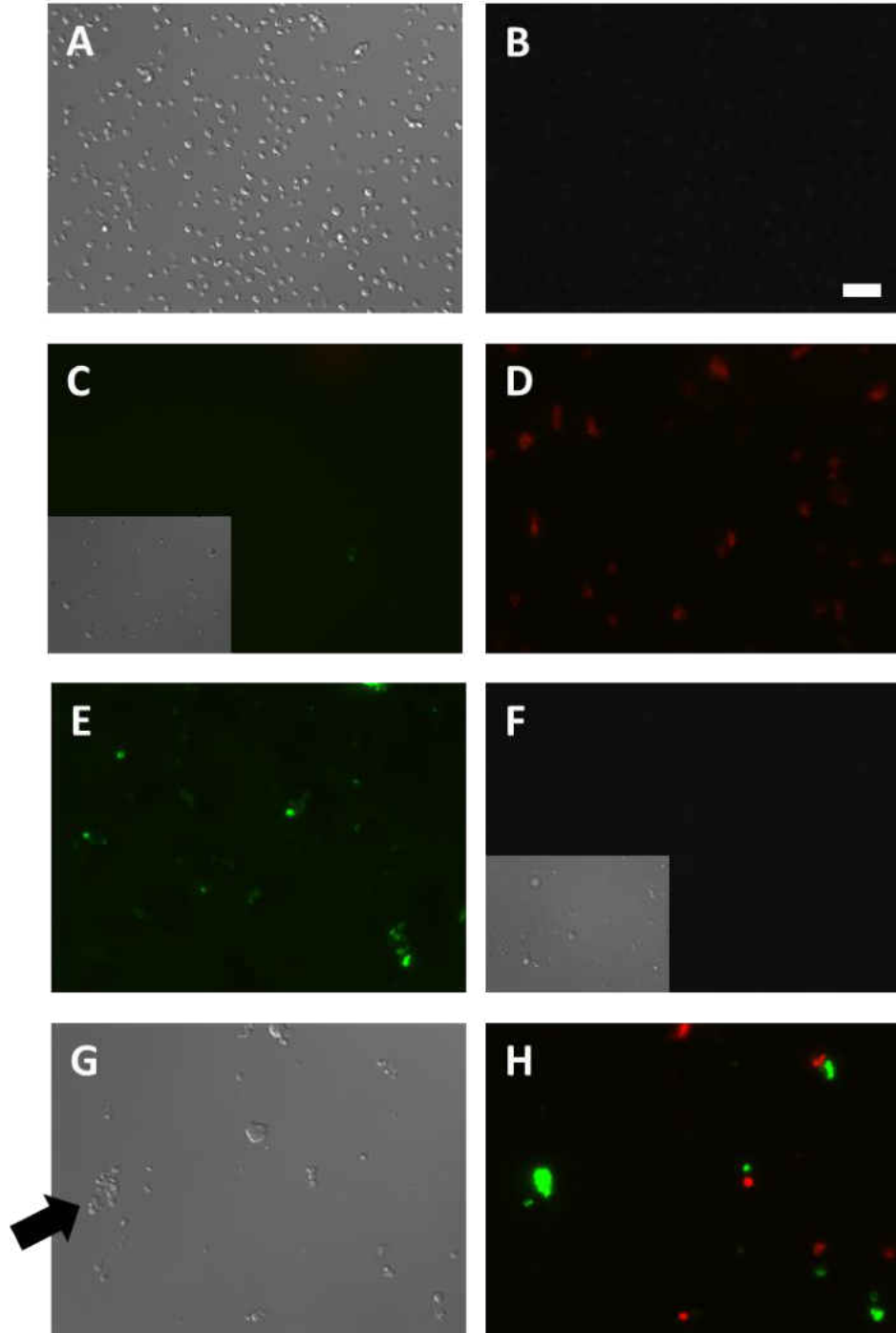
Figure 13
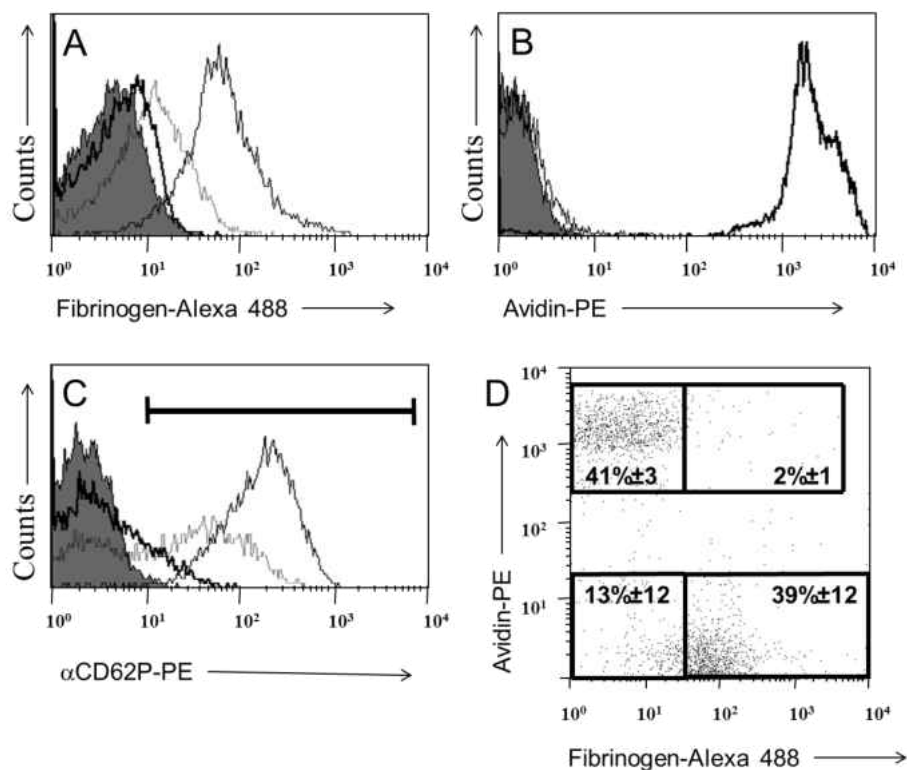
Figure 14. Flow cytometry analysis of biotinylated, unactivated platelets mixed with thrombin-activated platelets. Histograms depicting single populations of unactivated (filled); activated (thin black line); and unactivated, biotinylated (thick black line) are shown in (A,B,C), activated, biotinylated (gray line) platelets are further shown in (A,C). (A) shows binding of fibrinogen conjugated to AlexaFluor 488 to the platelet populations. Avidin conjugated to PE staining is shown in (B). (C) demonstrates staining for P-selectin (CD62P) using a PE-conjugated monoclonal antibody; the gate for CD62P-positive platelets is shown. A dot plot of the mixed populations of biotinylated and activated platelets stained together is shown in (D). The gates drawn in (D) represent populations of platelets positive or negative for fibrinogen and positive or negative for avidin derived using single label controls. Average percentage of platelets and standard deviation in each gate over 3 experiments is given.

Figure 15.   Singly-labeled negative controls for selectivity of nanoparticle conjugates for

unactivated (A,B); unactivated, biotinylated (C,D); and thrombin-activated platelets

(E,F).   SEM of human unactivated gel-filtered platelets labeled with fibrinogen

conjugated to 18 nm colloidal gold (FGN-Au), and streptavidin conjugated to 38 nm (SA-

Au) colloidal gold is shown in secondary (SE) (A) and backscattered electron (BSE) (B)

images.   Unactivated biotinylated platelets labeled with fibrinogen conjugated to 18 nm

colloidal gold are shown in SE (C) and BSE (D) images.   Activated platelets labeled with

streptavidin conjugate shown in SE (E) and BSE (F) imaging modes.   No labeling over

background levels can be detected in any of these specimens.   Size bar is 4 μm for all
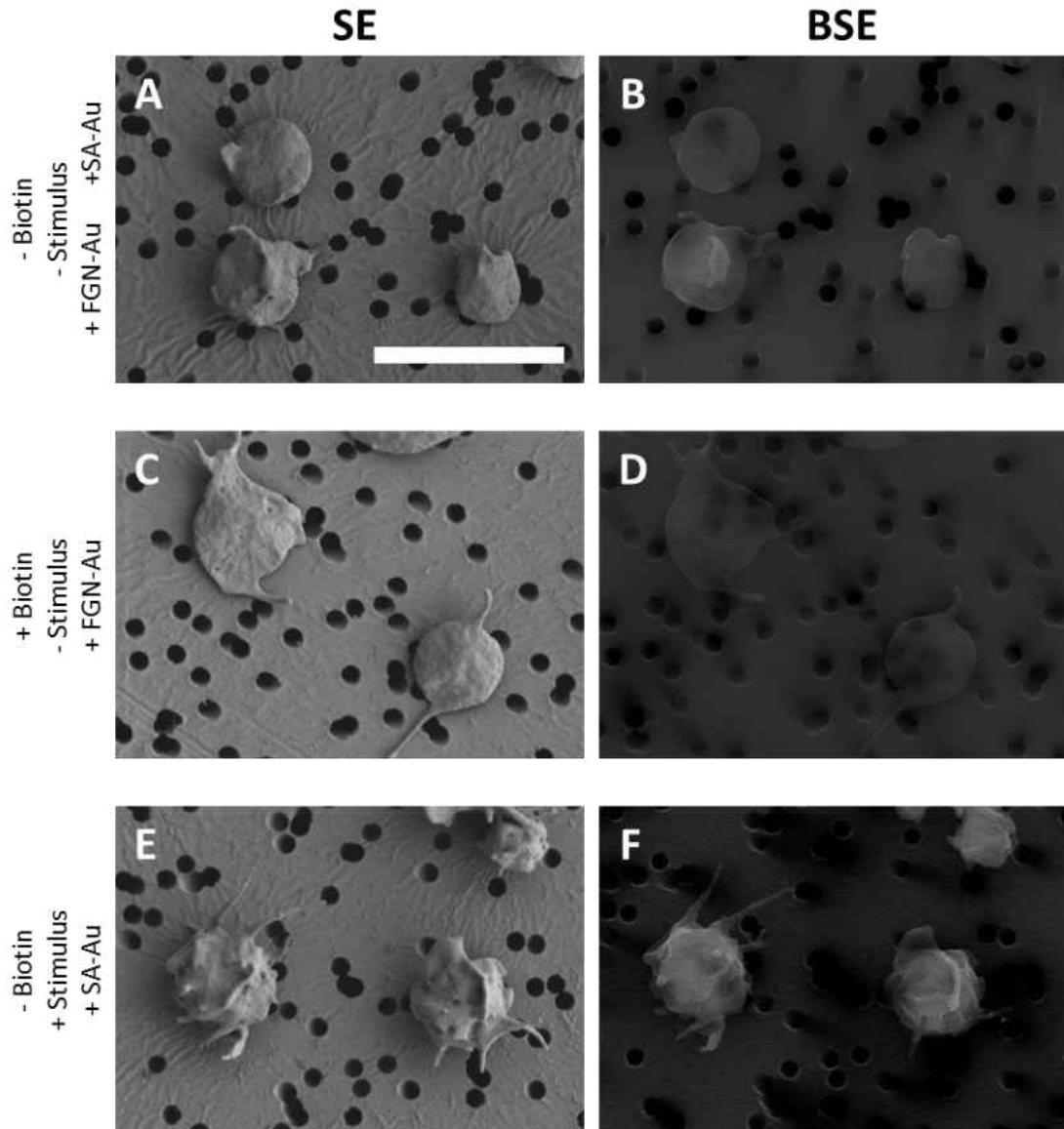
micrographs.

Figure 15

Figure 16. Singly-labeled positive control for streptavidin-conjugated nanoparticle binding to unactivated, biotinylated platelets. (A) shows a secondary electron micrograph of biotinylated platelets with the morphology typically observed after the biotinylation procedure. (B) demonstrates the same area imaged with backscattered electrons. Streptavidin labels appear over the entire surface of the platelets including on the short pseudopodial extensions. Size bar is 4 μm for both micrographs.
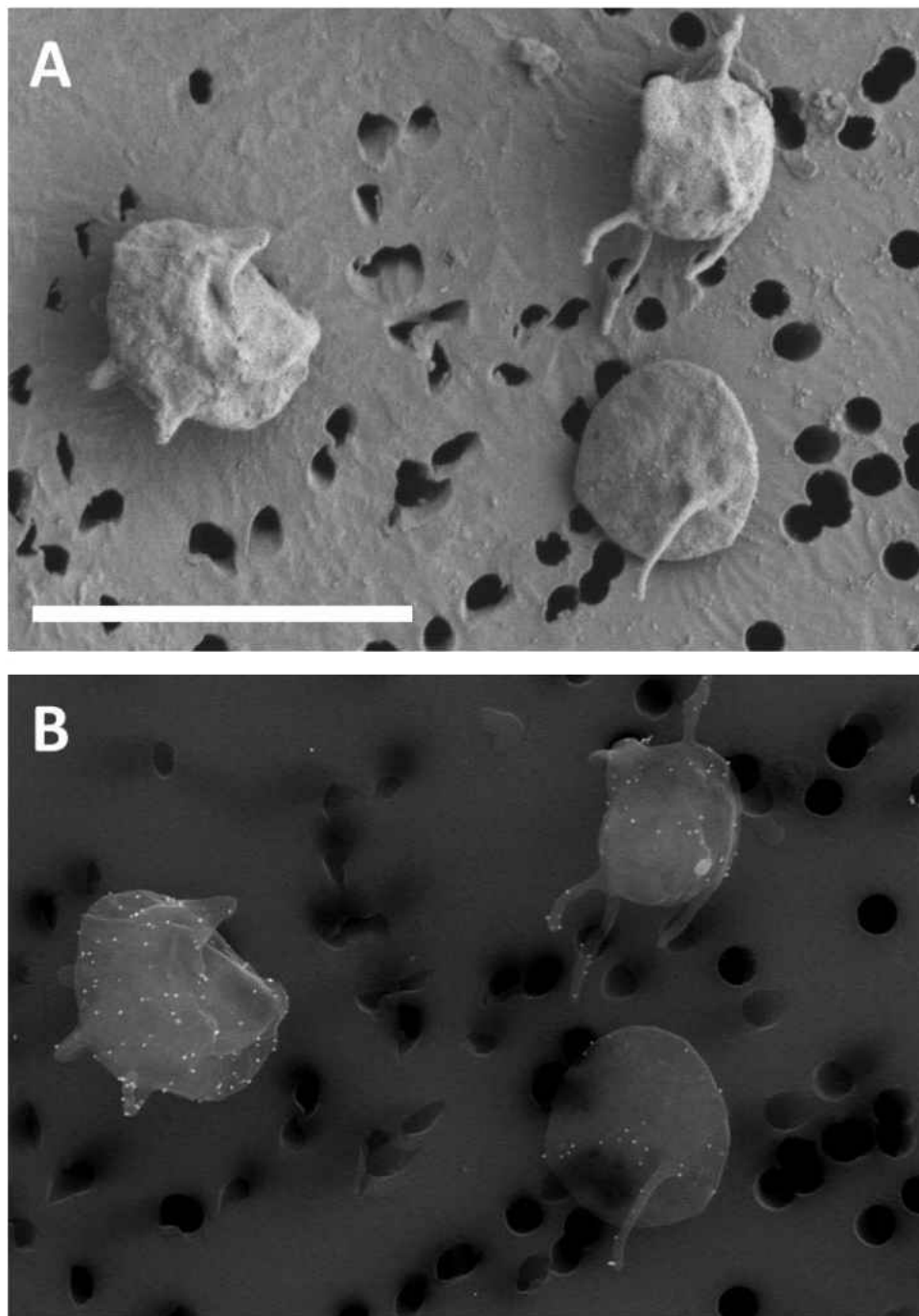
Figure 16

Figure 17. Thrombin-activated platelets labeled with fibrinogen conjugated to 18 nm colloidal gold. (A) shows a secondary electron micrograph of several activated platelets. (B) shows the backscattered electron micrograph in the same region showing labeling localization. Two distinct labeling patterns are observed, with heavy labeling shown as very bright platelets and moderate surface labeling showing distinct small nanoparticles on the surface, indicated with arrows. Size bar is 4 μm for both micrographs.
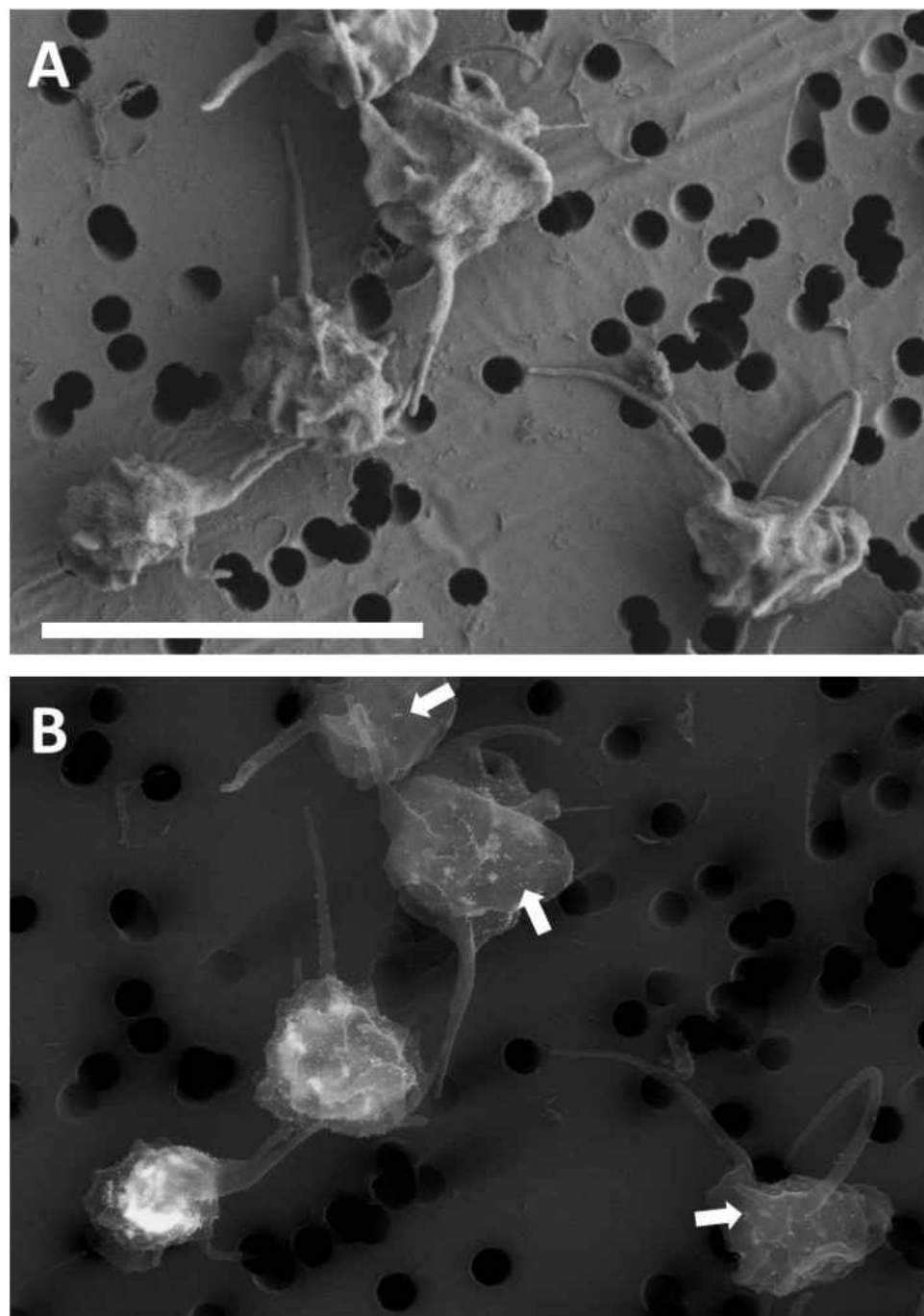
Figure 17

Figure 18. Activated and biotinylated, unactivated platelets mixed together and labeled with both fibrinogen conjugated to 18 nm colloidal gold and streptavidin conjugated to 38 nm colloidal gold. SE micrographs of two representative fields are shown in (A) and (C). Corresponding BSE micrographs are shown in (B) and (D). The field shown in (A) and (B) demonstrates all types of labeling observed in this sample. The top platelet is thrombin-activated, distinguished by heavy fibrinogen labeling, including extensive labeling of the platelet interior. The middle platelet demonstrates a thrombin-activated platelet distinguished by moderate labeling with 18 nm colloidal gold conjugated to fibrinogen covering nearly its entire surface. The bottom platelet is an unactivated, biotinylated platlet, which is shown by binding of streptavidin conjugated to 38 nm colloidal gold on the platelet surface and the lack of any surface or interior labeling with 18 nm fibrinogen labels. (C) and (D) show a typical field of platelets with two thrombin-activated platelets on the left and a single unactivated, biotinylated platelet on the right. Size bar is 4 μm for all micrographs.
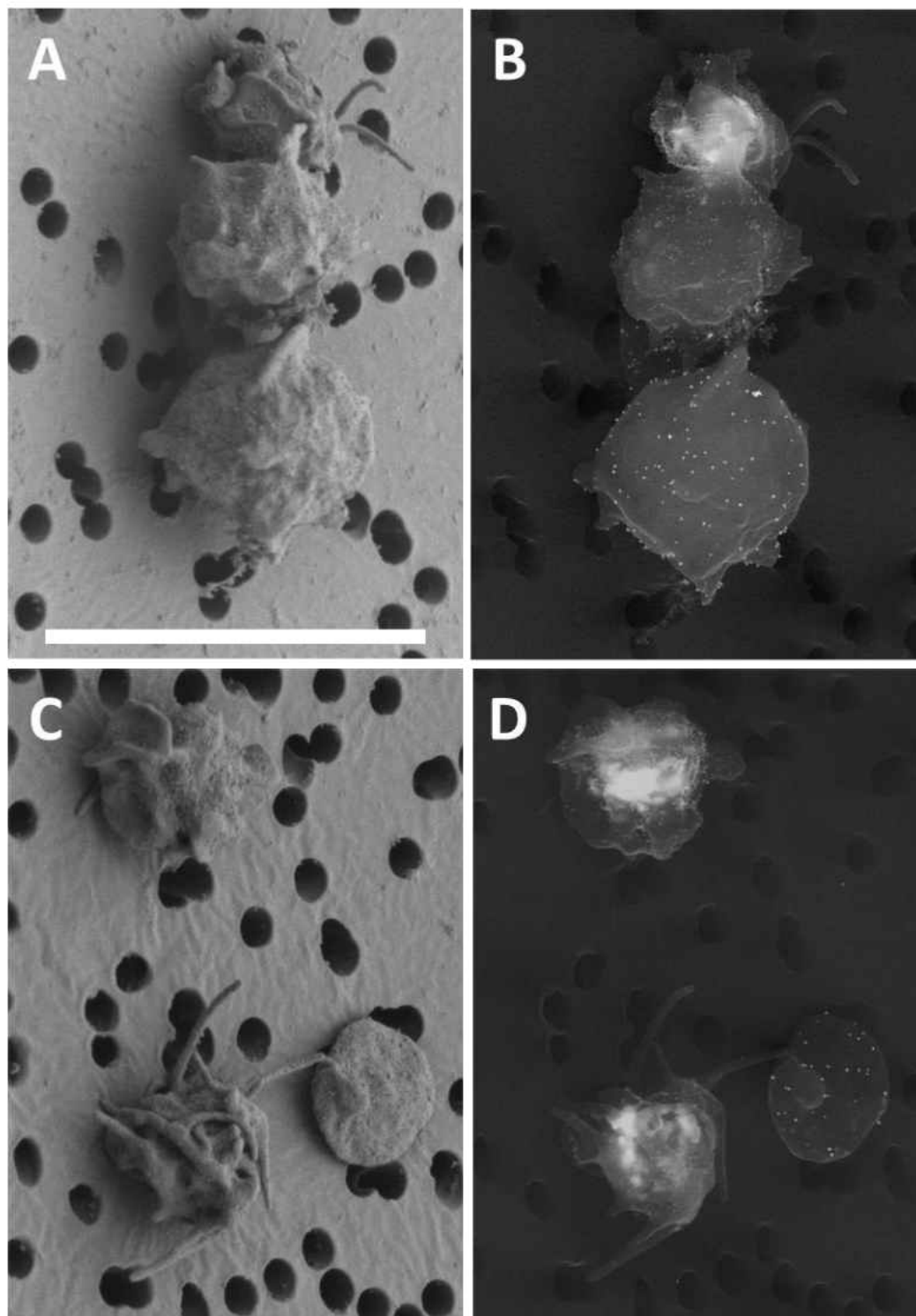
Figure 18

References

1. Peerschke, E. I., M. B. Zucker, R. A. Grant, J. J. Egan, and M. M. Johnson. 1980. Correlation between fibrinogen binding to human platelets and platelet aggregability. *Blood* 55:841-847.

2. Farrell, D. H., and P. Thiagarajan. 1994. Binding of recombinant fibrinogen mutants to platelets. *J. Biol. Chem.* 269:226-231.

3. Jumilly, A. L., A. Veyradier, A. S. Ribba, D. Meyer, and J. P. Girma. 2001. Selective inactivation of Von Willebrand factor binding to glycoprotein IIb/IIIa and to inhibitor monoclonal antibody 9 by site-directed mutagenesis. *Hematol. J.* 2:180-187.

4. Pytela, R., M. D. Pierschbacher, M. H. Ginsberg, E. F. Plow, and E. Ruoslahti. 1986. Platelet membrane glycoprotein IIb/IIIa: member of a family of Arg-Gly-Asp--specific adhesion receptors. *Science* 231:1559-1562.

5. Phillips, D. R., and P. P. Agin. 1977. Platelet membrane defects in Glanzmann's thrombasthenia. Evidence for decreased amounts of two major glycoproteins. *J. Clin. Invest.* 60:535-545.

6. Nurden, A. T., and J. P. Caen. 1975. Specific roles for platelet surface glycoproteins in platelet function. *Nature* 255:720-722.

7. Seligsohn, U. 2002. Glanzmann thrombasthenia: a model disease which paved the way to powerful therapeutic agents. *Pathophysiol. Haemost. Thromb.* 32:216-217.

8. Bennett, J. S., J. A. Hoxie, S. F. Leitman, G. Vilaire, and D. B. Cines. 1983. Inhibition of fibrinogen binding to stimulated human platelets by a monoclonal antibody. *Proc. Natl. Acad. Sci. USA* 80:2417-2421.

9. Shattil, S. J., J. A. Hoxie, M. Cunningham, and L. F. Brass. 1985. Changes in the platelet membrane glycoprotein IIb.IIIa complex during platelet activation. *J. Biol. Chem.* 260:11107-11114.

10. Coller, B. S., E. I. Peerschke, L. E. Scudder, and C. A. Sullivan. 1983. A murine monoclonal antibody that completely blocks the binding of fibrinogen to platelets produces a thrombasthenic-like state in normal platelets and binds to glycoproteins IIb and/or IIIa. *J. Clin. Invest.* 72:325-338.

11. Hartman, G. D., M. S. Egbertson, W. Halczenko, W. L. Laswell, M. E. Duggan, R. L. Smith, A. M. Naylor, P. D. Manno, and R. J. Lynch. 1992. Non-peptide

fibrinogen receptor antagonists. 1. Discovery and design of exosite inhibitors. *J. Med. Chem.* 35:4640-4642.

12.   Coller, B. S. 1985. A new murine monoclonal antibody reports an activation-dependent change in the conformation and/or microenvironment of the platelet glycoprotein IIb/IIIa complex. *J. Clin. Invest.* 76:101-108.

13.   Tcheng, J. E., S. G. Ellis, B. S. George, D. J. Kereiakes, N. S. Kleiman, J. D. Talley, A. L. Wang, H. F. Weisman, R. M. Califf, and E. J. Topol. 1994. Pharmacodynamics of chimeric glycoprotein IIb/IIIa integrin antiplatelet antibody Fab 7E3 in high-risk coronary angioplasty. *Circulation* 90:1757-1764.

14.   Gold, H. K., L. W. Gimple, T. Yasuda, R. C. Leinbach, W. Werner, R. Holt, R. Jordan, H. Berger, D. Collen, and B. S. Coller. 1990. Pharmacodynamic study of F(ab')2 fragments of murine monoclonal antibody 7E3 directed against human platelet glycoprotein IIb/IIIa in patients with unstable angina pectoris. *J. Clin. Invest.* 86:651-659.

15.   Adams, H. P., Jr., W. Hacke, B. Oemar, A. Dávalos, R. A. Cook, P. Trouillas, F. Fazekas, J. Bogousslavsky, J. Hilburn, J. Torner, L. Jacques, A. Shuaib, and P. Reid. 2005. Emergency administration of abciximab for treatment of patients with acute ischemic stroke: results of a randomized phase 2 trial. *Stroke* 36:880-890.

16.   Adams, H. P., Jr., M. B. Effron, J. Torner, A. Dávalos, J. Frayne, P. Teal, J. Leclerc, B. Oemar, L. Padgett, E. S. Barnathan, and W. Hacke. 2008. Emergency administration of abciximab for treatment of patients with acute ischemic stroke: results of an international phase III trial: Abciximab in Emergency Treatment of Stroke Trial (AbESTT-II). *Stroke* 39:87-99.

17.   Di Minno, G., P. Thiagarajan, B. Perussia, J. Martinez, S. Shapiro, G. Trinchieri, and S. Murphy. 1983. Exposure of platelet fibrinogen-binding sites by collagen, arachidonic acid, and ADP: inhibition by a monoclonal antibody to the glycoprotein IIb-IIIa complex. *Blood* 61:140-148.

18.   Farrell, D. H., P. Thiagarajan, D. W. Chung, and E. W. Davie. 1992. Role of fibrinogen alpha and gamma chain sites in platelet aggregation. *Proc. Natl. Acad. Sci. USA* 89:10729-10732.

19.   Nachman, R. L., and L. L. Leung. 1982. Complex formation of platelet membrane glycoproteins IIb and IIIa with fibrinogen. *J. Clin. Invest.* 69:263-269.

20.   Marguerie, G. A., E. F. Plow, and T. S. Edgington. 1979. Human platelets possess an inducible and saturable receptor specific for fibrinogen. *J. Biol. Chem.* 254:5357-5363.

21. Bennett, J. S., and G. Vilaire. 1979. Exposure of platelet fibrinogen receptors by ADP and epinephrine. *J. Clin. Invest.* 64:1393-1401.

22. Leong, L., P. E. Hughes, M. A. Schwartz, M. H. Ginsberg, and S. J. Shattil. 1995. Integrin signaling: roles for the cytoplasmic tails of alpha IIb beta 3 in the tyrosine phosphorylation of pp125FAK. *J. Cell. Sci.* 108:3817-3825.

23. Loh, E., W. Qi, G. Vilaire, and J. S. Bennett. 1996. Effect of cytoplasmic domain mutations on the agonist-stimulated ligand binding activity of the platelet integrin aIIbb3. *J. Biol. Chem.* 271:30233-30241.

24. Loftus, J. C., J. Choate, and R. M. Albrecht. 1984. Platelet activation and cytoskeletal reorganization: high voltage electron microscopic examination of intact and Triton-extracted whole mounts. *J. Cell Biol.* 98:2019-2025.

25. Albrecht, R. M., J. A. Oliver, and J. C. Loftus. 1985. Observation of colloidal gold labelled platelet surface receptors and the underlying cytoskeleton using high voltage electron microscopy and scanning electron microscopy. In *The Science of Biological Specimen Preparation*. R. P. B. M. Mueller, A. Boyde, and J. J. Wolosewick, Eds., ed. AMF O'Hare, Chicago. 185-193.

26. Loftus, J. C., and R. M. Albrecht. 1984. Redistribution of the fibrinogen receptor of human platelets after surface activation. *J. Cell Biol.* 99:822-829.

27. Simmons, S. R., P. A. Sims, and R. M. Albrecht. 1997. Alpha IIb beta 3 redistribution triggered by receptor cross-linking. *Arterioscler. Thromb. Vasc. Biol.* 17:3311-3320.

28. Olorundare, O. E., S. R. Simmons, and R. M. Albrecht. 1992. Cytochalasin D and E: effects on fibrinogen receptor movement and cytoskeletal reorganization in fully spread, surface-activated platelets: a correlative light and electron microscopic investigation. *Blood* 79:99-109.

29. Oliver, J. A., and R. M. Albrecht. 1987. Colloidal gold labelling of fibrinogen receptors in epinephrine- and ADP-activated platelet suspensions. *Scanning Microsc.* 1:745-756.

30. Belitser, N., M. Anischuk, Y. Veklich, T. Pozdnjakova, and O. Gorkun. 1993. Fibrinogen internalization by ADP-stimulated blood platelets. Ultrastructural studies with fibrinogen-colloidal gold probes. *Thromb. Res.* 69:413-424.

31. Escolar, G., E. Leistikow, and J. G. White. 1989. The fate of the open canicular system in surface and suspension-activated platelets. *Blood* 74:1983-1988.

32. White, J. G., and G. Escolar. 1991. The blood platelet open canalicular system: a two-way street. *Eur. J. Cell Biol.* 56:233-242.

33.   Wencel-Drake, J. D., C. Boudignon-Proudhon, M. G. Dieter, A. B. Criss, and L. Parise. 1996. Internalization of bound fibrinogen modulates platelet aggregation. *Blood* 87:602-612.

34.   Zhu, Y., P. Carmeliet, and W. P. Fay. 1999. Plasminogen activator inhibitor-1 is a major determinant of arterial thrombolysis resistance. *Circulation* 99:3050-3055.

35.   Konstantinides, S., K. Schäfer, T. Thinnes, and D. J. Loskutoff. 2001. Plasminogen activator inhibitor-1 and its cofactor vitronectin stabilize arterial thrombi after vascular injury in mice. *Circulation* 103:576-583.

36.   Kurz, K. D., B. W. Main, and G. E. Sandusky. 1990. Rat model of arterial thrombosis induced by ferric chloride. *Thromb. Res.* 60:269-280.

37.   Farrehi, P. M., C. K. Ozaki, P. Carmeliet, and W. P. Fay. 1998. Regulation of arterial thrombolysis by plasminogen activator inhibitor-1 in mice. *Circulation* 97:1002-1008.

38.   Wang, X., and L. Xu. 2005. An optimized murine model of ferric chloride-induced arterial thrombosis for thrombosis research. *Thromb. Res.* 115:95-100.

39.   Doolittle, R. F. 1983. The structure and evolution of vertebrate fibrinogen. *Ann. N. Y. Acad. Sci.* 408:13-27.

40.   Doolittle, R. F., K. McNamara, and K. Lin. 2012. Correlating structure and function during the evolution of fibrinogen-related domains. *Protein Sci.* 21:1808-1823.

41.   Doolittle, R. F., K. W. Watt, B. A. Cottrell, D. D. Strong, and M. Riley. 1979. The amino acid sequence of the alpha-chain of human fibrinogen. *Nature* 280:464-468.

42.   Sánchez-Cortés, J., and M. Mrksich. 2009. The platelet integrin αIIbβ3 binds to the RGD and AGD motifs in fibrinogen. *Chem. Biol.* 16:990-1000.

43.   Salsmann, A., E. Schaffner-Reckinger, F. Kabile, S. Plançon, and N. Kieffer. 2005. A new functional role of the fibrinogen RGD motif as the molecular switch that selectively triggers integrin αIIbβ3-dependent RhoA activation during cell spreading. *J. Biol. Chem.* 280:33610-33619.

44.   Harfenist, E. J., M. A. Packham, and J. F. Mustard. 1988. Effects of the cell adhesion peptide, Arg-Gly-Asp-Ser, on responses of washed platelets from humans, rabbits, and rats. *Blood* 71:132-136.

45.   Basani, R. B., G. D'Andrea, N. Mitra, G. Vilaire, M. Richberg, M. A. Kowalska, J. S. Bennett, and M. Poncz. 2001. RGD-containing peptides inhibit fibrinogen binding to platelet αIIbβ3 by inducing an allosteric change in the amino-terminal portion of αIIb. *J. Biol. Chem.* 276:13975-13981.

46.   Basani, R. B., H. Zhu, M. A. Thornton, C. S. Soto, W. F. DeGrado, M. A. Kowalska, J. S. Bennett, and M. Poncz. 2009. Species differences in small molecule binding to αIIbβ3 are the result of sequence differences in 2 loops of the αIIb β propeller. *Blood* 113:902-910.

47.   Gartner, T. K., D. L. Amrani, J. M. Derrick, N. E. Kirschbaum, G. R. Matsueda, and D. B. Taylor. 1993. Characterization of adhesion of "resting" and stimulated platelets to fibrinogen and its fragments. *Thromb. Res.* 71:47-60.

48.   Hawiger, J., S. Timmons, M. Kloczewiak, D. D. Strong, and R. F. Doolittle. 1982. Gamma and alpha chains of human fibrinogen possess sites reactive with human platelet receptors. *Proc. Natl. Acad. Sci. USA* 79:2068-2071.

49.   Rixon, M. W., D. W. Chung, and E. W. Davie. 1985. Nucleotide sequence of the gene for the gamma chain of human fibrinogen. *Biochemistry* 24:2077-2086.

50.   Mural, R. J., M. D. Adams, E. W. Myers, H. O. Smith, G. L. G. Miklos, R. Wides, A. Halpern, P. W. Li, G. G. Sutton, J. Nadeau, S. L. Salzberg, R. A. Holt, C. D. Kodira, F. Lu, L. Chen, Z. Deng, C. C. Evangelista, W. Gan, T. J. Heiman, J. Li, Z. Li, G. V. Merkulov, N. V. Milshina, A. K. Naik, R. Qi, B. C. Shue, A. Wang, J. Wang, X. Wang, X. Yan, J. Ye, S. Yooseph, Q. Zhao, L. Zheng, S. C. Zhu, K. Biddick, R. Bolanos, A. L. Delcher, I. M. Dew, D. Fasulo, M. J. Flanigan, D. H. Huson, S. A. Kravitz, J. R. Miller, C. M. Mobarry, K. Reinert, K. A. Remington, Q. Zhang, X. H. Zheng, D. R. Nusskern, Z. Lai, Y. Lei, W. Zhong, A. Yao, P. Guan, R. R. Ji, Z. Gu, Z.-Y. Wang, F. Zhong, C. Xiao, C. C. Chiang, M. Yandell, J. R. Wortman, P. G. Amanatides, S. L. Hladun, E. C. Pratts, J. E. Johnson, K. L. Dodson, K. J. Woodford, C. A. Evans, B. Gropman, D. B. Rusch, E. Venter, M. Wang, T. J. Smith, J. T. Houck, D. E. Tompkins, C. Haynes, D. Jacob, S. H. Chin, D. R. Allen, C. E. Dahlke, R. Sanders, K. Li, X. Liu, A. A. Levitsky, W. H. Majoros, Q. Chen, A. C. Xia, J. R. Lopez, M. T. Donnelly, M. H. Newman, A. Glodek, C. L. Kraft, M. Nodell, F. Ali, H. J. An, D. Baldwin-Pitts, K. Y. Beeson, S. Cai, M. Carnes, A. Carver, P. M. Caulk, A. Center, Y. H. Chen, M.-L. Cheng, M. D. Coyne, M. Crowder, S. Danaher, L. B. Davenport, R. Desilets, S. M. Dietz, L. Doup, P. Dullaghan, S. Ferriera, C. R. Fosler, H. C. Gire, A. Gluecksmann, J. D. Gocayne, J. Gray, B. Hart, J. Haynes, J. Hoover, T. Howland, C. Ibegwam, M. Jalali, D. Johns, L. Kline, D. S. Ma, S. MacCawley, A. Magoon, F. Mann, D. May, T. C. McIntosh, S. Mehta, L. Moy, M. C. Moy, B. J. Murphy, S. D. Murphy, K. A. Nelson, Z. Nuri, K. A. Parker, A. C. Prudhomme, V. N. Puri, H. Qureshi, J. C. Raley, M. S. Reardon, M. A. Regier, Y.-H. C. Rogers, D. L. Romblad, J. Schutz, J. L. Scott, R. Scott, C. D. Sitter, M. Smallwood, A. C. Sprague, E. Stewart, R. V. Strong, E. Suh, K. Sylvester, R. Thomas, N. N. Tint,

C. Tsonis, G. Wang, G. Wang, M. S. Williams, S. M. Williams, S. M. Windsor, K. Wolfe, M. M. Wu, J. Zaveri, K. Chaturvedi, A. E. Gabrielian, Z. Ke, J. Sun, G. Subramanian, and J. C. Venter. 2002. A comparison of whole-genome shotgun-derived mouse chromosome 16 and the human genome. *Science* 296:1661-1671.

51.   Tokutomi, K., T. Tagawa, M. Korenaga, M. Chiba, T. Asai, N. Watanabe, S. Takeoka, M. Handa, Y. Ikeda, and N. Oku. 2012. Ability of fibrinogen γ-derived dodecapeptides with different sequences to bind to rat platelets. *Int. J. Pharm.* 438:296-301.

52.   Jantzen, H. M., D. S. Milstone, L. Gousset, P. B. Conley, and R. M. Mortensen. 2001. Impaired activation of murine platelets lacking G alpha(i2). *J. Clin. Invest.* 108:477-483.

53.   Hechler, B., Y. Zhang, A. Eckly, J. P. Cazenave, C. Gachet, and K. Ravid. 2003. Lineage-specific overexpression of the P2Y1 receptor induces platelet hyper-reactivity in transgenic mice. *J. Thromb. Haemost.* 1:155-163.

54.   Léon, C., B. Hechler, M. Freund, A. Eckly, C. Vial, P. Ohlmann, A. Dierich, M. LeMeur, J. P. Cazenave, and C. Gachet. 1999. Defective platelet aggregation and increased resistance to thrombosis in purinergic P2Y(1) receptor-null mice. *J. Clin. Invest.* 104:1731-1737.

55.   Leng, X. H., S. Y. Hong, S. Larrucea, W. Zhang, T. T. Li, J. A. López, and P. F. Bray. 2004. Platelets of female mice are intrinsically more sensitive to agonists than are platelets of males. *Arterioscler. Thromb. Vasc. Biol.* 24:376-381.

56.   Kahn, M. L., M. Nakanishi-Matsui, M. J. Shapiro, H. Ishihara, and S. R. Coughlin. 1999. Protease-activated receptors 1 and 4 mediate activation of human platelets by thrombin. *J. Clin. Invest.* 103:879-887.

57.   Kahn, M. L., Y. W. Zheng, W. Huang, V. Bigornia, D. Zeng, S. Moff, R. V. Farese, Jr., C. Tam, and S. R. Coughlin. 1998. A dual thrombin receptor system for platelet activation. *Nature* 394:690-694.

58.   Hollenberg, M. D., M. Saifeddine, S. Sandhu, S. Houle, and N. Vergnolle. 2004. Proteinase-activated receptor-4: Evaluation of tethered ligand-derived peptides as probes for receptor function and as inflammatory agonists in vivo. *Br. J. Pharmacol.* 143:443-454.

59.   Faruqi, T. R., E. J. Weiss, M. J. Shapiro, W. Huang, and S. R. Coughlin. 2000. Structure-function analysis of protease-activated receptor 4 tethered ligand peptides: Determinants of specificity and utility in assays of receptor function. *J. Biol. Chem.* 275:19728-19734.

60.	Lapetina, E. G., K. A. Chandrabose, and P. Cuatrecasas. 1978. Ionophore A-23187- and thrombin-induced platelet aggregation: Independence from cycloxygenase products. *Proc. Natl. Acad. Sci. USA* 75:818-822.

61.	Ball, G., G. G. Brereton, M. Fulwood, D. M. Ireland, and P. Yates. 1970. Effect of prostaglandin E1 alone and in combination with theophylline or aspirin on collagen-induced platelet aggregation and on platelet nucleotides including adenosine 3':5'-cyclic monophosphate. *Biochem. J.* 120:709-718.

62.	Delgado, A. V., S. L. Alexander, A. T. McManus, and A. E. Pusateri. 2003. Antibodies against human cell receptors, CD36, CD41a, and CD62P crossreact with porcine platelets. *Cytometry B Clin. Cytom.* 56:62-67.

63.	Ellis, E. A. 2006. Solutions to the problem of substitution of ERL 4221 for vinyl cyclohexene dioxide in spurr low viscoity embedding formulations. *Microsc. Today* 14:32-33.

64.	Holdorf, M. M., H. A. Owen, S. R. Lieber, L. Yuan, N. Adams, C. Dabney-Smith, and C. A. Makaroff. 2012. Arabidopsis ETHE1 encodes a sulfur dioxygenase that is essential for embryo and endosperm development. *Plant Physiol.* 160:226-236.

65.	ThermoScientific. 2013. Product Instructions: #21335. http://piercenet.com/instructions/2161855.pdf

66.	Ardlie, N. G., M. A. Packham, and J. F. Mustard. 1970. Adenosine diphosphate-induced platelet aggregation in suspensions of washed rabbit platelets. *Br. J. Haematol.* 19:7-17.

67.	Harfenist, E. J., J. L. Wrana, M. A. Packham, and J. F. Mustard. 1985. Measurement of fibrinogen concentrations in suspensions of washed rabbit and human platelets by radioimmunoassays. *Thromb. Haemost.* 53:110-115.

68.	Mustard, J. F., D. W. Perry, N. G. Ardlie, and M. A. Packham. 1972. Preparation of suspensions of washed platelets from humans. *Br. J. Haematol.* 22:193-204.

69.	Bednar, B., C. Condra, R. J. Gould, and T. M. Connolly. 1995. Platelet aggregation monitored in a 96 well microplate reader is useful for evaluation of platelet agonists and antagonists. *Thromb. Res.* 77:453-463.

70.	Oliver, J. A. 1992. The relationship of platelet morphology, activation, and secretion. University of Wisconsin, Madison.

71.	Deng, Z. J., M. Liang, I. Toth, M. J. Monteiro, and R. F. Minchin. 2012. Molecular interaction of poly(acrylic acid) gold nanoparticles with human fibrinogen. *ACS Nano* 6:8962-8969.

72.   Grouse, L. H., and J. G. White. 1989. Gold-labeled bovine fibrinogen for study of human platelets. *Thromb. Haemost.* 62:1112-1115.

73.   Kaplan, K. L., M. J. Broekman, A. Chernoff, G. R. Lesznik, and M. Drillings. 1979. Platelet alpha-granule proteins: studies on release and subcellular localization. *Blood* 53:604-618.

74.   Handagama, P., R. M. Scarborough, M. A. Shuman, and D. F. Bainton. 1993. Endocytosis of fibrinogen into megakaryocyte and platelet alpha-granules is mediated by alpha IIb beta 3 (glycoprotein IIb-IIIa). *Blood* 82:135-138.

75.   White, J. G. 1968. Fine structural alterations induced in platelets by adenosine diphosphate. *Blood* 31:604-622.

76.   Allen, R. D., L. R. Zacharski, S. T. Widirstky, R. Rosenstein, L. M. Zaitlin, and D. R. Burgess. 1979. Transformation and motility of human platelets: Details of the shape change and release reaction observed by optical and electron microscopy. *J. Cell Biol.* 83:126-142.

Chapter 3: **Design and development of fibrinogen-conjugated gold-coated**

magnetite nanoparticles

Abstract:

Magnetite nanoparticles are of interest in biological systems for a variety of applications. We are interested in using magnetite nanoparticles to cause localized cellular hyperthermia upon exposure to an external oscillating magnetic field. To successfully target magnetite nanoparticles to cells it is necessary to functionalize them with a targeting protein and stabilize them at physiological pH and salt concentrations. One method of accomplishing these goals is to coat the magnetite with gold and then conjugate protein to the gold surface. Gold-coated magnetite is most often described as a core-shell structure, despite significant issues with the ability of gold to wet the surface of magnetite. Here we examined the structure and composition of lab-produced gold-coated magnetite, and found structures, different than core-shell structures, with exposed magnetite surfaces. We examined the ability of these nanoparticles to be conjugated to fibrinogen for both nanoparticle stability and specific targeting of human platelets. Gold-coated magnetite can be functionalized with fibrinogen, which stabilizes the nanoparticles at physiologic pH and salt concentration. Fibrinogen-conjugated gold-coated nanoparticles can be targeted toward activated platelets in a manner similar to the already established fibrinogen-conjugated colloidal gold system. The localization of fibrinogen-conjugated gold-coated magnetite on platelets was directly compared to the well established fibrinogen-conjugated colloidal gold labeling pattern and found to be very similar. Fibrinogen-conjugated gold-coated magnetite labeling was examined in an *in vitro* made artificial blood clot. Labeling was detectable, albeit at greatly reduced

values. Labeling was greatly reduced in conditions that resemble a blood clot but hyperthermia may still be possible.

Introduction:

Successful nanoparticle-based systems require a method to target cells and tissue and to cause a desired effect at the target site. Our proposed system uses fibrinogen as the targeting molecule to specifically target activated platelets within a blood clot. For ischemic stroke applications, we are most interested in magnetic field-induced hyperthermia (1-6) to disrupt occlusive thrombi. Combining the targeting and heating requires magnetite nanoparticles to be conjugated to proteins, while retaining the abilities of the protein to target specific cells. In this report, we focus on synthesis of magnetite nanoparticles that are coated with gold to allow conjugation of fibrinogen to the nanoparticle surface, thereby promoting the use of the nanoparticles in our specific biological application of targeting platelets.

Magnetic iron oxide nanoparticles have been studied for a variety of applications in biological systems including magnetic-assisted cell separation (7-9), MRI contrast (7, 10), drug delivery (2), and magnetic field-induced hyperthermia (1-6). The scientific principle underlying the design is that applying an external magnetic field to the cell-bound nanoparticles causes a significant temperature elevation and results in highly localized damage to the cell membrane immediately surrounding the nanoparticles (11, 12). The simplest application of the technology is direct injection of ferrofluid into a

tumor (4, 13) or nonspecfic cell uptake (phagocytosis) of nanoparticles (1, 6, 14), followed by heating. This type of bulk heating in the absence of specific targeting can be effective in destruction of a tumor site, but has serious limitations in that hyperthermia is likely to cause nonspecific damage to surrounding tissues (5, 14). Therefore, targeting the nanoparticles to specific cells or tissues is desirable. Tumor cell destruction by magnetic field-induced hyperthermia using magnetic nanoparticles conjugated to tumor-specific targeting proteins has been previously reported (5, 11, 12). For targeted disruption of arterial thrombi, nanoparticle localization through molecules with specificity for activated, as opposed to resting, platelets is of most interest.

Procedures for the synthesis of magnetic iron oxide nanoparticles can, in general, be placed in one of three categories: thermal decomposition (10, 15, 16), aqueous alkaline precipitation (17-19), or microemulsion synthesis (20-23). Thermal decomposition synthesis uses organometallic iron that is dissociated by heat and recombined into magnetite in an organic solvent. The result is nanoparticles of uniform size and shape (10, 16); however, these particles are difficult to use in biological applications due to their inherent hydrophobicity and the presence of potentially toxic organic residues (24). Aqueous alkaline precipitation uses dissolved iron salts that are oxidized by a strong base, which causes the iron oxide to precipitate from solution into nanoparticles. These nanoparticles are hydrophilic and can be readily suspended in solution by use of surfactant to impact a negative charge on the nanoparticle surface. A major drawback to aqueous methods is that they give imprecise control of the size of the resultant nanoparticles. Microemulsion synthesis attempts to bridge the gap between organic and

aqueous synthesis by using inverse micelles suspended in an organic medium. Iron salts are precipitated within the inverse micelle, which creates a natural size barrier and controls size of the nanoparticle. These particles have relatively homogenous size distributions (23, 25) like many organically-derived nanoparticles, but were created in an aqueous environment. They may exhibit either hydrophilic or hydrophobic behavior and organic residue contamination can still limit their use in biological systems. The best choice in type of synthesis method used depends directly on the ultimate application of the nanoparticles.

Nanoparticles that exhibit good magnetic behavior, are hydrophilic, non-toxic, and can be functionalized with a biologically-relevant targeting molecule are most desirable for platelet-targeted hyperthermia. Magnetite synthesized by an aqueous method has very strong magnetic behavior (26) and can be made between nm to μm diameter size ranges. Because these particles are synthesized in water, they have surfaces that are most compatible with an aqueous environment, and the reaction by-products are relatively non-toxic. However, addition of a surfactant such as tetramethylammonium hydroxide (TMAOH) is required for these nanoparticles to remain a colloid (2, 27). Even surfactant-stabilized iron oxide nanoparticles are unstable at physiologic salt and pH values (28, 29), and thus have limited biological utility in the absence of further surface modification. Functionalization of the surfaces of nanoparticles with simple organic molecules or proteins (19, 30, 31) or metal coatings (22, 27, 28, 32) can protect the iron oxide from agglomerating under physiologic conditions, and provides a means to keep the nanoparticles stable within a biological system.

Magnetic iron oxide nanoparticles with a gold coating have been developed to address some of the disadvantages associated with iron oxide colloids for biological applications. The gold coating improves stability of the iron oxide at physiologic conditions (28) and provides a surface for functionalization with proteins (32-34) or nucleic acids (35, 36), or for other well characterized gold surface modifications (9, 37, 38). These gold-magnetite nanoparticles have often been described as having a core-shell morphology, with a magnetite or maghemite core surrounded by a thin, uniform gold shell (27, 32, 37, 39). The surface modifications do not impair the magnetic properties of the nanoparticles (9, 27, 40), making them appropriate for biological applications that depend on magnetic susceptability.

There are conflicting accounts describing the structure of the nominal magnetite-gold core-shell nanoparticles. Many successful syntheses of magnetite core-gold shell nanoparticles by both aqueous and organic methods resulting in an iron oxide core and a gold shell have been reported (27, 32, 34, 37, 39, 41, 42). However, a true core-shell morphology is an unexpected outcome because metals typically do not wet the surfaces of oxides well (43) due to a mismatch in surface energies. Instead, gold is expected to grow in a Volmer-Weber pattern (44), creating three-dimensional islands on the magnetite surface and leaving portions of the magnetite uncoated. Volmer-Weber growth has been observed when gold is grown on the (100) and (111) surfaces of magnetite in high vacuum (45, 46). However, growth conditions in an aqueous environment may be different. While many of these core-shell studies have demonstrated by x-ray or electron

diffraction that their products contain both a magnetic iron oxide and gold, evidence of true core-shell structure has been largely indirect or lacking.

We hypothesize that coating magnetite nanoparticles with gold facilitates subsequent functionalization with proteins by increasing repulsive forces between nanoparticles to prevent the nanoparticles from agglomerating due to the magnetic and electrostatic forces of attraction that occur at physiologic pH and salt concentration. Gold nanoparticle have been used as markers in biological systems for over 30 years and provide a good model on which to base the functionalization of magnetic nanoparticles for targeting to specific cell types, such as through their conjugation with fibrinogen for targeting activated platelets in the current study. Most proteins can be conjugated to gold surfaces by non-ionic adsorption without loss of function (47, 48). Coating magnetite with gold is expected to provide a surface for non-ionic protein adsorption very similar to pure gold nanoparticles. We and others (49-54) have routinely used fibrinogen-conjugated gold nanoparticle in our light and electron microscopy studies of platelet physiology. Applying this technology to the specific targeting of activated platelets in thrombi with fibrinogen conjugates of gold-coated magnetite, and disruption of the targeted thrombus by hyperthermia, is a logical extension of the foundation established by previous work.

Here we describe the synthesis and characterization of gold-coated magnetite nanoparticles produced using an aqueous alkaline coprecipitation method for synthesis of magnetite nanoparticles and hydrazine reduction for coating the nanoparticles with gold. The composition and morphology of the resultant nanoparticles were characterized. The

structure was found to significantly differ from that of true core-shell nanoparticles. All morphologies of gold-coated magnetite nanoparticles produced were assessed for their ability to conjugate with protein by non-ionic adsorption. Lastly, the ability of fibrinogen-conjugated gold-coated magnetite to target activated platelets was evaluated and directly compared to targeting using fibrinogen-conjugated colloidal gold as described previously (Chapter 2).

Materials and Methods:

Magnetite synthesis:

Magnetite nanoparticles were synthesized by an aqueous alkaline coprecipitation method (17). Under argon, 5 mL of a solution of 0.64 M anhydrous $FeCl_3$ and 0.32 M anhydrous $FeCl_2$ (both salts from Sigma-Aldrich, St. Louis, MO) in 0.4 M HCl was slowly added to 50 mL of 1.5 M NaOH in 32-38°C degassed, double deionized H_2O (ddH_2O). The nanoparticles were allowed to settle, then washed three times by centrifugation at 3,000 g for 1 minute and resuspended in degassed ddH_2O. A final wash in 0.1 M tetramethylammonium hydroxide (TMAOH, Alfa Aesar, Ward Hill, MA) was performed in the same manner. Magnetite nanoparticles were size fractionated by centrifugation at 6,000 g for 5 minutes in 0.1 M TMAOH. The nanoparticles in the supernatant were characterized by TEM and were used in gold coating procedures. The desiccated weight and average diameter of isolated, individual nanoparticles, along with a Fe_3O_4 density of 5.15 g/cm^3, were used to calculate magnetite nanoparticle concentrations.

Gold growth on magnetite:

Magnetite nanoparticles were coated with gold in a manner similar to that of previous reports (27). Magnetite nanoparticles were aged at least 3 days at 4°C in 0.1 M TMAOH under an argon atmosphere, then diluted 100-fold in 0.00275% hydrazine hydrate (Sigma-Aldrich). Gold growth on the surface of magnetite nanoparticles was initiated by slow addition of 120 µL 4% aqueous $HAuCl_4 \cdot 3H_2O$ (Sigma-Aldrich) per 100 mL of dilute magnetite nanoparticles with stirring, resulting in a final concentration of 0.12 mM Au^{3+}. Growth of gold on the magnetite was assessed by UV-visible light spectroscopy and visually by the color of the resultant colloid. Blue sols were discarded; red or purple sols were stored under argon at room temperature until further testing. To determine the concentration of isolated gold-coated magnetite nanoparticles, the sol was mixed with a known concentration of 90 nm latex bead standard (Ted Pella, Redding, CA) and aerosolized onto carbon-coated TEM grids (Electron Microscopy Sciences, Hatfield, PA). The number of latex beads and Au-coated Fe_3O_4 nanoparticles in discrete dried droplets was determined by direct counting. From these values, the droplet volume and concentration of isolated gold-coated magnetite nanoparticles were calculated.

Electron microscopy of magnetite and gold-coated magnetite nanoparticles:
Both gold-coated and uncoated magnetite nanoparticle sols were air-dried from the solution in which they were synthesized onto TEM grids coated with holey or ultra-thin carbon films (Electron Microscopy Sciences) for TEM imaging and selected area diffraction. Nanoparticles were imaged using a Hitachi H-600 TEM (Dallas, TX) at 75 kV for amplitude contrast brightfield imaging and selected area diffraction. Selected area

electron diffraction and phase contrast high resolution TEM imaging were performed using a Hitachi H9000-NAR (Dallas, TX) operating at 300 kV, by Eric Mattson under the direction of Marija Gajdardziska-Josifovska at the University of Wisconsin – Milwaukee Department of Physics. Histograms displaying nanoparticle diameter were generated by measuring the longest axis of 500 isolated, individual nanoparticles using ImageJ software (National Institute of Health, http://rsbweb.nih.gov/ij/). Lattice spacing and angles were measured by fast Fourier transformation in Digital Micrograph (Gatan, Pleasanton, CA).

Conjugation of proteins to gold-coated magnetite

Proteins were conjugated to gold-coated magnetite through a modified non-ionic adsorption protocol (49). The pH of gold-coated magnetite was adjusted by addition of 1 M HEPES at the indicated pH to a final concentration of 10 mM. Conjugation was performed at pH 6.8 for human fibrinogen (plasminogen-, von Willebrand factor-, and fibronectin-depleted, Enzyme Research Laboratories, South Bend, IN), 7.0 for goat anti-mouse immunoglobulin G (IgG, γ chain specific, Southern Biotech, Birmingham, AL), and 5.1 for bovine serum albumin (BSA, heat shock treated, DNase-, RNase-, and protease-free, Fisher Scientific, Pittsburgh, PA). Gold-coated nanoparticles were immediately incubated for 5 minutes with protein at final concentrations of 16 μg/mL fibrinogen, 20 μg/mL IgG, or 40 μg/mL BSA. For platelet labeling experiments, the nanoparticles were further stabilized with 0.004% polyethylene glycol (average MW 20,000, Sigma-Aldrich). Conjugated nanoparticles were separated from free protein by

centrifugation at 16,000 x g for 5 minutes, and resuspended in either Tyrode's buffer or ddH$_2$O. Colloidal gold conjugates were prepared as described previously (Chapter 2).

The stability of nanoparticle conjugates was tested by addition of 10 μL saturated CaCl$_2$ per 1 mL nanoparticle conjugate resuspended in ddH$_2$O. Fully stabilized conjugates did not exhibit an obvious change in the nanoparticle absorbance spectrum as assessed either visually or using a Beckman Coulter DU 800 UV-Vis spectrophotometer. The magnetic character of the gold-coated magnetite was similarly observed by assaying UV-Visible absorbance of nanoparticles remaining in solution after the nanoparticles were allowed to interact with a neodymium static magnet for 12 hours.

Fibrinogen-conjugated nanoparticle labeling of surface-activated platelets:
Gel-filtered surface-activated human platelets were prepared as described previously (Chapter 2). Adherent platelets were labeled with fibrinogen conjugated to Au or Au-coated magnetite nanoparticles in the presence of 2 mM Ca^{2+} for 10 minutes at room temperature. Samples were then washed three times in Ca^{2+}-supplemented Tyrode's buffer to remove unbound nanoparticles. Grids were fixed in 1% glutaraldehyde for 30 minutes. Samples were not stained with any heavy metals except for SEM samples comparing fibrinogen-conjugated gold to gold-coated magnetite on platelet surfaces, which were postfixed in 0.05% OsO$_4$ for 15 minutes. The samples were dehydrated using a graded ethanol series and dried by the critical point procedure using a Balzers CPD020 critical point dryer (Schalksmühle, Germany). Samples were stabilized with a carbon coating applied in an EMItech 575 sputtercoater (Ashford, Kent, United

Kingdom) using a carbon evaporation head, except for SEM samples comparing

fibrinogen-conjugated gold to gold-coated magnetite labeling which were sputtercoated

with 2 nm Ir.

Electron microscopy of gold-coated magnetite nanoparticle morphology before and after

protein conjugation, and on platelet surfaces:

Fibrinogen-conjugated gold and gold-coated magnetite nanoparticles were prepared for

electron microscopy by two separate methods. First, nanoparticles were air-dried onto

carbon-coated TEM grids and then directly imaged. Nanoparticles were also adhered to

carbon-coated TEM grids coated with poly-L-lysine (Sigma-Aldrich) according to the

manufacturer's instructions. Non-adherent nanoparticles were removed with three, 5

minute washes accomplished by incubating the grids over successive 20 μL drops of

ddH$_2$O. The grids were stained with 1% uranyl acetate, dehydrated in a graded ethanol

series, and dried by the critical point procedure using a Balzers CPD020. Both

fibrinogen-conjugated nanoparticles and surface-activated platelets labeled with

functionalized nanoparticles were imaged using a Hitachi H-600 TEM at 75 kV for

brightfield studies. Secondary electron (SE) imaging SEM studies of labeled platelets

were carried out on a Hitachi S-4800 (Dallas, TX) operating at 1 kV and at 30 kV for SE

imaging of nanoparticles and for all backscattered electron (BSE) imaging, respectively.

Morphological analysis of gold-coated magnetite nanoparticles bound to surface-

activated platelets was performed using montaged high magnification BSE micrographs

or single lower magnification TEM micrographs containing entire platelets. The

nanoparticles on the BSE micrographs were counted around the periphery of the platelet, with the central area of the platelet, as defined by a circle one half the radius of the platelet's shortest axis, excluded in order to accurately assess the morphology of the nanoparticles which are difficult to resolve over the internal areas of platelets. Magnetite portions of nanoparticle aggregates were identified by their lower contrast in both TEM and SEM. The number of isolated and aggregated nanoparticles before and after conjugation, and on the platelet surface was compared by Chi-square analysis.

Platelet aggregation with fibrinogen-conjugated nanoparticles:

Gel-filtered platelets and platelet-rich plasma (PRP) were prepared as described earlier (Chapter 2). Gel-filtered platelets at 200,000 platelets/μL were supplemented with either 200 μg/mL unconjugated or approximately 96 μg/mL conjugated fibrinogen (see below), and 2 mM Ca^{2+}, and stimulated with 67 mM SFLLRN-NH_2 (Bachem Americas, Torrence, CA) to a final volume of 500 μL. Aggregation data was obtained as previously described (Chapter 2). The blanks used for 0% aggregation consisted of Tyrode's buffer with Ca^{2+} and either conjugated or unconjugated fibrinogen to account for nanoparticle absorbance. A sample of PRP was aggregated similarly to show the maximum platelet response obtainable each day.

Preformed platelet aggregates were produced using a Chronolog Dual Aggregometer (Havertown, PA) using 500 μL gel-filtered platelets (Chapter 2). Similarly, platelet-rich plasma was supplemented with 2 mM Ca^{2+} and aggregated using either 67 μM SFLLRN-NH_2 or 2 nM human thrombin (Haematolgoic Technologies, Essex Junction, VT) as the

stimulus. After the platelets aggregated for 5 minutes, the aggregates were labeled with the pooled soft pellet obtained from 6 mL of the fibrinogen and gold-coated magnetite conjugation reaction mixture. Assuming 8 µg/mL protein adsorption to the nanoparticle this represents addition of 48 mg of fibrinogen to 500 µL aggregation reaction or 96 µg/mL fibrinogen conjugate in the presence of the pre-existing 200 µg/mL unconjugated fibrinogen.

For SEM analysis, the gel-filtered platelets were fixed in 1% glutaraldehyde in 0.1 M HEPES for 30 minutes. The samples were collected onto 0.4 µm Nuclepore® membranes (General Electric, Fairfield, CT) and postfixed in 0.05% OsO_4 for 15 minutes. Samples were dehydrated using a graded ethanol series and dried by the critical point procedure in a Balzers CPD20. The filter membranes were mounted onto SEM stubs using carbon tabs (Electron Microscopy Sciences) and sputter coated with 2 nm Ir using an EMITech K575X sputter coater. Samples were imaged using a Hitachi S-4800 SEM at 1 kV for SE imaging and 30 kV for BSE imaging.

For TEM analysis, the gel-filtered platelets were fixed in 1% glutaraldehyde, 1% tannic acid in 0.1 M HEPES, pH 7.3, for 30 minutes. Platelet-rich plasma aggregates were fixed in 2% glutaraldehyde in 0.1 M HEPES, pH 7.3 for 10 minutes. Glutaraldehyde cross-linked plasma proteins were removed by centrifugation at 300 x g for 5 minutes, during which the proteins formed a very soft pellet on top of the pelleted platelet aggregates. Proteins were removed by gently removing the soft protein pellet above the platelets. The samples were fixed a second time in 2% glutaraldehyde, 1% tannic acid in 0.1 M

HEPES at room temperature for 1 hour and then 4° C overnight. Samples were washed

three times in HEPES and embedded into 1% agar (Difco, Detroit, MI) in 0.1 M HEPES

by combining warm agar and 4° C platelet samples in equal volume in small TEM

embedding molds. After the agar became dense at 4° C, samples were postfixed in 0.05%

OsO_4 for 1 hour at room temperature, washed 3 times in ddH_2O, and stained with 1%

uranyl acetate for 30 minutes. The samples were dehydrated in ethanol, transferred to

propylene oxide and then infiltrated with low viscosity Spurr's resin (55) but substituting

the accelerant N,N-dimethylbenzylamine with 2(dimethylamino)ethanol (56) (Electron

Microscopy Sciences). Ultrathin silver or pale gold sections were cut on a RMC MT-

7000 ultramicrotome (Tucson, AZ), and stained with 1% uranyl acetate. Samples were

imaged using a Hitachi H-600 TEM at 75 kV.

Results

Magnetite synthesis and characterization:

Magnetite synthesis was performed by an aqueous co-precipitation method using $FeCl_2$

and $FeCl_3$ at a ratio of 1:2 to promote magnetite $(Fe^{2+})(Fe^{3+})_2O_4$ over maghemite γ-

$(Fe^{3+})_2O_3$ formation (17, 57). Precipitation and growth of the particles occurred almost

immediately on contact with sodium hydroxide solution. We verified which particular

iron oxide was synthesized by several different techniques. Selected area electron

diffraction was performed on groups of nanoparticles. Reflections consistent with

magnetite (Fe_3O_4) and maghemite $(\gamma$-$Fe_2O_3)$ were observed (Figure 19A) (58).

Maghemite has additional low intensity reflections that were not detected in our

nanoparticles. Analysis of our synthesized product by infrared spectroscopy, electron energy loss spectroscopy, and HRTEM with direct comparison to magnetite and maghemite standards, further confirmed that the predominate iron oxide synthesized was magnetite (59).

The temperature of the solution during synthesis was found to strongly influence the size of the resultant nanoparticles. The optimal temperature for 7 nm (average diameter) magnetite nanoparticles was found to be between 32° to 38° C. The synthesized magnetite nanoparticles were analyzed by TEM. When the stock magnetite was air dried onto TEM grids, the nanoparticles were very agglomerated with few isolated particles (Figure 19B). However, diluting the nanoparticles 1:100 in 0.1 M TMAOH before drying prevented this artifact and the dispersion of the nanoparticles increased greatly (Figure 19C). Diluted nanoparticles appeared as isolated particles or in small aggregates. The size distribution of the magnetite nanoparticles were determined to be 7 ± 3 nm with a coefficient of variation of 42% (Figure 19D), indicative of a highly heterogeneous population.

Gold-coated magnetite structure and characterization:

Magnetite nanoparticles were coated with gold by reduction of $HAuCl_4$ with a low concentration of hydrazine as the reducing agent under conditions that do not favor gold nanoparticle nucleation. Successful production of gold-coated magnetite was assessed by color, electron microscopy, and stability following protein conjugation. Gold-coated magnetite of the desired size had a red to magenta color similar to that of colloidal gold;

unsuccessful batches of nanoparticles had a blue, purple, or black appearance. The unsuccessful batches of gold-coated magnetite were often unstable and precipitated quickly. These unstable batches often had large clumps of bare magnetite with no gold coating as observed by TEM (not shown).

Successful coating of the magnetite seed nanoparticles was dependent on the conditions used for the synthesis and storage of the magnetite. Seeds of the appropriate size and concentration were obtained when synthesis was conducted between 32-38° C. Temperatures greater than 38°C appeared to favor smaller, more highly concentrated magnetite nanoparticles. Temperatures lower than 32°C resulted in nanoparticle size and concentration that was difficult to reproduce. Too few magnetite seeds produced nanoparticles with an average diameter greater than 50 nm that were not susceptible to manipulation with a static magnet. Too many seeds resulted in precipitation of the "coated" nanoparticles, often within a day. Further, if the magnetite seeds were aged less than 3 days in 0.1 M TMAOH, the gold coating procedure resulted in larger nanoparticles, similar to that observed in samples with too few seeds.

Our synthesized gold-coated magnetite nanoparticles are a heterogeneous population. Brightfield TEM analysis of the nanoparticles showed several distinct classes of particles. Isolated rounded nanoparticles were the most commonly observed gold-coated magnetite nanoparticle. Minority populations of isolated faceted particles with very sharply defined edges, and aggregated nanoparticles consisting of a group of associated nanoparticles of low and high contrast were also observed (Figures 20A, 20B). The isolated nanoparticles

in three different batches of gold-coated magnetite nanoparticles were found to have average diameters of 16, 19, and 22 nm, with coefficient of variations of 24%, 25%, and 27%, respectively, and a concentration of $3 * 10^{11} \pm 1.3 * 10^{11}$ particles/mL. The size increase following gold coating was large in all cases, going from an average of 7 nm to 16 nm diameter in the example shown in Figure 20C. Selected area electron diffraction was performed on magnetite, colloidal gold, and gold-coated magnetite (Figure 20D). Gold-coated magnetite contains high intensity reflections from gold {111} and {200} and magnetite {220} and {311}. Gold {200} and magnetite {400} overlap, making their reflections difficult to interpret in gold-coated magnetite diffraction.

HRTEM was used to examine localization of the magnetite on and within the gold-coated magnetite nanoparticles. Isolated particles often had magnetite lattice fringes within the nanoparticle but not necessarily in the center of the particle. The lattice images were analyzed using Fourier filtering to determine the relative distribution of gold and magnetite within the nanoparticles. Magnetite fringes occasionally extended outside the gold fringes, demonstrating that some isolated nanoparticles have exposed magnetite surfaces. These isolated gold-coated magnetite nanoparticles usually had relatively thick gold coatings (not shown). A small population of faceted gold-coated magnetite had a structure consisting of a single layer of magnetite {311} extending to the edge of the nanoparticle and two sets of gold {111} fringes, both forming 62° angles with the magnetite {311} fringes, (Figures 21A, 21B, 21C). Aggregated gold-coated magnetite had large areas of uncoated magnetite, with gold growth occurring in Volmer-Weber morphology on some magnetite surfaces (Figures 21D, 21E, 21F).

Protein conjugation to gold-coated magnetite:

Gold-coated magnetite was conjugated to fibrinogen, goat anti-mouse IgG, or BSA by non-ionic protein adsorption. Attempts to conjugate any protein to uncoated magnetite were unsuccessful, as the magnetite quickly agglomerated when the pH was adjusted to near neutral (7.0). Gold-coated magnetite is partially stabilized at physiologic pH by the gold coating but is still unstable in physiologic salt solutions. Addition of saturated $CaCl_2$ to 1% (v/v) caused the particles to agglomerate, which resulted in a change in the visible absorbance spectrum as shown in Figure 22A. Adjusting the pH of the nanoparticles with a small volume of concentrated HEPES buffer, rather than the NaOH or KCO_3 that is commonly used for colloidal gold conjugations, greatly improved the conjugation success rate. After conjugation, addition of $CaCl_2$ did not cause the conjugated nanoparticles to agglomerate, as shown in Figure 22B. Conjugated particles were removed from solution via a static magnet as easily as unconjugated gold-coated magnetite, nearly eliminating the absorbance of visible light by the supernatants (Figure 23A). The particles bound visually to the static magnet poles (Figures 23B, 23C), demonstrating that the magnetic behavior of the nanoparticles is preserved after the protein conjugation procedure.

Fibrinogen-conjugated, gold-coated nanoparticles were observed by electron microscopy. Nanoparticles were air-dried on carbon-coated TEM grids, or incubated on poly-L-lysine carbon-coated grids followed by drying by the critical point procedure. Conjugated gold-coated magnetite nanoparticles air-dried onto TEM grids had a uniform distribution but lacked a characteristic protein halo indicative of protein coating (Figure 24A). Both

isolated and aggregated particles appeared in the conjugated population but a loss of

aggregated particles from 12.5% aggregated particles in the stock to 6.4% in the

conjugated population occurred. Conjugated nanoparticles dried by the critical point

procedure demonstrated the presence of protein coating as observed by TEM and SEM.

The different morphologies of gold-coated magnetite could be clearly observed in SEM

using BSE imaging. Areas containing mostly gold had high contrast, appearing bright,

while areas that were predominately magnetite had lower contrast. Protein was observed

to completely encompass nanoparticles, even at exposed magnetite edges (Figure 24B).

Both gold and gold-coated magnetite fibrinogen conjugates clumped extensively when

they were adhered to poly-L-lysine coated grids. Although clumping obscures the

distinction between what were isolated and aggregated nanoparticles prior to sample

preparation, protein can be observed to coat all available surfaces (Figure 25).

Unconjugated gold-coated magnetite also appeared clumped, while unconjugated gold

nanoparticles remained isolated. This level of clumping was not observed in any samples

air-dried directly onto carbon-coated grids.

Platelet targeting with fibrinogen-conjugated gold-coated magnetite:

The morphologies of fibrinogen-conjugated, gold-coated magnetite nanoparticles bound

to surface-activated platelets were assessed by SEM and TEM. Samples were prepared

without use of any heavy metal fixation, staining, or heavy metal sputtering that could

mask the relatively low contrast of magnetite and impede its detection. High

magnification BSE micrographs of three platelets were taken and montaged to assemble

images of entire platelets as illustrated in Figures 26A, 26B, and 26C. The numbers of

isolated and aggregated gold-coated magnetite nanoparticles was quantified on the periphery of platelets. Nanoparticles near the granulomere and in the open canalicular system (OCS) were excluded from SEM analysis to prevent ambiguous analysis of internalized nanoparticles. Similar analysis of three labeled platelets was done using TEM micrographs of surface-activated platelets, shown in Figure 26D. TEM analysis allowed for more of the platelet area to be quantified but required small and very thinly spread platelets. By both SEM and TEM, magnetite was detected as nanoparticles with weak contrast whereas gold generated a strong signal (bright for BSE imaging, dark in brightfield TEM). The percentage of aggregated gold-coated magnetite nanoparticles on platelets determined by SEM BSE imaging was 2.7% and by TEM imaging was 3.0%. The two quantification strategies produced data that was not significantly different. The proportion of aggregates in the nanoparticle population decreased with successive steps, the stock gold-coated magnetite nanoparticle contained 12.5% aggregated nanoparticles, after conjugation the aggregated nanoparticle proportion was reduced to 6.4%, targeted aggregated nanoparticles on the platelet surface were further reduced to 2.7% (SEM) or 3.0% (TEM). Chi-square analysis of the proportion of aggregated nanoparticles indicated the loss in each step was significant ($p < 0.001$). The stock sol contained twice as many aggregates as the protein conjugates. Further, half as many aggregates were found on the platelet surface as in the fibrinogen conjugates demonstrating a significant drop in aggregated fibrinogen-conjugated, gold-coated magnetite on the platelet surface.

Biological activity of nanoparticle conjugates:

Surface-activated platelets were labeled with gold and gold-coated magnetite conjugated

to fibrinogen in order to compare labeling between the types of nanoparticles. TEM

analysis (Figure 27) showed similar labeling patterns using conjugates of gold and gold-

coated magnetite nanoparticles. Platelet nanoparticle labeling was further characterized

by SEM (Figure 28) using both SE to image the platelet surface and BSE to determine

nanoparticle localization using the strong signal from gold in both types of nanoparticles.

Both types of nanoparticles were found centralized on the platelet membrane and cleared

away from the periphery, ultimately localized around the granulomere. This pattern has

been previously described using fibrinogen conjugated to colloidal gold (50, 60, 61) and

unconjugated fibrinogen (62, 63), indicative that fibrinogen function is preserved in the

gold-coated magnetite conjugates.

The biological activity of fibrinogen-conjugated, gold-coated magnetite nanoparticles

was further tested through their ability to support aggregation of gel-filtered platelets.

Their activity was directly compared to fibrinogen-conjugated gold nanoparticles as well

as to unconjugated fibrinogen. Platelet aggregation reactions were supplemented with

calcium and unconjugated fibrinogen, fibrinogen-conjugated to colloidal gold, or

fibrinogen-conjugated gold-coated magnetite and stimulated with a maximal dose of

SFLLRN-NH$_2$. The various treatments produced overlapping aggregometer tracings

(Figure 29) indicating the three fibrinogen sources behave equally well. PRP

supplemented with calcium and stimulated with SFLLRN-NH$_2$ aggregated to the

maximal possible extent, and served as a positive control. After 5 minutes, PRP

aggregated 87%, gel-filtered platelets supplemented with unconjugated fibrinogen, fibrinogen-conjugated to colloidal gold, and fibrinogen-conjugated, gold-coated magnetite aggregated to 80%, 79%, and 78%, respectively.

Aggregates supported by unconjugated fibrinogen, gold conjugates, or gold-coated magnetite conjugates were examined by SEM using both SE and BSE (Figure 30). Samples produced with unconjugated fibrinogen were used as an indicator of normal morphology and as a baseline for BSE brightness levels. The morphology of the aggregates in the three groups was similar, with neighboring platelets strongly interacting with one another. Gold and gold-coated magnetite samples had strong BSE signals emanating from deep within the platelet aggregates, similar to signals observed in aggregates labeled with colloidal gold nanoparticles described previously (Chapter 2).

Gel-filtered platelets aggregated with unconjugated fibrinogen and then labeled with fibrinogen conjugated to gold or gold-coated magnetite were further characterized by TEM, with particular attention to the nanoparticles localized in the aggregate interior (Figure 31). The localization of fibrinogen-conjugated gold nanoparticles in preformed platelet aggregates (Figure 31A) and fibrinogen-conjugated gold-coated magnetite nanoparticles in preformed platelet aggregates (Figure 31B) was similar. Results were also consistent with TEM analysis of platelet aggregates supplemented only with fibrinogen conjugates described earlier (Chapter 2). Nanoparticle labeling was found almost exclusively on the interior of the aggregates, with little labeling appearing on the surface of the platelet aggregates. Nanoparticles were predominately found at

platelet/platelet junctions and in the OCS. Fewer nanoparticles were typically observed in ultrathin sections of platelet aggregates labeled with gold-coated magnetite when compared to ultrathin sections of aggregates labeled with gold nanoparticles. Penetration of the label appeared equal between samples, with nanoparticles present throughout the entire aggregate but intensity was lower in gold-coated magnetite labeled aggregates when compared to colloidal gold labeled aggregates.

Lastly, the ability of fibrinogen-conjugated gold-coated magnetite to penetrate into platelet aggregates under *in vivo*-like conditions was tested. Platelet-rich plasma was aggregated using 67 µM SFLLRN-NH$_2$ (a non-proteolytic peptide) or 2 nM thrombin as agonists. Both agonists activate the same signaling pathway via the PAR1 receptor (64-66), but thrombin also mediates the proteolytic conversion of fibrinogen to fibrin, a much closer approximation of a true blood clot. After the platelet aggregates were formed, they were incubated with fibrinogen conjugated to gold-coated magnetite. Samples were analyzed by TEM to determine localization and relative density of labeling. Aggregates produced using SFLLRN-NH$_2$ (Figure 32A) had similar localization and extent of labeling as the platelet-rich plasma aggregates labeled with fibrinogen-conjugated gold nanoparticles previously described (Chapter 2). Nanoparticle labeling was observed primarily at platelet/platelet junctions and in the platelet OCS. Platelet aggregates created using thrombin had a different appearance. Large amounts of darkly stained fibrin were found within the aggregate and surrounding it, platelet fixation was poorer, and the interior of the aggregate was more difficult to interpret. Labeling in these aggregates was much sparser when compared to platelet-rich plasma aggregated with

SFLLRN-NH$_2$ (Figure 32B). Labels were found within or near fibrin bundles and between platelets.

Discussion

It is highly desirable to develop a magnetic nanoparticle that can be easily conjugated to proteins for cell-specific nanoparticle targeting and hyperthermic applications. Here we produced magnetite nanoparticles using a typical aqueous coprecipitation method and reduced gold onto the magnetite surface in an attempt to produce nanoparticles that have been previously described as "core-shell" structures (27). The resulting gold-coated magnetite nanoparticles did not exhibit the expected "core-shell" morphology and many had exposed magnetite on the nanoparticle surface. However, attempts to conjugate protein to the surface of gold-coated magnetite demonstrated that a complete gold coating over the entire magnetite surface is not required for protein adsorption. Further, these protein-conjugated nanoparticles were able to target platelets similarly to protein-conjugated colloidal gold.

Nanoparticle synthesis:

Production of magnetite nanoparticles by aqueous synthesis produces highly magnetic nanoparticles that are stable in an aqueous solution of TMAOH for up to one month. The synthesis procedure is relatively simple compared to many inverse micelle or organic synthesis procedures (20, 22, 38), but has the high degree of variability (21, 42). Typical nanoparticle synthesis occurs in two distinct phases: a seeding step where very small

nanocrystals are produced, followed by subsequent growth around the nanocrystal nucleus (67, 68). Some syntheses will also include a capping step that prevents further growth of nanoparticles after they reach a certain size/diameter/aspect ratio (69-71). In aqueous magnetite synthesis, the pH, ionic strength of the solution, and temperature are all critical parameters (18). It has further been suggested that the size of the iron salt droplets added to the reaction during magnetite synthesis plays a critical role in the nanoparticle size and distribution (72). In our synthesis, the strong NaOH base solution causes both seeding and growth to occur simultaneously, resulting in a combination of many small nanoparticles and larger magnetite structures. The larger structures were subsequently removed by centrifugation in TMAOH. The small nanoparticles remaining in the supernatant had a fairly broad size distribution as has been previously described for aqueous coprecipitation techniques (42).

Attempting to grow gold on magnetite nanoparticles produced mixed results. During the coating procedure, the color change of the sol created by the gold plasmon was the primary method of gauging initial success. After coating, success was further characterized by stability of the nanoparticle sol and the ability to conjugate the nanoparticles with protein. Our magnetite coating procedure revealed that the temperature of the coprecipitation reaction plays a critical role in obtaining nanoparticles that support gold growth. The temperature likely affected the size distribution of the nanoparticles, which in turn affects the concentration of the final product following removal of the large magnetite structures. It is also possible that gold growth is best supported by magnetite nanoparticles of a certain size range. Controlling the temperature

during magnetite synthesis provided a more consistent concentration of magnetite seeds, and considerably increased the coating success rate. Additionally, temperature control during coprecipitation may also affect the crystallographic termination planes of magnetite nanocrystals and may promote different subtle surface modifications. Repeated production of gold-coated magnetite still produces variable results when following the same procedure with the same reagents, demonstrating that some yet unknown variables also affect gold coating. Regardless, the procedure can be used to produce gold-coated magnetite nanoparticles in a relatively consistent manner. Our current success rate is approximately 70% of magnetite batches that can be coated with gold.

Gold-coated magnetite morphologies:

None of the gold-coated magnetite morphologies observed appeared as the commonly described "core-shell" nanoparticle consisting of a magnetite core surrounded by a thin uniform gold shell. The majority of the gold-coated magnetite nanoparticles produced were isolated (single), with a round morphology similar in appearance to colloidal gold of the same size. These isolated particles had a thick gold coating. Magnetite fringes could be observed in any part of the nanoparticle including the edges. Isolated rounded gold-coated magnetite most closely resembled "core-shell" morphology, but exhibited some clear differences. The magnetite was not centered in the "core" of the particle and was sometimes exposed on the outside of the nanoparticle. The isolated particle morphology can be explained by Volmer-Weber growth of gold on magnetite, where isolated islands of gold grow until coalesced into a single thick coating (45, 46). A subset of faceted

triangular particles had a different morphology consisting of two independent layers of gold and a single layer of magnetite. The definitive arrangement of the gold and magnetite planes cannot be determined by HRTEM due to the planes being in projection. One possibility is that the faceted nanoparticles may have a sandwich-type morphology in which the magnetite is fitted neatly between the layers of gold. This interpretation is supported by the observation that the angle between both gold {111} planes and the magnetite {311} plane have the same value. Additionally, the angle between the two gold {111} planes (56°) cannot occur in a single crystal.

The aggregated gold-coated magnetite nanoparticles had exposed magnetite seeds with small gold islands consistent with Volmer-Weber growth on some nanoparticle surfaces. Gold growth on these surfaces may not have reached the point of coalescence as appeared to occur with the isolated nanoparticles. We observed aggregated gold-coated magnetite nanoparticles in nearly all preparations, however this type of particle has not been described in other similar synthesis methods (27, 28, 39, 41).

The faceted nanoparticles appear to have a much more ordered gold growth mechanism. Gold growth appears confined to the predefined magnetite plane and gold growth occurs as a single crystal without the stacking faults observed in colloidal gold. Well oriented faceted gold-coated nanoparticles are a minority of the population and were difficult to study in this system. For future studies that attempt to elucidate the mechanism of gold growth on magnetite, depositing gold on thin films of magnetite may be a useful tool.

The exposed magnetite edges commonly observed run contrary to our prior assumptions regarding the role of the gold coating in nanoparticle stability and ability to be functionalized by non-ionic protein adsorption. At a bulk level, protein adsorption to the surface of nanoparticles stabilizes the vast majority of the population at physiologic pH and salt concentration. We further analyzed the nanoparticles at an individual level to determine which morphologies of gold-coated magnetite were successfully conjugated to fibrinogen, paying particular attention to exposed magnetite surfaces. Protein coating can be observed around both isolated nanoparticles and on smaller aggregates. Somewhat surprisingly, protein was observed coating apparently bare magnetite surfaces on gold-coated magnetite aggregates. However, when we quantified the population of aggregated nanoparticles in stock and conjugated nanoparticles, we found that the aggregated population was significantly reduced during the procedure. The largest gold-coated magnetite aggregates were lost after centrifugation during the conjugation procedure, indicating that the largest aggregates with the least gold coating were unstable during protein conjugation. This supports our hypothesis that the gold surface is important for non-ionic protein adsorption. The coating of bare magnetite surfaces with protein demonstrates that protein conjugation to magnetite directly is possible, but it likely requires neighboring gold to protect the magnetite from agglomeration at pH values approaching neutral during the conjugation process.

Biological activity of nanoparticle conjugates:

The labeling of platelets by fibrinogen conjugated to either colloidal gold or gold-coated magnetite were directly compared to one another. Labeling with the two types of

nanoparticle conjugates produced the same pattern in both the surface-activated and aggregated platelet systems. The localization of the labels was always consistent with previously described fibrinogen labeling (49, 50, 54, 61). Labeling intensity was either similar or somewhat lower with fibrinogen-conjugated, gold-coated magnetite nanoparticles when compared to colloidal gold. Differences in labeling intensity are most likely due to different nanoparticle concentrations in the conjugates, and may be corrected for by adjusting the concentration prior to labeling. The localization of gold and gold-coated magnetite nanoparticles validates the targeting methodologies established previously (Chapter 2) using fibrinogen conjugates to select for activated platelets.

Labeling platelets with fibrinogen-conjugated gold-coated magnetite under in vivo-*like conditions:*

PRP aggregated with the non-proteolytic peptide SFLLRN-NH$_2$ labeled with fibrinogen-conjugated gold-coated magnetite in the interior of the platelet aggregates, similar to the fibrinogen-conjugated colloidal gold nanoparticle labeling described previously (Chapter 2). The similar localization and number of fibrinogen conjugated gold-coated magnetite and colloidal gold labels present in platelet-rich plasma aggregates further confirms that the two types of nanoparticles behave in a similar manner. When platelet-rich plasma was aggregated with thrombin, the resulting labeling was significantly reduced. The TEM ultrathin sections contained a large amount of fibrin around platelets that were more completely degranulated and contracted. The labeling was much sparser than in any other labeling condition tested. The fibrin itself may act as a physical barrier preventing

nanoparticles from reaching the activated platelet surface, where we propose their effect on reopening occluded arteries will take place. However, it is possible that fibrinogen-conjugated nanoparticle-fibrin interactions could result in damage to the fibrin network could as a result of localized hyperthermia, in addition to the platelet damage we expect. The presence of fibrin certainly complicates our analytical approach. In any case, the labeling pattern suggests that targeting blood clots *in vivo* may be challenging, and will likely require a high concentration of fibrinogen-conjugated nanoparticles to achieve significant nanoparticle infiltration of an occlusive thrombus.
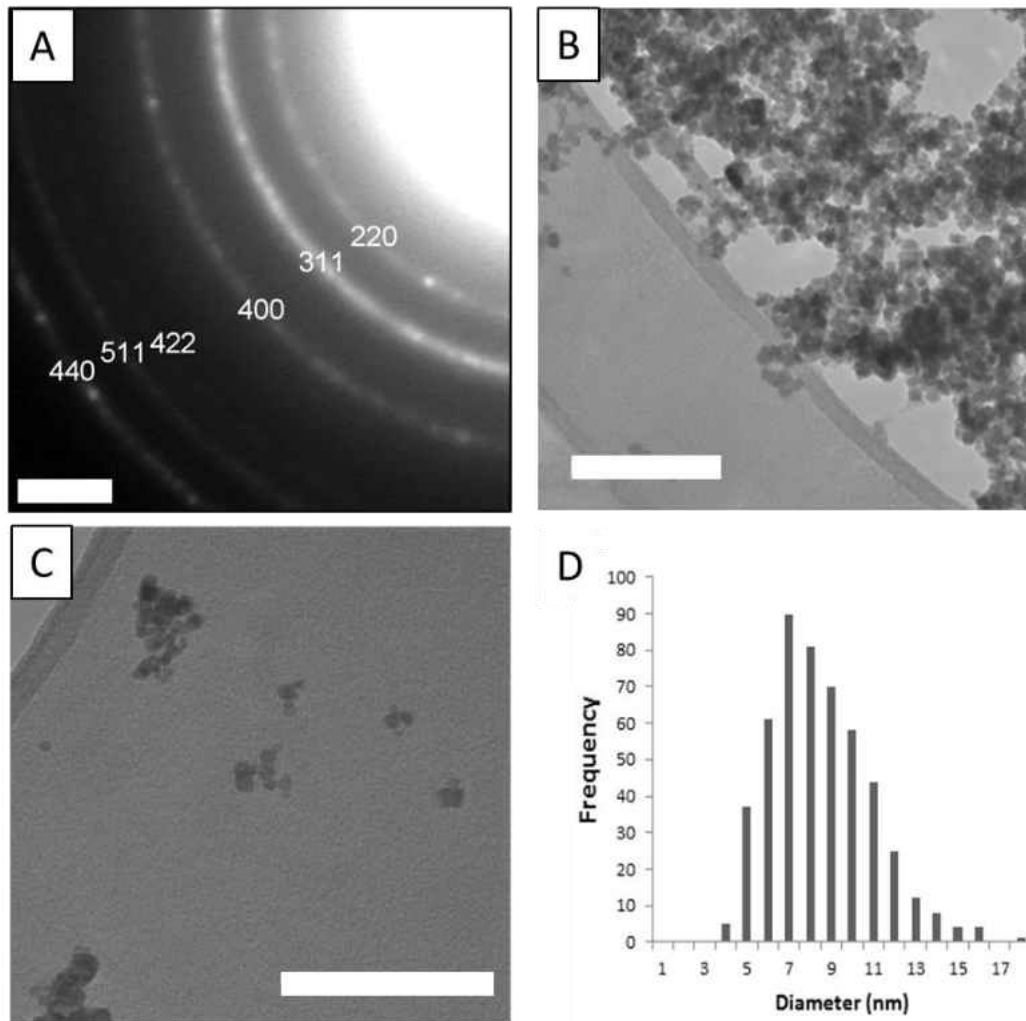
Figures Legends and Figures:

Figure 19. TEM analysis of the synthesized iron oxide nanoparticles. Selected area diffraction of a group of iron oxide nanoparticles is shown in (A). The reflections are indexed to magnetite lattice parameters as indicated. (B) demonstrates that when the prepared magnetite nanoparticles are dried onto a holey carbon grid, they appear nearly exclusively clumped together. When the magnetite nanoparticles are diluted 1:100 in TMAOH and dried in a similar manner, the nanoparticles remain mostly isolated or in small groups, as shown in (C). The size distribution of 500 nanoparticles measured along their longest axis is shown in (D). Size bars are 1 nm^{-1} for (A) and 50 nm for (B, C).

Figure 20. Brightfield TEM and selected area electron diffraction of gold-coated magnetite nanoparticles. (A) demonstrates commonly observed gold-coated magnetite morphology. White arrowheads show faceted nanoparticles, while black arrows indicate rounded nanoparticles. In (B) a minority of nanoparticles that consist of low contrast and high contrast particles aggregated together are indicated with black arrows. Size bars are 50 nm. A histogram of the size distribution of 500 magnetite particles (black squares) and of 500 isolated gold-coated magnetite (gray diamonds) is shown in (C). A composite image of selected area electron diffraction of gold, magnetite, and gold-coated magnetite is shown in (D). The image is inverted to better show the diffraction patterns. Reflections occurring from gold and uncoated magnetite nanoparticles are indexed as indicated with white arrows. The gold-coated magnetite diffraction pattern contains reflections from gold {111} and magnetite {220} and {311}. Gold {200} overlaps with magnetite {400}.
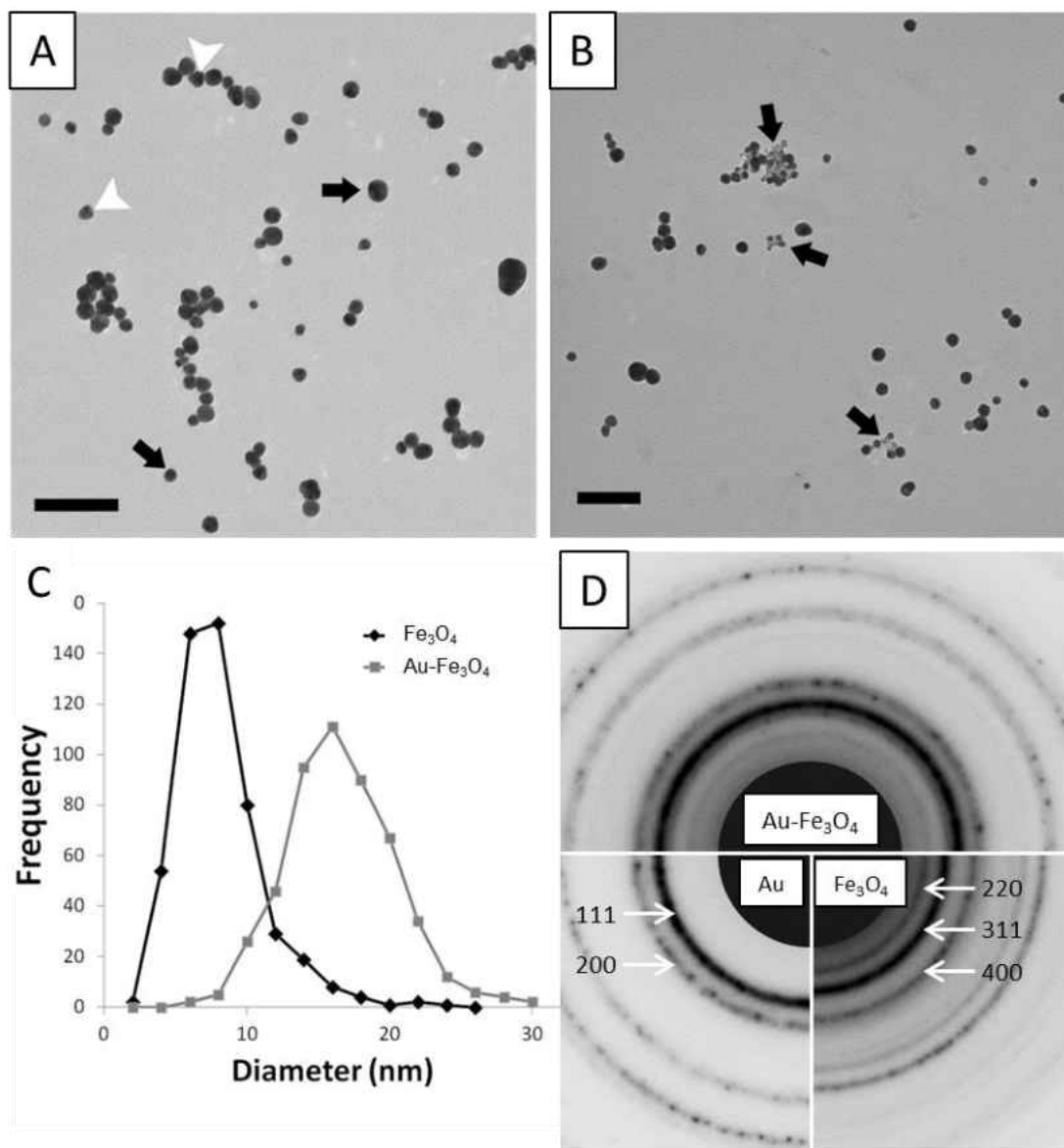
Figure 20

Figure 21. HRTEM of isolated and aggregated gold-coated magnetite. (A-C) shows an isolated gold-coated magnetite particle with three sets of lattice fringes present.   Fast Fourier transform filtering was performed to isolate fringes based on known lattice parameters. (A) shows the original HRTEM image, (B) is filtered to show magnetite {311} planes, (C) is similarly filtered to show gold {111} planes. The magnetite {311} plane makes 62° angles with both gold {111} planes, and the gold {111} planes make a 52° angle with each other. An aggregate of gold-coated magnetite nanoparticles is shown in (D-F). The original HRTEM image is shown in (D), the fast Fourier transform filtering showing magnetite {111} and {311} planes is shown in (E) and gold {111} planes are shown in (F). Arrows point in parallel with observed fringes. Size bars are 5 nm.
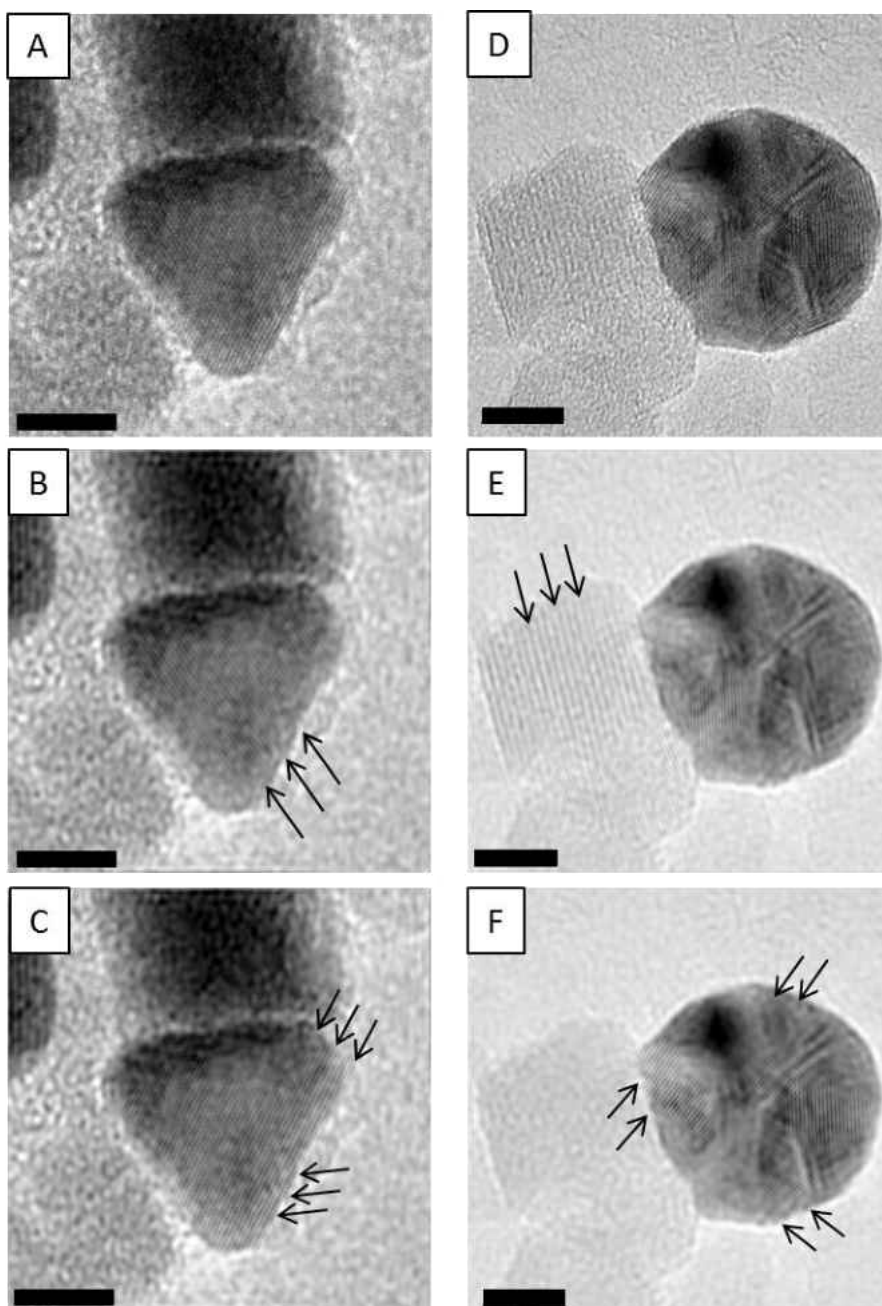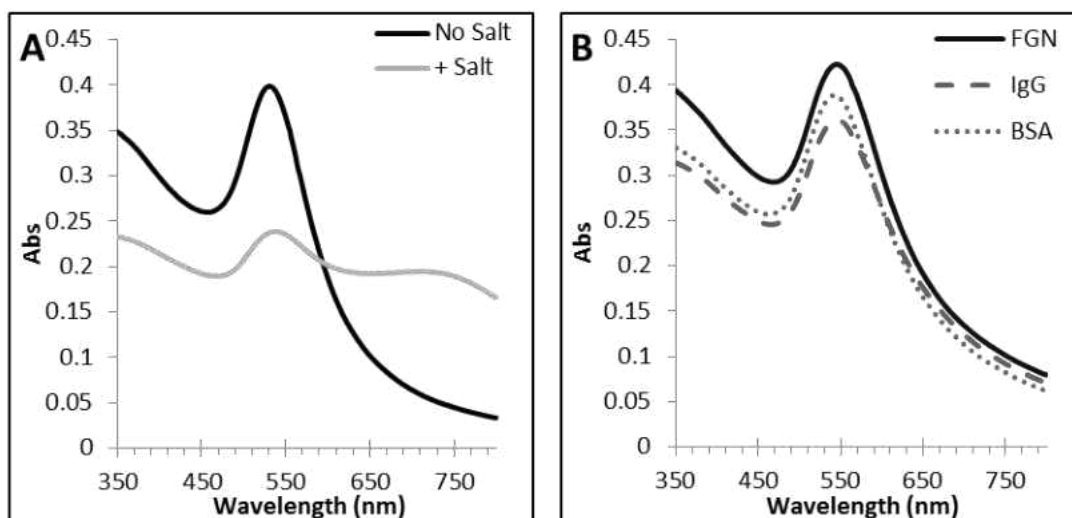
Figure 21

Figure 22. Visible light absorbance spectra of gold-coated magnetite nanoparticles. (A) demonstrates the normal absorbance spectrum of stock gold-coated magnetite (black line) and gold-coated magnetite nanoparticles that were agglomerated with salt (grey line). Nanoparticles challenged with salt had a spectrum with reduced absorbance in the gold plasmon near 520 nm, and an increase in absorption at longer wavelengths. Gold-coated magnetite nanoparticles conjugated to fibrinogen (FGN, solid black line), immunoglobulin G (IgG, dashed grey line), or bovine serum albumin (BSA, grey dotted line) and challenged with salt are shown in (B). All conjugated nanoparticles retain the spectral characteristics of stock nanoparticles with little absorbance in the longer wavelengths despite the salt challenge.

Figure 23. Magnetic behavior of gold-coated magnetite nanoparticles in response to a static magnet. (A) shows the visible light absorbance spectra of gold-coated magnetite nanoparticles (solid line), and conjugated (dotted line) or unconjugated (dashed line) nanoparticles remaining in solution after exposure to a static magnet. Images of conjugated gold-coated magnetite nanoparticles before and after exposure to a static magnet are shown in (B) and (C), respectively. The majority of fibrinogen-conjugated gold-coated nanoparticles are located on the poles of the static magnet, as indicated by arrows in (C). The magnet is attached to the vial with blue tape. Note that the liquid visible above the tape line in (C) has changed from the distinct red color seen in (B) to nearly colorless.
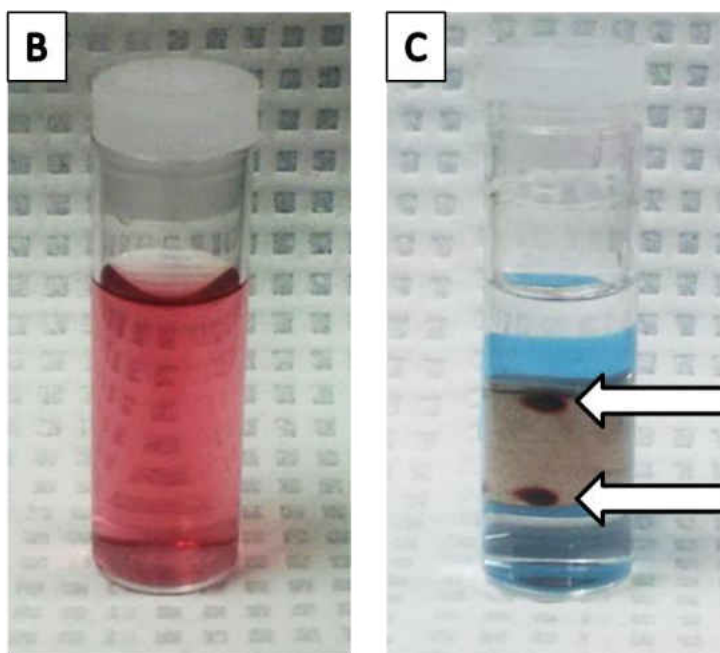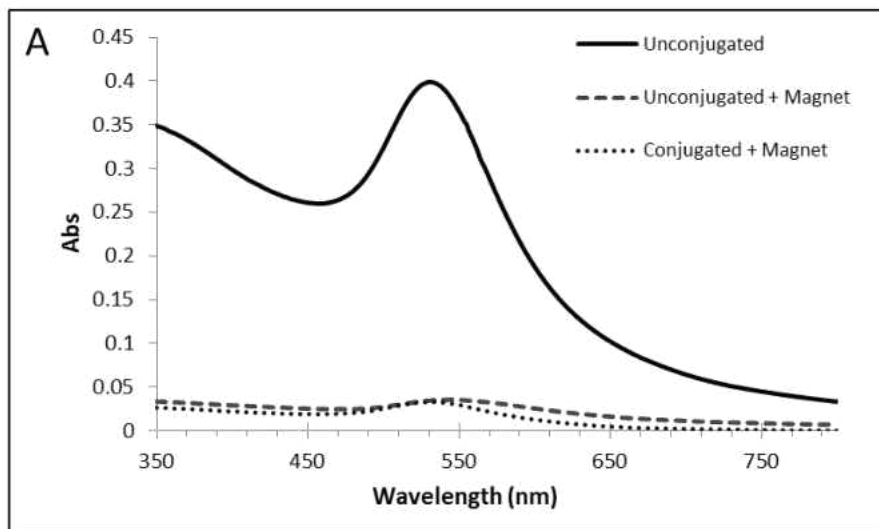
Figure 23

Figure 24. Brightfield TEM analysis of fibrinogen-conjugated gold-coated magnetite.

(A) demonstrates a representative field of fibrinogen-conjugated, gold-coated magnetite

nanoparticles air-dried onto the grid. Both isolated and aggregated (arrows) nanoparticles

are observed. Nanoparticles adhered to a poly-L-lysine coated grid and dried by the

critical point procedure are shown in (B). The poly-L-lysine treatment caused clumping

of the conjugated nanoparticles. Low contrast protein halos are present around the entire

group of nanoparticles. Arrows point to areas areas of bare magnetite that are covered
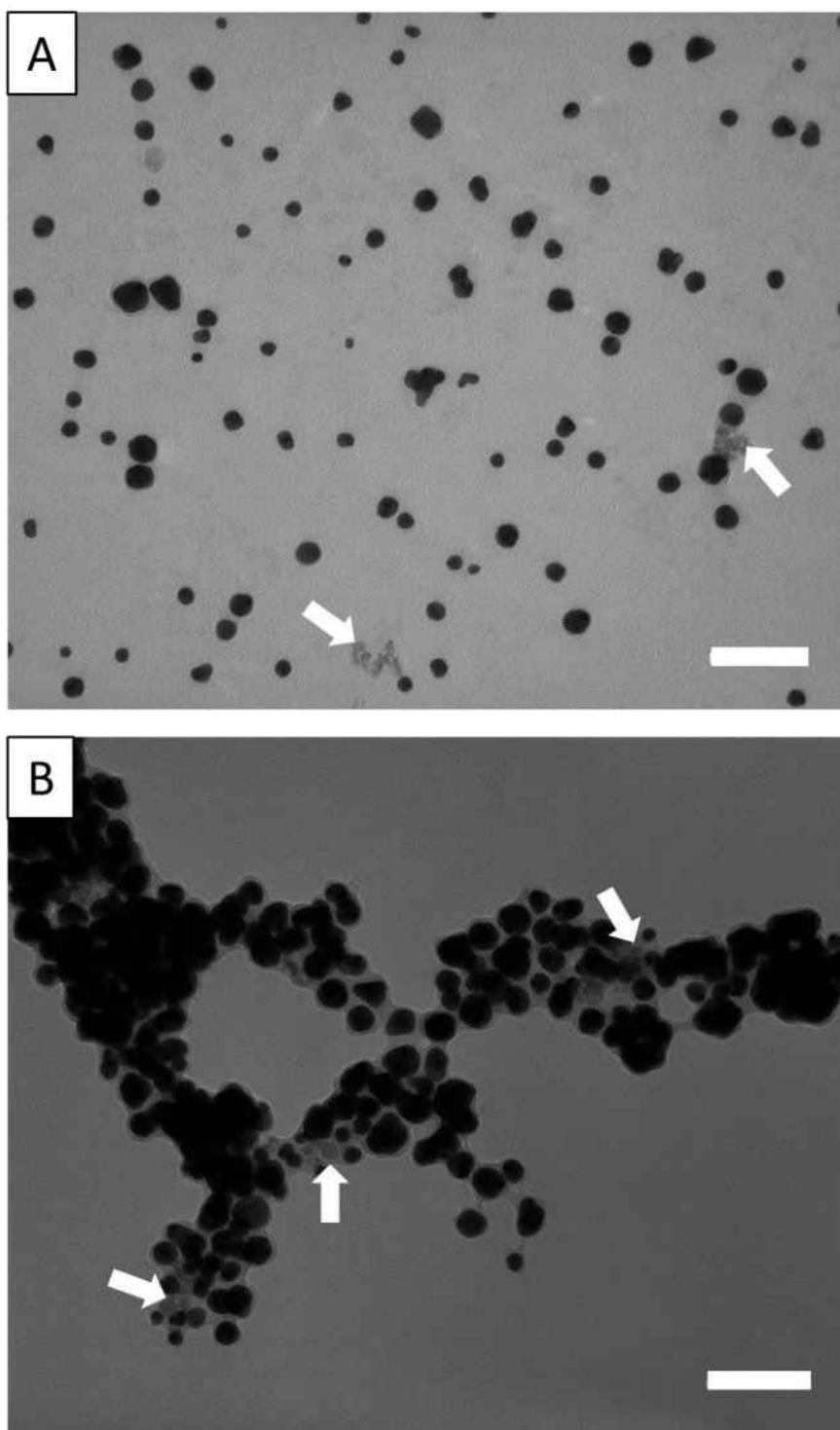
with protein. Size bars are 100 nm.

Figure 24

Figure 25. SEM of nanoparticles adhered to poly-L-lysine carbon-coated grids and dried by the critical point procedure. The left column shows secondary electron (SE) micrographs; the right column shows the same areas using backscattered electron (BSE) imaging. Unconjugated 18 nm colloidal gold (Au) is shown in (A) and (B). Fibrinogen-conjugated colloidal gold (FGN-Au) clumped during sample preparation, as shown in (C) and (D). Unconjugated gold-coated magnetite (Au-Fe$_3$O$_4$) also clumped during preparation as shown in (E) and (F). In BSE analysis, gold is observed as high contrast regions and magnetite as low contrast. Fibrinogen-conjugated gold-coated magnetite (FGN-Au-Fe$_3$O$_4$) is shown in (G) and (H). Protein binding is visible in the SE micrographs (C) and (G). Size bar is 100 nm for all images.
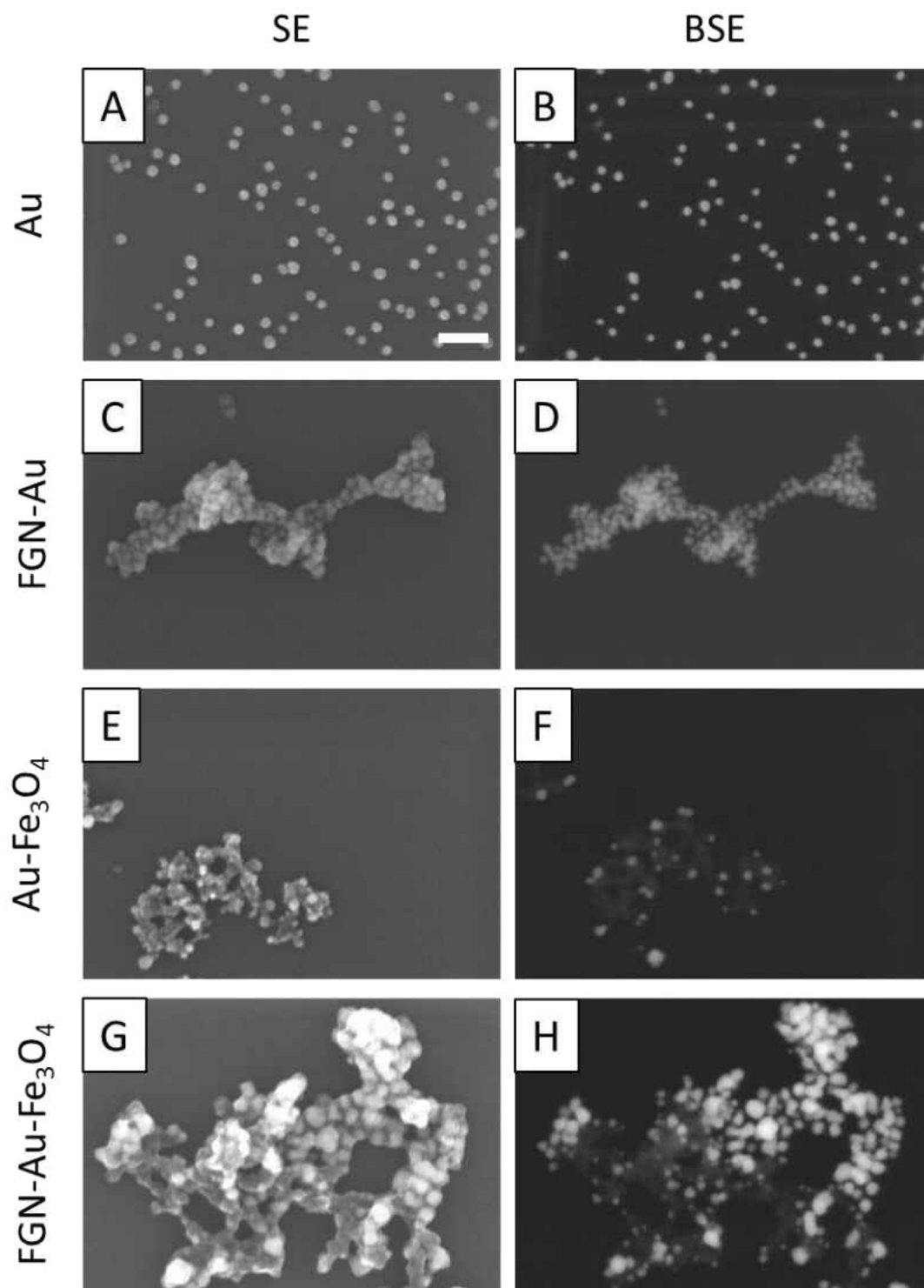
Figure 25

Figure 26. Analysis of gold-coated magnetite morphologies on surface-activated

platelets. (A) demonstrates a low magnification BSE micrograph of a surface-activated

platelet labeled with fibrinogen-conjugated gold-coated magnetite. (B) demonstrates a

high magnification micrograph used to quantify particle morphologies. (C) shows a

reconstructed montage of the entire platelet using higher magnification micrographs. The

dotted line shows the region around the granulomere excluded from SEM analysis,

arrowheads show regions of open canalicular system (OCS) also excluded from analysis.

TEM of similarly labeled platelet is shown in (D). Arrows point to low contrast

aggregated gold-coated magnetite on the platelet surface for both SEM and TEM. Scale

bar is 1 μm for all images.
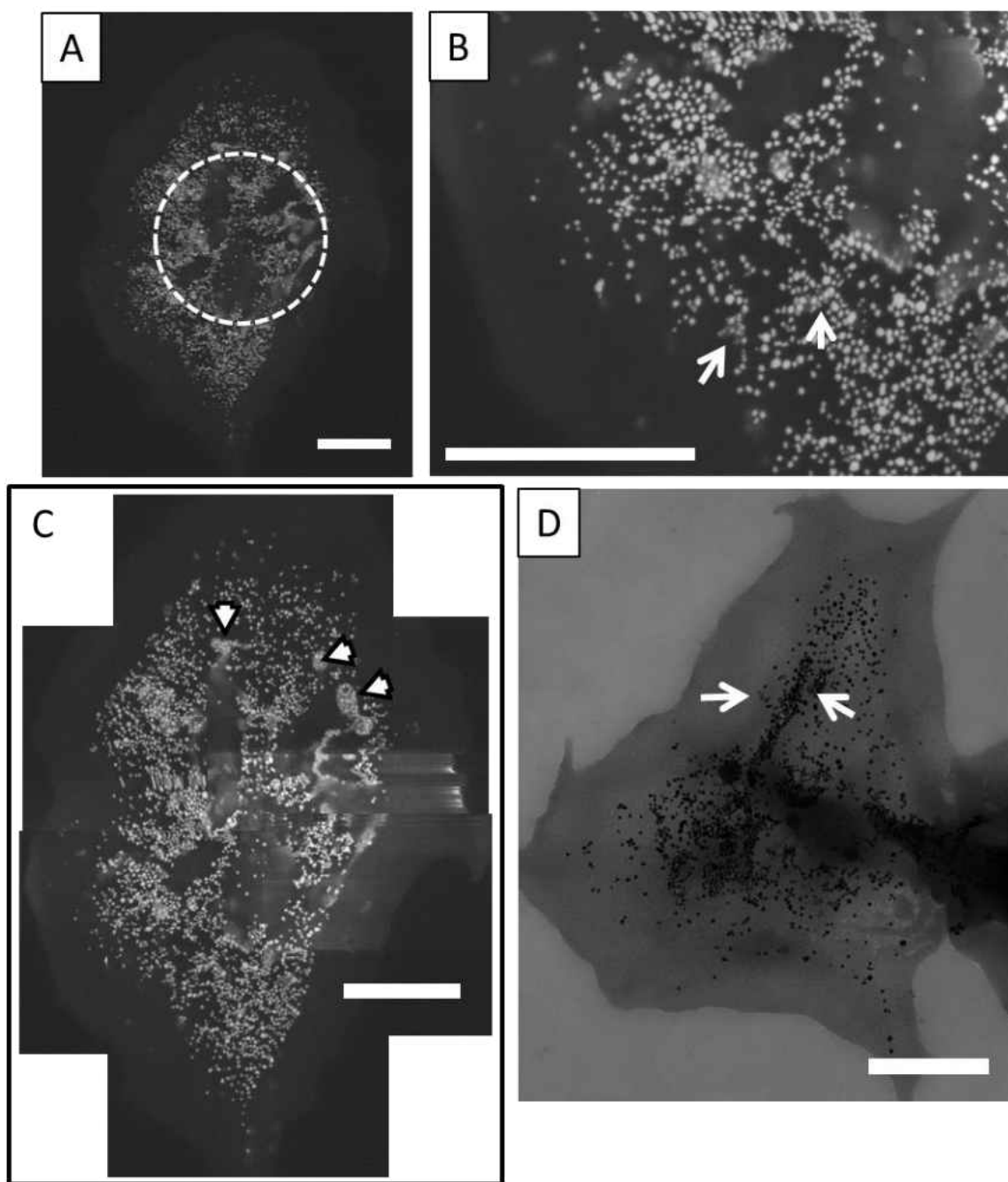
Figure 26

Figure 27. TEM analysis of whole mount surface-activated platelets labeled with fibrinogen-conjugated gold or gold-coated magnetite. The typical labeling of fibrinogen conjugated to 18 nm colloidal gold is shown in (A). (B) shows representative labeling with fibrinogen conjugated to gold-coated magnetite on surface-activated platelets. Insets are approximately 2.5x higher magnification micrographs of the white boxes to better show nanoparticle localization and presence of aggregated gold-coated magnetite. Scale bars are 1 μm for both images.
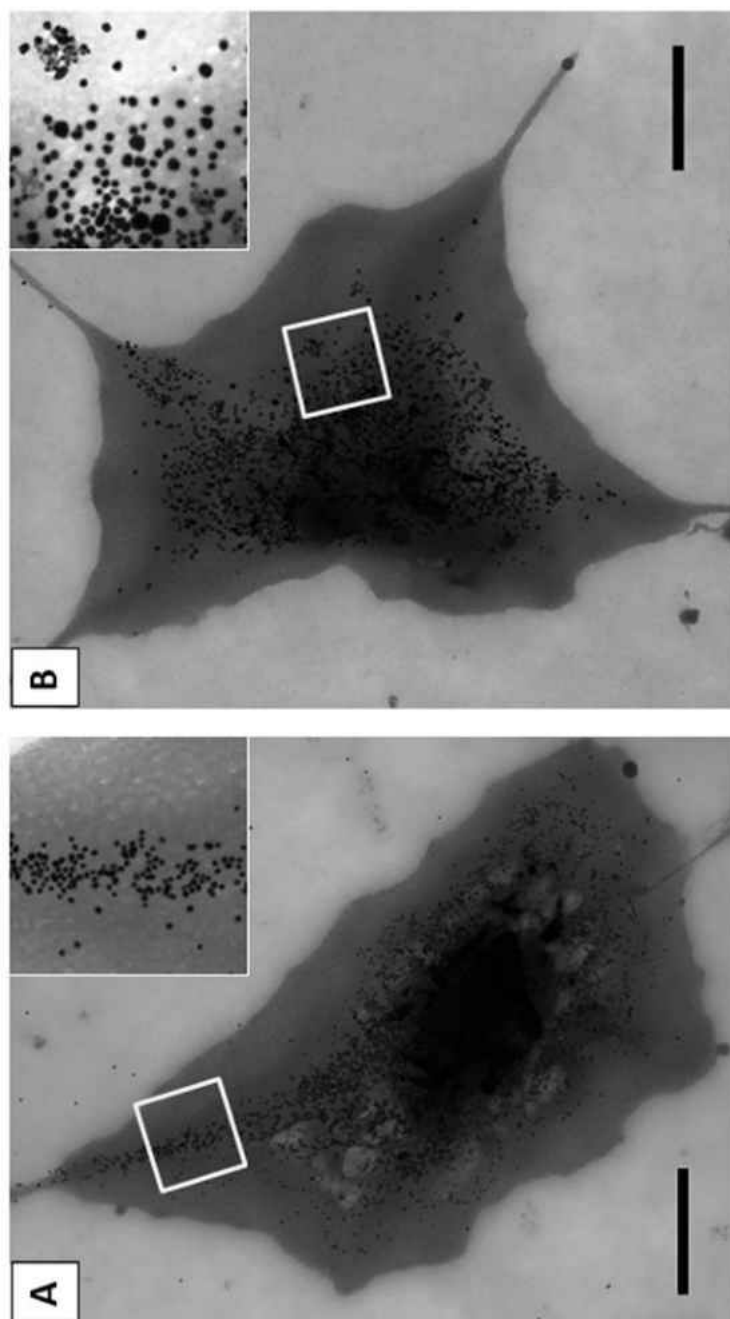
Figure 27
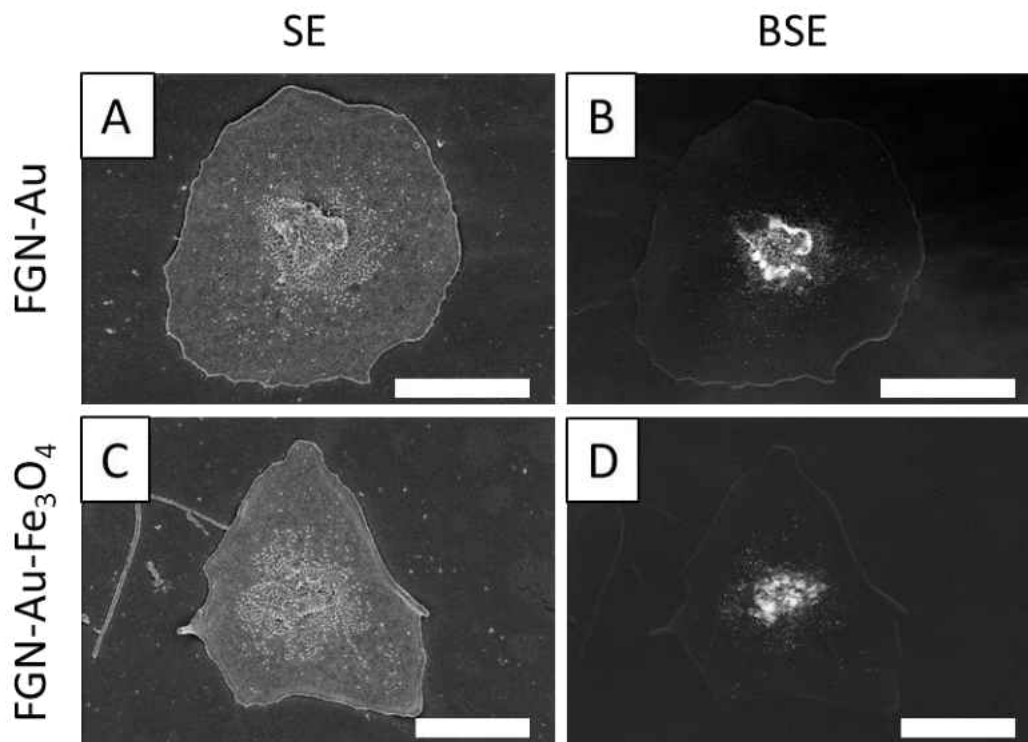
Figure 28.   SEM analysis of surface-activated platelets labeled with gold or gold-coated magnetite conjugated to fibrinogen. SE (A) and BSE (B) micrographs show surface-activated platelets labeled with fibrinogen conjugated to 18 nm colloidal gold (FGN-Au). Similarly, SE (C) and BSE (D) electron micrographs of platelets labeled with fibrinogen conjugated to gold-coated magnetite (FGN-Au-Fe$_3$O$_4$) are shown. Both fibrinogen-conjugated gold and gold-coated magnetite nanoparticles have translocated on the surface of the platelet membrane, and are found around the granulomere of well-spread platelets. Scale bar is 2 μm for all images.
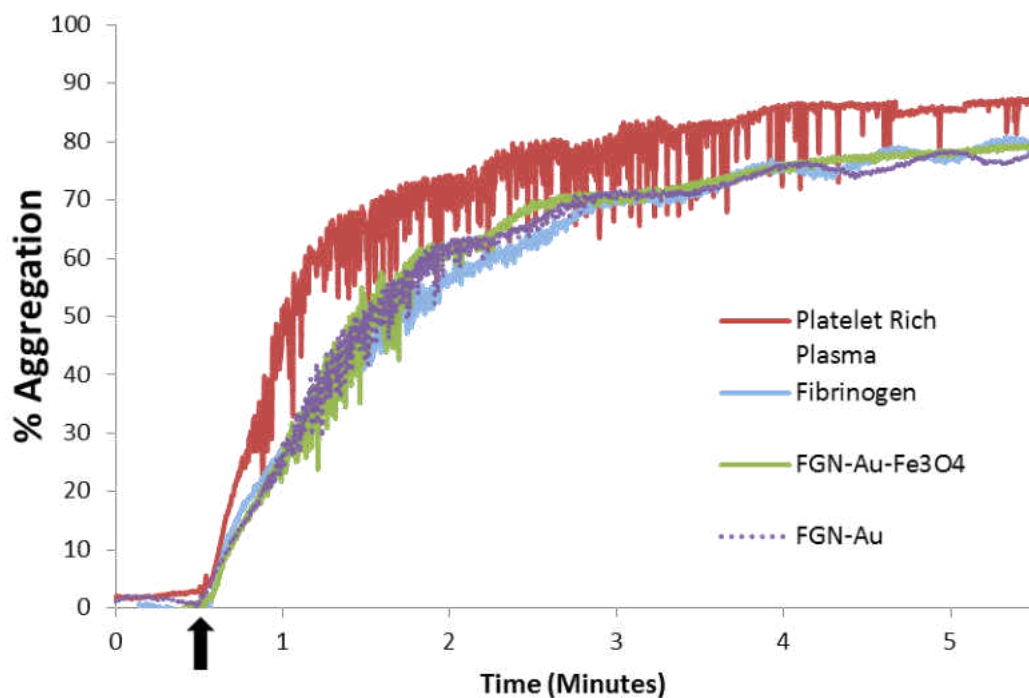
Figure 29. Aggregometer tracing of platelets stimulated with 67 μM SFLLRN-NH$_2$.

Gel-filtered platelets were supplemented with unconjugated fibrinogen (Fibrinogen,

blue), fibrinogen conjugated to colloidal gold (FGN-Au, purple), or fibrinogen

conjugated to gold-coated magnetite (FGN-Au-Fe$_3$O$_4$, green). Platelet-rich plasma was

similarly aggregated to show the maximal possible aggregation (red). Stimulation of

platelets was initiated at the 30 second time point, indicated by an arrow.

Figure 30. SEM analysis of gel-filtered platelets supplemented with unconjugated

fibrinogen, aggregated, and then labeled with fibrinogen conjugated to colloidal gold or

gold-coated magnetite. The left column shows SE micrographs of platelet aggregates, the

right column shows the same field of view using BSE imaging. Unlabeled platelet

aggregates (FGN) (A,B) serve as controls. Platelet aggregates labeled with fibrinogen

conjugated to 18 nm colloidal gold (FGN-Au) are shown in (C) and (D). Platelet

aggregates labeled with fibrinogen conjugated to gold-coated magnetite (FGN-Au-Fe_3O_4)

are shown in (E) and (F). Note that extensive incorporation of nanoparticles has

occurred, even though the aggregates were formed prior to incubation with labels. Size

bar is 10 μm for all images.
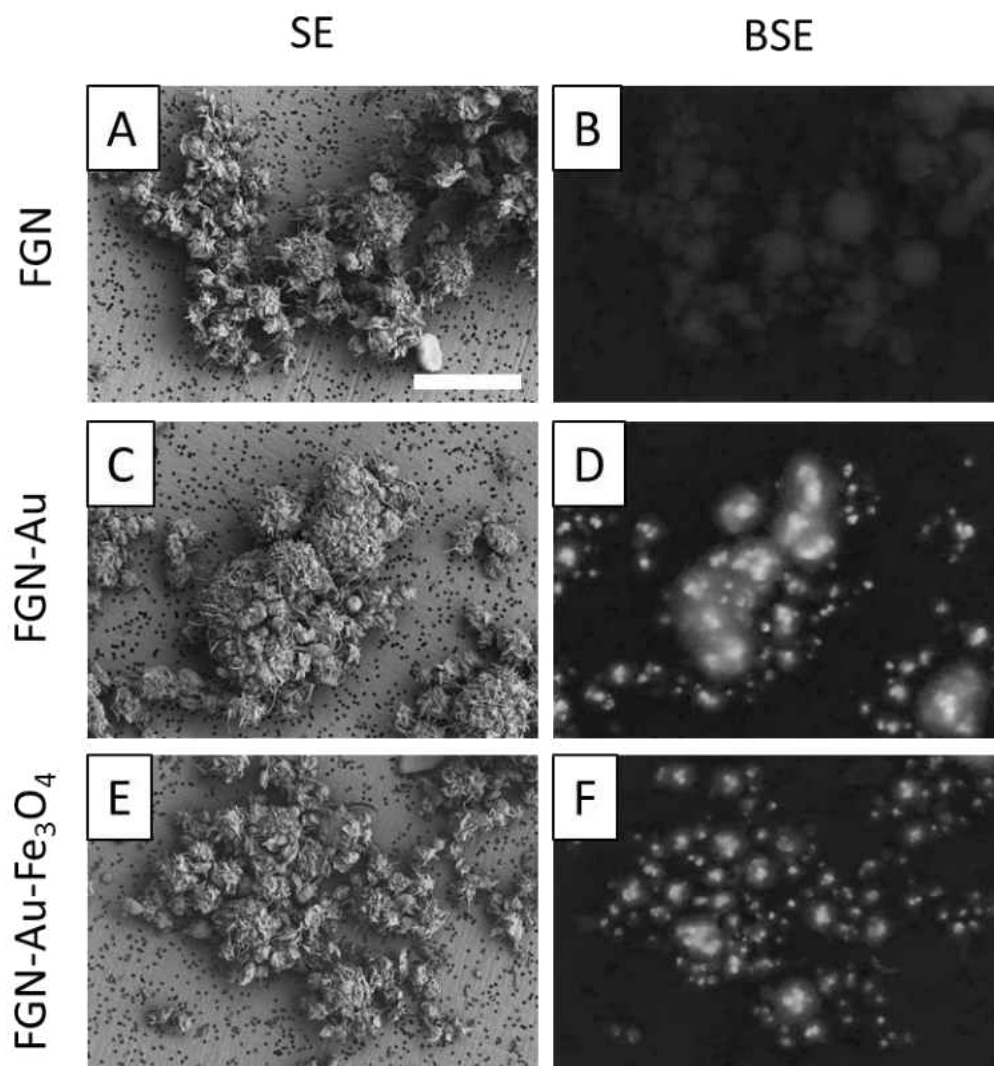
Figure 30
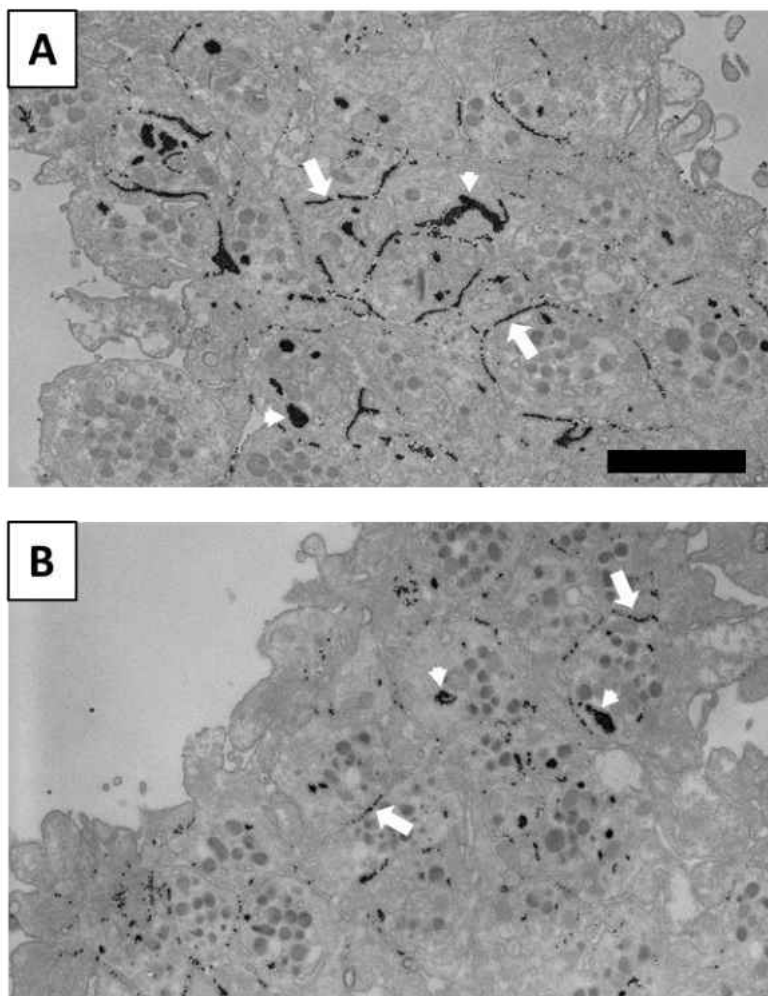
Figure 31. TEM images of ultrathin sections of platelet aggregates labeled with fibrinogen conjugated to 18 nm colloidal gold or gold-coated magnetite. Typical labeling observed using fibrinogen conjugated to gold nanoparticles is shown in (A); labeling is primarily in the aggregate interior at platelet/platelet junctions (arrows) and in the OCS (arrowheads). Labeling using fibrinogen conjugated to gold-coated magnetite is shown in (B). The labeling pattern is similar, but the number of nanoparticles observed is reduced. Size bar is 2 μm for both images.

Figure 32. TEM ultrathin sections of aggregated platelet-rich plasma labeled with fibrinogen conjugated gold-coated magnetite. Platelet-rich plasma was aggregated with either 67 μM SFLLRN-NH$_2$ (A) or 2 nM thrombin (B). Aggregation of platelet-rich plasma with thrombin results in fibrin production, indicated by black arrowheads. Thrombin-induced aggregates have significantly reduced incorporation of fibrinogen-conjugated, gold-coated magnetite labels, as shown with white arrows. Size bars are 1 μm.

Figure 32

References

1. Gordon, R. T., J. R. Hines, and D. Gordon. 1979. Intracellular hyperthermia. A biophysical approach to cancer treatment via intracellular temperature and biophysical alterations. *Med. Hypotheses* 5:83-102.

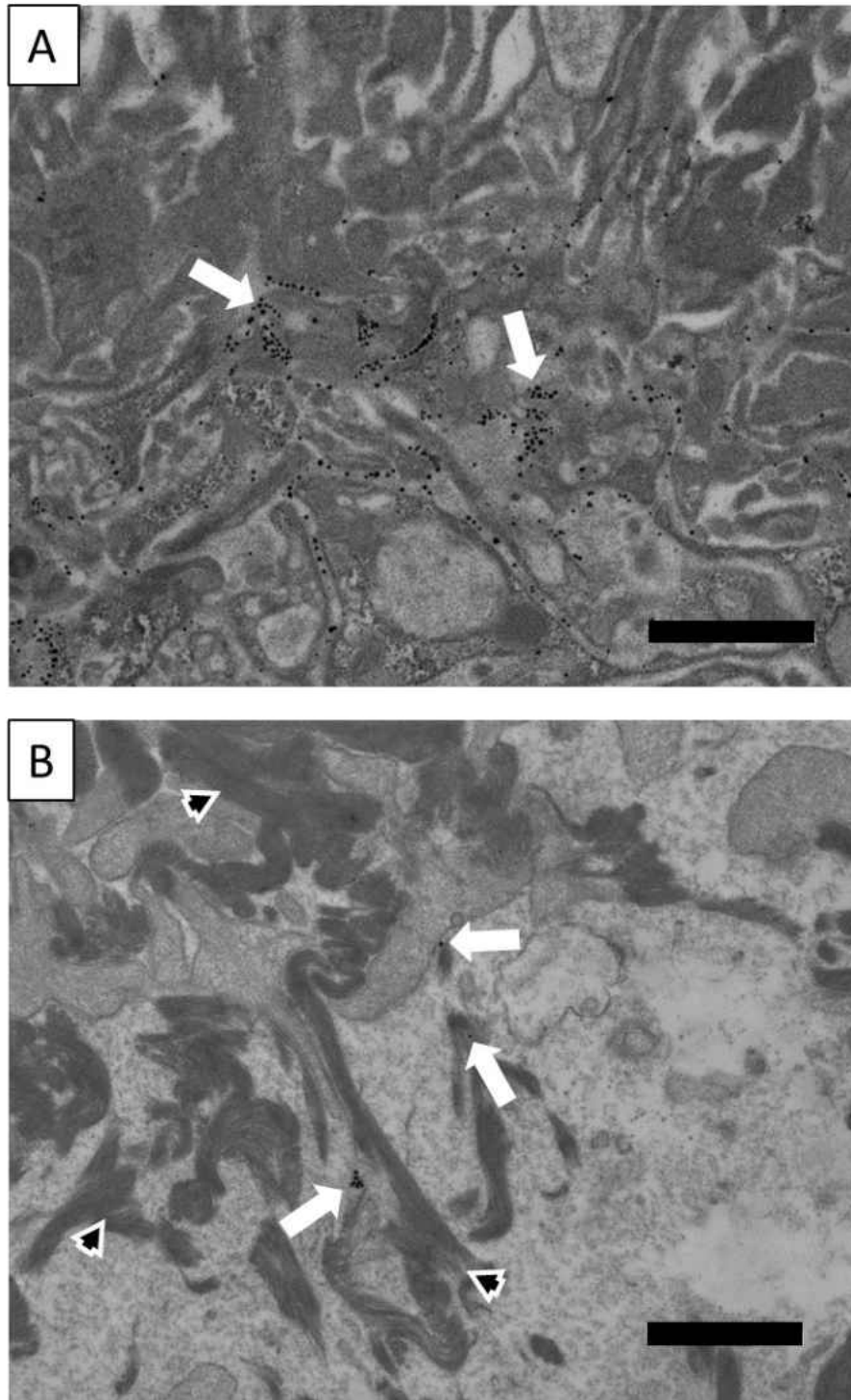2. Gangopadhyay, P., S. Gallet, E. Franz, A. Persoons, and T. Verbiest. 2005. Novel superparamagnetic core(shell) nanoparticles for magnetic targeted drug delivery and hyperthermia treatment. *IEEE Trans. Magn.* 41:4194-4196.

3. Zhao, D. L., H. L. Zhang, X. W. Zeng, Q. S. Xia, and J. T. Tang. 2006. Inductive heat property of Fe_3O_4/polymer composite nanoparticles in an ac magnetic field for localized hyperthermia. *Biomed. Mater.* 1:198-201.

4. Johannsen, M., B. Thiesen, A. Jordan, K. Taymoorian, U. Gneveckow, N. Waldöfner, R. Scholz, M. Koch, M. Lein, K. Jung, and S. A. Loening. 2005. Magnetic fluid hyperthermia (MFH) reduces prostate cancer growth in the orthotopic Dunning R3327 rat model. *Prostate* 64:283-292.

5. Tseng, H.-Y., C.-Y. Lee, Y.-H. Shih, X.-Z. Lin, and G.-B. Lee. 2007. Hyperthermia cancer therapy utilizing superparamagnetic nanoparticles. In *2nd IEEE International Conference on Nano/Micro Engineered and Molecular Systems*. 163-166.

6. Asin, L., M. R. Ibarra, A. Tres, and G. F. Goya. 2012. Controlled cell death by magnetic hyperthermia: Effects of exposure time, field amplitude, and nanoparticle concentration. *Pharm. Res.* 29:1319-1327.

7. Fan, Z., M. Shelton, A. K. Singh, D. Senapati, S. A. Khan, and P. C. Ray. 2012. Multifunctional plasmonic shell-magnetic core nanoparticles for targeted diagnostics, isolation, and photothermal destruction of tumor cells. *ACS Nano* 6:1065-1073.

8. Liu, H. L., C. H. Sonn, J. H. Wu, K. M. Lee, and Y. K. Kim. 2008. Synthesis of streptavidin-FITC-conjugated core-shell Fe3O4-Au nanocrystals and their application for the purification of CD4+ lymphocytes. *Biomaterials* 29:4003-4011.

9. Bao, J., W. Chen, T. Liu, Y. Zhu, P. Jin, L. Wang, J. Liu, Y. Wei, and Y. Li. 2007. Bifunctional Au-Fe_3O_4 nanoparticles for protein separation. *ACS Nano* 1:293-298.

10. Mazzucchelli, S., M. Colombo, C. De Palma, A. Salvade, P. Verderio, M. D. Coghi, E. Clementi, P. Tortora, F. Corsi, and D. Prosperi. 2010. Single-domain

protein A-engineered magnetic nanoparticles: Toward a universal strategy to site-specific labeling of antibodies for targeted detection of tumor cells. *ACS Nano* 4:5693-5702.

11.   Kaiser, M., J. Heintz, I. Kandela, and R. Albrecht. 2007. Tumor cell death induced by membrane melting via immunotargeted, inductively heated core/shell nanoparticles. *Microsc. Microanal.* 13:18-19.

12.   Krystofiak, E. S., V. Z. Matson, D. A. Steeber, and J. A. Oliver. 2012. Elimination of tumor cells using folate receptor targeting by antibody-conjugated, gold-coated magnetite nanoparticles in a murine breast cancer model. *J. Nanomat.* 2012:431012.

13.   Ito, A., K. Tanaka, H. Honda, S. Abe, H. Yamaguchi, and T. Kobayashi. 2003. Complete regression of mouse mammary carcinoma with a size greater than 15 mm by frequent repeated hyperthermia using magnetite nanoparticles. *J. Biosci. Bioeng.* 96:364-369.

14.   Gilchrist, R. K., R. Medal, W. D. Shorey, R. C. Hanselman, J. C. Parrott, and C. B. Taylor. 1957. Selective inductive heating of lymph nodes. *Ann. Surg.* 146:596-606.

15.   Herranz, F., M. P. Morales, A. G. Roca, R. Vilar, and J. Ruiz-Cabello. 2008. A new method for the aqueous functionalization of superparamagnetic Fe2O3 nanoparticles. *Contrast Media Mol. Imaging* 3:215-222.

16.   Roca, A. G., J. F. Marco, M. D. P. Morales, and C. J. Serna. 2007. Effect of nature and particle size on properties of uniform magnetite and maghemite nanoparticles. *J. Phys. Chem. C* 111:18577-18584.

17.   Massart, R. 1981. Preparation of aqueous magnetic liquids in alkaline and acidic media. *IEEE Trans. Magn.* 17:1247-1248.

18.   Gnanaprakash, G., S. Mahadevan, T. Jayakumar, P. Kalyanasundaram, J. Philip, and B. Raj. 2007. Effect of initial pH and temperature of iron salt solutions on formation of magnetite nanoparticles. *Mater. Chem. Phys.* 103:168-175.

19.   Mornet, S., J. Portier, and E. Duguet. 2005. A method for synthesis and functionalization of ultrasmall superparamagnetic covalent carriers based on maghemite and dextran. *J. Magn. Magn. Mater.* 293:127-134.

20.   Koutzarova, T., S. Kolev, C. Ghelev, D. Paneva, and I. Nedkov. 2006. Microstructural study and size control of iron oxide nanoparticles produced by microemulsion technique. *Phys. Status Solidi C* 3:1302-1307.

21. Lee, H. S., W. C. Lee, and T. Furubayashi. 1999. A comparison of coprecipitation with microemulsion methods in the preparation of magnetite. *J. Appl. Phys.* 85:5231-5233.

22. Mandal, M., S. Kundu, S. K. Ghosh, S. Panigrahi, T. K. Sau, S. M. Yusuf, and T. Pal. 2005. Magnetite nanoparticles with tunable gold or silver shell. *J. Colloid Interface Sci.* 286:187-194.

23. Esquivel, J., I. A. Facundo, M. E. Treviño, and R. G. López. 2007. A novel method to prepare magnetic nanoparticles: precipitation in bicontinuous microemulsions. *J. Mater. Sci.* 42:9015-9020.

24. Gonzales, M., L. M. Mitsumori, J. V. Kushleika, M. E. Rosenfeld, and K. M. Krishnan. 2010. Cytotoxicity of iron oxide nanoparticles made from the thermal decomposition of organometallics and aqueous phase transfer with Pluronic F127. *Contrast Media Mol. Imaging* 5:286-293.

25. Vidal-Vidal, J., J. Rivas, and M. A. López-Quintela. 2006. Synthesis of monodisperse maghemite nanoparticles by the microemulsion method. *Colloids Surf., A* 288:44-51.

26. Gupta, A. K., and M. Gupta. 2005. Synthesis and surface engineering of iron oxide nanoparticles for biomedical applications. *Biomaterials* 26:3995-4021.

27. Lyon, J. L., D. A. Fleming, M. B. Stone, P. Schiffer, and M. E. Williams. 2004. Synthesis of Fe oxide core/Au shell nanoparticles by iterative hydroxylamine seeding. *Nano Lett.* 4:719-723.

28. Cho, S.-J., J.-C. Idrobo, J. Olamit, K. Liu, N. D. Browning, and S. M. Kauzlarich. 2005. Growth mechanisms and oxidation resistance of gold-coated iron nanoparticles. *Chem. Mater.* 17:3181-3186.

29. Hu, J. D., Y. Zevi, X. M. Kou, J. Xiao, X. J. Wang, and Y. Jin. 2010. Effect of dissolved organic matter on the stability of magnetite nanoparticles under different pH and ionic strength conditions. *Sci. Total Environ.* 408:3477-3489.

30. Lattuada, M., and T. A. Hatton. 2006. Functionalization of monodisperse magnetic nanoparticles. *Langmuir* 23:2158-2168.

31. Hu, F. Q., L. Wei, Z. Zhou, Y. L. Ran, Z. Li, and M. Y. Gao. 2006. Preparation of biocompatible magnetite nanocrystals for in vivo magnetic resonance detection of cancer. *Adv. Mater.* 18:2553-2556.

32. Cui, Y.-R., C. Hong, Y.-L. Zhou, Y. Li, X.-M. Gao, and X.-X. Zhang. 2011. Synthesis of orientedly bioconjugated core/shell Fe3O4@Au magnetic nanoparticles for cell separation. *Talanta* 85:1246-1252.

33. Lim, J. K., S. A. Majetich, and R. D. Tilton. 2009. Stabilization of superparamagnetic iron oxide core-gold shell nanoparticles in high ionic strength media. *Langmuir* 25:13384-13393.

34. Wang, L., H.-Y. Park, S. I. I. Lim, M. J. Schadt, D. Mott, J. Luo, X. Wang, and C.-J. Zhong. 2008. Core@shell nanomaterials: gold-coated magnetic oxide nanoparticles. *J. Mater. Chem.* 18:2629-2635.

35. Akamatsu, K., M. Kimura, Y. Shibata, S. Nakano, D. Miyoshi, H. Nawafune, and N. Sugimoto. 2006. A DNA duplex with extremely enhanced thermal stability based on controlled immobilization on gold nanoparticles. *Nano Lett.* 6:491-495.

36. Robinson, I., D. Tung Ie, S. Maenosono, C. Walti, and N. T. Thanh. 2010. Synthesis of core-shell gold coated magnetic nanoparticles and their interaction with thiolated DNA. *Nanoscale* 2:2624-2630.

37. Wang, L., J. Luo, Q. Fan, M. Suzuki, I. S. Suzuki, M. H. Engelhard, Y. Lin, N. Kim, J. Q. Wang, and C. J. Zhong. 2005. Monodispersed core-shell Fe_3O_4@Au nanoparticles. *J. Phys. Chem. B* 109:21593-21601.

38. Jafari, T., A. Simchi, and N. Khakpash. 2010. Synthesis and cytotoxicity assessment of superparamagnetic iron-gold core-shell nanoparticles coated with polyglycerol. *J. Colloid Interface Sci.* 345:64-71.

39. Hien Pham, T. T., C. Cao, and S. J. Sim. 2008. Application of citrate-stabilized gold-coated ferric oxide composite nanoparticles for biological separations. *J. Magn. Magn. Mater.* 320:2049-2055.

40. Wu, W., Q. He, H. Chen, J. Tang, and L. Nie. 2007. Sonochemical synthesis, structure and magnetic properties of air-stable Fe3O4/Au nanoparticles. *Nanotechnology* 18:145609.

41. Lu, Q. H., K. L. Yao, D. Xi, Z. L. Liu, X. P. Luo, and Q. Ning. 2006. Synthesis and characterization of composite nanoparticles comprised of gold shell and magnetic core/cores. *J. Magn. Magn. Mater.* 301:44-49.

42. Jeong, J.-R., S.-J. Lee, J.-D. Kim, and S.-C. Shin. 2004. Magnetic properties of γ-Fe2O3 nanoparticles made by coprecipitation method. *Phys. Status Solidi (B)* 241:1593-1596.

43. Saiz, E., R. M. Cannon, and A. P. Tomsia. 2008. High-temperature wetting and the work of adhesion in metal/oxide systems. *Annu. Rev. Mater. Res.* 38:197-226.

44. Kajikawa, Y., and S. Noda. 2005. Growth mode during initial stage of chemical vapor deposition. *Appl. Surf. Sci.* 245:281-289.

45.   Gatel, C., and E. Snoeck. 2007. Epitaxial growth of Au and Pt on Fe_3O_4 (111) surface. *Surf. Sci.* 601:1031-1039.

46.   Gatel, C., and E. Snoeck. 2006. Comparative study of Pt, Au and Ag growth on Fe_3O_4 (001) surface. *Surf. Sci.* 600:2650-2662.

47.   Goodman, S. L., G. M. Hodges, and D. C. Livingston. 1980. A review of the colloidal gold marker system. *Scan. Electron Microsc.* Pt 2:133-146.

48.   Gole, A., C. Dash, V. Ramakrishnan, S. R. Sainkar, A. B. Mandale, M. Rao, and M. Sastry. 2001. Pepsin-gold colloid conjugates: preparation, characterization, and enzymatic activity. *Langmuir* 17:1674-1679.

49.   Oliver, J. A., and R. M. Albrecht. 1987. Colloidal gold labelling of fibrinogen receptors in epinephrine- and ADP-activated platelet suspensions. *Scanning Microsc.* 1:745-756.

50.   Albrecht, R. M., J. A. Oliver, and J. C. Loftus. 1985. Observation of colloidal gold labelled platelet surface receptors and the underlying cytoskeleton using high voltage electron microscopy and scanning electron microscopy. In *The Science of Biological Specimen Preparation*. R. P. B. M. Mueller, A. Boyde, and J. J. Wolosewick, Eds., ed. AMF O'Hare, Chicago. 185-193.

51.   Albrecht, R. M., O. E. Olorundare, S. R. Simmons, J. C. Loftus, D. F. Mosher, and J. H. Jacek. 1992. Use of correlative microscopy with colloidal gold labeling to demonstrate platelet receptor distribution and movement. *Methods Enzymol.* Volume 215:456-479.

52.   Olorundare, O. E., S. R. Simmons, and R. M. Albrecht. 1992. Cytochalasin D and E: effects on fibrinogen receptor movement and cytoskeletal reorganization in fully spread, surface-activated platelets: a correlative light and electron microscopic investigation. *Blood* 79:99-109.

53.   Grouse, L. H., and J. G. White. 1989. Gold-labeled bovine fibrinogen for study of human platelets. *Thromb. Haemost.* 62:1112-1115.

54.   Belitser, N., M. Anischuk, Y. Veklich, T. Pozdnjakova, and O. Gorkun. 1993. Fibrinogen internalization by ADP-stimulated blood platelets. Ultrastructural studies with fibrinogen-colloidal gold probes. *Thromb. Res.* 69:413-424.

55.   Ellis, E. A. 2006. Solutions to the problem of substitution of ERL 4221 for vinyl cyclohexene dioxide in spurr low viscoity embedding formulations. *Microsc. Today* 14:32-33.

56. Holdorf, M. M., H. A. Owen, S. R. Lieber, L. Yuan, N. Adams, C. Dabney-Smith, and C. A. Makaroff. 2012. Arabidopsis ETHE1 encodes a sulfur dioxygenase that is essential for embryo and endosperm development. *Plant Physiol.* 160:226-236.

57. Mürbe, J., A. Rechtenbach, and J. Töpfer. 2008. Synthesis and physical characterization of magnetite nanoparticles for biomedical applications. *Mater. Chem. Phys.* 110:426-433.

58. Sun, J., S. Zhou, P. Hou, Y. Yang, J. Weng, X. Li, and M. Li. 2007. Synthesis and characterization of biocompatible Fe3O4 nanoparticles. *J. Biomed. Mater. Res. Part A* 80:333-341.

59. Krystofiak, E. S., E. C. Mattson, P. M. Voyles, C. J. Hirschmugl, R. M. Albrecht, M. Gajdardziska-Josifovska, and J. A. Oliver. 2013. Multiple morphologies of gold–magnetite heterostructure nanoparticles are effectively functionalized with protein for cell targeting. *Microsc. Microanal.* 19:821-834.

60. Loftus, J. C., and R. M. Albrecht. 1984. Redistribution of the fibrinogen receptor of human platelets after surface activation. *J. Cell Biol.* 99:822-829.

61. Simmons, S. R., P. A. Sims, and R. M. Albrecht. 1997. Alpha IIb beta 3 redistribution triggered by receptor cross-linking. *Arterioscler. Thromb. Vasc. Biol.* 17:3311-3320.

62. Peerschke, E. 1995. Bound fibrinogen distribution on stimulated platelets. Examination by confocal scanning laser microscopy. *Am. J. Pathol.* 147:678-687.

63. Park, K., R. A. Gemeinhart, and H. Park. 1998. Movement of fibrinogen receptors on the ventral membrane of spreading platelets. *Biomaterials* 19:387-395.

64. Vu, T. K., D. T. Hung, V. I. Wheaton, and S. R. Coughlin. 1991. Molecular cloning of a functional thrombin receptor reveals a novel proteolytic mechanism of receptor activation. *Cell* 64:1057-1068.

65. Andersen, H., D. L. Greenberg, K. Fujikawa, W. Xu, D. W. Chung, and E. W. Davie. 1999. Protease-activated receptor 1 is the primary mediator of thrombin-stimulated platelet procoagulant activity. *Proc. Natl. Acad. Sci. USA* 96:11189-11193.

66. Kahn, M. L., M. Nakanishi-Matsui, M. J. Shapiro, H. Ishihara, and S. R. Coughlin. 1999. Protease-activated receptors 1 and 4 mediate activation of human platelets by thrombin. *J. Clin. Invest.* 103:879-887.

67. Turkevich, J., P. C. Stevenson, and J. Hillier. 1951. A study of the nucleation and growth processes in the synthesis of colloidal gold. *Discuss. Faraday Soc.* 11:55-75.

68. Shevchenko, E. V., D. V. Talapin, H. Schnablegger, A. Kornowski, Ö. Festin, P. Svedlindh, M. Haase, and H. Weller. 2003. Study of nucleation and growth in the organometallic synthesis of magnetic alloy nanocrystals: The role of nucleation rate in size control of CoPt3 nanocrystals. *J. Am. Chem. Soc.* 125:9090-9101.

69. Ge, J., Y. Hu, M. Biasini, C. Dong, J. Guo, W. P. Beyermann, and Y. Yin. 2007. One-step synthesis of highly water-soluble magnetite colloidal nanocrystals. *Chem. Eur. J.* 13:7153-7161.

70. Xu, Z., C. Shen, Y. Hou, H. Gao, and S. Sun. 2009. Oleylamine as both reducing agent and stabilizer in a facile synthesis of magnetite nanoparticles. *Chem. Mater.* 21:1778-1780.

71. Cobos Cruz, L. A., C. A. Martínez Perez, H. A. Monreal Romero, and P. E. García Casillas. 2008. Synthesis of magnetite nanoparticles–β-cyclodextrin complex. *J. Alloys Compd.* 466:330-334.

72. Lee, S.-J., J.-R. Jeong, S.-C. Shin, J.-C. Kim, and J.-D. Kim. 2004. Synthesis and characterization of superparamagnetic maghemite nanoparticles prepared by coprecipitation technique. *J. Magn. Magn. Mater.* 282:147-150.

Chapter 4:   Magnetic field-induced hyperthermia on platelets labeled with

fibrinogen-conjugated gold-coated magnetite

Abstract

Hyperthermia has long been recognized as a therapeutic method to eliminate unwanted cells or tissues. Nanoparticle mediated hyperthermia is the use of targeted nanoparticles to target a cell type and then convert an external energy source to localized thermal energy. There has been much interest in development of nanoparticle-mediated hyperthermia for anti-cancer applications. Here we examine the use of nanoparticle-mediated hyperthermia to cause damage to platelets with the intent of developing a novel treatment for ischemic stroke. We developed a system using fibrinogen-conjugated gold-coated magnetite nanoparticles to cause localized hyperthermia on human platelets when exposed to an oscillating magnetic field. Scanning electron microscopy was utilized to analyze hyperthermic damage to surface-activated platelets by directly observing intact and fragmented platelets. Platelet aggregates, which better approximate *in vivo* platelets in blood clots, were generated and treated with fibrinogen-conjugated gold-coated magnetite and exposed to an oscillating magnetic field. Afterwards, the platelets were analyzed by SEM and TEM. We developed a stereological method to estimate the extent of hyperthermia damage to platelet aggregates by estimating the area covered by intact platelets, damaged platelets and platelet-derived debris. Results indicate significantly more dead platelets and debris were present in platelet aggregate samples exposed to the fibrinogen-conjugated gold-coated magnetite than controls in both surface-activated and aggregated platelet systems. Further studies used the aggregate quantification method to optimize magnetic field exposure and dosages of nanoparticles to platelet aggregates. When the damage was quantified it was found that significantly more damage occurred

on platelets treated with fibrinogen-conjugated gold-coated magnetite with OMF

exposure than any other treatment. These results suggest that nanoparticle-mediated

hyperthermia has potential as an ischemic stroke treatment.

Introduction

Therapeutic hyperthermia is a method to disrupt cells of interest by increasing the cellular

temperature 3° C or more (1-4). Most hyperthermia treatments have been primarily

focused on the development of anti-cancer therapy. The effects of hyperthermia were

first characterized over 100 years ago in descriptions of cancer patients who experienced

high fever and subsequently recovered from cancer (5). Raising the temperature of a cell

can have effects on the metabolic balance (6, 7), lipid membrane dynamics and stability

(8, 9), and cytoskeletal arrangement of the cell (10, 11).

The outcome of hyperthermic treatment on cells is based on the ultimate temperature

reached (1, 12), the length of exposure (12, 13), and the cell type(s) exposed (14). A

variety of assays have been used to determine hyperthermia effects on cells, including

examining mitochondrial health using the 3-(4,5-dimethylthiazol)-2-diphenyltertrazolium

bromide (MTT) test (15), measuring apoptosis using the binding of annexin V to

phosphatidylserine (PS), staining with nuclear stains that are not permeable to intact

membranes (2), vital stains that measure cytoplasmic enzyme function (16), or by direct

observation using electron microscopy (4, 9, 13, 16, 17). In treatments using mild

hyperthermia, where cell temperatures are kept below approximately 46° C, cell death is

primarily caused by apoptosis, which is thought to be triggered by a combination of

factors, including disruptions of nuclear function (2, 6, 18), metabolic stress (7), and

disruption of normal organelle structure (4, 19-21). Mild hyperthermia treatments were

observed to disrupt microtubule and actin cytoskeleton localization, causing changes in

cell shape (10). In some cancer lines, mild hyperthermic conditions can trigger a heat

shock response, leading to production of chaperone proteins such as HSP 70 (3). These

chaperone proteins bind to proteins that are highly expressed in cancer cells. When some

of these cells die, they release the chaperone protein in complex with cancer proteins

which can lead to an increased immune response to the tumor (3, 22, 23). In

hyperthermic treatments greater than ~50° C, protein denaturation and membrane damage

become more prominent (2, 24). The damage leads to necrosis and can be directly

observed by TEM where damage to both cellular and organelle membranes is apparent

(25). Increasing the temperature in hyperthermic treatments leads to increased damage to

cancer cells, but at the expense of possibly damaging the surrounding normal tissue as

well.

Hyperthermia can be induced by a variety of methods ranging from relatively simple bulk

heating to quite complex targeted methods. The simplest method of inducing

hyperthermia is by increasing the systematic body temperature, which will cause effects

on every tissue. Systematic hyperthermia can be useful in treating cancer cells, as they

are less likely to tolerate mild temperature increases than normal cells (26, 27). Specific

regions of the body may be heated using heated fluid (28) or radio frequency (RF) tissue

heating (12, 29). However, these types of heating are rather crude and have limited

applications, due to the aforementioned possibility of nonspecific heating of surrounding tissues. It is therefore desirable to target a specific tissue, tumor, or cell type, which for most applications requires a method to produce highly localized heating. Nanoparticle-based heating methods using specific targeting molecules to target a tissue or cell type have been developed (10, 15, 20, 30, 31). These treatments utilize nanoparticles to convert an external energy source into localized heat, creating hyperthermia only in the areas containing nanoparticles. These nanoparticles can transfer energy to cells/tissue by two different means: absorption of infrared light (32-34), or by conversion of RF electric (35, 36) or magnetic fields (37, 38) to heat or kinetic energy.

Photothermal hyperthermia has been developed using gold nanoparticles that absorb light in the near infrared range to generate localized heat. In order to absorb light in the near-infrared range well, gold nanoparticles are synthesized in rod shapes (33), hollow sphere shapes (39) or as SiO_2-gold core-shell-like structures (40). An alternative strategy is to cause typical spherical gold nanoparticles to agglomerate at the site of interest. The nanoparticle aggregation causes an increases in near-infrared light absorption increasing the energy absorbed per unit area (34, 41). Basic protein conjugation procedures, such as non-ionic adsorption, can be used to functionalize the nanoparticles with cell targeting molecules (32, 41). Photothermal therapies work well *in vitro,* but often have limitations *in vivo* due to attenuation of the near-infrared light heating penetration by light scattering and absorption within the tissue (42, 43).

Magnetic induction based nanoparticle hyperthermia treatments have been developed for anti-cancer therapy in which iron oxide nanoparticles are heated by an external magnetic field (44-47). Of particular interest are systems that utilize superparamagnetic magnetite or maghemite to convert an oscillating magnetic field (OMF) into localized thermal energies using the Neel relaxation methodology of heating. The magnetic field used for heating typically oscillates in the order of 100 kHz and has a magnetic field strength in the 1-100 mT range (15, 48, 49). The frequency and power output of the OMF can be produced using relatively simple circuitry, which makes the methodology attractive. For specific cellular targeting, iron oxide nanoparticles may be functionalized with organic molecules or proteins (15, 50-52), or the iron oxide can be coated with gold and then conjugated with protein as discussed previously (Chapter 3).

We have already established a method to specifically target activated platelets using fibrinogen conjugated nanoparticles (Chapters 2, 3). We hypothesize that these nanoparticles can cause structural damage to platelets by localized hyperthermia. Hyperthermic effects on platelets are relatively poorly understood. Platelet activation and aggregation have been found to be inhibited by hyperthermia by decreasing platelet inside-out signaling which prevents platelets from binding fibrinogen (53, 54). Further, hyperthermia conditions inhibit platelet adhesion to surfaces (54), promote ectodomain shedding of glycoprotein Iα (53), inhibit platelet α-granule release (54), and cause PS expression on the outer leaflet of the platelet membrane (53). Whole body hyperthermia causes a reduction in platelet counts (55, 56) which has been attributed to platelet aggregate formation and adhesion (55), which is peculiar in light of the reports of

decreased platelet aggregation and adhesion following *in vitro* hyperthermia (53, 54).

These studies examined platelet hyperthermia as a pathological condition rather than a

possible treatment for ischemic stroke. Our interest is primarily in disrupting pre-existing

platelet structure to dissolve blood clots rather than producing systemic effects on platelet

aggregation and adhesion.

In these studies, we examine whether fibrinogen-based targeting previously described

(Chapter 2) using the gold-coated magnetite nanoparticles previously developed (Chapter

3) will cause structural damage to platelets by magnetic field-induced hyperthermia.

Differences between platelets and typical cancer cells may cause them to respond quite

differently to hyperthermic conditions. Mammalian platelets lack a nucleus and much of

the eukaryotic cellular machinery found in nucleated cells. Additionally, platelet

activation and apoptosis pathways are similar, both leading to PS expression on the outer

leaflet of the platelet membrane (57-59). For hyperthermia-mediated restoration of blood

flow following an ischemic stroke event, disruption of platelet integrity must occur in a

way in which the blood clot becomes structurally weakened and breaks apart. We

examined the effects of nanoparticle-mediated hyperthermia on two platelet systems.

First, we used the surface-activated platelet system to characterize hyperthermic damage

and quantify platelet damage. We then examined the aggregated platelet system to better

understand how hyperthermia is likely to affect blood clots *in vivo*.

Materials and Methods:

Platelet preparation:

Whole blood was obtained from healthy adult volunteers in accordance with the

University of Wisconsin – Milwaukee Institutional Review Board. Gel-filtered platelets

were obtained as described previously (Chapter 2).

Fibrinogen-conjugated gold-coated magnetite synthesis:

Magnetite and gold-coated magnetite were synthesized and conjugated to fibrinogen as

previously described (Chapter 3). Colloidal gold was similarly synthesized and

conjugated to fibrinogen as previously described (Chapter 2).

Oscillating magnetic field device:

A custom made OMF device was built using a basic LC (resonant) circuit. The circuit

consists of a hand-wound inductor connected as an autotransformer paired with a set of

fixed capacitors in series and a parallel variable air dielectric capacitor. The system was

powered by an AG Series 1024 RF amplifier (T&C Power Conversion, Rochester, NY)

using the internal signal generator of the amplifier to produce a 500 kHz waveform using

internal power output control to reach the desired field amplitude.

The inductor was built by winding 3.175 mm diameter copper tubing (Phillips and

Johnston, Glen Ellyn, IL) around a 5 cm diameter glass cylinder for a total of 50 turns.

Several coils were produced using different methods of electrical insulation. Early coils

utilized paper flags between each turn to prevent short circuiting. Later coils were coated by a layer of Formvar in addition to paper flags. These coil insulations proved to be vulnerable to high temperatures and were ultimately replaced by wrapping the copper in vinyl tape. The coil was cooled by running cold tap water through the copper tubing, preventing excessive heating of the inductor coil during operation.

The OMF circuit was tuned using a BK Precision 4017B signal generator (Yorba Linda, CA) producing a 5 volt sinusoidal wave at 500 kHz. The voltage drop between the set of capacitors was recorded as shown in Figure 33. The tap position for the autotransformer was selected where the voltage drop was 50% when the variable capacitor was at 50% maximal capacitance, giving the highest possible power transfer function. Tuning was further refined by varying the variable capacitor when the circuit was powered by the RF amplifier at 10 watt forward power. Optimal tuning was achieved when reflected power could no longer be detected. The magnetic field produced by the OMF device was measured using a 1 cm^2 area wire placed within the coil. The potential across the wire was measured with a BK Precision 2125A analog oscilloscope. The following equation used to calculate the magnetic field:

$$B = E/(2 * \pi * f * A)$$

Where B is the magnetic field produced, E is the potential across the copper loop, f is the frequency of the OMF, and A is the area of the copper loop.

Oscillating magnetic field heating:

The amount of heat generated by magnetite nanoparticles was measured by placing 100 μL drops of a 100-fold concentrated magnetite nanoparticle stock solution into a calorimeter. In a second chamber, a 100 μL drop of ddH_2O was placed to serve as a control for non-specific heating. A calibrated T-type thermocouple was positioned in each well, and an initial reading was taken with a CEN-TECH digital multimeter (Harbor Freight, Camarillo, CA). The samples were exposed to a 500 kHz, 8 mT OMF for 3 minutes and a second temperature reading was taken. The OMF system produced too much electronic noise to allow accurate heating measurements during operation. Gold-coated magnetite nanoparticles could not be sufficiently concentrated to accurately measure nanoparticle heating.

Temperatures of the inductive coil and non-magnetic samples were measured using a CEN-TECH infrared thermometer (Harbor Freight) pointed directly at the source being measured during OMF operation. With cold tap water cooling the system, these temperatures never exceeded 38°C, and therefore the OMF device was not considered to contribute to nonspecific sample heating.

Surface-activated platelet hyperthermia:

Gel-filtered platelets were supplemented with 2 mM Ca^{2+} and allowed to adhere to 300 mesh Formvar coated nickle grids for 10 minutes. The surface-activated platelets were labeled with fibrinogen-conjugated gold-coated magnetite or gold, or left unlabeled in Tyrode's buffer for 10 minutes. Unbound labels were washed away by dunking the grids

in excess Ca^{2+}-supplemented Tyrode's buffer, then washed 3 times by incubating the grids on successive 10 μL drops of Tyrode's buffer for 5 minutes. Samples exposed to the OMF were floated on 20 μL drops of Tyrode's buffer and exposed to an 8 mT OMF operating at 500 kHz for 5 x 2.5 minute cycles with 30 seconds between cycles. Negative controls receiving no magnetic field exposure were kept away from the OMF. After magnetic field exposure, samples were fixed in 1% glutaraldehyde in 0.1 M HEPES, pH 7.3 for 30 minutes. Samples were washed in HEPES and post-fixed in 0.05% OsO_4 in HEPES for 15 minutes. Samples were dehydrated in a graded ethanol series and brought through the critical point drying process. The grids were mounted onto SEM stubs with carbon tape and sputter coated with 2 nm Ir using an EMITech K575X sputter coater (Ashford, Kent, United Kingdom).

Samples were analyzed using a Hitachi S-4800 SEM (Dallas, TX) operating at 1 kV for secondary electron (SE) and 30 kV for backscattered electron (BSE) imaging. For hyperthermia quantification studies of surface-activated platelets, 5 fields of platelets centered between grid bars were imaged at randomly generated coordinates at 1,000 x magnification for each sample. The number of intact and fragmented platelets was determined for each field by examination of the structure of the platelets. Platelets with continuous membranes displaying no holes and normal platelet morphology were scored as intact. Platelets showing obvious structural damage or membranes with large tears were scored as fragmented. The percent of fragmented platelets was calculated per field and then averaged with the other fields of the sample. Significance between treatments was determined by Student's *t*-test comparing percent platelet fragmentation averaged

from all fields in a sample from 7 experiments, which had 5 unique blood donors and 7

unique nanoparticle batches.

Aggregated platelet hyperthermia:

Gel-filtered platelets were adjusted to 200,000 platelets/μL and supplemented with 2 mM

Ca^{2+} and 200 μg/mL unconjugated fibrinogen. The platelets were aggregated using 67

μM SFLLRN-NH$_2$ in the 24-well microtiter plate system or in an aggrogometer as

described previously (Chapter 2). Samples were labeled for 5 minutes post-aggregation

with fibrinogen-conjugated, gold-coated magnetite or fibrinogen-conjugated colloidal

gold.

In most experiments, aggregated samples were exposed to a 500 kHz OMF at 8 mT for

30 minutes. In experiments analyzing the time of exposure to the magnetic field, samples

were treated between 0 and 60 minutes.

For TEM studies, samples were fixed in 1% glutaraldehyde, 1% tannic acid in 0.1 M

HEPES, pH 7.3 for 1 hour at room temperature and then at 4°C overnight. Samples were

washed three times in HEPES by centrifugation and embedded in a drop of 1% agar

(Difco, Detroit, MI) prepared in 0.1 M HEPES. Equal volumes of warm agar and cold

platelet samples were combined in small TEM embedding molds. Samples were

postfixed *en bloc* in 0.05% OsO$_4$ for 30 minutes, washed 3 times in ddH$_2$O, and *en bloc*

stained in 1% uranyl acetate for 1 hour. Samples were dehydrated in a graded ethanol

series and then transferred to propylene oxide. Samples were infiltrated with low

viscosity Spurr's resin (60) but substituting the accelerant N,N-dimethylbenzylamine with 2(dimethylamino)ethanol (61). Ultrathin pale gold or silver sections were taken using an RMC MT-7000 ultramicrotome and sections were stained with 1% uranyl acetate. The sections were imaged at 75 kV using an Hitachi H-600 TEM (Dallas, TX).

For both qualitative and quantitative SEM studies, the aggregated samples were diluted 1:20 in 1% glutaraldehyde in 0.1 M HEPES, pH 7.3 and fixed for 30 minutes at room temperature. Platelets were collected onto 0.4 μm Nuclepore membranes and postfixed in 0.05% OsO_4 for 15 minutes. Samples were dehydrated in ethanol and brought through the critical point drying process. Samples were sputter coated with 2 nm Ir using an EMITech K575X sputter coater. Micrographs were taken using an Hitachi S-4800 SEM operating at 1 kV for SE and 30 kV for BSE imaging.

For quantitative analysis of hyperthermic damage of platelet aggregates, 5 fields of platelet aggregates on Nuclepore membranes were taken at 2000x magnification at random coordinates. The following criteria were established for including a field in the statistical analysis: 1) At least 50% of the field must contain platelets or platelet-derived debris; 2) the field must be mostly free of non-platelet debris (e.g. plastic shavings); and 3) the field must not overlap with a previously examined field. Fields were analyzed by point counting, with the estimated area covered by intact platelets, disrupted platelets, and platelet-derived debris (i.e. debris that no longer resembles a platelet) scored separately. To determine the number of sampling points required to accurately assess a field of view the entire area of several micrographs were quantified at a single pixel level.

The micrographs were then sampled using the point counting system, increasing the number of sampling points until the accuracy of the stereological method did not increase. It was found that 140 evenly distributed points counted on every field could provide accurate estimates. Points per field were scored and summarized for each treatment. The ratio of intact platelets to the sum of disrupted platelets and platelet-derived debris from each field were combined into a single sample mean for each sample which was used for statistical analysis. ANOVA, including models in which different variables were tested for their contribution to overall significance by defining them as fixed effects, was performed using the PROC MIXED procedure in SAS (SAS Institute, Cary, NC).

Results

Oscillating magnetic field heating of magnetite nanoparticles:

The OMF device was evaluated for use in heating the magnetite nanoparticles previously described (Chapter 3). Non-specific heating caused by electrical resistance in the inductive coil was removed by running cold tap water through the hollow induction coils. The temperature of the induction coil and nonmagnetic ddH$_2$O was measured by infrared thermometer, which could sample temperatures while the OMF was running, during a typical 2.5 minute OMF cycle at 8 mT power (Figure 34A). Coil temperature never exceeded 38°C. The sample temperature never exceeded 25°C under normal cooling conditions. When the pressure of the cooling water was increased to water mains pressure, the sample temperature was modestly reduced below normal cooling.

Heating of magnetic samples was measured in a calorimeter consisting of two TEM

embedding wells with T-type thermocouples that was constructed in-house (Figure 34B).

Thermocouples measure temperatures of small volumes of liquid more accurately than an

infrared thermometer, but do not function well with the electrical noise generated during

OMF operation. Inductive heating of magnetite nanoparticles could be measured by

concentrating the magnetite 100-fold and placing 100 μL in one well, while 100 μL

ddH$_2$O was placed in the other well as a control for non-specific heating. As described

previously (Chapter 3), batches of magnetite synthesized through aqueous coprecipitation

had variable properties. The level of OMF-induced inductive heating varied between

batches of magnetite and appeared correlated with the ability of those magnetite batches

to be coated with gold. Batches of magnetite that could be coated with gold typically

heated 5° to 10° C over the ddH$_2$O control (Figure 34C). Magnetite samples that failed to

coat with colloidal gold displayed a much larger range of possible final temperatures.

Only magnetite that could be coated with gold was used for further evaluation of

hyperthermia.

Magnetic field-induced hyperthermia on surface-activated platelets:

Surface-activated platelets were used as an initial model to test fibrinogen-conjugated,

gold-coated magnetite hyperthermia treatments. Platelets were allowed to surface

activate on Formvar coated TEM grids, then were labeled with fibrinogen-conjugated

gold-coated magnetite. Negative control platelets were labeled with non-magnetic

fibrinogen-conjugated colloidal gold or buffer. Samples were exposed to the OMF or

kept out of range of the OMF and then analyzed by SEM. Platelet controls labeled with colloidal gold with or without OMF exposure displayed the typical morphology and fibrinogen labeling pattern of surface-activated platelets observed previously (Chapters 2, 3) (Figures 35A, 35B). Similarly, platelets labeled with fibrinogen-conjugated gold-coated magnetite without OMF exposure displayed the same morphology and labeling pattern (Figures 35C, 35D) observed previously (Chapter 3). Platelets labeled with fibrinogen-conjugated, gold-coated magnetite nanoparticles and exposed to the OMF showed markedly different morphology. Many platelets exhibited fragmentation where the membrane of the platelet was significantly disrupted (Figure 36). In some damaged platelets, pieces of cellular membrane remained while the majority of the intracellular contents of the platelets appear to have leaked away leaving behind holey or non-continuous cell membrane (Figure 36A, 36B). While many platelets were damaged, other seemingly well-labeled, yet intact, platelets were often found near extremely fragmented platelets (Figures 36C, 36D).

The amount of damage caused by hyperthermia was quantified by comparing the number of intact healthy-looking platelets to that of fragmented platelets in low magnification fields (Figures 37A, 37B). Scoring across multiple fields and multiple experiments (n = 7) revealed that all control samples had nearly the same level of platelet fragmentation, which can be considered to represent a background level. Unlabeled platelets with or without OMF exposure had $22 \pm 6\%$ and $23 \pm 7\%$ fragmentation, respectively, demonstrating that exposure to the OMF has no effect independent of labeling ($p = 0.31$). Colloidal gold-labeled platelets exhibited $23 \pm 9\%$ fragmentation when exposed to the

OMF and 23 ± 6% in the absence of OMF exposure, demonstrating that labeling alone is insufficient to produce an OMF effect (p = 0.84). However, labeling with gold-coated magnetite and exposure to the OMF produced significantly more fragmented platelets (58 ± 6%) than was seen in the absence of OMF exposure (23 ± 6%, p < 0.01). In fact, gold-coated magnetite plus OMF exposure produced significantly more platelet damage than any other labeling/treatment combination tested (Figure 37C).

Magnetic field-induced hyperthermia on aggregated platelets:

The surface-activated platelet system provided a relatively simple method of analyzing the effects of gold-coated magnetite labeling plus OMF exposure on platelets. However, surface-activated platelets only represent a minority of the platelet population in an *in vivo* blood clot. To better approximate the effect of fibrinogen-conjugated, gold-coated magnetite nanoparticles on a blood clot, hyperthermia treatment was performed on preformed platelet aggregates produced with unconjugated fibrinogen.

To form aggregates, gel-filtered platelets were supplemented with unconjugated fibrinogen, stirred, and stimulated with 67 μM SFLLRN-NH$_2$, then labeled with fibrinogen conjugates and exposed to the OMF. Control samples labeled with fibrinogen-conjugated colloidal gold (Figure 38A) or fibrinogen-conjugated, gold-coated magnetite (Figure 38B) without OMF exposure showed the typical morphology observed with aggregated gel-filtered platelets (Chapter 2). Additional controls that were exposed to the OMF after incubation with unconjugated fibrinogen (Figure 38C) or fibrinogen-conjugated colloidal gold (Figure 38D) showed similar morphology to control samples

that did not receive OMF exposure. All negative controls displayed little damage on the surface of the platelet aggregate. However, platelet aggregates treated with fibrinogen-conjugated, gold-coated magnetite and exposed to the OMF often displayed obvious structural damage (Figures 38E, 38F). Platelets within the aggregate had disrupted membranes with tears or holes present. Interestingly, other areas of the same platelet aggregates often had a normal appearance, which demonstrated heterogeneous effects caused by hyperthermia on the same platelet aggregate.

The damage caused by hyperthermia to platelet aggregates labeled with gold-coated magnetite and exposed to the OMF was further examined by SEM at higher magnification to better understand platelet damage and nanoparticle localization. Aggregates with obvious structural damage were examined using SE imaging to characterize damage (Figure 39A) and BSE imaging to localize gold-coated magnetite (Figure 39B). Closer examination of damaged areas in platelet aggregates showed areas where platelet membranes appeared ruptured and the internal contents of the platelets were visible, including the cytoskeleton. Many apparently intact platelets found near the obviously damaged platelets had more subtle membrane damage such as small holes (Figure 39C) that were only visible at higher magnification. Large amounts of bound gold-coated magnetite were observed in the areas where obvious damage occurred to the platelet membranes.

The internal areas of treated platelet aggregates were examined by TEM to observe damage in areas not easily analyzed by SEM. Platelet aggregates labeled with

fibrinogen-conjugated colloidal gold in the absence (Figure 40A) or presence (Figure 40B) of OMF exposure displayed morphologies and labeling patterns similar to those previously described (Chapters 2, 3). Platelet aggregates treated with fibrinogen-conjugated, gold-coated magnetite but not exposed to the OMF displayed the same labeling pattern and morphology as previously described (Chapter 3) (Figure 40C), and appeared quite similar to the colloidal gold labeled aggregates. Platelet aggregates labeled with fibrinogen-conjugated, gold-coated magnetite and exposed to the OMF often had internal damage centered around areas with the highest nanoparticle concentration (Figure 40D). The damaged areas have disrupted ultrastructure, making interpretation of the damage difficult. It appears that the nanoparticles can disrupt the platelet membrane, and by extension the open canalicular system (OCS) membrane. Disruption of the membrane lead to areas where the cytoplasmic contents of the platelet were partially released. In gold-coated magnetite labeled platelets exposed to the OMF, there were areas within the platelet aggregate that had less nanoparticle labeling and appeared to have normal ultrastructure similar to controls. TEM analysis was also performed on string-like debris only observed in gold-coated magnetite labeled samples treated with the OMF (Figure 41A, 41B). These membrane fragments appear to be derived from labeled platelet membranes. The fragments were often heavily decorated with fibrinogen-conjugated nanoparticles and appeared to still contain some associated material from the cytoplasm (Figure 41B).

Quantification of hyperthermic damage:

Quantification of hyperthermic damage in the aggregated platelet system presents a unique challenge. Platelet aggregates are not discrete entities, but rather each consists of many individual platelets, not all of which will be analyzed at one time by SEM. Initial attempts to quantify damage to platelet aggregates were made using vital fluorescent dyes, such as calcein-AM which measures esterase activity in the platelet cytoplasm. These attempts were unsuccessful due to quenching of the fluorescent signal by colloidal gold and gold-coated magnetite (not shown). It became necessary to develop a system to quantify hyperthermic damage using a method that could directly observe the damage. A system to quantify the area of intact platelets, fragmented platelets, and platelet-derived debris was developed using SEM and a stereological point counting method. To validate the method, a set of hyperthermic experiments were performed using platelets from three blood donors. Platelets from each blood donor were treated with three different preparations of gold-coated magnetite to examine the effects of OMF, blood donor, and nanoparticle batch on hyperthermia. Multiple low magnification fields of platelets labeled with fibrinogen-conjugated gold-coated magnetite, colloidal gold, or unlabeled aggregates and exposed or unexposed to the OMF were imaged and quantified. Examples of platelet aggregates labeled with fibrinogen-conjugated, gold-coated magnetite with or without OMF exposure are shown in Figure 42A and Figure 42B, respectively. Qualitatively, the gold-coated magnetite plus OMF sample exhibited platelet damage and had large quantities of platelet-derived debris visible.

Statistical analysis was performed on the assembled data set to test for the significance of nanoparticle type, OMF exposure, gold-coated magnetite batch, and blood donor on damage to platelet aggregates. Data were analyzed by defining either the points scored as intact platelets, fragmented platelets, platelet-derived debris, (fragmented platelets + debris), or the ratio of intact platelets over (fragmented platelets + debris) as dependent variables. The ANOVA model that agreed best with the data generated in the surface-activated platelet system (Figure 37) used the ratio of intact platelets over (fragmented platelets + debris) as the dependent variable (Table 1), showing differences due to the type of label used (none, gold, gold-coated magnetite) and the OMF (present or absent), but no significance due to the batch of gold-coated magnetite nanoparticles or blood donor. For ease of comparison to the surface-activated platelet system, the ratio of intact platelets over (fragmented platelets + debris) was converted to a percentage and plotted (Figure 42C). A large increase in fragmented platelets and debris was observed in aggregates treated with gold-coated magnetite and OMF exposure, as compared to all other treatments, which did not show significant differences from one another.

Refinement of treatment parameters for platelet aggregate hyperthermia:
After validating the method to quantify hyperthermic damage to platelet aggregates, it became possible to refine hyperthermia conditions. The effects of length of exposure to the OMF were determined using the same quantification method, which used the ratio of intact platelets to (fragmented platelets + debris) as the dependent variable for statistical analysis. Samples were incubated for times ranging from 0 to 60 minutes in the OMF. All samples were fixed after 60 minutes regardless of OMF exposure time. Increasing

length of exposure to the OMF produced greater damage to platelets labeled with fibrinogen-conjugated gold-coated magnetite (Figure 43A). OMF exposure to platelet aggregates treated with fibrinogen-conjugated colloidal gold did not increase damage above the background level observed in samples that were not exposed to the OMF. Optimal treatment time appeared to be near the 30 minute exposure time point, with no further significant increases in damage detected after 20 minutes.

Nanoparticle dosage was evaluated in a similar manner. Samples of $4 * 10^7$ platelets were aggregated and labeled with different amounts fibrinogen-conjugated, gold-coated magnetite ranging from approximately $3.8 * 10^{10}$ nanoparticles (0.625% of the total reaction volume) to $1.2 * 10^{12}$ nanoparticles (20% of the total reaction volume). The resulting ratio of nanoparticles to platelets ranged from a minimum of approximately 950 nanoparticles/platelet to a maximum dose of $3 * 10^4$ nanoparticles/platelet. As in previous studies hyperthermic damage was observed only in samples treated with fibrinogen-conjugated gold-coated magnetite and exposed to the OMF. Gold-coated magnetite-treated samples without OMF exposure, samples labeled with fibrinogen-conjugated colloidal gold with or without OMF exposure, and no label controls with or without OMF exposure all displayed the same baseline level of platelet fragmentation. Hyperthermic damage increased with increasing dosage of nanoparticles until a dose of $3 * 10^{11}$ nanoparticles ($7.5 * 10^4$ nanoparticles/platelet) was reached (Figure 43B). Further increase in the nanoparticle dose did not produce a significant increase in observed hyperthermic damage.

Discussion

Fibrinogen-conjugated, gold-coated magnetite nanoparticles were evaluated for

hyperthermic based anti-platelet therapy. While hyperthermic effects on cancer cells have

been extensively studied, much less is known about platelet hyperthermia. We described

platelet hyperthermia, showing that it primarily affects the platelet membrane by causing

holes or tears, leaving internal areas of the platelet exposed. This was observed in both

the surface-activated and aggregated platelet systems. Hyperthermic damage was only

observed in platelets treated with targeted magnetite-containing nanoparticles and

exposed to an OMF. The hyperthermic damage was quantified using SEM to count the

damaged platelets or to estimate the sample area containing damaged platelets.

Quantification was later used to refine the hyperthermic conditions and increased

structural damage to platelets labeled with fibrinogen-conjugated gold-coated magnetite

and exposed to the OMF.

Basic hyperthermia components:

Magnetic field-induced hyperthermia would not be possible in our system without two

key components, an OMF generator and magnetic nanoparticles that can respond to the

OMF. Our lab-built OMF device was able to produce a 500 kHz, 8 mT magnetic field

while maintaining temperatures that will not cause non-specific hyperthermia. Specific

heating (*i.e.* temperature increase over the ddH_2O control) of concentrated magnetite

nanoparticles that were capable of being coated with gold was between 5° to 10° C when

exposed to the OMF for 3 minutes. The temperature increase initially appears modest,

but takes on greater significance when interpreted in the light of the fact that relatively few nanoparticles are heating bulk water temperature. Nanoparticles in contact with a cell surface are likely to transmit localized temperature increases far greater than what is observed in bulk heating. For hyperthermic applications, only localized heating is desired, and the heating we observed is expected to be sufficient.

Hyperthermic damage:

Hyperthermic damage was observed on surface-activated and aggregated platelets labeled with fibrinogen-conjugated gold-coated magnetite and exposed to the OMF. Interestingly, fragmented platelets were often found in the vicinity of healthy platelets. These platelets did not display any hyperthermic damage despite being exposed to identical conditions and residing mere μm away from fragmented platelets. The healthy platelets may not have bound as many nanoparticles or had different nanoparticle binding patterns that did not efficiently promote damage. One possibility is that nanoparticles did not become concentrated in the OCS of platelets that displayed little damage. Even in the platelet surface-activated system, some platelet OCS often remains and becomes heavily labeled with fibrinogen conjugated-nanoparticles (62, 63). A second possibility is that in our gold-coated magnetite synthesis, a sub-population of gold-coated magnetite nanoparticles is produced that is more capable of causing hyperthermia than rest of the population. Only platelets that bound enough of the "high damage" nanoparticle population would display significant damage, while other platelets are left intact. A third possibility is that the intact platelets observed are damaged in a subtle manner that we cannot easily detect by SEM. Hyperthermic membrane damage can appear subtle in

other cell types (13). Irrespective of the intact platelet population, many fragmented platelets were observed in the gold-coated magnetite with OMF treatment group, confirming that this method can be used to destroy at least some appropriately labeled platelets.

Hyperthermia primarily appeared to affect the integrity of the platelet membrane, leading to bulk loss of membrane or development of holes. This fits well with expected damage localization as every targeted gold-coated magnetite nanoparticle being heated is in close vicinity to the platelet membrane, either on the surface of the platelet or within the OCS which is still continuous with the outside of the platelet. In platelet aggregates, damage observed by SEM was primarily on the surface of the aggregates, but was also seen in internal portions of the aggregate by TEM. It is expected that much of the platelet aggregate damage is unobserved by SEM because the majority of nanoparticles are within the aggregate interior at platelet/platelet junctions or in the OCS.

Severe membrane damage had the secondary effect of causing cytoplasmic contents to leak out and to expose the platelet cytoskeleton to the extracellular environment. The loss of membrane integrity and weakening of cytoskeletal elements should reduce the structural integrity of platelets in an aggregate or participating in a blood clot, which is promising for the ultimate goal of disruption of a blood clot in an ischemic stroke. However, the release of platelet cytoplasm, pieces of platelet membrane, and exposure of polymerized actin filaments could increase inflammation levels at the blood clot site or downstream from the newly cleared occlusion site (64-67). This could result in new

occlusions, essentially causing another ischemic event. Further testing of the

prothrombotic molecules released by platelets during hyperthermia and testing the murine

in vivo system will help determine the levels of inflammation expected to arise as a

consequence of treatment.

Quantification of hyperthermic damage to platelets:

Platelets treated with nanoparticles present a difficult system for quantitative analysis of

cellular death due to a combination of platelet physiology and nanoparticle physics.

Many techniques used to study apoptosis or necrosis are ineffective at probing platelet

health. Mammalian platelets lack a nucleus, leading nuclear stains to only label the

mitochondria in platelets, limiting their potential utility. PS in most healthy cells is

confined to the inner leaflet of the cellular membrane, but moves to the outer leaflet

during apoptosis. However, PS is expressed on the platelet outer membrane leaflet

during activation. Our fibrinogen targeting methodology is designed to specifically target

activated, therefore PS-positive platelets, making PS detection an ineffective method to

quantify platelet damage. Perhaps the most confounding complication to analysis of

platelet death in our system is the ability of nanoparticles containing gold to quench

fluorescent signals both at the peak abosrption of gold nanoparticles (*i.e.* green

fluorochromes) and in areas where gold nanoparticles have weak absorption (*i.e.* red

fluorochromes). The quenching appeared to be caused by the sheer number of

nanoparticles binding to each platelet, effectively blocking the fluorescent signal. These

complications prevented us from using many commonly employed fluorescent assays for

apoptosis and necrosis.

We addressed the difficulty in measuring platelet damage by directly observing the treated samples using electron microscopy. The surface-activated platelet system was a relatively simple analysis approach, as platelets could be individually counted as intact or fragmented, making data collection fairly straightforward. The aggregated platelet system was more difficult to analyze. Platelet aggregates are not discrete units, but rather, are highly integrated collections of individual platelets, making quantitative analysis of damage difficult. We found the best way to characterize the damage was by estimating the area of the aggregated samples that contained intact platelets, fragmented platelets, and platelet-derived debris by point counting images of the filter membranes. Analyzing the effect of hyperthermia treatments on aggregated platelets using the ratio of intact platelets to (fragmented platelets + debris) provided a number of advantages. This ratio best accounted for the empty area of the membrane which was not otherwise counted. The results of this analysis mirrored those of the surface-activated platelet system, and also agreed well with the expectations based on our extensive experience with human platelet aggregation and the performance of many batches of nanoparticles. This method was validated by studying the effects of nanoparticle type, OMF exposure, blood donor, and batch of gold-coated magnetite on the level of intact platelets, fragmented platelets, and debris. The effects of nanoparticle type and OMF conditions greatly affected platelet fragmentation. Blood donor and the batch of gold-coated magnetite did not contribute significantly to the biological effect. However, their contributions approached significance, suggesting they may have some effect on the

trends observed for hyperthermia treatment. This is not surprising, given that both parameters carry a great deal of inherent variability.

Improvements to hyperthermia treatment:

Aggregate quantification allowed us to refine the hyperthermia treatment in a quantifiable manner. Optimal exposure time was found to be around 30 minutes, in agreement with other hyperthermic studies on different cell types (10). Nanoparticles containing magnetite likely gradually increase their temperature in response to the OMF until they reach a maximum. This heat is transferred to the nearby membrane causing localized damage to the cell. Heat transfer is cumulative, meaning nanoparticles in close proximity to one another can probably create a higher temperature, more quickly at a specific location than isolated nanoparticles. After that localized damage has occurred, further damage to the cellular surface is unlikely, meaning longer exposures to the OMF will not produce further damage. Hyperthermic damage to aggregated platelets was dependent on the concentration of fibrinogen-conjugated, gold-coated nanoparticles. By varying the dosage of nanoparticles per platelet through two orders of magnitude, it was possible to observe a clear difference between low dosages and high dosages of nanoparticles. The highest dose of nanoparticles tested approaches the estimated $4*10^4$ copy number of $\alpha_{IIb}\beta_3$ present on platelet surfaces (68-70). This makes sense given the higher dosages did not produce a significantly greater response, likely because the receptors were saturated by both the nanoparticle conjugate and competing unconjugated fibrinogen in solution.

Implications for in vivo development:

Fibrinogen-conjugated gold-coated magnetite appears suitable for further development in a murine *in vivo* model of arterial thrombosis. The nanoparticles in combination with the OMF treatment were capable of causing structural damage to platelet aggregates in a manner that may dissolve blood clots. Several important factors need to be considered for *in vivo* development: first, no ferro- or ferri-magnetic objects may be in the coil during operation, limiting options for murine temperature control. Further, dosing the mouse with enough nanoparticles to cause therapeutic effects may be difficult. For the maximum nanoparticle dose used *in vitro*, 20% of the entire reaction volume was the soft pellet of nanoparticles. Injection of large amounts of conjugated nanoparticles into the vasculature at once may cause inflammation or hemostatic problems, potentially systemically. It is also likely that not all the nanoparticles will reach the blood clot. Despite these concerns, tests of *in vivo* treatment to evaluate platelet hyperthermia as potential ischemic stroke therapy should be pursued.

Figures and Figure Legends:

Figure 33. Design of the oscillating magnetic field device. (A) shows the design of the device as viewed from the side. The inductor coil is seen on the left size of the image partially coated in vinyl tape. Coming off the inductor are copper conduction plates and water cooling lines. A set of capacitors in series is in the middle of the device and is in parallel with a variable capacitor on the right. The circuit is energized by the RF power amplifier below the circuit. Tuning is performed using the indicated oscilloscope and signal generator. During operation, the device is enclosed in a protective plexiglass box (not shown). The circuit diagram for the device is shown in (B), arrows indicate where the voltage drop is measured during tuning.
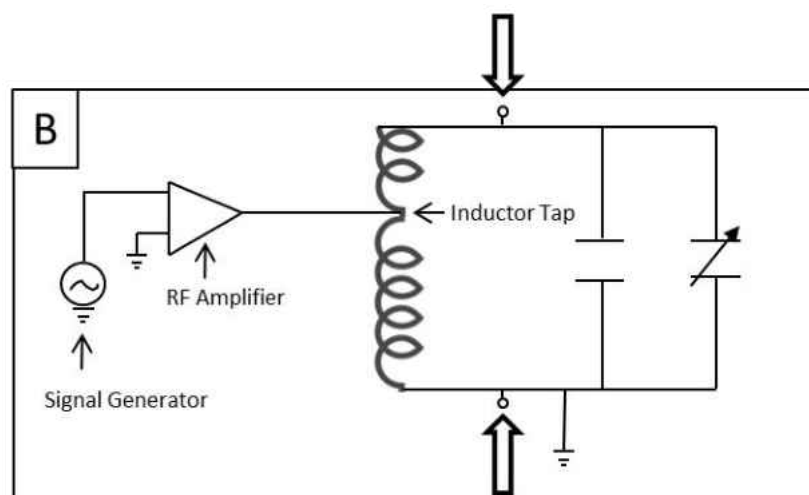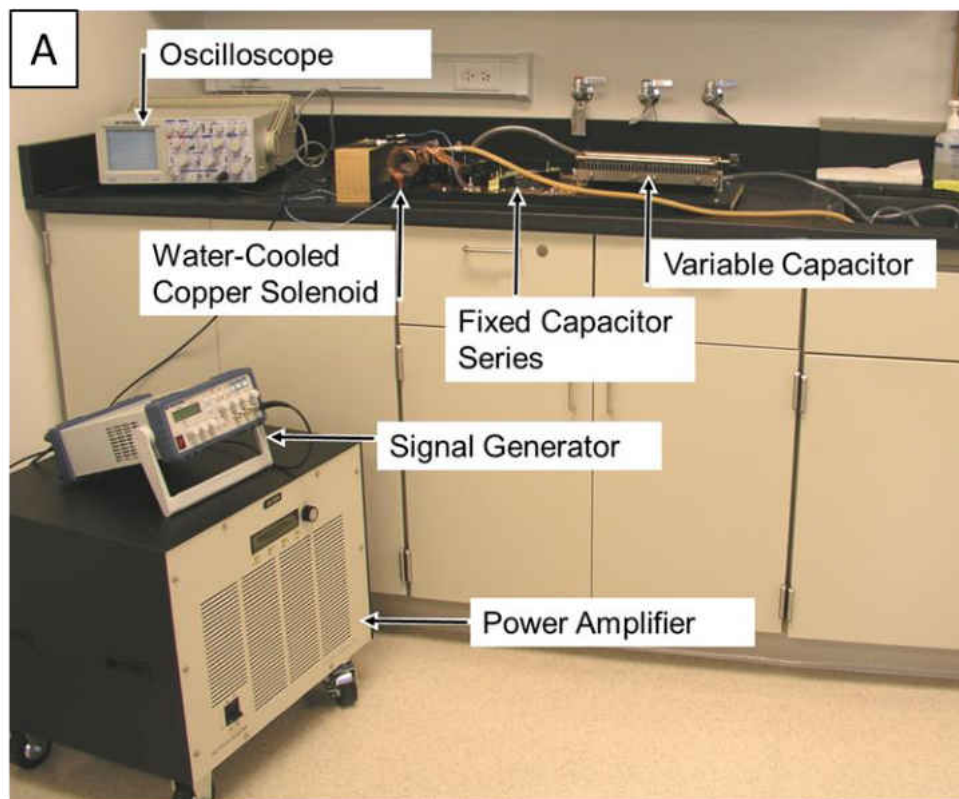
Figure 33

Figure 34. Temperature profiles of samples during OMF operation. (A) the localized temperature of a non-magnetic sample during operation of the OMF under normal cooling (squares), under maximum cooling (diamonds), and the measured temperature of the inductive coil during OMF cycled operation (trigangles). Dashed lines indicate the end of the on/off portion of the OMF cycle. (B) shows the calorimeter used to measure nanoparticle heating within the OMF. The right well is loaded with magnetite nanoparticles, the left well is loaded with ddH$_2$O which acts as a non-specific heating control. Thermocouples are visible leading into each well. A plot of the temperature increase over ddH$_2$O control of 23 batches of magnetite nanoparticles after 3 minutes of OMF exposure is shown in (C). Magnetite nanoparticles that were successfully coated with gold and subsequently produced platelet damage are indicated as diamonds. Magnetite nanoparticles that failed to coat with gold or failed to produce platelet damage are indicated as squares.
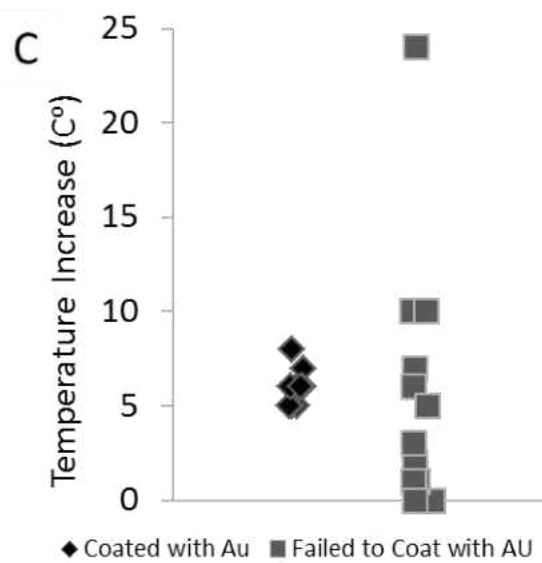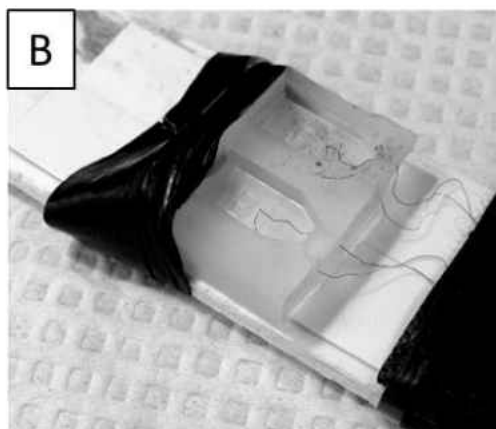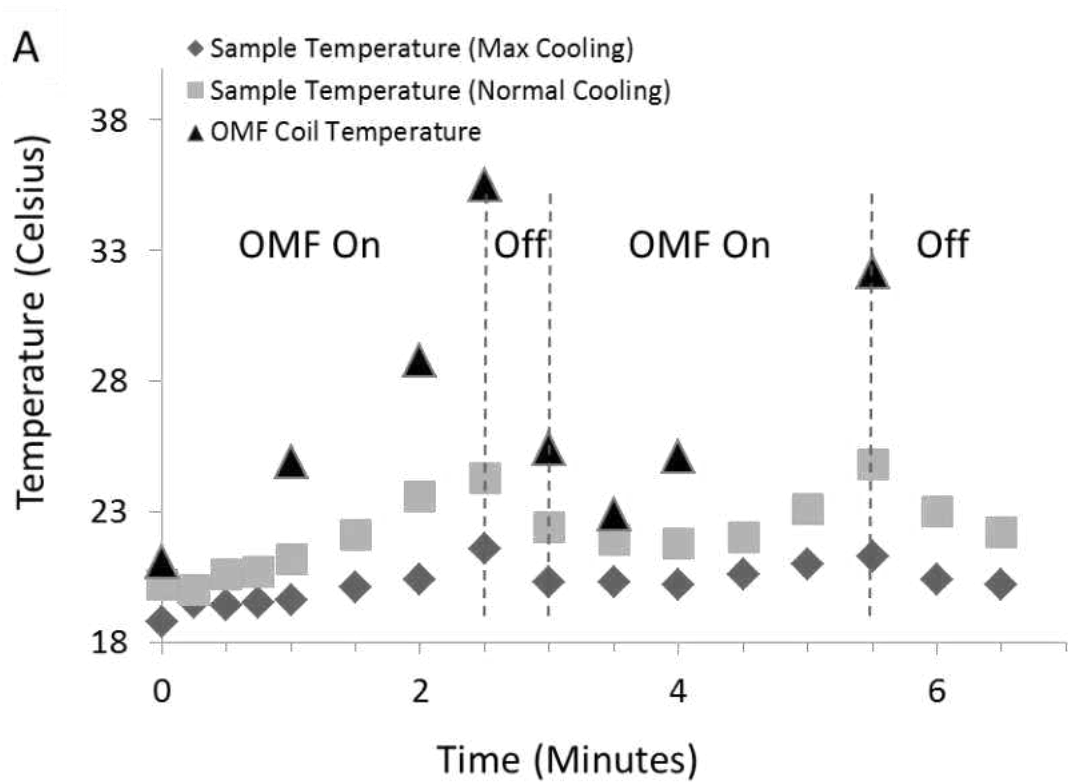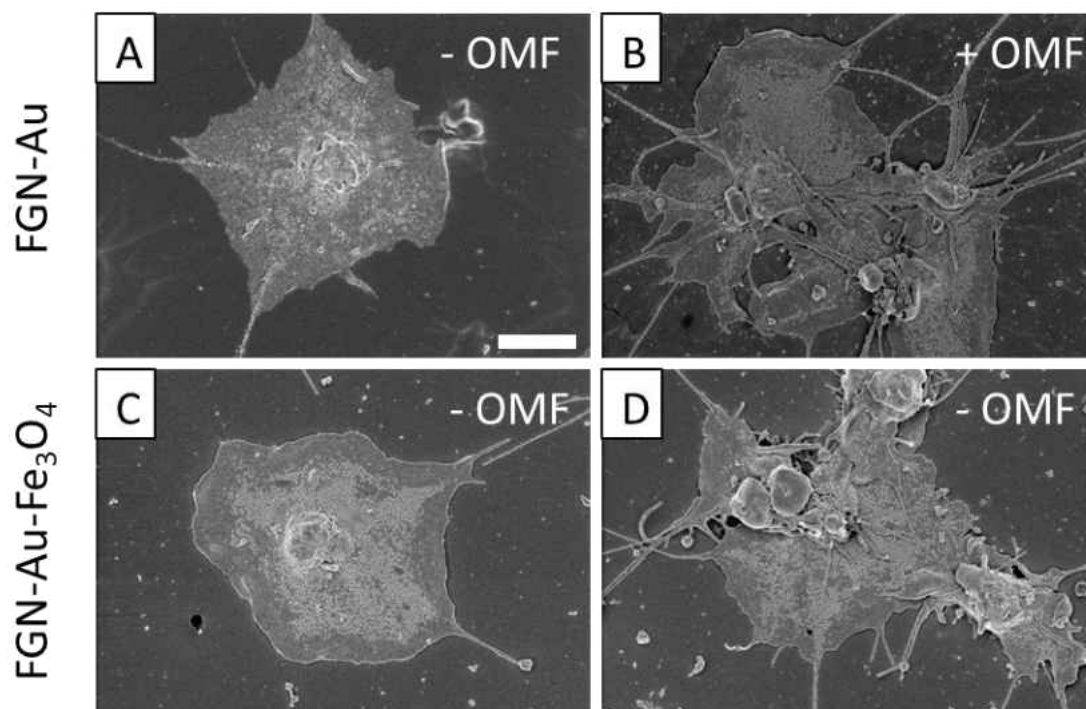
Figure 34

Figure 35. Controls for OMF-induced hyperthermia of fibrinogen-conjugated gold-coated magnetite-treated surface-activated platelets. A surface-activated platelet labeled with fibrinogen conjugated to colloidal gold (FGN-Au) and not exposed to the OMF is shown in (A). (B) shows a similarly labeled group of platelets that was exposed to the OMF. (C) and (D) show platelets labeled with fibrinogen-conjugated gold-coated magnetite (FGN-Au-Fe$_3$O$_4$), but not exposed to the OMF. All platelets display the expected morphology and show minimal damage to their surface. Size bar is 2 μm for all images.
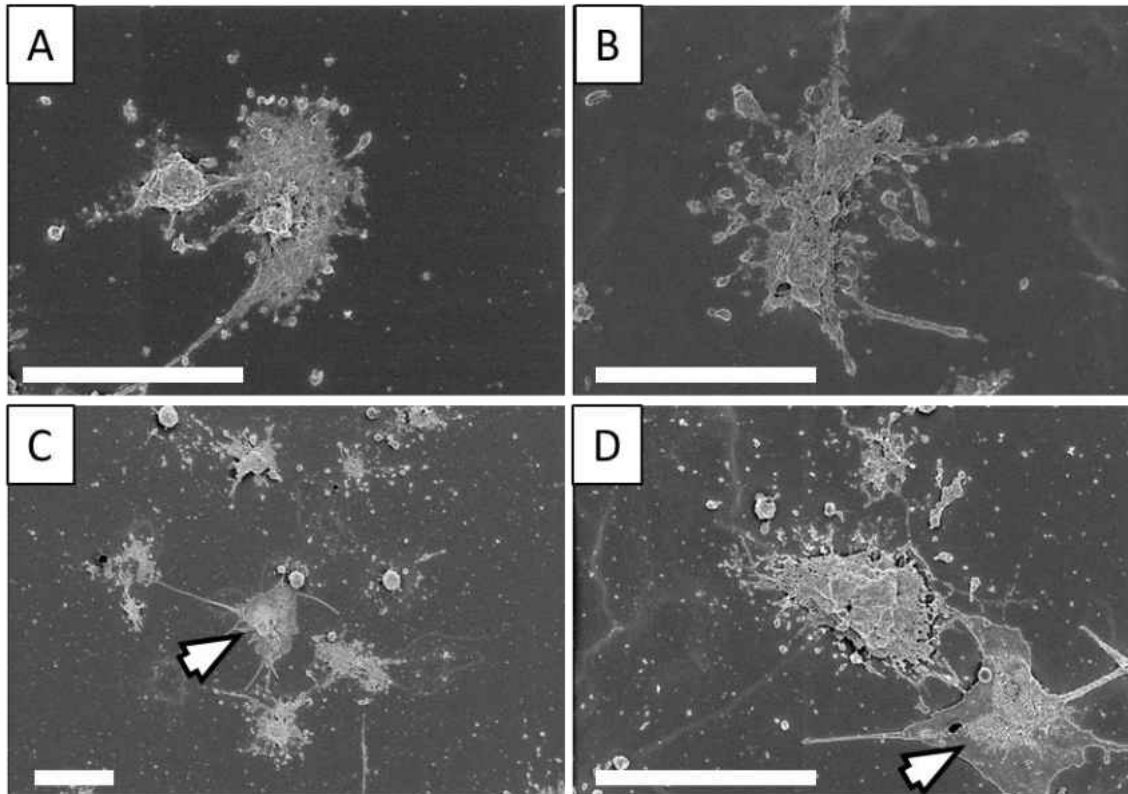
Figure 36. OMF induced hyperthermia of fibrinogen-conjugated gold-coated magnetite-treated surface-activated platelets. All micrographs depict the typical types of damage observed when surface-activated platelets are treated with fibrinogen-conjugated gold-coated magnetite nanoparticles and exposed to the OMF. Fragmented platelets show damaged surfaces with much of the cellular membrane missing, shown in (A, B). Remnants of the platelet membrane and internal platelet structures are often observed. Well-labeled, intact platelets can often be observed in the vicinity of highly fragmented platelets (arrowheads) in (C, D). Size bars are 5 µm.

Figure 37. Quantification of hyperthermic damage to surface-activated platelets. (A) and

(B) show typical low magnification fields used to quantify intact and fragmented

platelets. (A) demonstrates a field that was treated with fibrinogen-conjugated, gold-

coated magnetite not exposed to the OMF, (B) shows a similarly labeled sample that was

exposed to the OMF. Arrows indicate examples of fragmented platelets. Many more

fragmented platelets are observed in platelets labeled with gold-coated magnetite and

exposured to the OMF. Size bar is 50 μm for both images. Percent of fragmented

platelets found among platelets labeled with gold-coated magnetite, gold, or with no label

and either exposed to the OMF (dark bars) or unexposed (light bars) is shown in (C).

Only the platelet samples labeled with gold-coated magnetite and exposed to the OMF

demonstrated significantly levels of platelet fragmentation. Error bars show standard
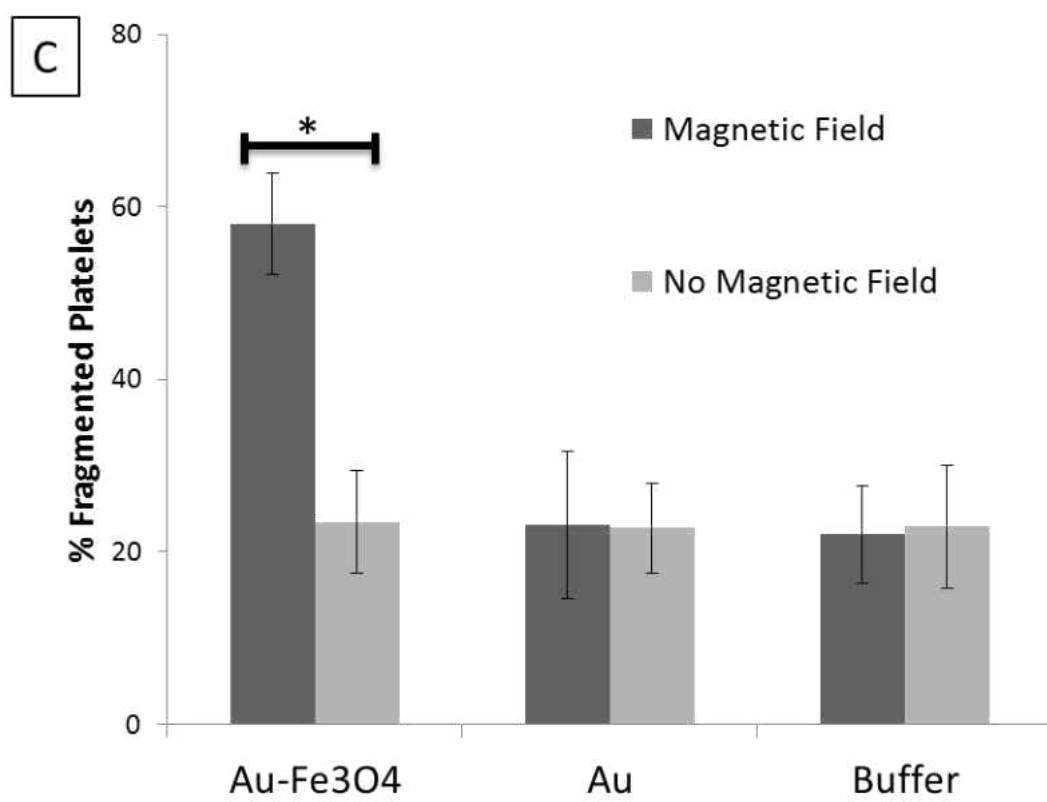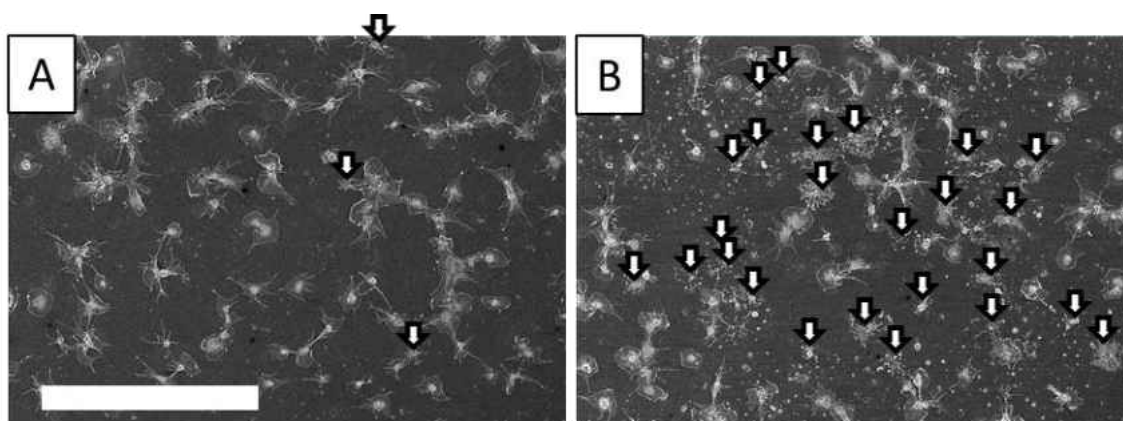
deviation, * indicates $p < 0.05$ (n = 7).

Figure 37

Figure 38. The effect of OMF exposure on platelet aggregates produced with unconjugated fibrinogen, then labeled with fibrinogen-conjugated nanoparticles. Control platelet aggregates that did not receive OMF exposure following labeling with fibrinogen-conjugated colloidal gold or fibrinogen-conjugated, gold-coated magnetite are shown in (A) and (B), respectively. Platelet aggregates exposed to the OMF after incubation with unconjugated fibrinogen (C) or fibrinogen-conjugated colloidal gold (D) have a similar appearance to aggregates that were not exposed to the OMF. Platelet aggregates treated with fibrinogen-conjugated gold-coated magnetite and exposed to the OMF had obvious structural damage, shown in two differently sized aggregates (E, F). Areas where the membrane integrity of platelets in the aggregate is compromised are indicated with arrows, demonstrating large holes or membranes with a "shredded" appearance. Size bars are 5 μm.
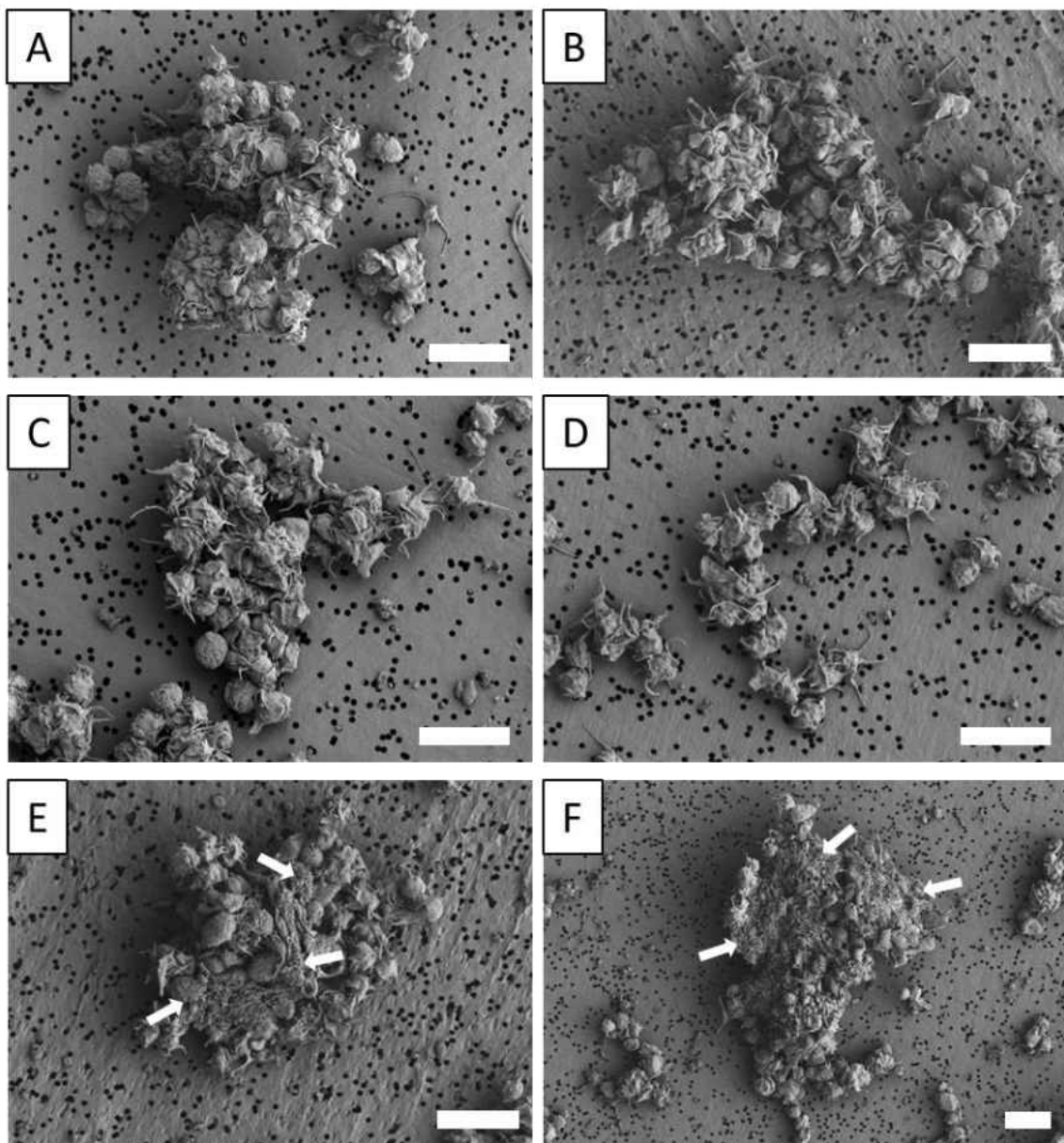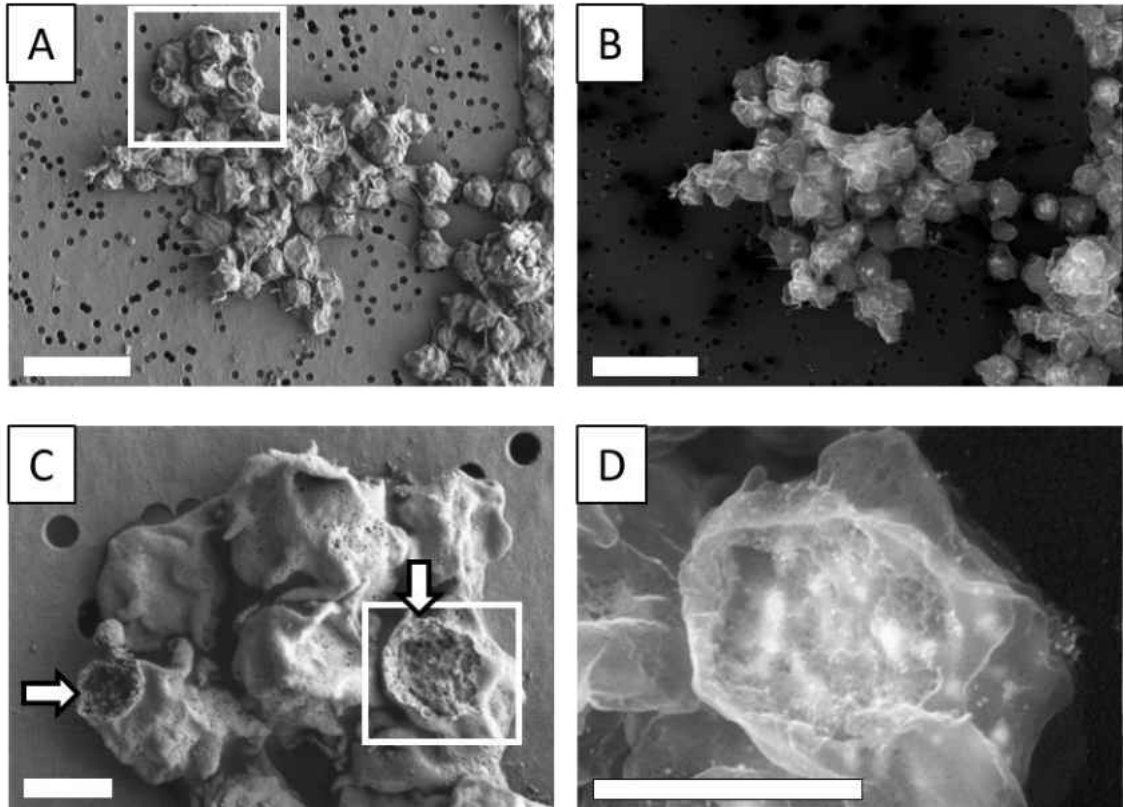
Figure 38

Figure 39. Characterization of hyperthermic damage observed on a platelet aggregate.

An example of a gold-coated magnetite-labeled platelet aggregate treated with the OMF

is shown using both SE imaging (A) and BSE imaging (B). (C) depicts the area

highlighted in by the box in (A) using secondary electron imaging at a higher

magnification. Arrows indicate areas where the platelet membrane has been significantly

disrupted. The damaged area encompassed by the box in (C) is shown at higher

magnification using backscattered electron imaging in (D). The damaged area is clearly

very strongly labeled with gold coated magnetite, observed as bright regions in the BSE

image. Size bars are 5 μm for (A,B) and 1 μm for (C,D).

Figure 40. TEM analysis of hyperthermic damage in platelets labeled with gold-coated

magnetite plus OMF exposure and control samples. Negative control platelet aggregates

labeled with fibrinogen-conjugated colloidal gold without OMF exposure (A) or with

OMF exposure (B). A platelet aggregate labeled with fibrinogen-conjugated gold-coated

magnetite but not exposed to the OMF is shown in (C). Hyperthermic damage to platelet

aggregates treated with fibrinogen-conjugated gold-coated magnetite and exposed to the

OMF is shown in (D). The lower portion of the aggregate is labeled heavily with gold-

coated magnetite and the platelet ultrastructure is extremely damaged. Areas with less

labeling such as the top half of (D) show little to no damage similar to (C). Size bars are

2 µm.
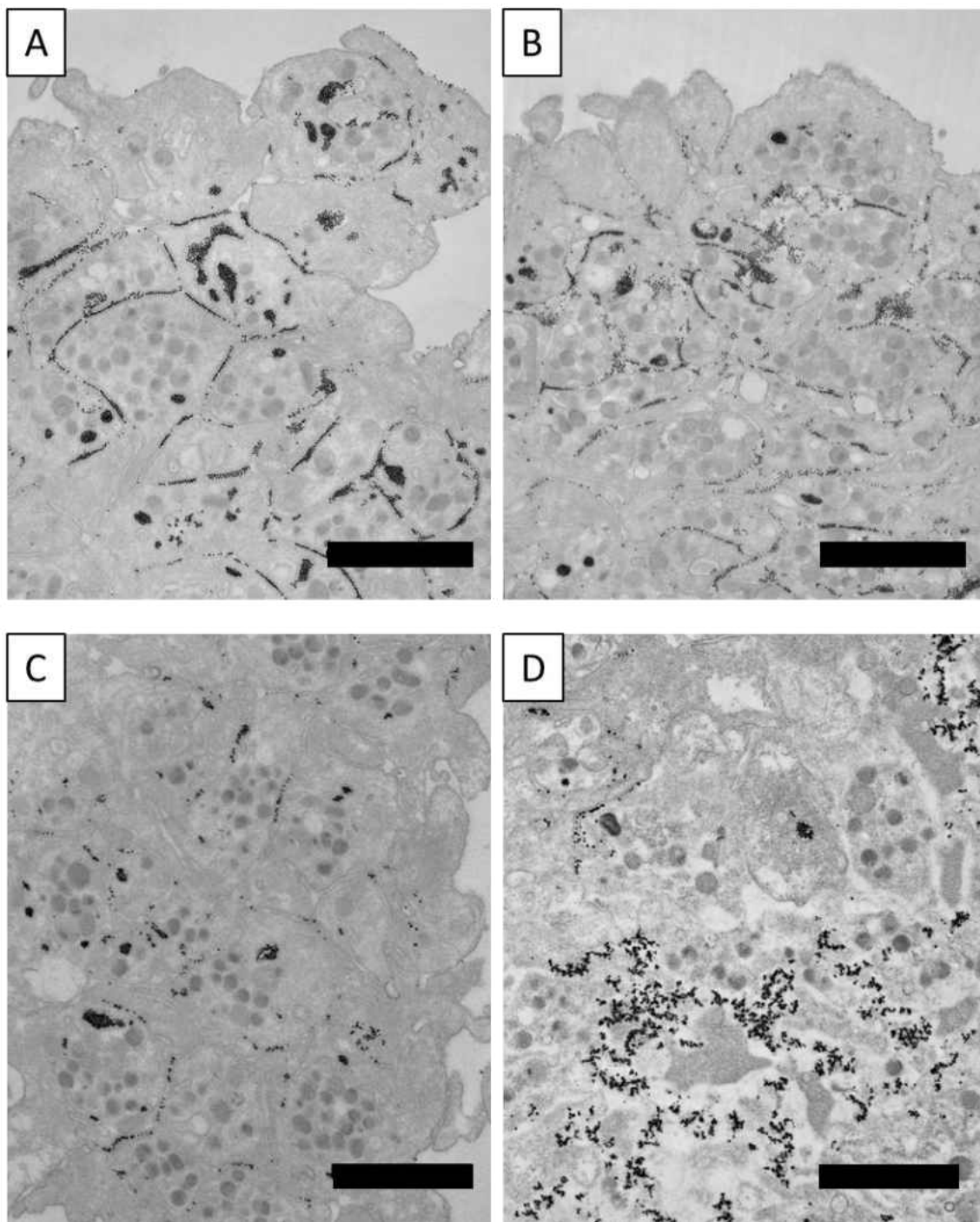
Figure 40

Figure 41. Platelet-derived membrane fragmentation observed by TEM after hyperthermia. The string-like platelet membrane fragments depicted in (A, B) were observed in ultrathin sections of platelet aggregates treated with fibrinogen-conjugated gold-coated magnetite and exposed to the OMF, but not in any of the negative controls. A higher magnification of the boxed area in (A) is shown in (B). The membrane fragments are still decorated with nanoparticles (arrows) and other membrane associated structures (arrowheads). Size bars are 1 μm.
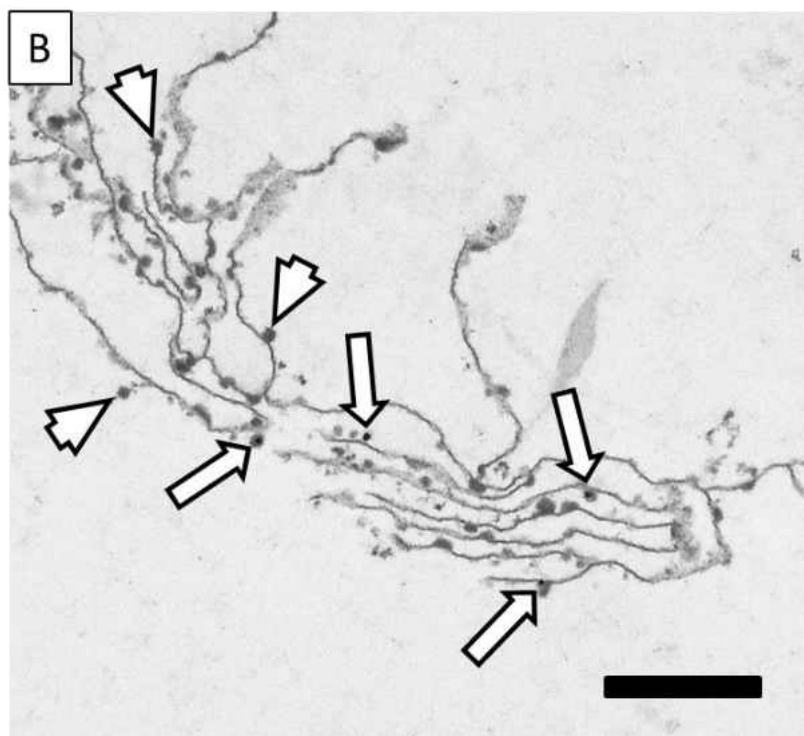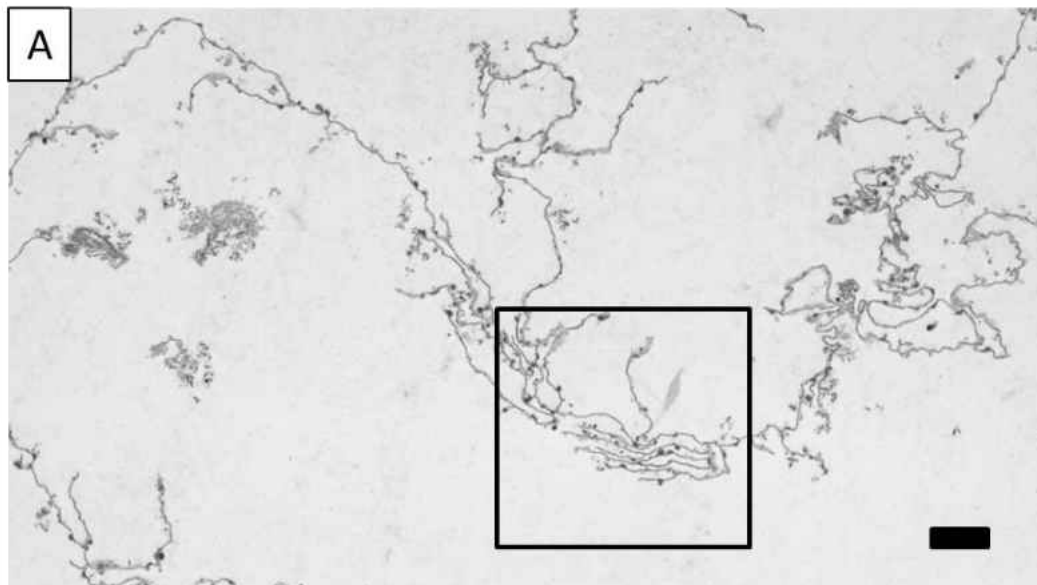
Figure 41

Figure 42. Quantification of hyperthermic damage to platelet aggregates. Typical fields of platelets treated with fibrinogen-conjugated gold-coated magnetite without OMF exposure (A) or with OMF exposure (B). The crosses indicate the exaggerated sampling points used to quantify the area of intact and fragmented platelets as well as platelet-derived debris. Size bar is 20 μm for (A, B). The percent of the sample covered by fragmented platelets plus debris for platelet aggregates labeled with gold-coated magnetite, gold, or with no label (buffer) and either exposed or not exposed to the OMF is shown in (C). Error bars show standard deviation, * indicates $p < 0.01$, $n = 9$ for gold-coated magnetite groups, $n = 3$ for colloidal gold and buffer controls.
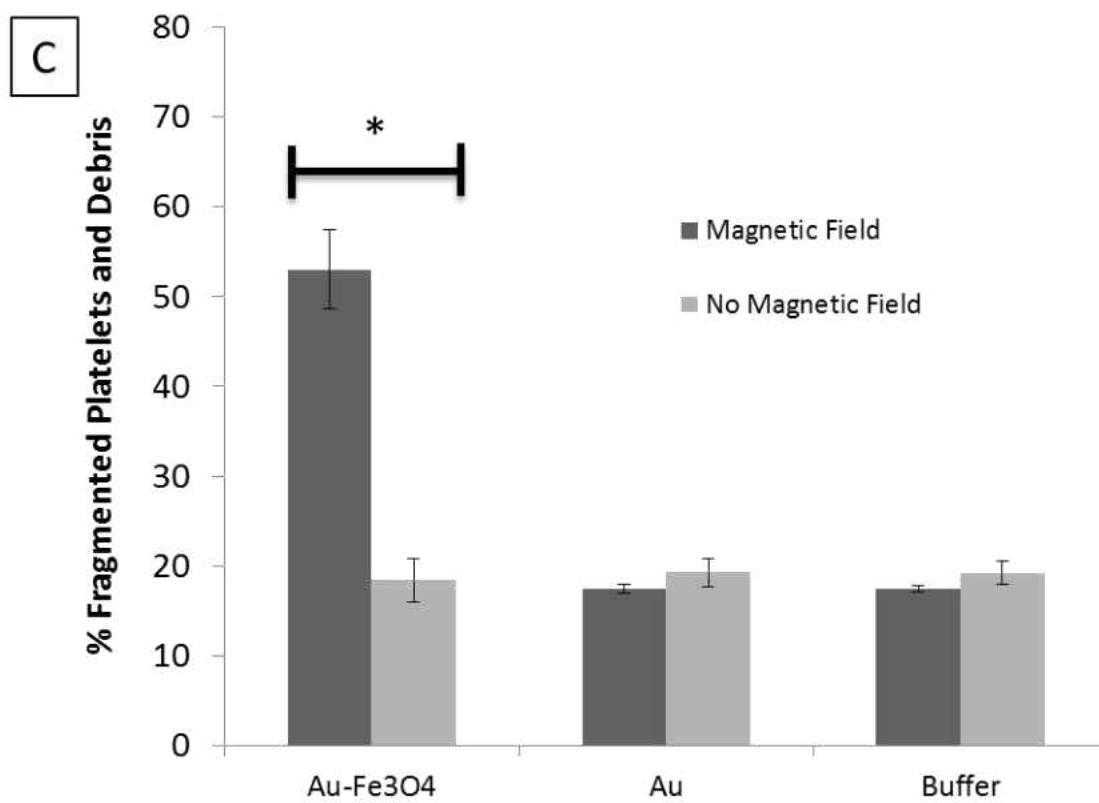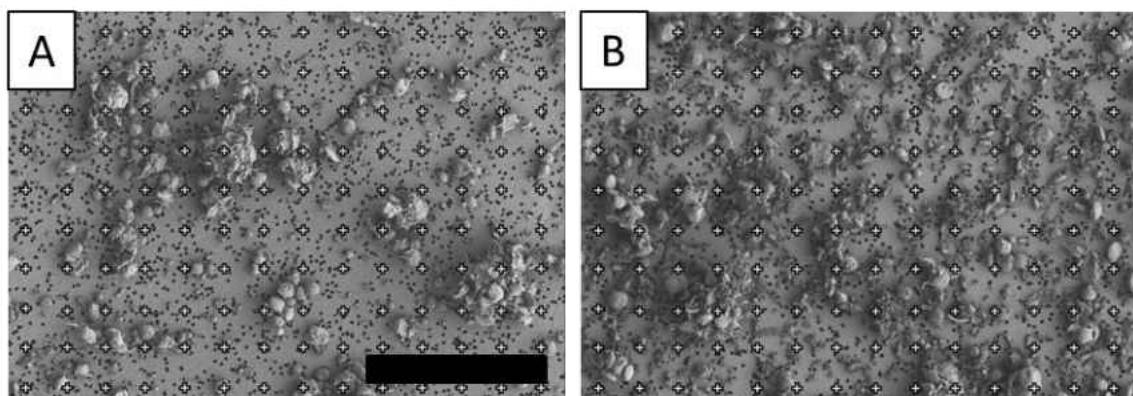
Figure 42

Figure 43. Quantification of aggregate damage under different OMF conditions. The percent fragmentation and platelet debris in platelet aggregates labeled with fibrinogen-conjugated gold-coated magnetite (diamonds) or fibrinogen-conjugated colloidal gold (squares) and exposed to the OMF for varying lengths of time is depicted in (A). Platelet aggregates were labeled with differing amounts of fibrinogen-conjugated, gold-coated magnetite and exposed to the OMF for 30 minutes in (B). Error bars are standard deviation, letters indicate groups that are at the same level of significance, n =3.
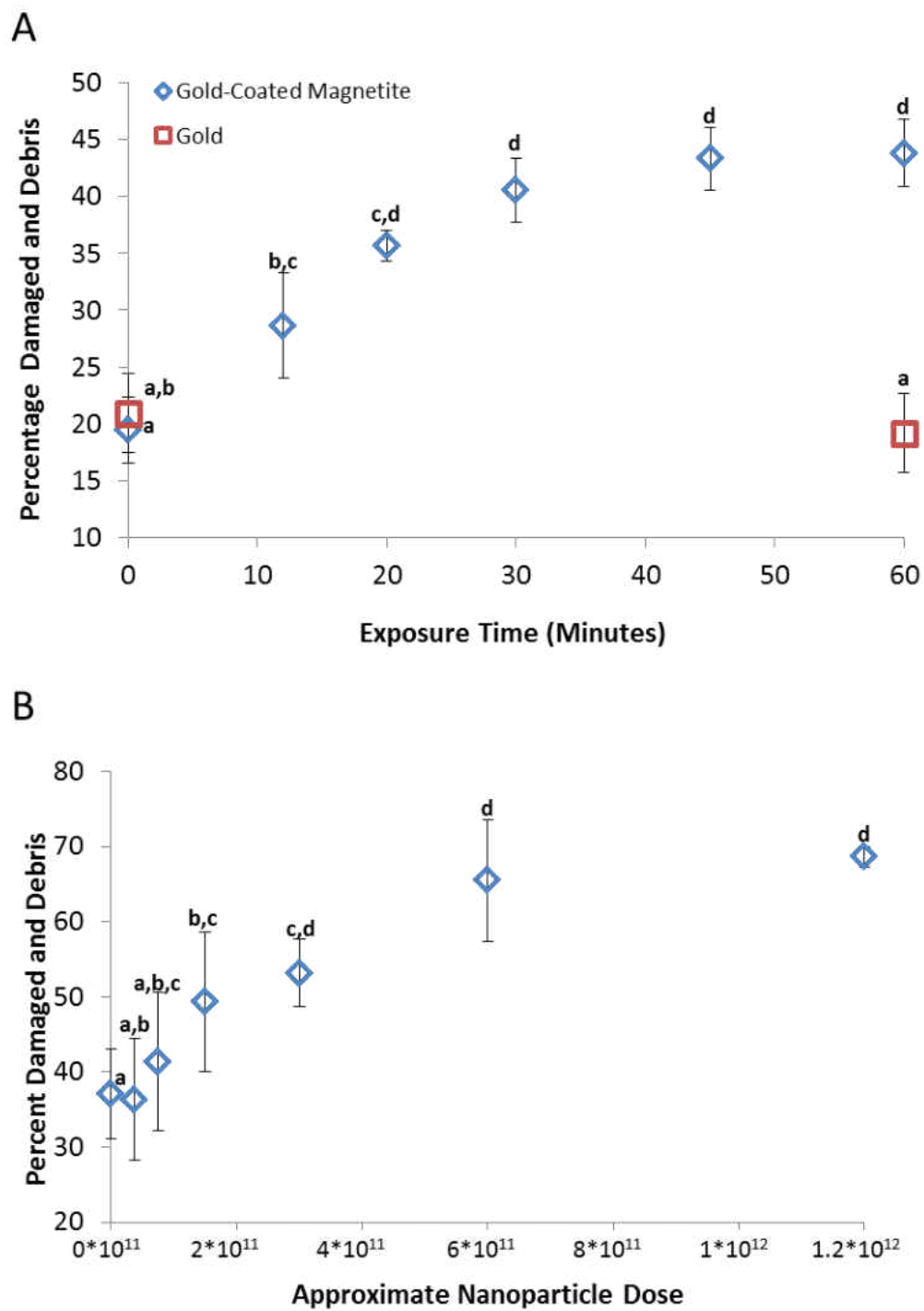
Figure 43

Tables

Variable	Intact Platelets	Fragmented Platelets	Platelet Debris	Intact Platelets/ (Fragmented + Debris)
Nanoparticle Type	0.39	0.0057	0.0018	0.0019
Gold-Coated Magnetite Batch	0.46	0.25	0.023	0.069
OMF	<0.0001	<0.0001	0.0003	0.0002
Blood Donor	0.0023	0.0016	0.26	0.13

Table 1. ANOVA analysis of the effects of hyperthermia on aggregated platelets using different models in the SAS PROC MIXED procedure. Models based on point counting of intact platelets, fragmented platelets, platelet-derived debris, and the ratio of intact platelets to (fragmented platelets + debris) were used as dependent variables. The significance of 4 independent variables, the type of nanoparticle, the specific batch of gold-coated magnetite used, OMF exposure, and the blood donor, was determined for each dependent variable. The amount of intact platelets was significantly affected by the OMF and the blood donor, but not by nanoparticle type or batch of gold-coated magnetite. When fragmented platelets were used as the dependent variable, nanoparticle type, OMF exposure, and the blood donor were significant. Platelet-derived debris was significantly affected by the nanoparticle type, batch of gold-coated magnetite, and the OMF. The ratio of intact platelets to (fragmented platelets + debris) demonstrated significance in nanoparticle type and OMF exposure, but not to gold-coated magnetite batch or blood donor. n = 30, sample means derived from 150 fields of view.

References:

1.   Roti Roti, J. L. 2008. Cellular responses to hyperthermia (40-46 C): Cell killing and molecular events. *Int. J. Hyperthermia* 24:3-15.

2.   Li, S., S. Chien, and P. I. Brånemark. 1999. Heat shock-induced necrosis and apoptosis in osteoblasts. *J. Orthop. Res.* 17:891-899.

3.   Ito, A., H. Honda, and T. Kobayashi. 2006. Cancer immunotherapy based on intracellular hyperthermia using magnetite nanoparticles: A novel concept of "heat-controlled necrosis" with heat shock protein expression. *Cancer Immunol. Immunother.* 55:320-328.

4.   Harmon, B. V., Y. S. Takano, C. M. Winterford, and G. C. Gobé. 1991. The role of apoptosis in the response of cells and tumours to mild hyperthermia. *Int. J. Radiat. Biol.* 59:489-501.

5.   Busch, W. 1866. Uber den Einfluss weichen Hefttigere Erysipelen zuweilen auf Organisierte Neubildugen Ausuken Verhandl. *Naturh. Ver. Preuss. Rheinl.* 23:28-30.

6.   Vidair, C. A., and W. C. Dewey. 1988. Two distinct modes of hyperthermic cell death. *Radiat. Res.* 116:157-171.

7.   Vaupel, P. W., and D. K. Kelleher. 2010. Pathophysiological and vascular characteristics of tumours and their importance for hyperthermia: Heterogeneity is the key issue. *Int. J. Hyperthermia* 26:211-223.

8.   Konings, A. 1988. Membranes as targets for hyperthermic cell killing. In *Preclinical Hyperthermia*. W. Hinkelbein, G. Bruggmoser, R. Englhardt, and M. Wannenmacher, eds. Springer, Berlin. 9-21.

9.   Mulcahy, R., M. Gould, E. Hidvergi, C. Elson, and M. Yatvin. 1981. Hyperthermia and surface morphology of P388 ascites tumour cells: Effects of membrane modifications. *Int. J. Radiat. Biol. Stud. Phys. Chem. Med.* 39:95-106.

10.   Prasad, N., K. Rathinasamy, D. Panda, and D. Bahadur. 2007. Mechanism of cell death induced by magnetic hyperthermia with nanoparticles of γ-MnxFe2− xO3 synthesized by a single step proces. *J. Mater. Chem.* 17:5042-5051.

11.   Coss, R. A., W. C. Dewey, and J. R. Bamburg. 1982. Effects of hyperthermia on dividing chinese hamster ovary cells and on microtubules in vitro. *Cancer Res.* 42:1059-1071.

12.	Storm, F. K., W. H. Harrison, R. S. Elliott, and D. L. Morton. 1980. Hyperthermic therapy for human neoplasms: Thermal death time. *Cancer* 46:1849-1854.

13.	Asin, L., M. R. Ibarra, A. Tres, and G. F. Goya. 2012. Controlled cell death by magnetic hyperthermia: Effects of exposure time, field amplitude, and nanoparticle concentration. *Pharm. Res.* 29:1319-1327.

14.	Jordan, A., R. Scholz, K. Maier-Hauff, M. Johannsen, P. Wust, J. Nadobny, H. Schirra, H. Schmidt, S. Deger, S. Loening, W. Lanksch, and R. Felix. 2001. Presentation of a new magnetic field therapy system for the treatment of human solid tumors with magnetic fluid hyperthermia. *J. Magn. Magn. Mater.* 225:118-126.

15.	Sonvico, F., S. Mornet, S. Vasseur, C. Dubernet, D. Jaillard, J. Degrouard, J. Hoebeke, E. Duguet, P. Colombo, and P. Couvreur. 2005. Folate-conjugated iron oxide nanoparticles for solid tumor targeting as potential specific magnetic hyperthermia mediators: Synthesis, physicochemical characterization, and in vitro experiments. *Bioconjugate Chem.* 16:1181-1188.

16.	Krystofiak, E. S., V. Z. Matson, D. A. Steeber, and J. A. Oliver. 2012. Elimination of tumor cells using folate receptor targeting by antibody-conjugated, gold-coated magnetite nanoparticles in a murine breast cancer model. *J. Nanomat.* 2012:431012.

17.	Kaiser, M., J. Heintz, I. Kandela, and R. Albrecht. 2007. Tumor cell death induced by membrane melting via immunotargeted, inductively heated core/shell nanoparticles. *Microsc. Microanal.* 13:18-19.

18.	Nikfarjam, M., V. Muralidharan, C. Malcontenti-Wilson, and C. Christophi. 2005. The apoptotic response of liver and colorectal liver metastases to focal hyperthermic injury. *Anticancer Res.* 25:1413-1419.

19.	Vlad, M., C. Şerboiu, A. T. Ispas, I. Giuvărăşteanu, E. Ungureanu, and N. Ionescu. 2013. Electron microscopy of the morphological changes in rat viscera during experimental hyperthermic shock. *J. Med. Life* 6:55-60.

20.	Chu, M., Y. Shao, J. Peng, X. Dai, H. Li, Q. Wu, and D. Shi. 2013. Near-infrared laser light mediated cancer therapy by photothermal effect of Fe3O4 magnetic nanoparticles. *Biomaterials* 34:4078-4088.

21.	Guardia, P., R. Di Corato, L. Lartigue, C. Wilhelm, A. Espinosa, M. Garcia-Hernandez, F. Gazeau, L. Manna, and T. Pellegrino. 2012. Water-soluble iron oxide nanocubes with high values of specific absorption rate for cancer cell hyperthermia treatment. *ACS Nano* 6:3080-3091.

22. Kobayashi, T. 2011. Cancer hyperthermia using magnetic nanoparticles. *Biotechnol. J.* 6:1342-1347.

23. Srivastava, P. K., A. Menoret, S. Basu, R. J. Binder, and K. L. McQuade. 1998. Heat shock proteins come of age: Primitive functions acquire new roles in an adaptive world. *Immunity* 8:657-665.

24. Huff, T. B., L. Tong, Y. Zhao, M. N. Hansen, J. X. Cheng, and A. Wei. 2007. Hyperthermic effects of gold nanorods on tumor cells. *Nanomedicine (Lond)* 2:125-132.

25. DeNardo, S. J., G. L. DeNardo, A. Natarajan, L. A. Miers, A. R. Foreman, C. Gruettner, G. N. Adamson, and R. Ivkov. 2007. Thermal dosimetry predictive of efficacy of 111In-ChL6 nanoparticle AMF–induced thermoablative therapy for human breast cancer in mice. *J. Nucl. Med.* 48:437-444.

26. Muckle, D. S., and J. A. Dickson. 1971. The selective inhibitory effect of hyperthermia on the metabolism and growth of malignant cells. *Br. J. Cancer* 25:771-778.

27. Shinkai, M., M. Yanase, H. Honda, T. Wakabayashi, J. Yoshida, and T. Kobayashi. 1996. Intracellular hyperthermia for cancer using magnetite cationic liposomes: in vitro study. *Jpn. J. Cancer Res.* 87:1179-1183.

28. Shiu, M. H., and J. G. Fortner. 1980. Intraperitoneal hyperthermic treatment of implanted peritoneal cancer in rats. *Cancer Res.* 40:4081-4084.

29. Storm, F. K., W. H. Harrison, R. S. Elliott, and D. L. Morton. 1979. Normal tissue and solid tumor effects of hyperthermia in animal models and clinical trials. *Cancer Res.* 39:2245-2251.

30. Mazzucchelli, S., M. Colombo, C. De Palma, A. Salvade, P. Verderio, M. D. Coghi, E. Clementi, P. Tortora, F. Corsi, and D. Prosperi. 2010. Single-domain protein A-engineered magnetic nanoparticles: Toward a universal strategy to site-specific labeling of antibodies for targeted detection of tumor cells. *ACS Nano* 4:5693-5702.

31. Gupta, A. K., and M. Gupta. 2005. Synthesis and surface engineering of iron oxide nanoparticles for biomedical applications. *Biomaterials* 26:3995-4021.

32. Huang, X., P. K. Jain, I. H. El-Sayed, and M. A. El-Sayed. 2006. Determination of the minimum temperature required for selective photothermal destruction of cancer cells with the use of immunotargeted gold nanoparticles. *Photochem. Photobiol.* 82:412-417.

33. Goodrich, G. P., L. Bao, K. Gill-Sharp, K. L. Sang, J. Wang, and J. D. Payne. 2010. Photothermal therapy in a murine colon cancer model using near-infrared absorbing gold nanorods. *J. Biomed. Opt.* 15:018001-018001.

34. Zharov, V. P., E. N. Galitovskaya, C. Johnson, and T. Kelly. 2005. Synergistic enhancement of selective nanophotothermolysis with gold nanoclusters: Potential for cancer therapy. *Lasers Surg. Med.* 37:219-226.

35. Gannon, C. J., C. R. Patra, R. Bhattacharya, P. Mukherjee, and S. A. Curley. 2008. Intracellular gold nanoparticles enhance non-invasive radiofrequency thermal destruction of human gastrointestinal cancer cells. *J. Nanobiotechnology* 6:2.

36. Moran, C. H., S. M. Wainerdi, T. K. Cherukuri, C. Kittrell, B. J. Wiley, N. W. Nicholas, S. A. Curley, J. S. Kanzius, and P. Cherukuri. 2009. Size-dependent joule heating of gold nanoparticles using capacitively coupled radiofrequency fields. *Nano. Res.* 2:400-405.

37. Rudolf, H., D. Silvio, M. Robert, and Z. Matthias. 2006. Magnetic particle hyperthermia: Nanoparticle magnetism and materials development for cancer therapy. *J. Phys: Condens. Matter* 18:S2919.

38. Laurent, S., S. Dutz, U. O. Häfeli, and M. Mahmoudi. 2011. Magnetic fluid hyperthermia: Focus on superparamagnetic iron oxide nanoparticles. *Adv. Colloid Interface Sci.* 166:8-23.

39. Prevo, B. G., S. A. Esakoff, A. Mikhailovsky, and J. A. Zasadzinski. 2008. Scalable routes to gold nanoshells with tunable sizes and response to near-infrared pulsed-laser irradiation. *Small* 4:1183-1195.

40. Cole, J. R., N. A. Mirin, M. W. Knight, G. P. Goodrich, and N. J. Halas. 2009. Photothermal efficiencies of nanoshells and nanorods for clinical therapeutic applications. *J. Phys. Chem. C* 113:12090-12094.

41. Huang, X., W. Qian, I. H. El-Sayed, and M. A. El-Sayed. 2007. The potential use of the enhanced nonlinear properties of gold nanospheres in photothermal cancer therapy. *Lasers Surg. Med.* 39:747-753.

42. Hirsch, L. R., R. J. Stafford, J. A. Bankson, S. R. Sershen, B. Rivera, R. E. Price, J. D. Hazle, N. J. Halas, and J. L. West. 2003. Nanoshell-mediated near-infrared thermal therapy of tumors under magnetic resonance guidance. *Proc. Natl. Acad. Sci. USA* 100:13549-13554.

43. Vera, J., and Y. Bayazitoglu. 2009. A note on laser penetration in nanoshell deposited tissue. *Int. J. Heat Mass Transfer* 52:3402-3406.

44. Gordon, R. T., J. R. Hines, and D. Gordon. 1979. Intracellular hyperthermia. A biophysical approach to cancer treatment via intracellular temperature and biophysical alterations. *Med. Hypotheses* 5:83-102.

45. Fortin, J. P., F. Gazeau, and C. Wilhelm. 2008. Intracellular heating of living cells through Neel relaxation of magnetic nanoparticles. *Eur. Biophys. J.* 37:223-228.

46. Strohbehn, J. W., and E. B. Douple. 1984. Hyperthermia and cancer therapy: A review of biomedical engineering contributions and challenges. *IEEE Trans. Biomed. Eng.* 31:779-787.

47. Pankhurst, Q. A., J. Connolly, S. K. Jones, and J. Dobson. 2003. Applications of magnetic nanoparticles in biomedicine. *J. Phys D: Appl. Phys.* 36:R167.

48. Hilger, I., R. Hiergeist, R. Hergt, K. Winnefeld, H. Schubert, and W. A. Kaiser. 2002. Thermal ablation of tumors using magnetic nanoparticles: An in vivo feasibility study. *Invest. Radiol.* 37:580-586.

49. Johannsen, M., B. Thiesen, A. Jordan, K. Taymoorian, U. Gneveckow, N. Waldöfner, R. Scholz, M. Koch, M. Lein, K. Jung, and S. A. Loening. 2005. Magnetic fluid hyperthermia (MFH) reduces prostate cancer growth in the orthotopic Dunning R3327 rat model. *Prostate* 64:283-292.

50. Lattuada, M., and T. A. Hatton. 2006. Functionalization of monodisperse magnetic nanoparticles. *Langmuir* 23:2158-2168.

51. Mornet, S., J. Portier, and E. Duguet. 2005. A method for synthesis and functionalization of ultrasmall superparamagnetic covalent carriers based on maghemite and dextran. *J. Magn. Magn. Mater.* 293:127-134.

52. Hu, F. Q., L. Wei, Z. Zhou, Y. L. Ran, Z. Li, and M. Y. Gao. 2006. Preparation of biocompatible magnetite nanocrystals for in vivo magnetic resonance detection of cancer. *Adv. Mater.* 18:2553-2556.

53. Wang, Z., Q. Shi, S. Li, J. Du, J. Liu, and K. Dai. 2010. Hyperthermia induces platelet apoptosis and glycoprotein Ibα ectodomain shedding. *Platelets* 21:229-237.

54. Etulain, J., M. J. Lapponi, S. J. Patrucchi, M. A. Romaniuk, R. Benzadón, G. L. Klement, S. Negrotto, and M. Schattner. 2011. Hyperthermia inhibits platelet hemostatic functions and selectively regulates the release of alpha-granule proteins. *J. Thromb. Haemost.* 9:1562-1571.

55. Nakayama, T., and W. Nakamura. 1984. Platelet aggregation induced in mice by whole-body hyperthermia. *Radiat. Res.* 98:583-590.

56. Strother, S. V., J. M. Bull, and S. A. Branham. 1986. Activation of coagulation during therapeutic whole body hyperthermia. *Thromb. Res.* 43:353-360.

57. Bevers, E. M., P. Comfurius, and R. F. Zwaal. 1983. Changes in membrane phospholipid distribution during platelet activation. *Biochim. Biophys. Acta* 736:57-66.

58. Leytin, V., D. J. Allen, E. Lyubimov, and J. Freedman. 2007. Higher thrombin concentrations are required to induce platelet apoptosis than to induce platelet activation. *Br. J. Haematol.* 136:762-764.

59. Vanags, D. M., S. Orrenius, and M. Aguilar-Santelises. 1997. Alterations in Bcl-2/Bax protein levels in platelets form part of an ionomycin-induced process that resembles apoptosis. *Br. J. Haematol.* 99:824-831.

60. Ellis, E. A. 2006. Solutions to the problem of substitution of ERL 4221 for vinyl cyclohexene dioxide in spurr low viscoity embedding formulations. *Microsc. Today* 14:32-33.

61. Holdorf, M. M., H. A. Owen, S. R. Lieber, L. Yuan, N. Adams, C. Dabney-Smith, and C. A. Makaroff. 2012. Arabidopsis ETHE1 encodes a sulfur dioxygenase that is essential for embryo and endosperm development. *Plant Physiol.* 160:226-236.

62. Simmons, S. R., and R. M. Albrecht. 1996. Self-association of bound fibrinogen on platelet surfaces. *J. Lab. Clin. Med.* 128:39-50.

63. Escolar, G., E. Leistikow, and J. G. White. 1989. The fate of the open canalicular system in surface and suspension-activated platelets. *Blood* 74:1983-1988.

64. Ginsberg, M. H., F. Kozin, M. O'Malley, and D. J. McCarty. 1977. Release of platelet constituents by monosodium urate crystals. *J. Clin. Invest.* 60:999-1007.

65. Ahrens, S., S. Zelenay, D. Sancho, P. Hanč, S. Kjaer, C. Feest, G. Fletcher, C. Durkin, A. Postigo, M. Skehel, F. Batista, B. Thompson, M. Way, C. Reis e Sousa, and O. Schulz. 2012. F-actin is an evolutionarily conserved damage-associated molecular pattern recognized by DNGR-1, a receptor for dead cells. *Immunity* 36:635-645.

66. Blair, P., and R. Flaumenhaft. 2009. Platelet α-granules: Basic biology and clinical correlates. *Blood Rev.* 23:177-189.

67. McNicol, A., and S. J. Israels. 1999. Platelet dense granules: Structure, function and implications for haemostasis. *Thromb. Res.* 95:1-18.

68.   Marguerie, G. A., E. F. Plow, and T. S. Edgington. 1979. Human platelets possess an inducible and saturable receptor specific for fibrinogen. *J. Biol. Chem.* 254:5357-5363.

69.   Bennett, J. S., and G. Vilaire. 1979. Exposure of platelet fibrinogen receptors by ADP and epinephrine. *J. Clin. Invest.* 64:1393-1401.

70.   McEver, R. P., N. L. Baenziger, and P. W. Majerus. 1980. Isolation and quantitation of the platelet membrane glycoprotein deficient in thrombasthenia using a monoclonal hybridoma antibody. *J. Clin. Invest.* 66:1311-1318.

Chapter 5: Conclusions

Fibrinogen targeting to select for activated platelets:

Targeting platelets through their fibrinogen receptor, the integrin $\alpha_{IIb}\beta_3$, has been recognized as a powerful tool for anti-platelet therapy (1). This integrin is present at high copy number on each platelet (2-4) and its competency to bind fibrinogen is tightly controlled through distinct conformational changes in the integrin (5). Ligand cross-linked $\alpha_{IIb}\beta_3$ centralizes along the platelet membrane, concentrating the bound fibrinogen (6, 7). This can be exploited to concentrate fibrinogen conjugates to increase therapeutic effects such as localized hyperthermia. We built upon earlier studies to show that fibrinogen-conjugated nanoparticles will selectively bind to an activated platelet population. Antibody treatments, such as abciximab, that do not discriminate well between populations of activated and quiescent platelets, are associated with increased bleeding risk (8). The capacity of fibrinogen to select for the activated population of platelets provides a powerful tool to directly target platelets involved in a thrombus while leaving circulating platelets unaffected, and is therefore expected to deliver significant therapeutic benefit.

Fibrinogen-based targeting, however, has some complications that must be considered. In both the murine and human *in vivo* systems, activated platelets will be bathed in unconjugated free fibrinogen from the blood. Fibrinogen from blood binds to unoccupied $\alpha_{IIb}\beta_3$ receptors. Once these $\alpha_{IIb}\beta_3$ receptors are occupied, the targeted fibrinogen conjugate will no longer be able to bind to that site. In our studies we observed reduced conjugate binding when we labeled preformed aggregates in the presence of

unconjugated fibrinogen as compared to gel-filtered platelets aggregated with fibrinogen conjugates as the only source of supplemental fibrinogen. Similarly, labeling with fibrinogen-conjugated colloidal gold or gold-coated magnetite was further reduced in aggregated platelet-rich plasma. While the number of bound nanoparticles was reduced when compared to aggregates produced using conjugated nanoparticles, the labeling was still at a fairly high density. Nanoparticle labeling was inhibited even further in blood clot-like platelet aggregates that contained fibrin, the polymerized product of thrombin-cleaved fibrinogen, as observed in platelet-rich plasma samples aggregated with thrombin. The reduction in binding is likely caused by binding of plasma fibrinogen to the platelets in combination with steric hindrance from the fibrin within the platelet aggregate. A true blood clot would likely have similar labeling to thrombin-aggregated platelet-rich plasma.

The reduction in binding may be dealt with by modifications to the original targeting strategy. Many ligand-induced binding site monoclonal antibodies have been developed against $\alpha_{IIb}\beta_3$ (9-12). These antibodies select for the activated conformation of $\alpha_{IIb}\beta_3$ which is only present on activated platelets. Careful selection or development of a new antibody that recognizes the active conformation of $\alpha_{IIb}\beta_3$ and is not sterically hindered by fibrinogen bound to $\alpha_{IIb}\beta_3$ would allow for the same $\alpha_{IIb}\beta_3$ targeting methodology we employed. However, the antibody would alleviate the problem of unconjugated fibrinogen limiting the number of binding sites. Penetration of the conjugate into the clot may still be problematic, although we expect the normal movement of cross-linked receptors to at least partially address this issue.

Fibrin within blood clots can likely impair conjugates, fibrinogen- or antibody-based, from binding to the activated platelets through steric hindrance. This may be dealt with in future studies in two different ways, first, nanoparticles could be conjugated with fragments of fibrinogen rather than the entire molecules, this will reduce the hydrated nanoparticle diameter causing less steric hindrance. Second, the therapy could include co-administration of tPA along with conjugated nanoparticles. The tPA will lyse the fibrin within the blood clot causing a reduction in the structural integrity of the blood clot. tPA will have the added benefit in this situation of reducing the amount of fibrin around the blood clot, allowing the nanoparticles to more easily reach their targets and cause their desired effect. Further, with or without tPA, fibrinogen conjugates may integrate into the fibrin network in a blood clot and may be able to promote clot release by causing hyperthermia to the fibrin network thereby directly, providing a second method to help dissolve the blood clot.

Hyperthermia on platelets labeled with gold-coated magnetite in the presence of a magnetic field:

The effects of hyperthermia on cancer are well represented in the literature (13-18). The effects of hyperthermia on platelets are poorly understood and even contain some apparent contradictory claims of both impairing platelet aggregation and adhesion, and causing them (19-21). We examined the effects of localized hyperthermia on platelets by use of fibrinogen-conjugated gold-coated magnetite that was exposed to an oscillating

magnetic field. The primary effect of hyperthermia on platelets was disruption of the

platelet membrane. Surface-activated platelets lost a large portion of their membrane and

associated structure during hyperthermic treatments. Similarly, aggregated platelets often

displayed areas of the aggregate containing holes that revealed apparent internal

cytoskeletal elements. The extent of damage observed is expected to be sufficient to

cause a reduction in the structural integrity of the platelets, weakening a potential blood

clot.

In all experiments where fibrinogen-conjugated, gold-coated magnetite-labeled platelets

were exposed to the OMF, some platelets appeared unaffected by hyperthermia. It is

possible we were unable to detect more subtle damage to the platelets using electron

microscopy, but it is also unlikely that damage so subtle that it is beyond the resolution of

electron microscopy would structurally weaken the platelets enough to have any

significant biological effect. Alternatively, the intact platelet may not have experienced

the same hyperthermic conditions as the neighboring fragmented platelets due to

differences in labeling intensity or localization. Nanoparticles localized close together on

the platelet membrane will cause a greater temperature rise at that site than if they were

evenly dispersed. A second possibility is that the different morphologies of gold-coated

magnetite have different abilities to cause hyperthermic damage. Platelets that bind a

large amount of one particular nanoparticle morphology may experience greater localized

hyperthermia, causing those platelets to fragment while others do not. These

morphologies include the isolated and aggregated nanoparticles described here, but may

also include yet uncharacterized morphologies. Modulation of the length of exposure to

the OMF and dosage of nanoparticles to platelets demonstrates that optimization of the hyperthermic protocol increases the level of platelet fragmentation. Additional iterations of optimization may produce even more dramatic results.

Further improvements to platelet hyperthermia may come from adjustment of the oscillation frequency of the magnetic field. These studies utilized a 500 kHz oscillation that was previously described for hyperthermic applications using gold-coated magnetite nanoparticles (22). Because superparamagnetic nanoparticles may be heated at lower frequencies below 500 kHz (18, 23-25), it is possible that our gold-coated magnetite may heat more efficiently at lower frequencies. The existing design of the OMF device makes it difficult to vary the frequency of the OMF in a time efficient manner, and essentially requires the entire circuit to be rebuilt and retuned. Replacing the capacitive elements with an impedance matching network would allow real time frequency modifications without causing reflective power. Refinements in the OMF frequency could result in hyperthermic treatments that are more effective and shorter in duration.

Implications for in vivo *treatment in a murine model:*

The next logical step for evaluation of fibrinogen-conjugated gold-coated magnetite for use as a platelet targeted ischemic stroke treatment is *in vivo* testing using a murine model of carotid artery thrombosis. We already examined the use of conjugated human fibrinogen in a murine system and found that its targeting ability was similar to that of conjugated murine fibrinogen. We have further examined the use of conjugates in

systems that approximate an *in vivo* blood clot as closely as possible in an *in vitro* system and found that nanoparticle binding does occur. Future studies will use the ferric chloride injury model to produce platelet-rich thrombi in murine carotid arteries. The occlusive clots formed with this method closely resemble those seen in human stroke patients (26, 27). Fibrinogen-conjugated gold-coated nanoparticles would be administered and either the entire mouse, or the anterior one-half to one-third of the animal, treated within the OMF. The treatment could be monitored by measuring blood flow through the artery by use of an ultrasonic probe. After the treatment is complete the success of the treatment can be assessed by electron microscopy. The entire procedure would be technically challenging. Microsurgery exposing the carotid artery of an anesthetized mouse must be performed in a manner that minimizes damage to the vessel and surrounding tissue. Our studies into the effect of nanoparticle dose on platelet hyperthermia showed a strong correlation between dose and level of platelet disruption. For the murine studies, it will be essential to deliver as many nanoparticles to the blood clot as possible. Effective delivery of fibrinogen-conjugated gold-coated magnetite nanoparticles to the blood clot will not be trivial. The best possible delivery method is to administer the nanoparticles by catheter to the site of the blood clot, but would be technically challenging due to the size of the murine vasculature and the fact that catheterizing an artery can often cause thrombotic events in itself. Alternatively, nanoparticles could be administered at the highest possible levels by tail vein injection and use normal blood circulation to distribute the nanoparticles to the activated platelets at the occlusion site. Blood flow at the site of occlusion is severely restricted which

might prevent nanoparticles from reaching the occlusion site when administered in this

manner.

While technically challenging, the results of our evaluation of fibrinogen-conjugated

gold-coated magnetite for anti-platelet therapy suggest that murine feasibility studies

should be pursued in an effort to further develop this ischemic stroke treatment.

References

1.   Coller, B. S., and S. J. Shattil. 2008. The GPIIb/IIIa (integrin αIIbβ3) odyssey: A technology-driven saga of a receptor with twists, turns, and even a bend. *Blood* 112:3011-3025.

2.   Marguerie, G. A., E. F. Plow, and T. S. Edgington. 1979. Human platelets possess an inducible and saturable receptor specific for fibrinogen. *J. Biol. Chem.* 254:5357-5363.

3.   Bennett, J. S., and G. Vilaire. 1979. Exposure of platelet fibrinogen receptors by ADP and epinephrine. *J. Clin. Invest.* 64:1393-1401.

4.   McEver, R. P., N. L. Baenziger, and P. W. Majerus. 1980. Isolation and quantitation of the platelet membrane glycoprotein deficient in thrombasthenia using a monoclonal hybridoma antibody. *J. Clin. Invest.* 66:1311-1318.

5.   Shattil, S. J., J. A. Hoxie, M. Cunningham, and L. F. Brass. 1985. Changes in the platelet membrane glycoprotein IIb.IIIa complex during platelet activation. *J. Biol. Chem.* 260:11107-11114.

6.   Loftus, J. C., and R. M. Albrecht. 1984. Redistribution of the fibrinogen receptor of human platelets after surface activation. *J. Cell Biol.* 99:822-829.

7.   Belitser, N., M. Anischuk, Y. Veklich, T. Pozdnjakova, and O. Gorkun. 1993. Fibrinogen internalization by ADP-stimulated blood platelets. Ultrastructural studies with fibrinogen-colloidal gold probes. *Thromb. Res.* 69:413-424.

8.   Adams, H. P., Jr., M. B. Effron, J. Torner, A. Dávalos, J. Frayne, P. Teal, J. Leclerc, B. Oemar, L. Padgett, E. S. Barnathan, and W. Hacke. 2008. Emergency administration of abciximab for treatment of patients with acute ischemic stroke:

results of an international phase III trial: Abciximab in Emergency Treatment of Stroke Trial (AbESTT-II). *Stroke* 39:87-99.

9. Kouns, W. C., C. D. Wall, M. M. White, C. F. Fox, and L. K. Jennings. 1990. A conformation-dependent epitope of human platelet glycoprotein IIIa. *J. Biol. Chem.* 265:20594-20601.

10. Nurden, P., M. Humbert, R. S. Piotrowicz, C. Bihour, C. Poujol, A. T. Nurden, and T. J. Kunicki. 1996. Distribution of ligand-occupied alpha IIb beta 3 in resting and activated human platelets determined by expression of a novel class of ligand-induced binding site recognized by monoclonal antibody AP6. *Blood* 88:887-899.

11. Mazurov, A. V., S. G. Khaspekova, T. V. Byzova, O. Tikhomirov, M. C. Berndt, B. Steiner, and W. C. Kouns. 1996. Stimulation of platelet glycoprotein IIb-IIIa (alpha IIb beta 3-integrin) functional activity by a monoclonal antibody to the N-terminal region of glycoprotein IIIa. *FEBS Lett.* 391:84-88.

12. Chen, P., C. X. Sun, and J. N. Liu. 2005. A novel anti-platelet monoclonal antibody (3C7) specific for the complex of integrin alpha IIb beta3 inhibits platelet aggregation and adhesion. *J. Biol. Chem.* 280:25403-25408.

13. Vidair, C. A., and W. C. Dewey. 1988. Two distinct modes of hyperthermic cell death. *Radiat. Res.* 116:157-171.

14. Vaupel, P. W., and D. K. Kelleher. 2010. Pathophysiological and vascular characteristics of tumours and their importance for hyperthermia: Heterogeneity is the key issue. *Int. J. Hyperthermia* 26:211-223.

15. Konings, A. 1988. Membranes as targets for hyperthermic cell killing. In *Preclinical Hyperthermia*. W. Hinkelbein, G. Bruggmoser, R. Englhardt, and M. Wannenmacher, eds. Springer, Berlin. 9-21.

16. Mulcahy, R., M. Gould, E. Hidvergi, C. Elson, and M. Yatvin. 1981. Hyperthermia and surface morphology of P388 ascites tumour cells: Effects of membrane modifications. *Int. J. Radiat. Biol. Stud. Phys. Chem. Med.* 39:95-106.

17. Prasad, N., K. Rathinasamy, D. Panda, and D. Bahadur. 2007. Mechanism of cell death induced by magnetic hyperthermia with nanoparticles of γ-MnxFe2$-$ xO3 synthesized by a single step proces. *J. Mater. Chem.* 17:5042-5051.

18. Asin, L., M. R. Ibarra, A. Tres, and G. F. Goya. 2012. Controlled cell death by magnetic hyperthermia: Effects of exposure time, field amplitude, and nanoparticle concentration. *Pharm. Res.* 29:1319-1327.

19. Wang, Z., Q. Shi, S. Li, J. Du, J. Liu, and K. Dai. 2010. Hyperthermia induces platelet apoptosis and glycoprotein Ibα ectodomain shedding. *Platelets* 21:229-237.

20. Etulain, J., M. J. Lapponi, S. J. Patrucchi, M. A. Romaniuk, R. Benzadón, G. L. Klement, S. Negrotto, and M. Schattner. 2011. Hyperthermia inhibits platelet hemostatic functions and selectively regulates the release of alpha-granule proteins. *J. Thromb. Haemost.* 9:1562-1571.

21. Nakayama, T., and W. Nakamura. 1984. Platelet aggregation induced in mice by whole-body hyperthermia. *Radiat. Res.* 98:583-590.

22. Kaiser, M., J. Heintz, I. Kandela, and R. Albrecht. 2007. Tumor cell death induced by membrane melting via immunotargeted, inductively heated core/shell nanoparticles. *Microsc. Microanal.* 13:18-19.

23. Sonvico, F., S. Mornet, S. Vasseur, C. Dubernet, D. Jaillard, J. Degrouard, J. Hoebeke, E. Duguet, P. Colombo, and P. Couvreur. 2005. Folate-conjugated iron oxide nanoparticles for solid tumor targeting as potential specific magnetic hyperthermia mediators: Synthesis, physicochemical characterization, and in vitro experiments. *Bioconjugate Chem.* 16:1181-1188.

24. Hilger, I., R. Hiergeist, R. Hergt, K. Winnefeld, H. Schubert, and W. A. Kaiser. 2002. Thermal ablation of tumors using magnetic nanoparticles: An in vivo feasibility study. *Invest. Radiol.* 37:580-586.

25. Johannsen, M., B. Thiesen, A. Jordan, K. Taymoorian, U. Gneveckow, N. Waldöfner, R. Scholz, M. Koch, M. Lein, K. Jung, and S. A. Loening. 2005. Magnetic fluid hyperthermia (MFH) reduces prostate cancer growth in the orthotopic Dunning R3327 rat model. *Prostate* 64:283-292.

26. Kurz, K. D., B. W. Main, and G. E. Sandusky. 1990. Rat model of arterial thrombosis induced by ferric chloride. *Thromb. Res.* 60:269-280.

27. Wang, X., and L. Xu. 2005. An optimized murine model of ferric chloride-induced arterial thrombosis for thrombosis research. *Thromb. Res.* 115:95-100.

CURRICULUM VITAE

Evan S. Krystofiak

Education
University of Wisconsin – Milwaukee, Milwaukee, WI
PhD Biological Sciences 2007-2013
Thesis Advisor: Dr. Julie Oliver
Thesis Title: Fibrinogen-conjugated gold-coated magnetite nanoparticles for targeted antiplatelet therapy

University of Minnesota, Minneapolis, MN
B.S. Biomedical Engineering 2003-2007

Awards
Ruth Walker Grant-in-Aid 2008, 2009, 2011, 2012
Joseph B. Baier Award 2008, 2010
Best Graduate Student Poster at Biological Sciences Symposium 2009
Midwest Microscopy and Microanalysis Student Travel Award 2012 (Declined)
Microscopy Society of American Presidential Student Award 2012

Publications

*Shared first author

E.S Krystofiak*, V.Z. Matson*, D.A. Steeber, and J.A. Oliver. 2012. Elimination of tumor cells using folate receptor targeting by antibody-conjugated gold-coated magnetite nanoparticles in a murine breast cancer model. *Journal of Nanomaterials* 2012: 431012. *Shared first author

E.S. Krystofiak*, E.C. Mattson*, R.M. Albrecht, P.M. Voyles, M. Gajdardziska-Josifovska, and J.A. Oliver. 2013. Novel morphologies and functionalization of gold-coated magnetite nanoparticles. *Microscopy and Microanalysis* 19:821-834.

J.K. Larson, M.J. Carvan III, R. Klaper, J. Teeguarden, G. Watanabe, K. Taya, **E.S. Krystofiak**, and R.J. Hutz. Low-dose gold nanoparticles exert endocrine-modulating effects on rat steroidogenesis *ex vivo* independent of oxidative stress. (submitted to *Nanotoxicology*)

E.S. Krystofiak, J.A. Oliver. Human fibrinogen supports normal hemostatic function in a mouse platelet system. (in preparation for submission to *Thromb. Res.*)

Peer-Reviewed Proceedings and Abstracts

E.S. Krystofiak, E.C. Mattson, R.M. Albrecht, M. Gajdardziska-Josifovska, J.A. Oliver. Multiple morphologies of gold-coated magnetite nanoparticles are conjugated with ligands and can produce receptor-mediated biological effects. *Microsc.Microanal.,* 19(Suppl 2).

E.S. Krystofiak, E.C. Mattson, M. Gajdardziska-Josifovska, J.A. Oliver. 2012. Protein conjugation by non-ionic adsorption both functionalizes and stabilizes gold-coated magnetite nanoparticles, *Microsc. Microanal.*, 18(Suppl 2). 1650-1651.

E.C. Mattson, **E.S. Krystofiak**, P.M. Voyles, M. Gajdardziska-Josifovska, and J.A. Oliver. 2012. Understanding gold growth on magnetite nanoparticles using probe-corrected scanning transmission electron microscopy, *Microsc. Microanal.*, 18(Suppl 2). 358-359.

J.A. Oliver, **E.S. Krystofiak**, L.G. Westrick. 2011. Fibrinogen binding to activated platelets in the presence of plasma concentration of the natural ligand may be sufficient to allow therapeutic targeting, *J. Thromb. Haemost.*, 9(Suppl. 2):P-TH-038.

J.A. Oliver, **E.S. Krystofiak**. 2011. Destruction of activated platelets with fibrinogen-conjugated core-shell nanoparticles, *J. Thromb. Haemost.* 7(Suppl. 2): P-TH-040.

E.C. Mattson, **E.S. Krystofiak**, P.M. Voyles, C. Hirschmugl, M. Gajdardziska-Josifovska, J.A. Oliver. 2011. Synthesis, structure, and morphology of magnetic core-shell nanoparticles, *Microsc. Microanal.*, 17(Suppl. 2):1428-1429.

E.S. Krystofiak, S. Rajput, R.M. Albrecht, M. Gajdardziska-Josifovska, J.A. Oliver. 2010. Synthesis and characterization of magnetite-gold core-shell nanoparticles, *Microsc. Microanal.*, 16(Suppl. 2): 1714-1715.

L.G. Westrick, **E.S. Krystofiak**, J.A. Oliver. 2010. Extensive reserve capacity for the binding and movement of fibrinogen on the surface of activated human platelets, *Circulation* 122: A13212.

E.S. Krystofiak, J.A. Oliver. 2009. Human fibrinogen supports normal hemostatic function in a mouse platelet system. *J. Thromb. Haemost.*, 7(Suppl. 2): PP-MO-039.

Presentations

E.S. Krystofiak, E.C. Mattson, R.M. Albrecht, M. Gajdardziska-Josifovska, J.A. Oliver. Multiple morphologies of gold-coated magnetite nanoparticles are conjugated with ligands and can produce receptor-mediated biological effects. Microscopy & Microanalysis 2013, August 04-08, Indianpolis, IN (**Oral** Presentation)

(**Invited**) **E.S. Krystofiak**, E.C. Mattson, M. Gajdardziska-Josifovska, J.A. Oliver. Protein conjugation by non-ionic adsorption both functionalizes and stabilizes gold-coated magnetite nanoparticles, Midwest Microscopy & Microanalysis 55th Anniversary Meeting, November 15, 2012, Deerfield, IL.

E.S. Krystofiak, E.C. Mattson, M. Gajdardziska-Josifovska, J.A. Oliver. Protein conjugation by non-ionic adsorption both functionalizes and stabilizes gold-coated magnetite nanoparticles. Microscopy & Microanalysis 2012, July 29 – August 2, 2012, Phoenix, AZ (Poster presentation).

E.S. Krystofiak, L.G. Westrick, J.A. Oliver. Evaluating fibrinogen binding for targeting activated platelets. Biological Sciences Research Symposium 2012, April 26, 2012, University of Wisconsin-Milwaukee (Oral presentation).

E.S. Krystofiak, S. Rajput, R.M. Albrecht, M. Gajdardziska-Josifovska, J.A. Oliver. 2010. Synthesis and characterization of magnetite-gold core-shell nanoparticles. Microscopy & Microanalysis 2010, August 01-05, 2010, Portland, OR (Oral presentation, presented by Dr. Oliver)

E.S. Krystofiak, J.A. Oliver. Human fibrinogen supports normal hemostatic function in a mouse platelet system. XXII Congress of the International Society on Thrombosis and Haemostasis, July 11-16, 2009, Boston, MA (Poster presentation).